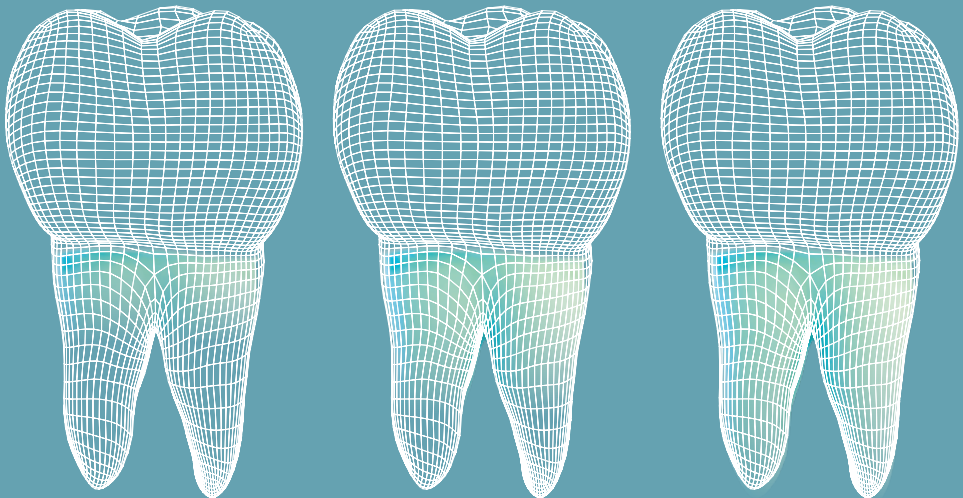


Mostafa EzEldeen

DENTAL TISSUE REGENERATION IN CHILDREN CAN WE MIMIC NATURE?



KU LEUVEN
BIOMEDICAL SCIENCES GROUP
FACULTY OF MEDICINE
DEPARTMENT OF IMAGING & PATHOLOGY
OMFS-IMPATh RESEARCH GROUP



Dental Tissue Regeneration in Children, Can We Mimic Nature?

Mostafa EzEldeen

PROMOTOR:
PROF. DR. REINHILDE JACOBS

CO-PROMOTORS:
PROF. DR. IVO LAMBRICHTS
PROF. DR. GHISLAIN OPDENAKKER

CHAIR:
PROF. DR. TANIA ROSKAMS

JURY MEMBERS:
PROF. DR. PAUL LAMBRECHTS
PROF. DR. SOFIE STRUYF
PROF. DR. IMAD ABOUT
PROF. DR. SARAH BAATOUT

Dissertation presented in partial fulfilment of
the requirements for the degree of
Doctor in Biomedical sciences

Leuven, December 2021



KU LEUVEN
GROEP BIOMEDISCHE WETENSCHAPPEN
FACULTEIT GENEESKUNDE
DEPARTMENT BEELDVORMING & PATHOLOGIE
OMFS-IMPATh ONDERZOEKSGROEP



Regeneratie Van Tandweefsel Bij Kinderen, Kunnen We De Natuur Imiteren?

Mostafa EzEldeen

PROMOTOR:

PROF. DR. REINHILDE JACOBS

CO-PROMOTOREN:

PROF. DR. IVO LAMBRECHTS

PROF. DR. GHISLAIN OPDENAKKER

CHAIR:

PROF. DR. TANIA ROSKAMS

JURYLEDEN:

PROF. DR. PAUL LAMBRECHTS

PROF. DR. SOFIE STRUYF

PROF. DR. IMAD ABOUT

PROF. DR. SARAH BAATOUT

Proefschrift voorgedragen
tot het behalen van de graad van
Doctor in de Biomedische Wetenschappen

Leuven, December 2021

"Look deep into nature,
and then you will understand everything better."

ALBERT EINSTEIN

Graphic design by Janine Kopatz
www.janinekopatz.com

©Mostafa EzEldeen, 2021

All rights reserved. No part of this thesis may be reproduced or transmitted in any form or by any means, without prior written permission of the authors, or when appropriate, from the publishers of the publications.

TABLE OF CONTENTS

List of abbreviations.....09
Introduction and aims..... 11

- The burden of oral disease 11
- Regenerative procedures for the management
of dental tissue loss in children..... 12
- Chemokine-mediated dental tissue regeneration..... 15
- Aim and objectives 17

PART I

**Developing and optimizing the tools to study
regenerative dental procedures**

CHAPTER 1

3-Dimensional Analysis of Regenerative Endodontic Treatment Outcome.....22

CHAPTER 2

As Low Dose as Sufficient Quality: Optimization of Cone-Beam
Computed Tomographic Scanning Protocol for Tooth Autotransplantation
Planning and Follow-up in Children38

PART II

**Tooth Autotransplantation as a current solution
full of future inspirations**

CHAPTER 3

Use of CBCT-guidance for Tooth Autotransplantation in Children 58

CHAPTER 4

Influence of Different 3D Printing Technologies on Accurate Tooth Replica
Fabrication Intended for CBCT-Guided Tooth Autotransplantation.....78

8	CHAPTER 5	
		3D Printed Temporary Veneer Restoring Autotransplanted Teeth in Children: Design and Concept Validation Ex Vivo 90

	CHAPTER 6	
		Multi-modality Imaging for the Characterization of the Patterns of Dental Pulp Healing After Tooth Autotransplantation and Regenerative Endodontic Treatment 104

PART III

**The role of COAM in a chemokine-mediated
dental tissue regeneration**

	CHAPTER 7	
		Chlorite Oxidized Oxyamylose Differentially Influences the Microstructure of Fibrin and Self Assembling Peptide Hydrogels as Well as Dental Pulp Stem Cell Behavior 134

	CHAPTER 8	
		Application of COAM as a Novel Strategy for Hydrogel Functionalization with Chemokines: Towards Chemokine-Mediated Dental Tissue Regeneration..... 156

	CHAPTER 9	
		Discussion and Future Perspectives 182

- Beyond cone-beam computed tomography..... 183
- Tooth transplantation: old dog new tricks 184
- The role of COAM in a chemokine-mediated
dental tissue regeneration 186
- Future Perspectives 187

- From biocompatible to biological dental tissue replacement:
a needed paradigm shift in dentistry 187
- From bench-side to chair-side..... 188
- Concluding remarks on future perspectives 192

		Summary 201
		Samenvatting 206
		Scientific acknowledgements..... 211
		Conflict of interest 212
		Acknowledgements 213
		Curriculum vitae and list of publications 219

LIST OF ABBREVIATIONS

2D	Two- dimensional
3D	Three-dimensional
αMEM	Eagle's Minimal Essential Medium, alpha modification
AFA	Apical foramen area
AFM	Atmoic force microscopy
ANOVA	Analysis of variance
BrdU	Bromodeoxyuridine
BSA	Bovine serum albumin
C1	Cluster 1
C2	Cluster 2
C3	Cluster 3
C4	Cluster 4
CBCT	Cone-beam computed tomography
CEJ	Cement enamel junction
COAM	Chlorite-oxidized oxyamylose
DICOM	Digital Imaging and Communications in Medicine
DN	Deoxyribonucleic acid
DPP4	Dipeptidyl peptidase 4
ECM	Extracellular matrix
EDTA	Ethylenediaminetetraacetic acid
eGFP	enhanced green fluorescent protein
ED	Effective dose
ELISA	Enzyme-linked immunosorbent assay
ESMs	Equivalent source models
FACS	Flow cytometry analysis
FBS Fetal	bovine serum
GAG	Glycosaminoglycan
GCP-2	Granulocyte chemotactic protein-2
GPTR	Guided Periodontal Tissue Regeneration
H&E	Hematoxylin and eosin
hDSCs	Human dental stem/stromal cells
hDPSCs	Human dental pulp stem/stromalcells
HS	Heparan sulphate
HPCs	Haematopoeticstem cells
HVL	Half value layer
IGF-1	Insulin-like growth factor-1
Max-DWT	Maximum dentin wall thickness
Mean-DWT	Mean dentin wall thickness

10	MCP-1	Monocyte chemoattractant protein-1
	μCT	Micro-computed tomography
	MHC	Class II major histocompatibility complex antigen-presenting cells
	MSCs	Mesenchymal stem/stromal cells
	MTC	Masson trichrome staining
	MW	Molecular weight
	NF	Neurofilament
	PCA	Principle component analysis
	PDL	Periodontal ligament
	PDE	Partial differential equation
	PI	Propidium iodide
	RADA-16	Arginine-alanine-aspartic acid-alanine-16
	RBM	Bone marrow
	RET	Regenerative Endodontic Treatment
	RGD	Arginine-glycine-aspartic acid
	RL	Root length
	RNA	Ribonucleic acid
	ROI	Region of interest
	RV	Root hard tissue volume
	SAP	Self-assembling peptide
	SDF-1	Stromal derived factor-1
	SEM	Scanning electron microscopy
	SCAPs	Stem cells of the apical papilla
	SHED	Stem cells from human exfoliated deciduous teeth
	SHG	Second harmonic generation
	STL	Standard tessellation language file
	TAT	Tooth autotransplantation
	TDIs	Traumatic dental injuries
	TERM	Tissue engineering and regenerative medicine

The burden of oral disease

Oral health has a vital role in our daily lives, affecting the quality of life and contributing to good overall health. Oral conditions have a high prevalence, affecting almost half of the world population. These may cause excruciating pain, disabilities, and risk of severe acute infections, especially in children and medically compromised patients (1). The age-standardized prevalence for oral conditions in 2015 was 48.0% globally and 50.6% in Western Europe. Moreover, age-standardized years lived with disability rate caused by impaired oral conditions was found to be 2.40 globally and 2.89 in Western Europe (1). According to the Eurobarometer 72.3 report (2, 3), a minority of Europeans still have all their natural teeth: 41% state that they have all their natural teeth, while only a third of the participants reported having 20 natural teeth or more. Among those suffering tooth losses, almost one third is wearing a removable denture, with slight differences from one country to another. Moreover, 43% of the Belgian population have a non-functional dentition, with 21% being edentulous and 22% having one or more impacts on daily life because of oral health-related conditions (3).

Oral health care is associated with a high socio-economic burden. The yearly cost globally was €362 billion in 2010 (4). In Europe, the cost was €79 billion for the same year and was estimated to reach €93 billion in 2020. Similarly, Belgium's annual oral health care cost amounted to €916.6 million for 2016, with 12% of this budget spent on tooth prostheses and oral implants. This high cost is mainly related to the frequency of treatments. Periodontitis is the sixth most common chronic inflammatory disease in the world (5) and traumatic dental injuries (TDIs) alone affect one billion people worldwide (6). TDIs have a relatively high prevalence (15.2%), with children and adolescents most affected (6). Management of TDIs can be expensive and time-consuming life-long treatment, especially when the developing dentition is involved. The mean total cost for complex and non-complex injuries over one year was reported to be €1687.9 and €1350.8, respectively, per patient (7).

12 **Regenerative procedures for the management of dental tissue loss in children**

Over the past decades, dentistry has successfully restored damaged dental tissues in the coronal part of the tooth by utilizing a wide range of biocompatible inert materials (8-11). However, repairing the dental root and surrounding tissue (pulp-dentin complex, periodontium & alveolar bone) has been more challenging, eventually resulting in dentoalveolar tissue loss (12-15). Because of the complex anatomy of the dentoalveolar structures (Figure 1), full recovery of tissues from trauma, inflammation, resective surgeries, or congenital malformations is highly challenging (16). Dental pulp necrosis due to caries, trauma or developmental anomalies is standardly treated by filling the root canal space with bio-inert plastic-like materials, thus depriving the tooth of vascularization, immune response and innervation. Immature teeth with pulp necrosis are rendered fragile even after treatment, and the roots fail to reach complete development. To date, complete tooth loss is widely replaced with biocompatible titanium dental implants, and this is primarily limited to adult patients and by the presence of sufficient alveolar bone (17). Nevertheless, peri-implantitis, progressive inflammation of the tissue (mucosa and alveolar bone) surrounding the titanium implant, is a challenging problem that often results in implant loss (18). For children and adolescents, treatment options are limited by the ongoing dentoalveolar development (19), while orthodontic tooth alignment is challenging unless skeletal anchorage is applied (20).

Regenerative medicine can be generally defined as an emerging interdisciplinary field of research and clinical applications focused on the repair, replacement or regeneration of cells, tissues or organs to restore impaired function resulting from any cause, including congenital defects, disease, trauma and aging. It uses a combination of several technological approaches that moves it beyond traditional transplantation and replacement therapies. These approaches may include but are not limited to, the use of soluble molecules, gene therapy, stem cell transplantation, tissue engineering and the reprogramming of cell and tissue types (21). In the dentoalveolar and craniofacial region, tissue engineering strategies or regenerative medicine therapies aim to replace damaged structures, including alveolar bone, periodontal membrane, dentin and tooth-root structures, dental pulp, and eventually damaged nerve tissue. Clinical treatments that are currently applied, such as (i) Regenerative Endodontic treatment (RET) (22, 23), (ii) Guided Periodontal Tissue Regeneration (GPTR) (24), (iii) alveolar bone augmentation (25, 26), and (iv) Tooth Auto-transplantation (TAT) (27), provide evidence for potential dentoalveolar tissue regeneration. However, the clinical successes remain limited to small defects and still suffer from a limited reproducibility as reported for RET (28) and GPTR

(24) or from the absence of a donor tooth at the appropriate developmental stage for TAT.

RET and TAT offer unique opportunities to gain clinical insights into dental tissue repair and regeneration, especially in children and adolescents. Regenerative endodontics have gained much attention in the past decade because it offers an alternative approach to treating teeth with pulp necrosis. Instead of filling the canal space with bio-inert materials, it attempts to restore tooth vitality (28). A clinical protocol that intends to re-establish pulp/dentin tissues has been developed, known under the synonyms pulp revitalization, root-ca-

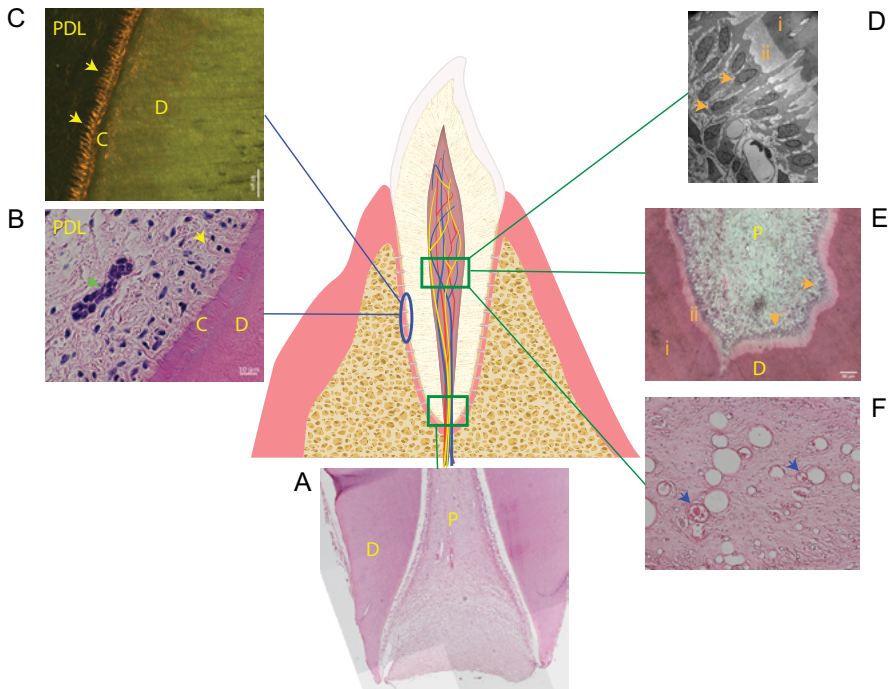


Figure 1: The complex dentoalveolar tissue morphology. In the central illustration, normal tooth tissue is shown and consists of enamel (grey), dentin (striped yellow), vascularized and innervated pulp tissue (red), trabecular bone (yellow), periodontal ligaments (horizontal lines) and gingival tissue (pink). The surrounding panels illustrate light, confocal or electron microscopy tissue sections, taken from the indicated tooth areas, as follows. (A) Apical part of the tooth root showing natural tissue organization (D) root dentine and (P) pulp tissue (Hematoxylin and Eosin staining). (B) Section of healthy periodontal ligament (PDL) containing epithelial rest of Malassez (green arrowhead) and showing Sharpey's fibers (yellow arrowhead) extending into the cementum (C)(Hematoxylin and Eosin staining). (C) Section of healthy PDL, imaged with the use of second harmonic generation confocal microscopy and showing the high collagen content in the Sharpey's fibers (yellow arrowhead) extending into cementum (C). (D) Transmission electron microscopy (TEM) image showing the dentin pulp complex, (i) dentin, (ii) pre-dentin, (iii) odontoblast layer. Note the odontoblastic processes extending into the dentin layer. (E) Dentin pulp complex and dentin architecture with odontoblast layers (orange arrowheads) (i) dentin, (ii) pre-dentin (Hematoxylin and Eosin staining). (F) Vascularization within the pulp tissue (blue arrowheads) (Hematoxylin and Eosin staining).

- 14 nal revascularization, or RET (30-32). This protocol involves the formation of a blood-clot derived fibrin-based matrix in a previously decontaminated, minimal, or non-instrumented root canal space through the intentional laceration of periapical tissues. The blood clot acts as a natural scaffold that, together with endogenously produced growth factors and stem cells from the apical papillae (SCAPs), fills the root canal space, inducing dentinal wall thickening, root maturation and, in some cases, the formation of reparative cementum-like tissue (29-34) (Figure 2). RET has been associated with highly variable outcomes (21, 22, 27). The histologic studies from animal and human teeth have shown that true and reproducible pulp regeneration using the current protocol is difficult to achieve (27, 30, 35). Nevertheless, RET has opened the door for a shift from biocompatible to biological paediatric endodontics.

TAT involves mostly transplanting a developing immature donor tooth into a recipient site within the same patient (36) (Figure 3). TAT offers a viable biological approach to tooth replacement in children and adolescents after TDIs, agenesis, developmental anomalies or specific orthodontic problems

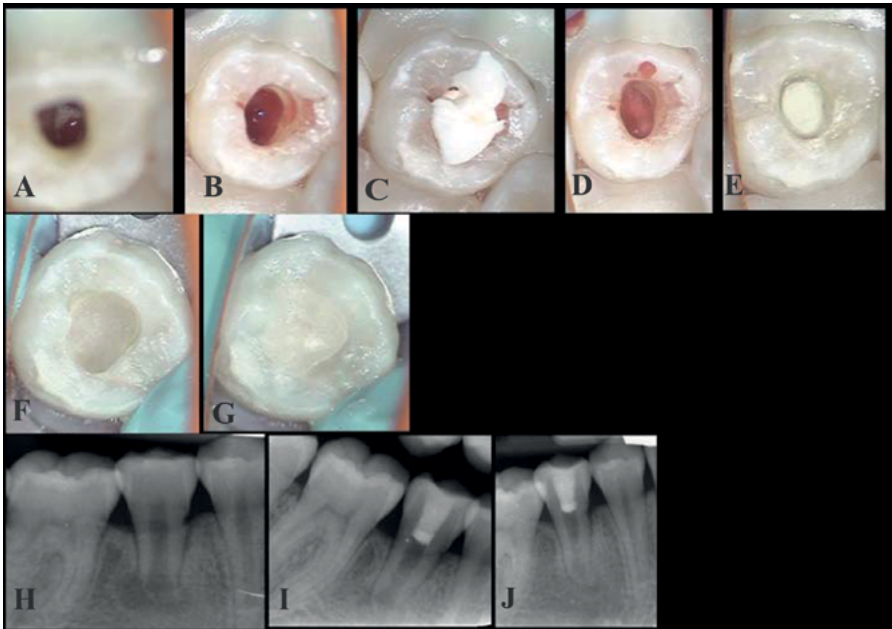


Figure 2: Regenerative Endodontic Treatment procedure. (A & B) induction of bleeding inside the canal, (C & D) placement of collaplug to act as a barrier for MTA condensation, (E) MTA placement, (F & G) At the second visit the hardness of MTA is controlled and coronal seal is established using glass ionomer and adhesive composite resin, (H) pre-operative radiograph, (I) periapical radiograph directly after the second visit, (J) periapical radiograph 3 months after RET.

(37). TAT allows for periodontal and pulp healing, preserving the alveolar ridge and maintaining the possibility of function and growth (38-40). The evidence of continued root development after TAT of immature teeth is undisputed (36, 37, 40-42), rendering TAT a unique clinical model of stem cell transplantation and tooth-root repair and regeneration.

Chemokine-mediated dental tissue regeneration

The classical regenerative medicine approach employs a combination of cells with biomaterials to induce tissue regeneration. The economic and regulatory hurdles associated with cell-based therapies have also led to the proliferation of cell-free biomaterial approaches, which stimulate the activity of endogenous stem cells. Therefore, regenerative medicine can be approached either in a cell-free or in a cell-based manner. Immune-modulated tissue regeneration can be applied as an independent cell-free approach or adjunct for cell-based approaches (43).

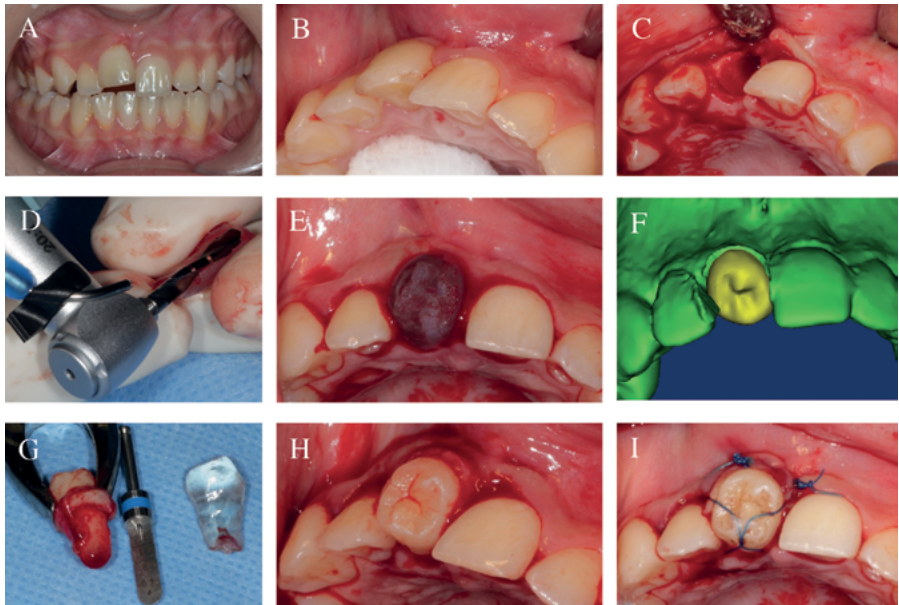


Figure 3: Tooth autotransplantation surgical procedure. (A&B) Clinical picture before surgery showing ankylosis of the maxillary right central incisor, (C) clinical image during the surgery after atraumatic extraction and maintenance of the buccal bone plate, (D&E) the use of the replica during the surgery, (F) planned position for the donor tooth, (G) accuracy of the replica and atraumatic extraction of the donor tooth, (H&I) realized position after TAT and flexible fixation.

- 16** Chemokines are small, secreted proteins that signal through G protein-coupled receptors (45, 46). By quickly mobilizing blood cells, chemokines are involved in various biological processes, such as neural development, atherosclerosis, angiogenesis, inflammation, and viral pathogenesis (46-49). Further, chemokine signalling promotes cell survival, proliferation and provides directional guidance to migrating cells (46, 47, 49-51).

Specific chemokines generally play a pivotal role in (stem) cell homing (50) and differentiation (52). Mesenchymal stromal cells (MSCs) express chemokine receptors CCR1, CCR3, and CXCR4 and exhibit significant chemotaxis induced by macrophage inflammatory protein 1-alpha (MIP-1a or CCL3), a ligand of CCR1, and by stromal cell-derived factor-1 (SDF-1 α or CXCL12), the natural ligand for CXCR4 (48). Especially for tissue repair and regeneration, the latter ligand/receptor pair (SDF-1 α /CXCR4) has attracted much attention for the migration of hematogenic stem cells and progenitor cells, such as dental pulp stem/stromal cells (DPSCs) (51) to the site of injury. This contributes to tissue repair and regeneration. This ligand and receptor pair play a pivotal role in the mobilization, migration, homing, proliferation and differentiation of CD34+ haematopoietic stem cells (HPCs) (50). Moreover, odontoblastic differentiation was stimulated by SDF-1 activation and repressed by SDF-1/CXCR4 inhibition (52). Additionally, the monocyte chemoattractant protein-1 (MCP-1) was shown to play an important role in the induction of so-called M2 macrophages and subsequent tissue regeneration (53). In contrast with classical inflammatory macrophages elected by infections (M1), M2 macrophages play roles in the resolution phase of inflammatory reactions.

Chlorite-oxidized oxyamylose (COAM) is a polyanionic polysaccharide derivative that acts as an antiviral (54), antibacterial (55), and as an immunomodulator by interference with glycosaminoglycan (GAG) binding of chemokines (56). This binding potential has shown varying affinities to a multitude of chemokines in mouse, and it was concluded that COAM formed a binding complex with chemokines that in turn influenced chemokine localization and selectivity of leukocyte responses and migration (56). Therefore, COAM doping by chemokine incorporation, especially with SDF-1, and inducing CXCR4 signalling combined with MCP-1/M2 macrophage induction may be a new therapeutic strategy to promote repair and regeneration in teeth and alveolar bone.

Aim and objectives

The general aim of this PhD project was to bridge part of the gap between in vitro studies and the clinical application for dental tissue regeneration with the main use of a cell-free approach. We tried to accomplish this by the following objectives:

PART I — Hypothesis: Three-dimensional imaging and analysis of regenerative dental procedure outcomes will offer insights into healing patterns and treatment outcomes. Furthermore, optimized indication-oriented scanning protocols will help in minimizing paediatric effective radiation doses.

- **Objective 1:** A standard method for the evaluation of regenerative dental procedures is lacking. Therefore, the first objective was to develop and validate an accurate tooth and root canal space segmentation and a volumetric analysis tool based on cone-beam computed tomography (CBCT). (Chapter 2)
- **Objective 2:** Optimization of a low radiation dose 3D scan protocol for paediatric dental applications. (Chapter 3)

PART II — Hypothesis: CBCT-guided TAT will enhance periodontal ligament healing and pulp vitality resulting in higher TAT success rates. Furthermore, 3D analysis of TAT outcomes will provide clues for the 3D printing of bio-engineered dental root.

- **Objective 3:** To evaluate the healing patterns after TAT using three-dimensional imaging (CBCT) to gain insights into the development of the tissue engineering approach. (Chapters 3, 4, 5 &6)

PART III — Hypothesis: The application of COAM in combination with a bio-active scaffold will act as a binding site for chemokines, promoting the recruitment/migration of MSCs and progenitor cells to the root canal space. MSCs/progenitor cells will aid in pulp/dentin complex regeneration.

- **Objective 4:** Develop and evaluate a cell-free approach for dental tissue regeneration utilizing COAM, chemokines and tailored scaffolds mimicking the extra-cellular matrix. (Chapters 7 & 8)

1. Kassebaum NJ, Smith AGC, Bernabe E, Fleming TD, Reynolds AE, Vos T, et al. Global, Regional, and National Prevalence, Incidence, and Disability-Adjusted Life Years for Oral Conditions for 195 Countries, 1990-2015: A Systematic Analysis for the Global Burden of Diseases, Injuries, and Risk Factors. *J Dent Res.* 2017;96(4):380-7.
2. Commission TOSatrotE. Eurobarometer 72.3. 2009.
3. Guarnizo-Herreno CC, Tsakos G, Sheiham A, Watt RG. Oral health and welfare state regimes: a cross-national analysis of European countries. *Eur J Oral Sci.* 2013;121(3 Pt 1):169-75.
4. Listl S, Galloway J, Mossey PA, Marcenes W. Global Economic Impact of Dental Diseases. *J Dent Res.* 2015;94(10):1355-61.
5. Kassebaum NJ, Bernabe E, Dahiya M, Bhandari B, Murray CJ, Marcenes W. Global burden of severe periodontitis in 1990-2010: a systematic review and meta-regression. *J Dent Res.* 2014;93(11):1045-53.
6. Petti S, Glendor U, Andersson L. World traumatic dental injury prevalence and incidence, a meta-analysis-One billion living people have had traumatic dental injuries. *Dent Traumatol.* 2018;34(2):71-86.
7. Bani-Hani TG, Olegario IC, O'Connell AC. The cost of dental trauma management: A one-year prospective study in children. *Dent Traumatol.* 2020;36(5):526-32.
8. da Veiga AM, Cunha AC, Ferreira DM, da Silva Fidalgo TK, Chianca TK, Reis KR, et al. Longevity of direct and indirect resin composite restorations in permanent posterior teeth: A systematic review and meta-analysis. *J Dent.* 2016;54:1-12.
9. Demarco FF, Collares K, Coelho-de-Souza FH, Correa MB, Cenci MS, Moraes RR, et al. Anterior composite restorations: A systematic review on long-term survival and reasons for failure. *Dent Mater.* 2015;31(10):1214-24.
10. Peumans M, De Munck J, Van Landuyt K, Van Meerbeek B. Thirteen-year randomized controlled clinical trial of a two-step self-etch adhesive in non-carious cervical lesions. *Dent Mater.* 2015;31(3):308-14.
11. Vagropoulou GI, Klifopoulou GL, Vlahou SG, Hirayama H, Michalakis K. Complications and survival rates of inlays and onlays vs complete coverage restorations: A systematic review and analysis of studies. *J Oral Rehabil.* 2018;45(11):903-20.
12. Chercoles-Ruiz A, Sanchez-Torres A, Gay-Escoda C. Endodontics, Endodontic Retreatment, and Apical Surgery Versus Tooth Extraction and Implant Placement: A Systematic Review. *J Endod.* 2017;43(5):679-86.
13. Mavridou AM, Bergmans L, Barendregt D, Lambrechts P. Descriptive Analysis of Factors Associated with External Cervical Resorption. *J Endod.* 2017;43(10):1602-10.
14. Torabinejad M, Anderson P, Bader J, Brown LJ, Chen LH, Goodacre CJ, et al. Outcomes of root canal treatment and restoration, implant-supported single crowns, fixed partial dentures, and extraction without replacement: A systematic review. *J Prosth Dent.* 2007;98(4):285-311.
15. Torabinejad M, White SN. Endodontic treatment options after unsuccessful initial root canal treatment: Alternatives to single-tooth implants. *J Am Dent Assoc.* 2016;147(3):214-20.
16. Obregon F, Vaquette C, Ivanovski S, Huttmacher DW, Bertassoni LE. Three-Dimensional Bioprinting for Regenerative Dentistry and Craniofacial Tissue Engineering. *J Dent Res.* 2015;94(9 Suppl):143S-52S.
17. Chatzopoulos GS, Koidou VP, Lunos S, Wolff LF. Implant and root canal treatment: Survival rates and factors associated with treatment outcome. *J Dent.* 2018;71:61-6.
18. Giannobile WV, Lang NP. Are Dental Implants a Panacea or Should We Better Strive to Save Teeth? *J Dent Res.* 2016;95(1):5-6.
19. Sharma AB, Vargervik K. Using implants for the growing child. *J Calif Dent Assoc.* 2006;34(9):719-24.
20. Becker K, Wilmes B, Grandjean C, Vasudavan S, Drescher D. Skeletally anchored mesialization of molars using digitized casts and two surface-matching approaches : Analysis of treatment effects. *J Orofac Orthop.* 2018;79(1):11-8.

21. Greenwood HL, Singer PA, Downey GP, Martin DK, Thorsteinsdottir H, Daar AS. Regenerative medicine and the developing world. *PLoS Med.* 2006;3(9):e381.
22. EzEldeen M, Van Gorp G, Van Dessel J, Vandermeulen D, Jacobs R. 3-dimensional analysis of regenerative endodontic treatment outcome. *J Endod.* 2015;41(3):317-24.
23. Meschi N, EzEldeen M, Torres Garcia AE, Jacobs R, Lambrechts P. A Retrospective Case Series in Regenerative Endodontics: Trend Analysis Based on Clinical Evaluation and 2- and 3-dimensional Radiology. *J Endod.* 2018;44(10):1517-25.
24. Kinane DF, Stathopoulou PG, Papananou PN. Periodontal diseases. *Nat Rev Dis Primers.* 2017;3:17038.
25. Mangano F, Macchi A, Shibli JA, Luongo G, Iezzi G, Piattelli A, et al. Maxillary ridge augmentation with custom-made CAD/CAM scaffolds. A 1-year prospective study on 10 patients. *J Oral Implantol.* 2014;40(5):561-9.
26. Mangano C, Giuliani A, De Tullio I, Raspanti M, Piattelli A, Iezzi G. Case Report: Histological and Histomorphometrical Results of a 3-D Printed Biphasic Calcium Phosphate Ceramic 7 Years After Insertion in a Human Maxillary Alveolar Ridge. *Front Bioeng Biotechnol.* 2021;9:614325.
27. EzEldeen M, Wyatt J, Al-Rimawi A, Coucke W, Shaheen E, Lambrechts I, et al. Use of CBCT Guidance for Tooth Autotransplantation in Children. *J Dent Res.* 2019;98(4):406-13.
28. Meschi N, Hilken P, Van Gorp G, Strijbos O, Mavridou A, Cadenas de Llano Perula M, et al. Regenerative Endodontic Procedures Posttrauma: Immunohistologic Analysis of a Retrospective Series of Failed Cases. *J Endod.* 2019;45(4):427-34.
29. Galler KM, D'Souza RN. Tissue engineering approaches for regenerative dentistry. *Regen Med.* 2011;6(1):111-24.
30. Chueh LH, Huang GT. Immature teeth with periradicular periodontitis or abscess undergoing apexogenesis: a paradigm shift. *J Endod.* 2006;32(12):1205-13.
31. Huang GT, Garcia-Godoy F. Missing Concepts in De Novo Pulp Regeneration. *J Dent Res.* 2014;93(8):717-24.
32. Chueh LH, Ho YC, Kuo TC, Lai WH, Chen YH, Chiang CP. Regenerative endodontic treatment for necrotic immature permanent teeth. *J Endod.* 2009;35(2):160-4.
33. Albuquerque MT, Valera MC, Nakashima M, Nor JE, Bottino MC. Tissue-engineering-based strategies for regenerative endodontics. *J Dent Res.* 2014;93(12):1222-31.
34. Huang GT, Sonoyama W, Liu Y, Liu H, Wang S, Shi S. The hidden treasure in apical papilla: the potential role in pulp/dentin regeneration and bioroot engineering. *J Endod.* 2008;34(6):645-51.
35. Murray PE, Garcia-Godoy F, Hargreaves KM. Regenerative endodontics: a review of current status and a call for action. *J Endod.* 2007;33(4):377-90.
36. Austah O, Joon R, Fath WM, Chrepa V, Diogenes A, Ezeldeen M, et al. Comprehensive Characterization of 2 Immature Teeth Treated with Regenerative Endodontic Procedures. *J Endod.* 2018;44(12):1802-11.
37. Andreasen JO, Hjorting-Hansen E. Replantation and autotransplantation of teeth. *Trans Int Conf Oral Surg.* 1970:430-3.
38. Akhlef Y, Schwartz O, Andreasen JO, Jensen SS. Autotransplantation of teeth to the anterior maxilla: A systematic review of survival and success, aesthetic presentation and patient-reported outcome. *Dent Traumatol.* 2018;34(1):20-7.
39. Andreasen JO, Paulsen HU, Yu Z, Schwartz O. A long-term study of 370 autotransplanted premolars. Part III. Periodontal healing subsequent to transplantation. *Eur J Orthod.* 1990;12(1):25-37.
40. Kallu R, Vinckier F, Politis C, Mwalili S, Willems G. Tooth transplantations: a descriptive retrospective study. *Int J Oral Maxillofac Surg.* 2005;34(7):745-55.
41. Denys D, Shahbazian M, Jacobs R, Laenen A, Wyatt J, Vinckier F, et al. Importance of root development in autotransplantations: a retrospective study of 137 teeth with a follow-up period varying from 1 week to 14 years. *Eur J Orthod.* 2013;35(5):680-8.
42. Czochrowska EM, Stenvik A, Album B, Zachrisson BU. Autotransplantation of premolars to replace maxillary incisors: a comparison with natural incisors. *Am J Orthod Dentofacial Orthop.* 2000;118(6):592-600.

43. Kafourou V, Tong HJ, Day P, Houghton N, Spencer RJ, Duggal M. Outcomes and prognostic factors that influence the success of tooth autotransplantation in children and adolescents. *Dent Traumatol.* 2017;33(5):393-9.
 44. Freire MO, You HK, Kook JK, Choi JH, Zadeh HH. Antibody-mediated osseous regeneration: a novel strategy for bioengineering bone by immobilized anti-bone morphogenetic protein-2 antibodies. *Tissue Eng Part A.* 2011;17(23-24):2911-8.
 45. Rollins BJ. Chemokines. *Blood.* 1997;90(3):909-28.
 46. Wang J, Knaut H. Chemokine signaling in development and disease. *Development.* 2014;141(22):4199-205.
 47. Lapidot T, Dar A, Kollet O. How do stem cells find their way home? *Blood.* 2005;106(6):1901-10.
 48. Takano T, Li YJ, Kukita A, Yamaza T, Ayukawa Y, Moriyama K, et al. Mesenchymal stem cells markedly suppress inflammatory bone destruction in rats with adjuvant-induced arthritis. *Lab Invest.* 2014;94(3):286-96.
 49. Wu Y, Zhao RC. The role of chemokines in mesenchymal stem cell homing to myocardium. *Stem cell Rev.* 2012;8(1):243-50.
 50. Lataillade JJ, Domenech J, Le Bousse-Kerdiles MC. Stromal cell-derived factor-1 (SDF-1)\CXCR4 couple plays multiple roles on haematopoietic progenitors at the border between the old cytokine and new chemokine worlds: survival, cell cycling and trafficking. *Eur Cytokine Netw.* 2004;15(3):177-88.
 51. Suzuki T, Lee CH, Chen M, Zhao W, Fu SY, Qi JJ, et al. Induced migration of dental pulp stem cells for in vivo pulp regeneration. *J Dent Res.* 2011;90(8):1013-8.
 52. Kim DS, Kim YS, Bae WJ, Lee HJ, Chang SW, Kim WS, et al. The role of SDF-1 and CXCR4 on odontoblastic differentiation in human dental pulp cells. *Int Endod J.* 2014;47(6):534-41.
 53. Zhuang Z, Yoshizawa-Smith S, Glowacki A, Maltos K, Pacheco C, Shehabeldin M, et al. Induction of M2 Macrophages Prevents Bone Loss in Murine Periodontitis Models. *J Dent Res.* 2019;98(2):200-8.
 54. Li S, Martens E, Dillen C, Van den Steen PE, Opdenakker G. Virus entry inhibition by chlorite-oxidized oxyamylose versus induction of antiviral interferon by poly(I:C). *Biochem Pharmacol.* 2008;76(7):831-40.
 55. Zi Y, Zhu M, Li X, Xu Y, Wei H, Li D, et al. Effects of carboxyl and aldehyde groups on the antibacterial activity of oxidized amylose. *Carbohydr Polym.* 2018;192:118-25.
 56. Li S, Pettersson US, Hoorelbeke B, Kocaczkowska E, Schelfhout K, Martens E, et al. Interference with glycosaminoglycan-chemokine interactions with a probe to alter leukocyte recruitment and inflammation in vivo. *PLoS One.* 2014;9(8):e104107.
-

PART I

**Developing and optimizing the tools to study
regenerative dental procedures**

CHAPTER 1

This chapter is based on the following publication

EzEldeen, M., Van Gorp, G., Van Dessel, J., Vandermeulen, D., Jacobs, R. (2015).
3-dimensional Analysis of Regenerative Endodontic Treatment Outcome. *Journal of Endodontics*, 41 (3).

- (A) OIC, OMFS IMPATH Research Group, Faculty of Medicine, Department of Imaging and Pathology, KU Leuven and Oral and Maxillofacial Surgery, University Hospitals Leuven, Leuven, Belgium
- (B) Department of Oral Health Sciences, KU Leuven and Paediatric Dentistry and Special Dental Care, University Hospitals Leuven, Leuven, Belgium
- (C) Medical Image Computing, ESAT/PSI, Department of Electrical Engineering, KU Leuven, Leuven, Belgium.

3-Dimensional Analysis of Regenerative Endodontic Treatment Outcome

M. EzEldeen (A,B), G. Van Gorp (B), J. Van Dessel (A), D. Vandermeulen (C), R. Jacobs (A)

ABSTRACT

Introduction — A growing body of evidence supports the regeneration potential of dental tissues after Regenerative Endodontic Treatment (RET). Nevertheless, a standard method for the evaluation of RET outcome is lacking. The aim of this study was to develop a standardized quantitative method for RET outcome analysis based on Cone Beam CT (CBCT) volumetric measurements.

Methods — Five human-teeth embedded in mandibular bone samples were scanned using both an Accuitomo 170® CBCT (Morita, Kyoto, Japan) and a SkyScan 1174® μ CT system (SkyScan, Antwerp, Belgium). For subsequent clinical application, clinical data and low dose CBCT scans (pre-operatively and follow-up) from 5 immature permanent teeth treated with RET were retrieved. *In-vitro* and clinical 3D image data sets were imported into a dedicated software tool. Two segmentation steps were applied to extract the teeth of interest from the surrounding tissue (live-wire) and further to separate tooth hard tissue and root canal space (level-set methods). *In-vitro* and clinical volumetric measurements were assessed separately for differences using Wilcoxon matched paired test. Pearson correlation analysis and Bland and Altman plots were used to evaluate the relation and agreement between the segmented CBCT and μ CT volumes.

Results — The results showed no statistical differences and strong agreement between CBCT and μ CT volumetric measurements. Volumetric comparison of the root hard tissue showed significant hard tissue formation [mean volume of newly formed hard tissue was $27.9 (\pm 10.5) \text{ mm}^3$, ($p < 0.05$)].

Conclusion — Analysis of 3D data for teeth treated with RET offers valuable insights into the treatment outcome and patterns of hard-tissue formation.

KEY WORDS

Cone-beam computed tomographic imaging, MeVislab, regenerative endodontic treatment, teeth segmentation

INTRODUCTION

Humans, unlike species such as salamander or newt, lack the ability to naturally regenerate their own tissues. To overcome this limitation, tissue engineering strategies utilizing combinations of biocompatible scaffolds, growth factors, and stem cells to mimic natural morphogenesis, are currently in development (1). Amongst those strategies are the regenerative endodontic procedures, that can be defined as biologically-based processes designed to replace damaged structures, including dentin and root structures, as well as cells of the pulp-dentin complex (2).

The potential for dental tissue regeneration and continued root development is well-documented in studies of replanted and auto-transplanted teeth (3-5). There is a growing body of evidence from case reports to suggest that regenerative endodontics may in fact be possible in teeth with pulpal necrosis, apical pathosis, and immature apices (6-9). This treatment procedure has acquired many names such as pulp revitalization, root-canal revascularization or regenerative endodontic treatment (RET) (2;9-11). The outcomes of these case reports have been evaluated clinically and radiographically in two dimensions (2D). The most frequent pretreatment diagnosis of these cases was of pulpal necrosis with or without apical periodontitis. Postoperative recalls demonstrated regression of clinical symptoms in addition to radiographic evidence of hard-tissue formation and apical closure (6-10;12). However, the application of non-standardized 2D radiographs to evaluate an increase in the root length and dentine thickness should be interpreted with caution because a slight change in the angulation at the preoperative or recall appointment might produce inconsistent images and inaccurate interpretations (12).

Taking into consideration the limitations of 2D imaging, three-dimensional imaging using Cone Beam Computer Tomography (CBCT) has proven itself as a valuable tool in dentistry (13-15), as long as radiation doses are controlled at reasonably low levels (16). Moreover, volumetric measurements from CBCT data have been reported and validated in several studies *in-vitro* and *in-vivo* (13-15;17-20).

The overall aim of this study was to develop a standardized quantitative method for the evaluation and analysis of the outcome of RET based on CBCT volumetric measurements.

MATERIALS AND METHODS

In vitro validation

(CBCT Versus Micro-computed Tomographic Imaging)

Image acquisition and export

The samples were subsequently scanned with the SkyScan 1174® μ CT system (SkyScan, Antwerp, Belgium). The μ CT parameters were 30 μ m voxel size, 50 kVp, 800 mA, 1mm aluminum filter, angular rotation step 0.8°, 360° scanning, 450 projections and an exposure time of 5s with a total scan duration of 1h 31.6 min. All data sets were imported using the DICOM file format with the voxel size of 30 μ m.

Clinical application

Study sample

This case series included 5 immature permanent teeth with infected necrotic pulps and apical periodontitis/abscess from 4 patients who attended the Pediatric Dental Clinic of the University Hospital of the KU Leuven (Belgium). Table 1 presents the demographic details of the subjects, signs and/or symptoms, and pulpal and periapical status of involved teeth. The age of the patients ranged between 9.9–14.8 years at the start of treatment. The patients presented with dental trauma (1 maxillary incisor), dens evaginatus (3 maxillary incisors) and pulp necrosis after auto-transplantation (1 premolar). Radiographically, all teeth demonstrated evidence of periapical lesions caused by root canal infection; one tooth showed early signs of external cervical root resorption (pre-molar). All teeth had an immature apex, either blunderbuss or in the form of a wide canal with parallel walls and an open apex. After clinical and radiographic examination, a vitality pulp test was performed on the affected tooth and a control (contralateral but unaffected) tooth. The patients and their parents were informed of the treatment plan (for regenerative endodontic treatment) and the potential risks before giving their consent to the treatment.

RET technique

All teeth were anesthetized using Mepivacaine 3% without epinephrine (Scandonest®, Septodont, Saint Maur des Fosses, France) to avoid compromising the blood supply, and then isolated with rubber dam. The access cavity was prepared with a #2 high speed access bur (round end cutting tapered diamond bur) (Maillefer, Dentsply®, Switzerland) and copious water spray. The canals gently rinsed with sodium hypochlorite (NaOCl) 2.5% solution without instrumentation. The canal was then dried by aspiration (without air blow) and application of sterile paper points (Henri Schein®, Melville, N.Y.). A bi-antibi-

26 otic mixture of ciprofloxacin and metronidazole was placed in the root canal and left for 10-14 days. The access cavity was sealed with resin modified glass ionomer cement (Fuji VII, GC®, Tokyo, Japan). In the next visit, under endodontic microscope, the root canal was re-entered and irrigated with a copious amount of 2.5% NaOCl to remove the antibiotic dressing material and all debris. The root canal dentine was conditioned using ethylenediaminetetraacetic acid (EDTA) 17% (21). The canal was then dried with sterile paper points and was confirmed to have no exudate. A size #10 K-file was introduced into the root canal until vital tissue was felt, and this instrument was used to irritate this tissue to create some bleeding into the root canal (Fig. 1A). The bleeding was allowed to reach a level of 3-4 mm to the cemento enamel junction (Fig. 1B). Then an absorbable collagen barrier (CollaPlug®, Zimmer Dental, Carlsbad, USA) was placed to create a barrier to apply a dense layer of 4 mm of white mineral trioxide aggregate (ProRoot MTA, Dentsply®, USA) till the cemento enamel junction (Fig. 1C, D and E). The tooth was then temporarily sealed using a moist sterile paper point, to provide the water needed for MTA to fully set, and resin modified glass ionomer cement (Fuji VII, GC®, Tokyo, Japan). After 7-14 days, the temporary filling and moist paper point were removed, and the hardness of MTA was inspected. The final coronal seal was established using adhesive composite restoration, and the patient was scheduled for recall (Fig. 1F-J).

Image Acquisition and Export

Cone Beam Computed Tomographic (CBCT) images were obtained based on clinical justification by treating endodontist as part of the treatment protocol (pre-operatively and at >12 months follow-up) due to the severity of the lesions and in the framework of the insurance case follow-up. Images were obtained

Table 1: Demographic details of the subjects, signs and/or symptoms, and pulpal and periapical status of involved teeth.

Case number	Age	Gender	Tooth number	Signs/Symptoms	Pulpal status	Periapical lesion
1	9.9	F	Maxillary right central incisor	Swelling & pain	Necrosis	+
2	8.9	F	Maxillary right central incisor	Swelling & pain	Necrosis	+
3	14.8	F	Mandibular right first premolar	No	Necrosis	+
4	11.8	F	Maxillary right lateral incisor	Swelling & pain	Necrosis	+
5	12.2	F	Maxillary left lateral incisor	Swelling & pain	Necrosis	+

with the Accuitomo® 170 (J. Morita corporation, Kyoto, Japan) using the 80 x 80 mm FOV. Images were acquired under the exposure condition of 90.0 kV (X-ray tube voltage) and 5.0 mA (X-ray tube electric current). The exposure time was 17.5 seconds. All data sets were exported using the Digital Imaging and Communication in Medicine (DICOM) file format with the voxel size of 160 μm and a slice interval of 160 μm (1 voxel).

Segmentation Strategy

All scanned samples (CBCT & μCT) and full CBCT scans (case series study) were imported into MeVisLab® (MeVis Research, Bremen, Germany) a highly developed free framework system that provides an easy to learn modular visual programming interface with a comprehensive suite of image processing and visualization tools (<http://www.mevislab.de/>). For the clinical data, the region of interest (ROI) including the tooth treated with RET (pre and post-operative) and the contralateral negative control tooth was saved as a new image in DICOM format to reduce computation time. All ROI images were normalized using an intensity windowing filter and then a median filter to suppress any noise and decrease confounding variables between the images.

Two segmentation steps were applied to extract the teeth of interest from the surrounding tissue (bone) and further to separate tooth hard tissue (enamel and dentine) and root canal space. The first step is a dedicated tool developed in MeVisLab® that applies interactive live-wire boundary extraction to extract the tooth of interest from the surrounding tissue. Live-wire allows for a semi-interactive segmentation of structures with prominent edge image features. Internally, the module generates a graph representation of the image to work on. The graph's nodes represent image pixels and edges connect neighboring pixels. The edges are weighted on base of the cost function (image gradient magnitude). If starting and ending points are defined on such a graph, the shortest path (minimal cost path) is computed using dynamic programming (F*-algorithm) (22;23). The second step applies semi-automatic user guided 3D active contour segmentation using level-set methods (23;24), available in the ITK-SNAP tool kit (www.itksnap.org) (24). In a first step a probability map was computed by applying a one-sided smooth threshold once for hard tissue and another for the root canal space. In a second step the segmentation was initialized by placing one or more spherical seeds in the region of interest (hard tissue or canal). The last step was specifying the weights of the various terms in the active contour evolution partial differential equation (PDE), and running the evolution interactively (24).

3D-reconstruction and Quantitative visualization of hard tissue formation

After segmentation, the 3D triangle-based surface of the hard-tissue and the root canal was reconstructed without being smoothed, to preserve its raw volume measurement. The volumes of the root hard-tissue and root canal were calculated starting from the cemento-enamel junction up to the apex pre and post-operatively. Geometry quantification was carried out in MeVisLab® using the framework described by Gao, Y et al., (2009) (25). The root canal diameter (thickness) was measured and color coded, then the root hard-tissue thickness measurement (starting from the cemento-enamel junction up to the apex) was expressed as a color coded map showing the calculated minimal distances from the canal surface to the external root surface (25).

Volumetric Comparison and Statistical analysis

All data were analyzed with statistical software package STATISTICA 8.0 (Stat-Soft, Inc., Tulsa, USA). In a first step, the accuracy of the volume measurements using CBCT was evaluated by comparing the segmented volumes for hard-tissue and root canal of the same samples to the volume segmented from μ CT scans using the Wilcoxon matched pairs test. Pearson correlation analysis was performed to examine the potential linear relationship between the segmented volumes (hard-tissue and root canal separately) from CBCT and μ CT. The degree of agreement between the segmented volumes from CBCT and μ CT was compared using the method of Bland and Altman (26). In this method, the difference between the measurements is plotted against their mean, since the mean is considered to be the best estimate of the true values. The volumetric changes after RET were tested by comparing the root hard-tissue volume pre and post-operatively starting from the cemento-enamel junction up to the apex using the Wilcoxon matched pairs test.

RESULTS*In vitro validation*

Hard-tissue and root canal segmented volumes for the samples were used to test the correlation between the μ CT and CBCT volumes, a strong correlation was found [(hard-tissue at 80 μ m and 160 μ m: $r= 0.99$, $p< 0.0001$) (root-canal at 80 μ m and 160 μ m: $r= 0.99$, $p< 0.001$)]. The comparison of the measurements of segmented volumes (hard tissue and root canal) from μ CT and CBCT did not show any significant differences (Wilcoxon test, $p > 0.05$) (Fig. 2A and B).

The degree of agreement between μ CT and CBCT segmented volumes were analyzed using the Bland-Altman method. The plots for the hard tissue and root canal volumes showed an agreement between the μ CT and CBCT segmented volumes. The segmented hard tissue volume from CBCT at 80 μ m and 160 μ m were slightly bigger (4.20 mm³ and 5.12 mm³) than the segmented volume from μ CT at 30 μ m (Fig. 2C and D). Further, the segmented root canal volume at from CBCT at 80 μ m and 160 μ m were slightly smaller (-0.35 mm³ and -0.95 mm³) than the segmented volume from μ CT at 30 μ m (Fig. 2E and F).

Clinical application: RET Outcome

Table 2 summarizes the results of the regenerative endodontic treatment (RET). The mean follow-up period was 19.4 (\pm 5.4) months. All subjects showed clinical evidence of resolution of signs and symptoms at follow-up visits related to the treated teeth. All teeth were free of any signs of soft tissue pathology, all teeth reacted normal to palpation, percussion tests and showed normal mobility. Cone Beam CT evaluation showed complete healing of periapical lesions with bone formation (Figs. 3 and 4). Table 3 summarizes the results of the 3D analysis, all teeth showed thickening of the root canal walls and continuing of root maturation (apex formation). All teeth showed hard tissue formation on the internal walls of the root canal with 2 teeth showing progressive apical obliteration (Fig. 4B and D). Three-dimensional (3D) volumetric comparison of the root hard tissue showed significant hard tissue formation (P value <0.05), the mean volume of newly formed hard tissue was 27.9 (\pm 10.5) mm³ (Table 3).

DISCUSSION

This study reports a novel method for the evaluation and analysis of the RET outcome. The presented data confirms the accuracy of volumetric measurements from CBCT compared to μ CT data. Liu et al.,(2010) reported a slight deviation of segmented teeth volumes from the physical volumes within -4% to 7% using manual segmentation strategies and without any smoothing operations (17). Further, Michetti et al., (2010) reported a slightly smaller segmented root canal volumes from CBCT data (less than 3%) compared to the volumes measured from digitized images from histological sections (19).

The current study applied volumetric measurements from CBCT data obtained for pre and post RET to analyze the treatment outcome in a standardized quantitative method. All teeth included in the current study showed hard-tissue volume gain demonstrating the success of RET in stimulating hard-tissue formation and root maturation. Three-dimensional root canal reconstructions

30 showed progressive root canal calcification (obliteration) mostly in the apical part when compared to the contralateral teeth. This finding has been reported in previous studies of the RET outcome (6;7), root canal obliteration is a common finding after traumatic dental injuries and a desired outcome after auto-transplantation of teeth acting as a sign of pulp revitalization (3-5;27). Moreover, visualization the pattern of hard-tissue formation using color coded maps for root dentine thickness before and after treatment clearly showed the non-uniform nature of hard tissue formation on root canal walls which was unique for each tooth included in this case report. So far, the significance of the pattern of the hard tissue formation is unknown. Future studies including a larger sample size or a multi-center study could implement the method described in the current study to evaluate the relation between baseline situation and the pattern of hard tissue deposition, thus exploring the determinants of success.

The segmentation strategy applied in the current report seems to offer the advantages of increasing the accuracy and reducing the working time. Using the live-wire boundary technique, boundaries are extracted in one-fifth of the time required for manual tracing, but with 4.4 times greater accuracy and 4.8 times greater reproducibility (22). This proved to be of great value especially for teeth in the posterior area of the mandible where the segmentation is more difficult because of the cortical bone (17). Further, using 3D semi-automatic active contour level-set methods available in ITK-SNAP offers the advantages of greatly reducing the working time, high accuracy and real time interaction with the segmentation process in contrast to the commonly used low-level methods (region growing). Level-set methods offer the possibility of adjusting the contours behavior making it more suitable for segmenting areas with constrictions around the tooth apex.

Table 2: Summary of RET outcome

Case number	Follow-up period (months)	Healing of periapical lesion	Apical obliteration	Apical foramen diameter before RET* (mm)	Apical foramen diameter after RET* (mm)
1	24	Yes	Yes	1.63	0.50
2	16	Yes	Yes	2.02	0.0
3	12	Yes	Yes	4.48	0.20
4	25	Yes	Yes	3.84	0.3
5	20	Yes	Yes	3.38	1.13

* = measured in axial view at the most apical part

Table 3: Summary of 3D analysis

Case number	Three-dimensional thickening of the root walls	Volumetric change* (mm ³)	Increase in root length* (mm)	Pattern of hard tissue deposition on root canal walls
1	Yes	+19.9	+1.4	On apical 1/3, on buccal and palatal walls, apex formation
2	Yes	+21.8	+0.8	On apical and middle 1/3, random deposition, apical blunting
3	Yes	+36.4	+5.5	Root canal obliteration from apex till middle 1/3, apex formation
4	Yes	+19.6	+0.8	On apical 1/3, on buccal and palatal walls, apical blunting
5	Yes	+41.9	+1.7	On apical 1/3, on buccal and palatal walls, apex formation

*= measured from the cemento-enamel junction

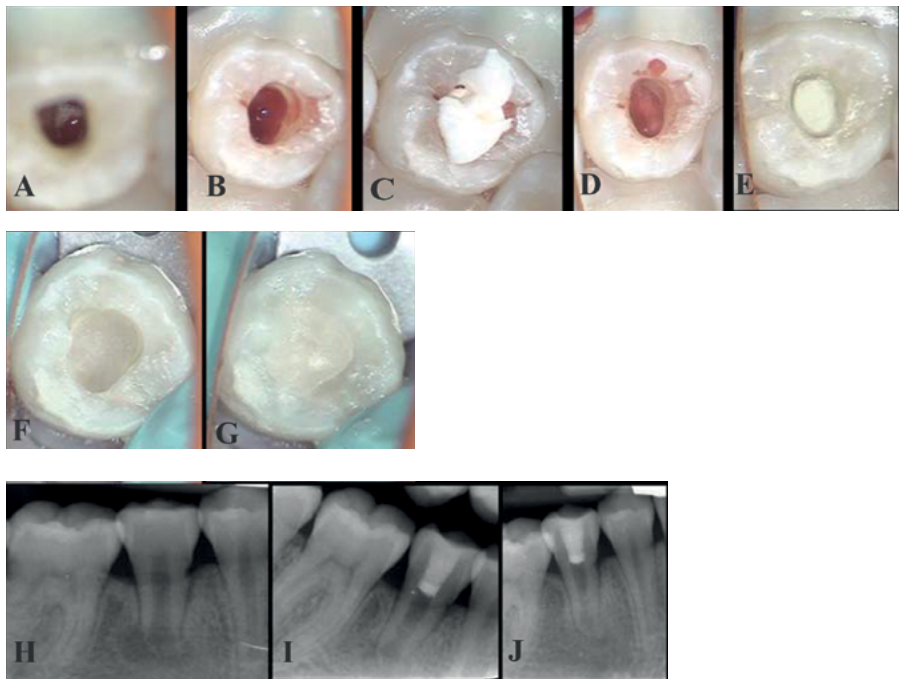


Figure 1: Regenerative Endodontic Treatment procedure. (A & B) induction of bleeding inside the canal, (C & D) placement of collaplug to act as a barrier for MTA condensation, (E) MTA placement, (F & G) At the second visit the hardness of MTA is controlled and coronal seal is established using glass ionomer and adhesive composite resin, (H) pre-operative radiograph, (I) periapical radiograph directly after the second visit, (J) periapical radiograph 3 months after RET.

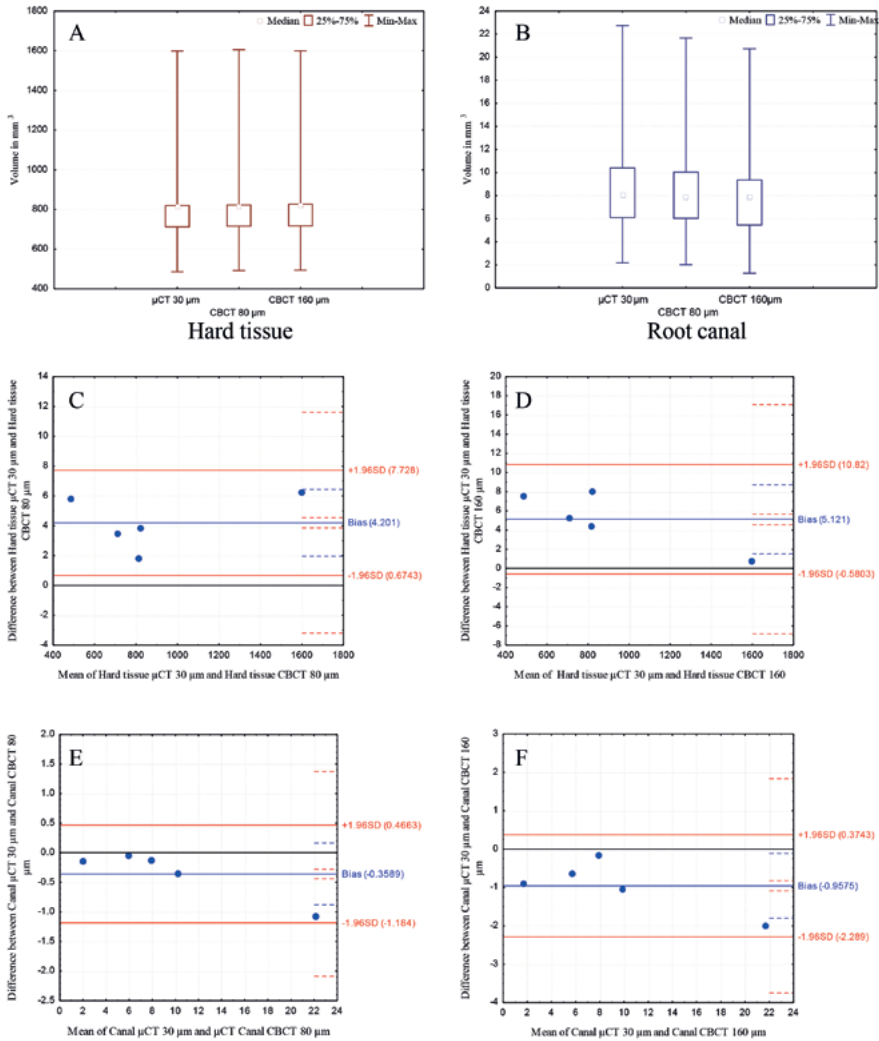


Figure 2: In vitro validation. (A) box-plot comparison between segmented volumes in mm³ (hard tissue) from μ CT at 30 μ m and CBCT at 80 μ m and 160 μ m, (B) box-plot comparison between segmented volumes mm³ (root canal) from μ CT at 30 μ m and CBCT at 80 μ m and 160 μ m, (C & D) Bland and Altman plot between the hard tissue segmented volumes from μ CT at 30 μ m and CBCT at 80 μ m and 160 μ m (the difference between the measurements is plotted against their mean), (E & F) Bland and Altman plot between the root canal segmented volumes from μ CT at 30 μ m and CBCT at 80 μ m and 160 μ m (the difference between the measurements is plotted against their mean).

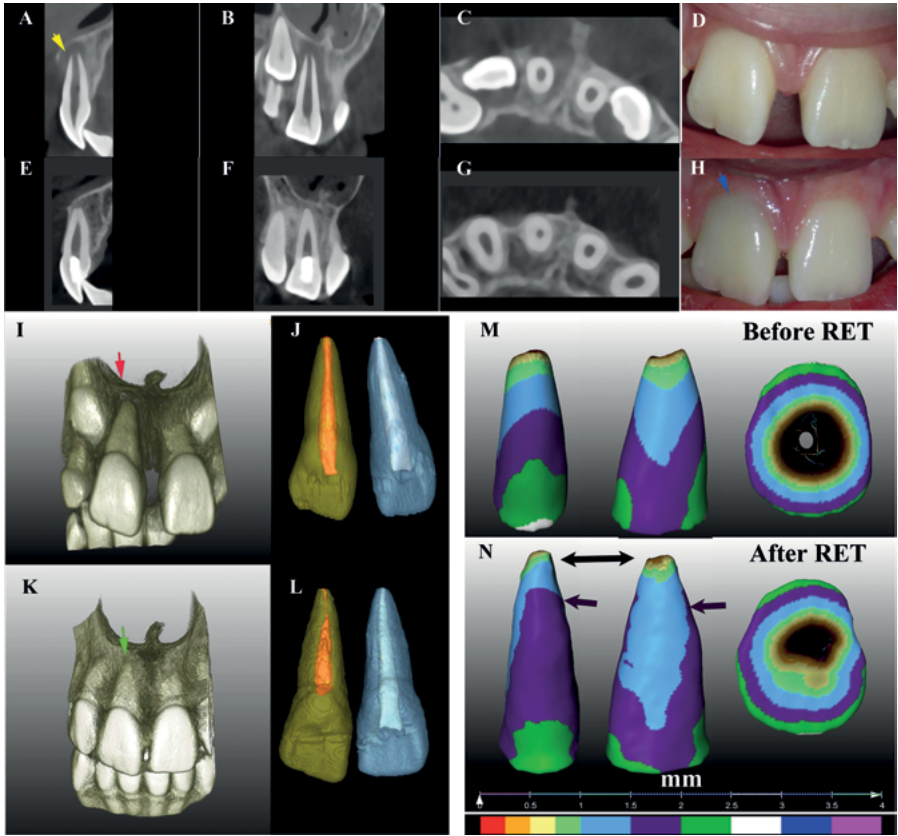


Figure 3: Case 1, a 9.9 years-old girl presented with pain related to dense evaginatus on the maxillary right central incisor. (A, B & C) CBCT scan showed immature apex, periapical lesion and excessive buccal bone loss (yellow arrow), (D) clinical picture before treatment, (E, F & G) co-registered CBCT scan 24 months after RET showing periapical and buccal bone healing and formation of hard tissue apically, (H) clinical picture 24 months after RET (note the grey discoloration in the cervical region caused by MTA) (blue arrow), (I) 3D reconstruction showing the extent of buccal bone loss (red arrow), (J) 3D segmentation for the maxillary right central incisor (yellow) and the contralateral (blue), (K) 3D reconstruction 24 months after RET showing buccal bone healing (green arrow), (L) 3D segmentation demonstrating apical maturation after RET (note the progressive nature of apical hard tissue formation compared to the contralateral control), (M & N) 3D volumetric analysis of hard tissue changes after RET demonstrating newly formed hard tissue apically (black arrow), increased root thickness in the bucco-lingual dimension (purple color on the root surface and purple arrows).

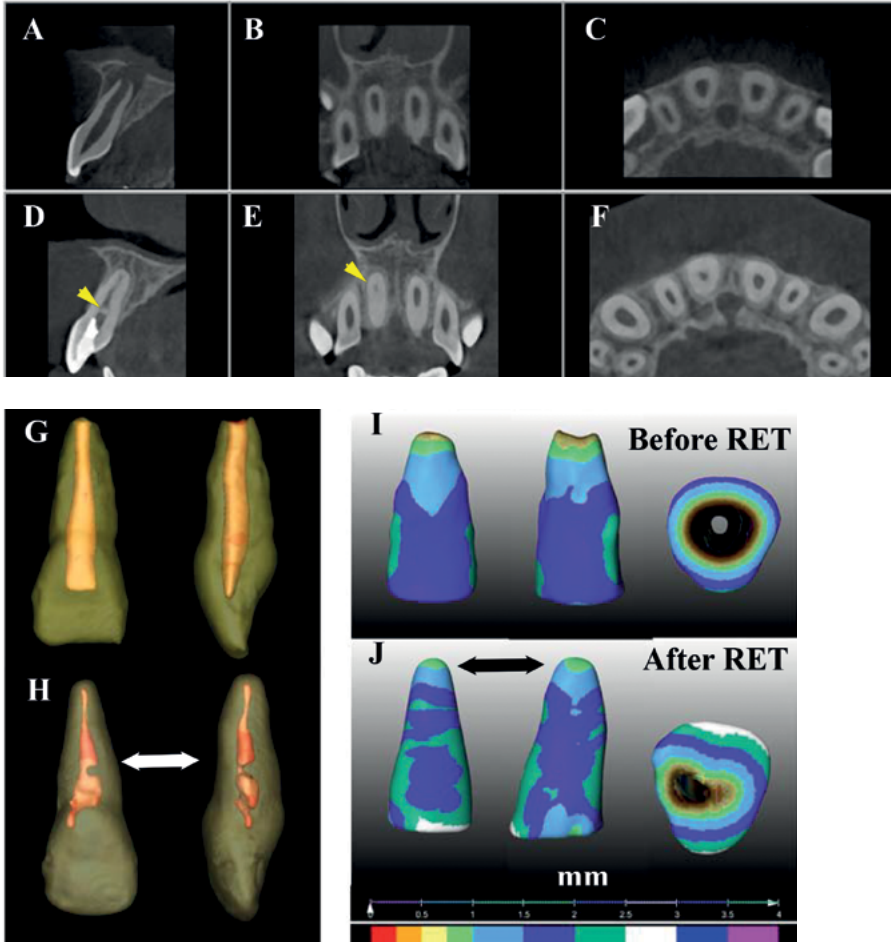


Figure 4: Case 2, a 8.9 years-old girl presented with pain and swelling related to the maxillary right central incisor (7 months after dental trauma in a car accident). (A, B & C) CBCT scan showed immature apex, periapical lesion and bone loss related to the maxillary right central incisor, (D, E & F) co-registered CBCT scan 16 months after RET showing healing of periapical lesion, thickening of root walls with root canal obliteration (yellow arrows) (G) 3D reconstruction before RET showing the size of root-canal and root-dentine thickness, (H) 3D reconstruction showing the non-uniform nature of hard tissue deposition on the canal walls and progressive root canal obliteration (white arrow), (I & J) 3D volumetric analysis of the root (sectioned from the cemento-enamel junction demonstrating non-uniform hard tissue gain after RET (purple and dark green color on root surface), apical blunting (black arrow).

This case series described the outcome of 4 patients who presented with 5 immature teeth with periapical infection and pulp necrosis. The RET outcome was in harmony with reported cases in the literature, showing resolution of periapical lesions, bone healing, hard tissue formation of the root canal walls and root maturation (6-9;12;28). The treatment applied a bi-antibiotic mix instead of the commonly used tri-antibiotic mix to reduce the potential risk of discoloration due to the presence of minocycline in the tri-antibiotic mix (29). Further, EDTA 17% was used in root canal conditioning after NaOCl irrigation and directly before induction of bleeding into the canal to remove smear layer, expose dentinal tubules and collagen fibrils, and release of growth factors from the dentin matrix (21). EDTA is thought to enhance the outcome of RET through optimizing the conditions for cellular differentiation, tissue formation, and regeneration (21).

The aim of this study was to report the outcome of RET using 3D CBCT data and to analyze the outcome in a quantitative method. CBCT images overcome the limitations of 2D images such as the lack of the bucco-lingual dimension, masking of areas of interest by overlying anatomy (anatomic noise), and avoid geometrical distortion. A high spatial resolution and true volumetric information can be obtained due to the isotropic nature of CBCT images (16;30). Moreover, it has been shown that dental trauma and developmental anomalies can be better assessed in three dimensions (16;30-32). Nevertheless, CBCT has its own limitation, the effective radiation dose delivered by CBCT devices available in the market vary enormously from around 10 μ Sv to 1200 μ Sv (which is an equivalent of 2-240 panoramic radiographs) (33;34). Therefore, a proper balance (optimization) between on the one hand costs and radiation dose and on the other hand information required needs to be maintained (16). Further, the scanned area should not exceed the area of interest. This will limit the dose substantially, thus justifying its use (16;31;32). More research is still needed to validate the benefit of applying CBCT in routine monitoring of RET cases.

Quantitative methods using 2D data were successfully reported and validated (12;35). However, working with 2D data has its limitations such as; image standardization and the lack of volumetric measurements. Moreover, 2D does not account for the presence of intracanal calcifications, which is a common finding in cases treated with RET (35). Nevertheless, a standard quantitative method is highly needed to compare results from different studies and to be applied in multi-center prospective studies. Three-dimensional images offer the unique possibility of analyzing the pattern and position of hard tissue formation. The use of standardized 2D data from short-term monitoring combined with 3D data on the long-term in a study with a large sample size might offer much needed information regarding the outcome of regenerative

- 36 endodontic procedures. Finally, future research including larger sample, control group and comparison to the available 2D methods is needed to validate the clinical application of the method proposed in the current study.

CONCLUSION

Analysis of 3D data for teeth treated with regenerative endodontic procedures offers valuable insights into the treatment outcome and patterns of hard-tissue formation.

ACKNOWLEDGMENTS

The authors deny any conflicts of interest related to this study.

REFERENCES

1. Sfeir C, Onishi S, Yoshizawa S, Syed-Picard Fet al. Introduction to Regenerative Dentistry. In: Marei M, editor. Regenerative Dentistry. 2010. p. 1-17.
2. Murray PE, Garcia-Godoy F, Hargreaves KM. Regenerative endodontics: a review of current status and a call for action. *J Endod* 2007;33:377-90.
3. Andersson L, Andreasen JO, Day P, et al. International Association of Dental Traumatology guidelines for the management of traumatic dental injuries: 2. Avulsion of permanent teeth. *Dent Traumatol* 2012;28:88-96.
4. Cvek M, Cleaton-Jones P, Austin J, . Pulp revascularization in reimplanted immature monkey incisors--predictability and the effect of antibiotic systemic prophylaxis. *Endod Dent Traumatol* 1990;6:157-69.
5. Tsukiboshi M. Autotransplantation of teeth: requirements for predictable success. *Dent Traumatol* 2002;18:157-80.
6. Chen MY, Chen KL, Chen CA, et al. Responses of immature permanent teeth with infected necrotic pulp tissue and apical periodontitis/abscess to revascularization procedures. *Int Endod J* 2012;45:294-305.
7. Chueh LH, Ho YC, Kuo TC, et al. Regenerative endodontic treatment for necrotic immature permanent teeth. *J Endod* 2009;35:160-4.
8. Hargreaves KM, Geisler T, Henry M, et al. Regeneration potential of the young permanent tooth: what does the future hold? *Pediatr Dent* 2008;30:253-60.
9. Torabinejad M, Turman M. Revitalization of tooth with necrotic pulp and open apex by using platelet-rich plasma: a case report. *J Endod* 2011;37:265-8.
10. Pramila R, Muthu MS. Regeneration potential of pulp-dentin complex: Systematic review. *J Conserv Dent* 2012;15:97-103.
11. Reynolds K, Johnson JD, Cohenca N. Pulp revascularization of necrotic bilateral bicuspids using a modified novel technique to eliminate potential coronal discoloration: a case report. *Int Endod J* 2009;42:84-92.
12. Bose R, Nummikoski P, Hargreaves K. A retrospective evaluation of radiographic outcomes in immature teeth with necrotic root canal systems treated with regenerative endodontic procedures. *J Endod* 2009;35:1343-9.
13. Esposito SA, Huybrechts B, Slagmolen P, et al. A novel method to estimate the volume of bone defects using cone-beam computed tomography: an in vitro study. *J Endod* 2013;39:1111-5.

14. Shahbazian M, Jacobs R, Wyatt J, et al. Validation of the cone beam computed tomography-based stereolithographic surgical guide aiding autotransplantation of teeth: clinical case-control study. *Oral Surg Oral Med Oral Pathol Oral Radiol* 2013;115:667-75.
 15. Yang F, Jacobs R, Willems G. Dental age estimation through volume matching of teeth imaged by cone-beam CT. *Forensic Sci Int* 2006;15:159 Suppl 1:S78-S83.
 16. Jacobs R. Dental cone beam CT and its justified use in oral health care. *JBR-BTR* 2011;94:254-65.
 17. Liu Y, Olszewski R, Alexandroni ES, et al. The validity of in vivo tooth volume determinations from cone-beam computed tomography. *Angle Orthod* 2010;80:160-6.
 18. Maret D, Molinier F, Braga J, et al. Accuracy of 3D reconstructions based on cone beam computed tomography. *J Dent Res* 2010;89:1465-9.
 19. Michetti J, Maret D, Mallet JP, et al. Validation of cone beam computed tomography as a tool to explore root canal anatomy. *J Endod* 2010;36:1187-90.
 20. Shahbazian M, Jacobs R, Wyatt J, et al. Accuracy and surgical feasibility of a CBCT-based stereolithographic surgical guide aiding autotransplantation of teeth: in vitro validation. *J Oral Rehabil* 2010 ;37:854-9.
 21. Galler KM, D'Souza RN, Federlin M, et al. Dentin conditioning codetermines cell fate in regenerative endodontics. *J Endod* 2011;37:1536-41.
 22. Barrett WA, Mortensen EN. Interactive live-wire boundary extraction. *Med Image Anal* 1997;1:331-41.
 23. Suetens P. Medical image analysis. Fundamentals of Medical Imaging. 2th ed. New York, USA: Cambridge Univeristy Press; 2009:160-89.
 24. Yushkevich PA, Piven J, Hazlett HC, et al. User-guided 3D active contour segmentation of anatomical structures: significantly improved efficiency and reliability. *Neuro-image* 2006;31:1116-28.
 25. Gao Y, Peters OA, Wu H, et al. An application framework of three-dimensional reconstruction and measurement for endodontic research. *J Endod* 2009;35:269-74.
 26. Bland JM, Altman DG. Statistical methods for assessing agreement between two methods of clinical measurement. *Lancet* 1986;1:307-10.
 27. Tsukiboshi M. Autogenous tooth transplantation: a reevaluation. *Int J Periodontics Restorative Dent* 1993;13:120-49.
 28. Torabinejad M, Faras H. A clinical and histological report of a tooth with an open apex treated with regenerative endodontics using platelet-rich plasma. *J Endod* 2012;38:864-8.
 29. Krastl G, Allgayer N, Lenherr P, et al. Tooth discoloration induced by endodontic materials: a literature review. *Dent Traumatol* 2013;29:2-7.
 30. Patel S. New dimensions in endodontic imaging: Part 2. Cone beam computed tomography. *Int Endod J* 2009;42:463-75.
 31. Bornstein MM, Wolner-Hanssen AB, Sendi P, et al. Comparison of intraoral radiography and limited cone beam computed tomography for the assessment of root-fractured permanent teeth. *Dent Traumatol* 2009;25:571-7.
 32. May JJ, Cohenca N, Peters OA. Contemporary management of horizontal root fractures to the permanent dentition: diagnosis--radiologic assessment to include cone-beam computed tomography. *J Endod* 2013 March;39(3 Suppl):S20-S25.
 33. Loubele M, Bogaerts R, Van Dijck E., et al. Comparison between effective radiation dose of CBCT and MSCT scanners for dentomaxillofacial applications. *Eur J Radiol* 2009;71:461-8.
 34. Pauwels R, Beinsberger J, Collaert B, et al. Effective dose range for dental cone beam computed tomography scanners. *Eur J Radiol* 2012;81:267-71.
 35. Flake NM, Gibbs JL, Diogenes A, Hargreaves KM, et al. A standardized novel method to measure radiographic root changes after endodontic therapy in immature teeth. *J Endod* 2014;40:46-50.
-

CHAPTER 2

This chapter is based on the following publication

EzEldeen, M., Stratis, A., Coucke, W., Codari, M., Politis, C., Jacobs, R. (2017). As Low Dose as Sufficient Quality: Optimization of Cone-beam Computed Tomographic Scanning Protocol for Tooth Autotransplantation Planning and Follow-up in Children. *Journal of Endodontics*, 43 (2).

- (A) OMFS IMPATH Research Group, Faculty of Medicine, Department of Imaging and Pathology, KU Leuven and Oral and Maxillofacial Surgery, University Hospitals Leuven, Leuven, Belgium
- (B) Department of Oral Health Sciences, KU Leuven and Paediatric Dentistry and Special Dental Care, University Hospitals Leuven, Leuven, Belgium
- (C) Freelance statistician, Heverlee, Belgium

As low dose as sufficient quality: optimization of CBCT scanning protocol for tooth autotransplantation planning and follow-up in children

M. EzEldeen (A,B), A. Stratis (A), W. Coucke (C), M. Codari (A), C. Politis (A), R. Jacobs (A)

ABSTRACT

Introduction — Tooth auto-transplantation (TAT) offers a viable biological approach to tooth replacement in children. To enhance outcome predictability of the TAT procedure, a CBCT-based surgical planning and transfer technique has been developed. The aim of this study was to optimize the CBCT scanning protocol to achieve a dose as low as possible and to maintain sufficient image quality.

Methods — A Sectional Head Phantom (SK150) was scanned using 18 exposure protocols in 3 different CBCT machines; 3D Accuitomo 170® (Morita, Kyoto, Japan), the ProMax® 3D MAX (Planmeca, Helsinki, Finland) and the NewTom® VGI EVO (QR Verona, Verona, Italy). Effective dose (ED) was calculated using Monte-Carlo simulation and pediatric voxel phantoms (5 & 8 years-old male, 12 years-old female). Image quality was assessed by comparing segmented teeth volumes, evaluation of the visibility of lamina-dura, and morphological surface analysis of 3D models. A general linear mixed model was fit to combine image quality parameters and radiation effective dose for each protocol in order to rank and compare all the protocols examined in the study.

Results — The ED for the pre-operative scan can be reduced to the range of 74.6-157.9 μSv with ProMax ULD-HDR 100x90 scoring highest ranking. ED for the post-operative scan can be reduced to the range of 24.2-41.5 μSv with ProMax ULD-NDR 50x55 and NewTom 50x50 standard scoring highest ranking.

Conclusion — A considerable reduction in the pediatric effective dose can be achieved while maintaining sufficient image quality for tooth auto-transplantation planning and follow-up using the dose optimization protocols.

KEY WORDS

Cone-beam computed tomographic imaging, CBCT, tooth auto-transplantation, pediatric radiation effective dose

INTRODUCTION

Permanent teeth loss or agenesis in children is confronting the dentist with challenging therapeutical problems mainly related to the ongoing dentoalveolar development. While implant placement is not a viable option and should be withheld until the completion of dentoalveolar development (1), tooth auto-transplantation (TAT) offers a viable biological approach to tooth replacement in children. It enables preservation of the alveolar ridge and allows for periodontal healing and preserving the possibility of function and growth (2-9). To enhance outcome predictability of the TAT procedure, a low dose CBCT-based surgical planning and transfer technique has been developed, involving donor tooth selection and stereolithographic tooth replica fabrication (8, 10, 11). CBCT-based surgical planning may aid the clinician seeking answers regarding surgical feasibility and best new position for the donor tooth meanwhile maximizing esthetics and function (8). The use of stereolithographic tooth replica provides individualized bone adaptability and reduces extra-alveolar time for the donor tooth. It may thus help to preserve the periodontal ligament and pulp vitality, reducing the risk for necrosis and resorption (8, 9). Moreover, 3D planning has been applied in the field of endodontics to treat successfully teeth with pulp canal calcification and apical pathology (12). Further, stereolithographic tooth replicas have been used to plan the endodontic treatment of anomalous anterior teeth (13).

The aim of this study was to optimize the CBCT scanning protocol to achieve a dose as low as possible and to maintain sufficient image quality for; (i) CBCT-based 3D planning and tooth replica fabrication serving TAT, and (ii) post-operative follow-up.

MATERIALS AND METHODS

Image Acquisition and Export

To allow dose optimization, while maintaining sufficient image quality for CBCT-based tooth replica fabrication, various CBCT scanning protocols were applied to a Sectional Head Phantom (SK150) (The Phantom Laboratory, Salem, NY, USA). This phantom is manufactured with a natural human skull and

STATEMENT OF CLINICAL RELEVANCE

This study provides effective radiation doses for three pediatric models. Applying the dose optimization protocols allows considerable dose reduction while maintaining sufficient image quality for CBCT-based 3D-planning, 3D-printing of tooth replica and post-operative follow-up.

upper cervical vertebrae. The phantom's natural bones are cast from RANDO® material (The Phantom Laboratory, Salem, NY, USA) with an internal air cavity representing the oral, pharynx and trachea anatomy. The opaque RANDO® material (The Phantom Laboratory, Salem, NY, USA) simulates the x-ray absorptency, atomic number and specific gravity of soft human tissue.

In order to determine the clinically optimized scanning protocol serving accurate visualization of tooth morphology, tooth segmentation, replica fabrication and post-operative follow-up the head phantom was scanned using 18 exposure protocols in 3 different CBCT machines; 3D Accuitomo 170® (Morita, Kyoto, Japan) (2 protocols), the ProMax® 3D MAX with ultra-low dose option (Planmeca, Helsinki, Finland) (10 protocols) and the NewTom® VGI EVO with tube current modulation option (QR Verona, Verona, Italy) (6 protocols). Table 1 presents the detailed scanning parameters and the exposure factors for all the protocols. Moreover, the protocols were divided into 2 groups depending on the indication: large field of view protocols for pre-operative scanning and small field of view protocols for post-operative follow-up (Table 1).

Image quality of the aforementioned CBCT protocols were compared to a reference CBCT scanning protocol (clinical reference), validated for accurate tooth (14) and bone (15) segmentation. The latter existed of a high-resolution CBCT (80 µm) scan (3D Accuitomo 170®; Morita, Kyoto, Japan) for maxillary incisors, canines, and mandibular premolars (Table 1).

Dosimetry

Monte Carlo dose simulations

A fully validated Monte Carlo (MC) framework, developed in our group, was used for dosimetric calculations (16, 17). The framework is built in EGSnrc MC code and is capable of simulating the entire CBCT imaging chain (18, 19). It was customized for the three scanners used in this study via creating scanner-specific input files to the source code; these files were including scanner-specific technical, geometric and acquisition details. The x-ray tube modelling was based on the equivalent source models concept (ESMs) (20, 21), consisting of an equivalent energy spectrum for each clinical protocol, obtained by half value layer (HVL) measurements, and the x-ray tube equivalent filter description based on air kerma measurements across the radiation field.

Voxel models

Organ doses were calculated via our MC framework for three pediatric voxel models. We retrieved three pediatric head and neck multislice CT image datasets (5 and 8 years old-males, 12 years old female) from the PACS system of the

42 **Table 1: Scanning parameters and exposure factors for the used protocols**

Brand name	Protocol	Rotation (degrees)	Voxel size (µm)	FOV (mm)	x-ray tube voltage (kV)	x-ray tube loading (mAs)	DICOM Export parameters (voxel size x slice interval)
Accuitomo	High Resolution*	360	80	40x40	90	154	80 x 80
Accuitomo	Standard Resolution	360	125	60x60 ^x	90	87.5	125 x 125
Accuitomo	Standard Resolution	360	160	80x80 ^{xx}	90	87.5	160 x 160
Planmeca 3D MAX	Ultra Low Dose Low-dose reconstruction (ULD-LDR)	210	400	100x90 ^{xx}	96	6	400 x 400
Planmeca 3D MAX	Ultra Low Dose Normal-dose reconstruction (ULD-NDR)	210	200	100x90 ^{xx}	96	16	200 x 200
Planmeca 3D MAX	Ultra Low Dose High-definition reconstruction (ULD-HDR)	210	150	100x90 ^{xx}	96	25	150 x 150
Planmeca 3D MAX	Normal Dose Low-dose reconstruction (ND-LDR)	210	400	100x90 ^{xx}	96	21.6	400 x 400
Planmeca 3D MAX	Normal Dose Normal-dose reconstruction (ND-NDR)	210	200	100x90 ^{xx}	96	67.2	200 x 200
Planmeca 3D MAX	Normal Dose High-definition reconstruction (ND-HDR)	210	150	100x90 ^{xx}	96	105	150 x 150
Planmeca 3D MAX	Ultra Low Dose Low-dose reconstruction (ULD-LDR)	210	400	50x55 ^x	96	6	400 x 400
Planmeca 3D MAX	Ultra Low Dose Normal-dose reconstruction (ULD-NDR)	210	200	50x55 ^x	96	16	200 x 200
Planmeca 3D MAX	Ultra Low Dose High-definition reconstruction (ULD-HDR)	210	150	50x55 ^x	96	25	150 x 150
Planmeca 3D MAX	Normal Dose High-definition reconstruction (ND-HDR)	210	150	50x55 ^x	96	105	150 x 150
NewTom VGI evo	Standard mode	360	200	80x80 ^{xx}	110	TCM**	200 x 200
NewTom VGI evo	Eco mode	360	200	80x80 ^{xx}	110	TCM**	200 x 200
NewTom VGI evo	Standard mode	360	200	80x50 ^{xx}	110	TCM**	200 x 200
NewTom VGI evo	Eco mode	360	200	80x50 ^{xx}	110	TCM**	200 x 200
NewTom VGI evo	Standard mode	360	200	50x50 ^x	110	TCM**	200 x 200
NewTom VGI evo	Eco mode	360	200	50x50 ^x	110	TCM**	200 x 200

* Reference CBCT scanning protocol ** Tube current modulation ^x Small Field of View for Post-operative follow-up ^{xx} Large Field of View for Pre-operative scanning

Table 2: The segmented organs and their density

ID	Organ	Density (g cm ⁻³)
0	Vacuum	0.000
1	Air cavities	0.001
2	Blood	1.060
3	Brain	1.050
4	Cartilage	1.100
5	Connective tissue	1.120
6	Skin	1.090
7	Esophagus	1.030
8	Eye	1.050
9	Eye Lens	1.070
10	Fat	0.950
11	Mandible	1.920
12	Muscle	1.050
13	ET	1.030
14	Spinal cord	1.030
15	Teeth	2.750
16	Tongue	1.050
17	Trachea	1.060
18	Bone	1.920
19	Thyroid	1.040
20	Salivary glands	1.030
21	Tissue	0.950
22	Oral mucosa	1.050
23	Red Bone Marrow	1.030

- 44 University Hospitals Leuven. It is only multislice CT datasets that can be used for accurate dose calculations, since the resulting voxel models represent a full head. The organs in the head and neck region were fully segmented in Image J (<http://imagej.nih.gov/ij/>) leading to voxel models consisting of 23 organs (Table 2). Each organ's density and elemental composition were derived from the ICRP Publication 89 and from Woodard et al (22, 23).

Effective dose calculations

After organ doses were calculated via Monte Carlo simulations, the radiation induced risk was determined by estimating the effective dose. Before applying the organ specific radio-sensitivity weighting factors to the respective calculated absorbed organ doses (24), the fraction of any radiosensitive organ which is present into each phantom was calculated as the quotient of the radiosensitive organ's mass in the phantom to the respective reference mass value at each age category. To calculate the dose to the bone marrow (RBM), the distribution of the RBM in the body was calculated for each age category (22). The doses to the bone surface and the lymph nodes were calculated by employing validated formulas of the organ doses to substitute organs (25). The effective dose was calculated as the sum of the radiosensitive organs' equivalent doses.

Assessment of Image Quality

Image processing and evaluation

All data were imported into MeVisLab (MeVis Research, Bremen, Germany). A region of interest (ROI) was created for each tooth (4 maxillary incisors, 4 canines and 4 mandibular premolars) and saved as a new image in DICOM format to reduce computation time in the following steps. All ROIs from the different protocols were first spatially aligned to the corresponding ROI from the reference image using maximization of mutual information as a registration metric (26). Teeth segmentation was then performed using a dedicated tool developed in MeVisLab and validated for accurate teeth segmentation (14). The method applies interactive livewire boundary extraction to extract the tooth of interest from the surrounding tissue (14, 27).

During the segmentation process the operators evaluated the visibility of the periodontal ligament space on an ordinal scale ranging from 1 for very unclear to 5 for very clear. In addition, the time consumed, and the number of contours needed for the segmentation of each tooth were recorded.

3D Reconstruction and Morphological Surface Analysis

After segmentation, the 3D triangle-based surface of the tooth was reconstructed without being smoothed to preserve its raw volume measurement and exported as a Standard Tessellation Language (STL) file. All STLs were then imported in the 3-matic® software (Materialize NV, Leuven, Belgium) to perform a morphological surface comparison between the 3D model for each tooth/protocol vs. the 3D model from the reference image. A cut-off value for accuracy was set at 0.2 mm median deviation from the reference image (10, 28). Further, the percentage of surface points under the cut-off value was recorded in a dedicated tool in Matlab. Binary images for segmented teeth (per tooth type; maxillary central incisor, maxillary canine, mandibular premolar) were used in calculating the percentage of area difference per slice for the segmented object from the clinical reference starting from root apex down to the crown.

Statistical Analysis and Protocol Comparison

Statistical modelling and analysis were performed in S-plus for Linux 8.0 (Tibco Software, Palo Alto, CA). Graphs were plotted using the statistical software package STATISTICA 8.0 (StatSoft Inc, Tulsa, OK). A general linear mixed model (GLM) was fit with tooth as random variable and protocol as fixed variable to combine image quality parameters and radiation effective dose for each protocol in order to rank all the protocols examined in the study. This ranking was meant to choose the best protocols, with sufficient image quality while minimizing the dose, for further detailed comparison. Image quality parameters were condensed in a Cartesian distance between each protocol and the clinical reference. A normal quantile plot of the residuals and a residual dot plot showed that the residuals were normally distributed with equal variance. Two distances were considered: the 1st distance included the image quality parameters (log of the segmented volume difference with clinical reference, median surface deviation from the clinical reference, percentage of points under cut-off value of surface deviation (0.2 mm), visibility of lamina dura, number of contours needed for tooth segmentation and time consumed for tooth segmentation). The last two quality parameters were included with a lower weight than the others. The 2nd distance included the quality parameters mentioned above in addition to the effective radiation dose, in which a lower dose is considered as more favorable than a higher dose.

Since the visibility of the lamina dura is an ordinal parameter, a value was assigned to the different classes as follows; class 1 received value 0, classes 2 to 4 received values 2 to 4 respectively and class 5 received value 6. These values were used for the calculation of the distances. Moreover, all parameters included in the distances was rescaled in order to give them the same scale for the

Table 3: The effective dose determined for each scanning protocol

Brand name	Protocol	FOV (mm)	5 years-old boy ED in (µSv)	8 years-old boy ED in (µSv)	12 years-old girl ED in (µSv)
Accuitomo	Standard Resolution	60x60	149,2	161,3	121,1
Accuitomo	Standard Resolution	80x80	269,0	239,9	267,3
Planmeca 3D MAX	Ultra Low Dose Low-dose reconstruction (ULD-LDR)	100x90	40,1	34,8	41,0
Planmeca 3D MAX	Ultra Low Dose Normal-dose reconstruction (ULD-NDR)	100x90	106,9	92,9	109,2
Planmeca 3D MAX	Ultra Low Dose High-definition reconstruction (ULD-HDR)	100x90	167,0	145,1	170,7
Planmeca 3D MAX	Normal Dose Low-dose reconstruction (ND-LDR)	100x90	144,2	125,4	147,5
Planmeca 3D MAX	Normal Dose Normal-dose reconstruction (ND-NDR)	100x90	448,8	390,2	458,7
Planmeca 3D MAX	Normal Dose High-definition reconstruction (ND-HDR)	100x90	701,2	609,6	716,8
Planmeca 3D MAX	Ultra Low Dose Low-dose reconstruction (ULD-LDR)	50x55	10,4	10,2	7,9
Planmeca 3D MAX	Ultra Low Dose Normal-dose reconstruction (ULD-NDR)	50x55	27,7	27,2	21,2
Planmeca 3D MAX	Ultra Low Dose High-definition reconstruction (ULD-HDR)	50x55	43,2	42,5	33,1
Planmeca 3D MAX	Normal Dose High-definition reconstruction (ND-HDR)	50x55	181,5	178,4	139,0
NewTom VGI evo	Standard mode	80x80	149,5	92,5	56,8
NewTom VGI evo	Eco mode	80x80	56,1	35,8	27,7
NewTom VGI evo	Standard mode	80x50	42,5	65,9	54,3
NewTom VGI evo	Eco mode	80x50	24,3	22,4	17,3
NewTom VGI evo	Standard mode	50x50	30,9	53,5	29,5
NewTom VGI evo	Eco mode	50x50	6,6	7,1	5,2

Table 4: Comparison table for Large FOV, Distance 2 (Including radiation dose)

Brand name	Protocol	FOV (mm)	Rating*	Doesn't differ from best (95%)
Planmeca 3D Max	ULD-HDR	100x90	2.51	X
NewTom VGI evo	Eco mode	80x50	3.05	X
NewTom VGI evo	Regular mode	80x50	3.13	X
NewTom VGI evo	Regular mode	80x80	3.17	X
Planmeca 3D Max	ULD-NR	100x90	3.20	X
NewTom VGI evo	Eco mode	80x80	3.27	X
Planmeca 3D Max	ND-NR	100x90	3.87	
Accuitomo	Standard resolution	80x80	3.97	
Planmeca 3D Max	ND-LR	100x90	4.53	
Planmeca 3D Max	ND-HDR	100x90	5.53	
Planmeca 3D Max	ULD-LR	100x90	6.01	

*The closer the rating to zero the better the balance between image quality and radiation dose

Table 5: Comparison table for Small FOV, Distance 2 (Including radiation dose)

Brand name	Protocol	FOV (mm)	Rating*	Doesn't differ from best (95%)
Planmeca 3D Max	ULD-NR	50x55	2.81	X
NewTom VGI evo	Regular mode	50x50	2.97	X
Planmeca 3D Max	ULD-HDR	50x55	2.98	X
NewTom VGI evo	Eco mode	50x50	3.51	X
Accuitomo	Standard resolution	60x60	4.09	
Planmeca 3D Max	ND-HDR	50x55	4.24	
Planmeca 3D Max	ULD-LR	50x55	5.92	

*The closer the rating to zero the better the balance between image quality and radiation dose

48 distance calculations. For the effective radiation dose included in the model, the mean of the dose for the three age groups examined was used. A comparison with the hypothetical best (clinical standard protocol for image quality and minimum radiation dose), at 95% confidence interval, was performed for each protocol (29).

Finally, the top-ranking protocols were included in a detailed statistical and graphical comparison for each of the parameters to obtain insights on how these protocols differ from each other.

RESULTS

Dosimetry

Table 3 presents the results for the effective doses for the three pediatric models (5 & 8 years-old males, 12 years-old female). For the large field of view protocols; the lowest measured average effective dose was 21.3 (± 3.6) μSv (NewTom 80x50 Eco), while the highest was 675.8 (± 57.9) μSv (ProMax ND-HDR). For the small field of view protocols; the lowest measured average effective dose was 6.3 (± 0.9) μSv (NewTom 50x50 Eco), while the highest was 166.3 (± 23.6) μSv (ProMax ND-HDR).

Protocol optimization based on GLM rankings

Based on image quality

The overall ranking for the large field of view protocols showed that only 3 protocols differed significantly from the clinical standard: Accuitomo standard resolution 80x80, ProMax ND-LDR 100x90, ProMax ULD-LDR 100x90. While for the small field of view only 1 protocol differed significantly from the clinical standard: ProMax ULD-LDR 50x55.

Based on image quality combined with effective radiation dose

The overall ranking for the large field of view protocols showed that 6 protocols didn't differ significantly from the best with the ProMax ULD-HDR 100x90 scoring the highest ranking (Table 4). Further, for the small field of view, 4 protocols did not differ significantly from the best with the ProMax ULD-NDR 50x55 scoring the highest ranking with a very small margin above the NewTom 50x50 standard (Table 5).

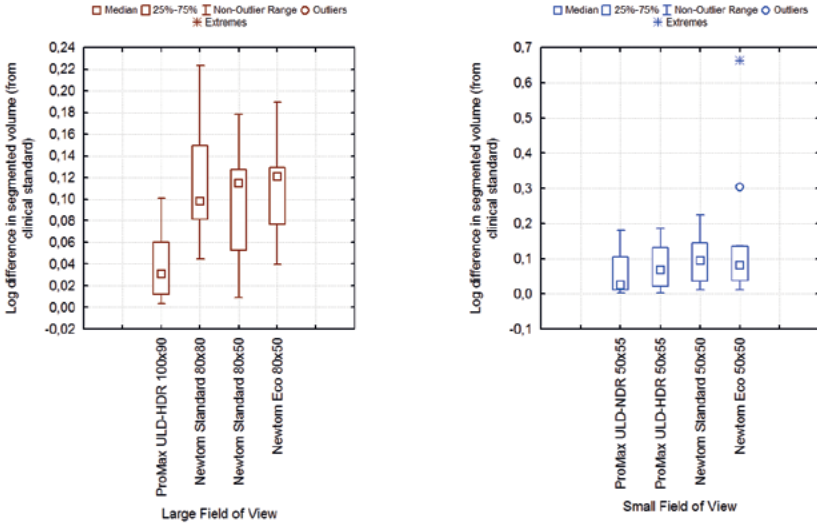


Figure 1: (A) A box plot comparison between the percentage difference in segmented volume from clinical standard for top ranking large field of view protocols, (B) A box plot comparison between the percentage difference in segmented volume from clinical standard for top ranking small field of view protocols.

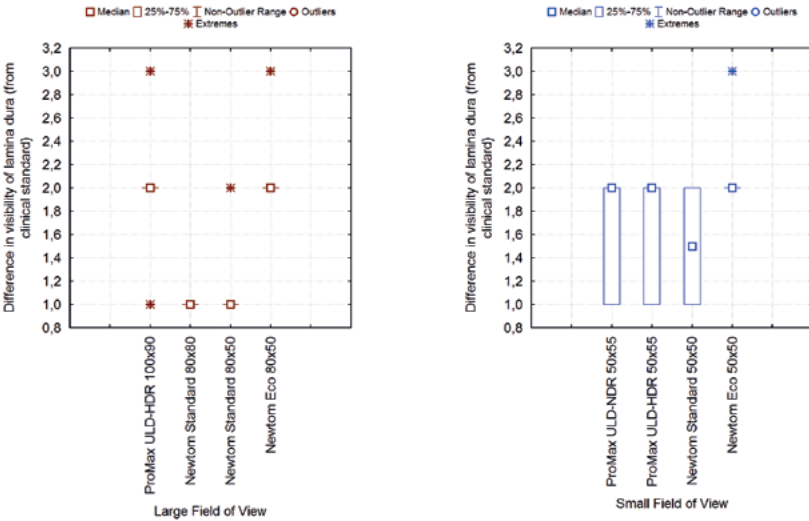


Figure 3: (A) A box plot comparison between the difference in visibility of lamina dura from clinical standard for top ranking large field of view protocols, (B) A box plot comparison between the difference in visibility of lamina dura from clinical standard for top ranking small field of view protocols.

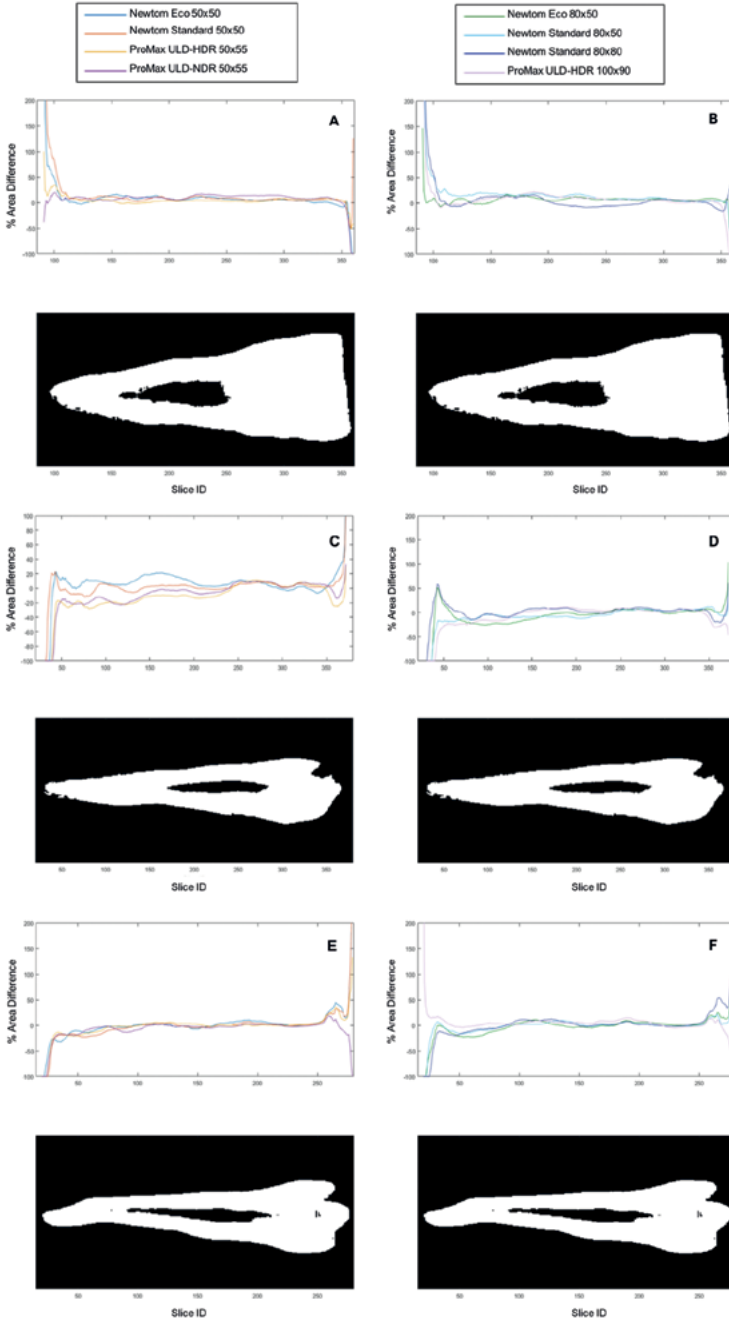


Figure 2: Slice area comparison for large field of view protocols (A, C & E) and small field of view protocols (B, D & F). Comparison shows the percentage difference in area per slice starting from the apex down to the crown per tooth type; A&B central incisor, C&D maxillary canine, E&F mandibular premolar.

Detailed comparison of top-ranking protocols

The first 4 top ranking protocols (from Tables 4&5) were included in a detailed comparison of image quality parameters (separately for the large field of view and the small field of view).

Segmented volume difference from the clinical standard

The comparison for the large field of view protocols (Figure 1) showed statistically significant differences between the ProMax ULD-HDR 100x90 and the other 3 protocols (NewTom 80x50 Standard, NewTom 80x50 Eco & NewTom 80x80 Standard) (P-values = 0.009, 0.001 & 0.0003). The comparison did not show any differences between the top 4 ranking small field of view protocols (P-values > 0.05) (Figure 1).

Median surface deviation and percentage of points under the cut-off value

The comparison did not show any statistically significant differences between the top 4 ranking large and small field of view protocols respectively (P-values > 0.05). Further, slice area comparison showed that the main surface deviation was seen for the maxillary canine with the small field of view protocols (Figure 2). This deviation was localized on the middle and apical thirds of the root ($\pm 20\%$). The best performing protocol for this tooth type was the NewTom 50x50 standard ($\pm 0\%$) (Figure 2).

Visibility of the lamina dura

Comparison of the difference in visibility of the lamina dura from the clinical standard for the large field of view (Figure 3) showed statistically significant differences between the NewTom 80x80 Standard and the NewTom 80x50 Standard on the one hand and ProMax ULD-HDR 100x90 & NewTom 80x50 Eco on the other hand (P-values < 0.0001). While for the small field of view protocols the NewTom 50x50 Standard was the closest to the clinical standard (Figure 3) with statistically significant differences with only 1 protocol the NewTom 50x50 Eco (P-value < 0.05).

Time consumed for segmentation

Comparison of the time consumed for tooth segmentation showed that for the large field of view protocols the NewTom 80x50 Eco had the shortest segmentation time on average (7.2 mins). The differences with average time consumed

52 with the NewTom 80x50 Standard (8.0 mins) and the NewTom 80x80 Standard (8.5 mins) were not statistically significant (P -value > 0.05). This was not the case for the ProMax ULD-HDR 100x90 as the average time consumed was doubled (14.9 mins) (P -value < 0.05). Moreover, for the small field of view protocols, the NewTom 50x50 Standard & 50x50 Eco scored the shortest average time (8.9 mins & 9.8 mins). This was statistically significant when compared to the ProMax ULD-NDR 50x55 & ULD-HDR 50x55 (14.1 mins & 15.9 mins) (P -value < 0.001).

DISCUSSION

CBCT-based TAT offers several advantages for pediatric patients and the surgeon (8, 10, 11). Furthermore, CBCT-based applications such as guided endodontics (12, 13) have been successfully reported due to the recent increased availability of 3D-planning software and the great reduction in the cost of stereolithographic tooth replica fabrication. Nevertheless, there is a pressing need for scanning protocol optimization. The effective radiation dose delivered by CBCT devices available in the market varies enormously from around 10–1200 μ Sv (which is an equivalent of 2–240 panoramic radiographs) (30, 31). Therefore, a proper balance (optimization) between, on the one hand, costs and radiation dose and, on the other hand, information required needs to be maintained (28). Moreover, the scanned area should not exceed the area of interest. This will limit the dose substantially, thus justifying its use (28, 32, 33). Furthermore, there is a substantial variation in image quality intra and inter CBCT devices (34, 35), where the investigations on clinically oriented image quality are almost never combined with dosimetry. Therefore, the main aim of this study was to reduce the pediatric dose for the CBCT scan while maintaining sufficient image quality to be used for the surgical planning, printing of the tooth replica and post-operative follow-up.

The accuracy of teeth volumetric measurements from CBCT data is well documented and has been reported by several authors (36, 37). Furthermore, a recent study from our group (14) reported a slight deviation of segmented teeth volumes from CBCT data (at 80 μ m & 160 μ m voxel sizes) within 0.5% to 0.8%, compared to the segmented volumes from μ CT data (at 30 μ m voxel size) using the same method applied in the current study. The results from EzEldien et al (14) allowed the use of the Accuitomo-170[®] CBCT (FOV 40x40, 80 μ m voxel size) as a clinical reference for tooth segmentation and image quality, in this optimization procedure.

Accurate tooth segmentation is affected by the visibility of the anatomic structures, mainly the periodontal ligament space and the lamina dura. Furthermore, the accuracy of the segmentation determines the accuracy of the 3D

printed surgical replica. Thus, the present study examined the effect of effective dose reduction on image quality parameters that are vital for CBCT-based TAT. Analysis revealed that the effective dose for the pre-operative scan can be reduced to the range of 74.6-157.9 μSv , while maintaining sufficient image quality for accurate 3D planning and surgical replica fabrication. Moreover, the dose for the post-operative follow-up, using the small field of view protocols, can be reduced to the range of 24.2-41.5 μSv . The optimization of the small field of view protocols has an importance extended to other indications such as 1- the diagnosis and treatment of traumatic dental injuries, 2- guided endodontics for anomalous teeth and teeth with pulp canal calcifications, and 3- regenerative endodontic procedures including the treatment planning and long-term follow-up.

Generally, high energy, high resolution scans are not needed for TAT planning and follow-up. Nevertheless, the best performing protocols in the current study have segmented volumes and visibility of anatomic structures, comparable to a high-resolution scan. Therefore, these results encourage the regular use of dose-reducing protocols, especially for pediatric patients.

The present study highlights the need for indication-oriented optimization studies to provide data for evidence-based practice. Such data might encourage the manufacturers to consider indication-guided image acquisition protocols. Moreover, combining age and gender specific protocols may aid in keeping the effective dose for pediatric patients at minimum levels.

Finally, it is fair to mention that this study has its limitations. It was not possible to compare the accuracy of the segmented volumes from different protocols to the physical teeth volume and was only applied to single rooted teeth. However, the data presented in this study is unique. This study has provided effective doses for three pediatric models (5, 8 and 12 years-old) combined with a systematic evaluation for image quality, which is specifically oriented for TAT planning and follow-up. Furthermore, the protocols optimized using the image quality parameters in the current study can be easily extended to the field of endodontics for diagnostic and therapeutic purposes. Future optimization studies should be indication-oriented in order to minimize the dose and maximize the benefits for the patient.

CONCLUSIONS

A considerable reduction in the pediatric effective dose can be achieved while maintaining sufficient image quality for tooth auto-transplantation planning and follow-up using the dose optimization protocols.

ACKNOWLEDGMENTS

The authors deny any conflicts of interest related to this study. The authors would like to acknowledge Fernando Sánchez Ugarte, Juan Jose Escobar, Javiera Diaz Amtmann, Manuelita Vinagre and Apoorv Kakar for their participation in teeth segmentation. This research is funded by FWO Vlaanderen (Fonds Wetenschappelijk Onderzoek). Grant number G089213N.

REFERENCES

1. Sharma AB, Vargervik K. Using implants for the growing child. *J Calif Dent Assoc* 2006;34:719-724.
2. Andreasen JO, Paulsen HU, Yu Z, Ahlquist R, Bayer T, Schwartz O. A long-term study of 370 autotransplanted premolars. Part I. Surgical procedures and standardized techniques for monitoring healing. *Eur J Orthod* 1990;12:3-13.
3. Andreasen JO, Paulsen HU, Yu Z, Bayer T. A long-term study of 370 autotransplanted premolars. Part IV. Root development subsequent to transplantation. *Eur J Orthod* 1990;12:38-50.
4. Andreasen JO, Paulsen HU, Yu Z, Bayer T, Schwartz O. A long-term study of 370 autotransplanted premolars. Part II. Tooth survival and pulp healing subsequent to transplantation. *Eur J Orthod* 1990;12:14-24.
5. Andreasen JO, Paulsen HU, Yu Z, Schwartz O. A long-term study of 370 autotransplanted premolars. Part III. Periodontal healing subsequent to transplantation. *Eur J Orthod* 1990;12:25-37.
6. Czochrowska EM, Stenvik A, Album B, Zachrisson BU. Autotransplantation of premolars to replace maxillary incisors: a comparison with natural incisors. *Am J Orthod Dentofacial Orthop* 2000;118:592-600.
7. Czochrowska EM, Stenvik A, Bjercke B, Zachrisson BU. Outcome of tooth transplantation: Survival and success rates 17-41 years posttreatment. *Am J Orthod Dentofacial Orthop* 2002;121:110-119.
8. Shahbazian M, Jacobs R, Wyatt J, Denys D, Lambrechts I, Vinckier F, et al. Validation of the cone beam computed tomography-based stereolithographic surgical guide aiding autotransplantation of teeth: clinical case-control study. *Oral Surg.Oral Med.Oral Pathol. Oral Radiol.* 2013;115:667-675.
9. Tsukiboshi M. Autotransplantation of teeth: requirements for predictable success. *Dent. Traumatol.* 2002;18:157-180.
10. Shahbazian M, Jacobs R, Wyatt J, Willems G, Pattijn V, Dhoore E, et al. Accuracy and surgical feasibility of a CBCT-based stereolithographic surgical guide aiding autotransplantation of teeth: in vitro validation. *J.Oral Rehabil.* 2010;37:854-859.
11. Jang Y, Choi YJ, Lee SJ, Roh BD, Park SH, Kim E. Prognostic Factors for Clinical Outcomes in Autotransplantation of Teeth with Complete Root Formation: Survival Analysis for up to 12 Years. *J Endod* 2016;42:198-205.
12. Krastl G, Zehnder MS, Connert T, Weiger R, Kuhl S. Guided Endodontics: a novel treatment approach for teeth with pulp canal calcification and apical pathology. *Dent Traumatol* 2016;32:240-246.
13. Byun C, Kim C, Cho S, Baek SH, Kim G, Kim SG, et al. Endodontic Treatment of an Anomalous Anterior Tooth with the Aid of a 3-dimensional Printed Physical Tooth Model. *J Endod* 2015;41:961-965.
14. EzEldeen M, Van Gorp G, Van Dessel J, Vandermeulen D, Jacobs R. 3-dimensional analysis of regenerative endodontic treatment outcome. *J Endod* 2015;41:317-324.
15. Van Dessel J, Huang Y, Depypere M, Rubira-Bullen I, Maes F, Jacobs R. A comparative evaluation of cone beam CT and micro-CT on trabecular bone structures in the human mandible. *Dentomaxillofac Radiol* 2013;42:20130145.

16. Zhang G, Marshall N, Bogaerts R, Jacobs R, Bosmans H. Monte Carlo modeling for dose assessment in cone beam CT for oral and maxillofacial applications. *Med Phys* 2013;40:072103.
17. Zhang G, Pauwels R, Marshall N, Shaheen E, Nuyts J, Jacobs R, et al. Development and validation of a hybrid simulation technique for cone beam CT: application to an oral imaging system. *Phys Med Biol* 2011;56:5823-5843.
18. Rogers DWO, Walters, B., Kawrakow, L., BEAMnrc Users Manual. NRCC Report; 2007.
19. Walters B, Kawrakow, L., Rogers, D.W.O., DOSXYZnrc Users Manual. NRCC Report; 2001.
20. Turner AC, Zhang D, Kim HJ, DeMarco JJ, Cagnon CH, Angel E, et al. A method to generate equivalent energy spectra and filtration models based on measurement for multidetector CT Monte Carlo dosimetry simulations. *Med Phys* 2009;36:2154-2164.
21. Siewerdsen JH, Waese AM, Moseley DJ, Richard S, Jaffray DA. Spektr: a computational tool for x-ray spectral analysis and imaging system optimization. *Med Phys* 2004;31:3057-3067.
22. Protection ICoR. Basic anatomical and physiological data for use in radiological protection: reference values. A report of age- and gender-related differences in the anatomical and physiological characteristics of reference individuals. ICRP Publication 89. *Ann ICRP* 2002;32:5-265.
23. Woodard HQ, White DR. The composition of body tissues. *Br J Radiol* 1986;59(708):1209-1218.
24. Protection ICoR. The 2007 Recommendations of the International Commission on Radiological Protection. ICRP publication 103. *Ann ICRP* 2007;37:1-332.
25. Ludlow JB, Davies-Ludlow LE, Brooks SL. Dosimetry of two extraoral direct digital imaging devices: NewTom cone beam CT and Orthophos Plus DS panoramic unit. *Dentomaxillofac Radiol* 2003;32:229-234.
26. Maes F, Collignon A, Vandermeulen D, Marchal G, Suetens P. Multimodality image registration by maximization of mutual information. *IEEE Trans Med Imaging* 1997;16:187-198.
27. Barrett WA, Mortensen EN. Interactive live-wire boundary extraction. *Med Image Anal* 1997;1:331-341.
28. Jacobs R. Dental cone beam CT and its justified use in oral health care. *JBR.-BTR*. 2011;94:254-265.
29. Hsu J. Multiple comparisons: theory and methods. CRC Press; 1996.
30. Loubele M, Bogaerts R, Van DE, Pauwels R, Vanheusden S, Suetens P, et al. Comparison between effective radiation dose of CBCT and MSCT scanners for dentomaxillofacial applications. *Eur J Radiol* 2009;71:461-468.
31. Pauwels R, Beinsberger J, Collaert B, Theodorakou C, Rogers J, Walker A, et al. Effective dose range for dental cone beam computed tomography scanners. *Eur J Radiol* 2012;81:267-271.
32. Bornstein MM, Wolner-Hanssen AB, Sendi P, von AT. Comparison of intraoral radiography and limited cone beam computed tomography for the assessment of root-fractured permanent teeth. *Dent Traumatol*. 2009;25:571-577.
33. May JJ, Cohenca N, Peters OA. Contemporary management of horizontal root fractures to the permanent dentition: diagnosis--radiologic assessment to include cone-beam computed tomography. *Pediatr Dent* 2013;35:120-124.
34. Liang X, Jacobs R, Hassan B, Li L, Pauwels R, Corpas L, et al. A comparative evaluation of Cone Beam Computed Tomography (CBCT) and Multi-Slice CT (MSCT) Part I. On subjective image quality. *Eur J Radiol* 2010;75:265-269.
35. Liang X, Lambrichts I, Sun Y, Denis K, Hassan B, Li L, et al. A comparative evaluation of Cone Beam Computed Tomography (CBCT) and Multi-Slice CT (MSCT). Part II: On 3D model accuracy. *Eur J Radiol* 2010;75:270-274.
36. Liu Y, Olszewski R, Alexandroni ES, Enciso R, Xu T, Mah JK. The validity of in vivo tooth volume determinations from cone-beam computed tomography. *Angle Orthod*. 2010;80:160-166.
37. Michetti J, Maret D, Mallet JP, Diemer F. Validation of cone beam computed tomography as a tool to explore root canal anatomy. *J.Endodod*. 2010;36:1187-1190.

PART II

**Tooth Autotransplantation as a current solution
full of future inspirations**

CHAPTER 3

This chapter is based on the following publication

EzEldeen, M., Wyatt, J., Al-Rimawi, A., Coucke, W., Shaheen, E., Lambrichts, I., Willems, G., Politis, C., Jacobs, R. (2019). Use of CBCT Guidance for Tooth Autotransplantation in Children. *Journal of Dental Research*, 98(4), 406-413.

- (A) OMFS IMPATHResearch Group, Faculty of Medicine, Department of Imaging and Pathology, KU Leuven and Oral and Maxillofacial Surgery, University Hospitals Leuven, Kapucijnenvoer 33, 3000 Leuven, Belgium
- (B) Department of Oral Health Sciences, KU Leuven and Paediatric Dentistry and Special Dental Care, University Hospitals Leuven, Kapucijnenvoer 33, 3000 Leuven, Belgium
- (C) Certified freelance statistician, Heverlee, 3001 Heverlee, Belgium
- (D) Biomedical Research Institute, Hasselt University, Campus Diepenbeek, Agoralaan Building C, B-3590 Diepenbeek, Belgium
- (E) Department of Oral Health Sciences, KU Leuven and Orthodontics and Dentistry, University Hospitals Leuven, Kapucijnenvoer 33, 3000 Leuven, Belgium

Use of CBCT-guidance for Tooth Autotransplantation in Children

M. EzEldeen (A,B), J. Wyatt (B), A. Al-Rimawi (A), W. Coucke (C), E. Shaheen (A),
I. Lambrichts (D), G. Willems (E), C. Politis (A), R. Jacobs (A)

ABSTRACT

Introduction — Tooth autotransplantation (TAT) offers a viable biological approach to tooth replacement in children and adolescents. Objectives: The aim of this study was to evaluate the outcome of the cone-beam computed tomographic (CBCT)-guided tooth autotransplantation (TAT) compared to the conventional TAT protocol, and to assess the 3D patterns of healing after CBCT-guided TAT (secondary aim).

KEY WORDS

CAD, Computed tomography, Digital imaging/radiology, Tooth regeneration/transplantation, (PDL) Periodontal ligament, Clinical outcomes

Methods — This study included 100 autotransplanted teeth in 88 patients. Each experimental group consisted of 50 transplants in 44 patients (31 males and 19 females). The mean age at the time of surgery was 10.7 (± 1.1) years-old for the CBCT-guided group. This was 10.6 (± 1.3) years-old for the conventional-group. The mean follow-up period was 4.5 (± 3.1) years (range 1.1-10.4 years).

Results — Overall survival rate for the CBCT-guided TAT was 92% and success rate was 86% compared to 84% survival rate and 78% success rate for the conventional-group ($P > 0.005$). The following measurements were extracted from the 3D analysis: root hard tissue volume (RV), root length (RL), apical foramen area (AFA), mean and maximum dentin wall thickness (Mean-DWT & Max-DWT). Overall, the mean percentage of tissue change was RV gain by 65.8% (± 34.6), RL gain by 37.3% (± 31.5), AFA reduction by 91.1% (± 14.9), Mean-DWT increase by 107.9% (± 67.7), and Max-DWT increase by 26.5% (± 40.1). Principle component analysis (PCA) identified the Mean-DWT, RV and Max-DWT as the parameters best describing the tissue change after TAT. Cluster analysis applied to the variables chosen by the PCA classified the CBCT-group into 4 distinct clusters (C1=37.2%, C2=17.1%, C3=28.6%, C4=17.1%) revealing different patterns of tissue healing after TAT.

Conclusion — The CBCT-guided approach increased the predictability of the treatment. The 3D analysis provided insights into the patterns of healing. CBCT-guided TAT could be adopted as an alternative for the conventional approach. (Clinical trial center and ethical board University Hospitals, KU Leuven: S55287) (ClinicalTrials.gov Identifier: NCT02464202)

INTRODUCTION

Tooth autotransplantation (TAT) offers a viable biological approach to tooth replacement in children and adolescents after traumatic dental injuries (TDIs), agenesis, developmental anomalies or specific orthodontic problems (1-3). TDIs have a relatively high prevalence (15.2%) with children being the most affected (4). The treatment options available, for example implant placement, are limited by the ongoing dentoalveolar development (5) while, orthodontic tooth alignment is challenging unless skeletal anchorage is applied (6, 7). TAT allows for periodontal healing and enables preservation of the alveolar ridge maintaining the possibility of function and growth (1, 8-10). To enhance outcome predictability of the TAT procedure, a low-dose cone-beam computed tomographic (CBCT)-guided surgical planning and transfer technique has been developed, involving donor tooth selection and tooth replica fabrication (11, 12). The primary aim of this study was to evaluate the outcome of the CBCT-guided TAT compared to the conventional TAT protocol, and the secondary aim was to assess the 3D patterns of healing after CBCT-guided TAT.

MATERIALS AND METHODS

Study Design

This study was designed as a controlled prospective clinical trial and included 100 autotransplanted teeth in 88 patients. Starting from 2007, all patients referred to the pediatric dentistry department of the University Hospitals of the KU Leuven (Belgium) for TAT and meeting the inclusion criteria were included in the CBCT-guided TAT group (test group). Ethical approval was obtained by the local clinical trial center and ethical board (S55287, University Hospitals, KU Leuven), in compliance with the Helsinki Declaration. This study conformed with STROBE guidelines for human observational studies. Informed consent was obtained. Inclusion criteria were: American Society of Anesthesiologists' (ASA) score 1, ≤ 18 years-old, premolar as a donor tooth. The conventional TAT group (control group) consisted of historically matched controls, randomly allocated to each subject at the time of inclusion focusing on similar surgical challenge, age, gender, matching donor tooth with the same stage of root development and recipient site.

Pre-operative procedure

A low dose CBCT scan (Appendix CBCT scanning parameters) (13, 14) was obtained followed by donor tooth segmentation (Fig. 1A & B) and digital 3D model creation of the donor tooth (Fig. 1C & D) and recipient site (Fig. 1E). A virtual TAT was then performed to determine the surgical feasibility and the

best new position for the donor tooth (Fig. 1E). When it was decided for TAT, tooth replica and the surgical guide were 3D-printed and surgery was planned (Fig. 1F, G & H). The method for CBCT-guided surgical planning and tooth replica fabrication was validated and described in detail in previous publications (11, 12).

In the conventional group two dimensional (2D) panoramic radiographs were used to evaluate the recipient site and donor tooth (10).

Surgical procedure

The procedure for the CBCT-guided group was described in (12). Briefly, all surgeries took place under general anesthesia by one of two surgeons. All recipient sites were anesthetized using mepivacaine 3% without epinephrine (Scandonest; Septodont, Saint Maur des Fosses, France) to avoid vasoconstriction. The guides and replicas were used to shape the recipient site to match the virtually planned position (12). After preparation of the recipient site, the replica was left in place to avoid formation of blood clot (Appendix fig. 1). The donor tooth was then carefully extracted avoiding injury to the periodontal ligament membrane, and immediately transplanted to the recipient site. The extra-alveolar time of the donor tooth, the number of repositioning attempts, total surgery time and any surgical complications were recorded. All donor teeth were placed in infraocclusion and initially stabilized with flexible splints allowing physiological movement. The splinting was carried out using either; a flexible orthodontic wire (0.2 mm thickness), which was attached using composite to the buccal surfaces of the transplanted and adjacent teeth, or a non-absorbable nylon suture crossed over the occlusal surface and attached to the tooth occlusal surface using composite (Appendix fig. 1). All patients were prescribed antibiotics (Amoxicillin 50 mg/kg/d. in 3 doses) for 1 week postoperatively and instructed to apply chlorhexidine mouth wash locally.

In the conventional group the surgeries were performed by the same team, according to the procedure described by Andreasen et al. (15).

Post-operative clinical and radiographic assessment

In the CBCT-guided group, the subjects were recalled at 1, 4-6 and 12 months followed by a yearly recall. In the conventional group, clinical and radiographic information were collected from the medical records. At the last recall visit, clinical and radiographic (CBCT imaging) examination were performed.

62 Detailed clinical and radiographic examination were previously described in (12). Clinical examination included the following parameters: sensibility, color, mobility, tenderness to percussion, percussion tone, probing pocket depth and gingival status of the transplanted teeth. Radiographic examination included periapical radiographs at recall visits and CBCT at 1 year, 2 and ≥ 5 years post-operatively. Radiographs were used to evaluate signs of pulp canal obliteration, status of the periradicular area, root length, root crown ratio, periodontal ligament space (PDL) and root resorption.

A TAT was considered successful when the transplanted tooth had normal clinical and radiographic findings with the absence of ankylosis, progressive root resorption or infection, the presence of root canal obliteration, normal mobility and normal gingival contour, attachment level and pocket depth. The tooth survival was defined as the transplanted tooth still being present at the follow-up period with or without fulfilling the success criteria.

TAT was considered a failure when the transplanted tooth was already extracted or when there was replacement resorption (RR), hypermobility or progressive root resorption due to infection.

3D analysis of TAT outcome

For the CBCT-guided group, CBCT scans were imported into MeVisLab (MeVis Medical Solutions AG, Bremen, Germany). The transplanted teeth (pre- and postoperatively at last follow-up) were then segmented using a dedicated tool developed in MeVisLab and validated for accurate tooth/root canal space segmentation as described (16). Briefly, the imaging analysis tool applies semi-interactive livewire boundary extraction (17) to create a set of orthogonal contours, followed by a variational interpolation algorithm that reconstructs the surface of an object with energy-minimizing, smooth, and implicit functions (18). At this point, the apical foramen area (AFA) at the most apical axial slice was measured and the root canal space was subtracted from the segmented image of the tooth pre- and postoperatively. For each tooth the segmented hard tissue preoperative image was then spatially aligned to the segmented postoperative image using the dentin-enamel and the cement-enamel junctions as alignment landmarks and maximization of mutual information as a registration metric (19). The 3D triangle-based surface of the hard tissue was reconstructed. The root hard tissue volume (RV) and its length (RL) were calculated measuring from the cement-enamel junction (CEJ) to the apex pre- and postoperatively. Morphological quantification was performed in 3matic (Materialise; Leuven, Belgium). The root hard tissue was analyzed to record the mean and maximum dentin wall thickness (Mean-DWT & Max-DWT) pre- and postoperatively and

then expressed as a color-coded map showing the calculated minimal distances from the canal surface to the external root surface. The measurements were then normalized and expressed as the percentage of change related to the pre-operative form.

Statistical analysis

Statistical modeling and analysis were performed in S-plus for Linux 8.0 (Tibco Software, Palo Alto, CA) by a certified statistician. Graphs were plotted using the statistical software package GraphPad Prism 7.00 (GraphPad Software, La Jolla California USA). The overall survival, periodontal ligament (PDL) healing and pulp healing of the CBCT-guided and the Conventional groups were modeled and compared using Frailty regression models to account for the dependence in the data. Frailty regression models were fit to the CBCT-group to examine if any factors had an influence on the survival of TAT (Appendix variables regression models). A Principle Component Analysis (PCA) was performed to determine the parameters best describing the total variability in the 3D tissue change after TAT. A Cluster analysis (Elbow Method), using the parameters chosen by the PCA, was then applied to classify the study sample based on the pattern of tissue change.

RESULTS

Study Sample

Figure 1A presents the distribution of patients in both groups. Each experimental group consisted of 50 transplants in 44 patients (31 males and 19 females). The mean age at the time of surgery was 10.7 (± 1.1) (range: 8-13) years-old for the CBCT-guided group compared to 10.6 (± 1.3) (range: 8-13) years-old for the conventional-group. The mean follow-up period for both groups was 4.5 (± 3.1) years (range 1.1-10.4 years) (25-75% percentile range 1.7-7.4 years).

CBCT-guided vs. Conventional TAT

Overall survival rate for the CBCT-guided TAT was 92% and success rate was 86% compared to 84% survival rate and 78% success rate for the conventional-group (Fig. 2B). Differences between both groups were not statistically significant ($P > 0.05$). The PDL and pulp healing rates for the CBCT-group were 86% and 92%, respectively, compared to 82% and 88% for the conventional-group. Differences between both groups were not statistically significant ($P > 0.05$). Figure 3 presents an example for the long-term outcome after TAT. The use of the tooth replica reduced the number of repeated attempts of repo-

64 sitioning the donor tooth to 0-3 attempts for the CBCT-group compared to 4-7 attempts for the conventional-group. The extra-alveolar time was reduced to <1min for the CBCT-group compared to 3-10 mins for the conventional-group. Moreover, the total surgery time was reduced from 40-90 mins for the conventional-group to 30-45 mins for the CBCT-group.

Reasons for failures in the CBCT-group were ankylosis accompanied by RR (three TATs), or untreated caries leading to periapical infection (one TAT). While for the conventional group reasons were inflammatory root resorption (five TATs), ankylosis with RR (two TATs), or external cervical root resorption (one TAT).

The regression model constructed with the pre- and intraoperative variables did not reveal any variables with significant relation to the outcome. Only gender appeared to have a close relationship to the overall survival ($P = 0.074$) with males more likely to have a higher TAT survival rate than females.

3D analysis of TAT outcome and radiographic patterns of healing

The following measurements were extracted from the 3D analysis: root hard tissue volume (RV), root length (RL), apical foramen area (AFA), mean and maximum dentin wall thickness (Mean-DWT & Max-DWT). Overall, the mean percentage of tissue change was RV gain by 65.8% (± 34.6), RL gain by 37.3% (± 31.5), AFA reduction by 91.1% (± 14.9), Mean-DWT increase by 107.9% (± 67.7), and Max-DWT change by 26.5% (± 40.1).

Principle component analysis (PCA) showed that a total of 87.5% of the variability in tissue change after TAT could be explained using a 3-dimensional space consisting of 3 components (Appendix fig 2A). PCA revealed that the main descriptor for tooth hard tissue change post-operatively was the change in the Mean-DWT (explaining 57.8% of the variability) (Appendix fig 2A & B). This was followed by the change in RV (17.1%) and the change in Max-DWT (12.6%) (Appendix fig 2A & C). Moreover, factor (component) analysis (Varimax rotation method) showed that the change in Mean-DWT is strongly correlated to the reduction in AFA (1st component) and the change in RV is strongly correlated to the change in RL (2nd component). AFA and RL had less power explaining the 1st and 2nd components; thus they were excluded from further analysis (Appendix fig 2B & C). Interestingly, the change in the Max-DWT had a strong relation to the 3rd component, but with a low relation to the 1st and 2nd components (Appendix fig 2C). Frailty regression model revealed a significant relationship between the change in Mean-DWT and the time interval until PDL and pulp healing ($P < 0.0001$). This relationship was not possible

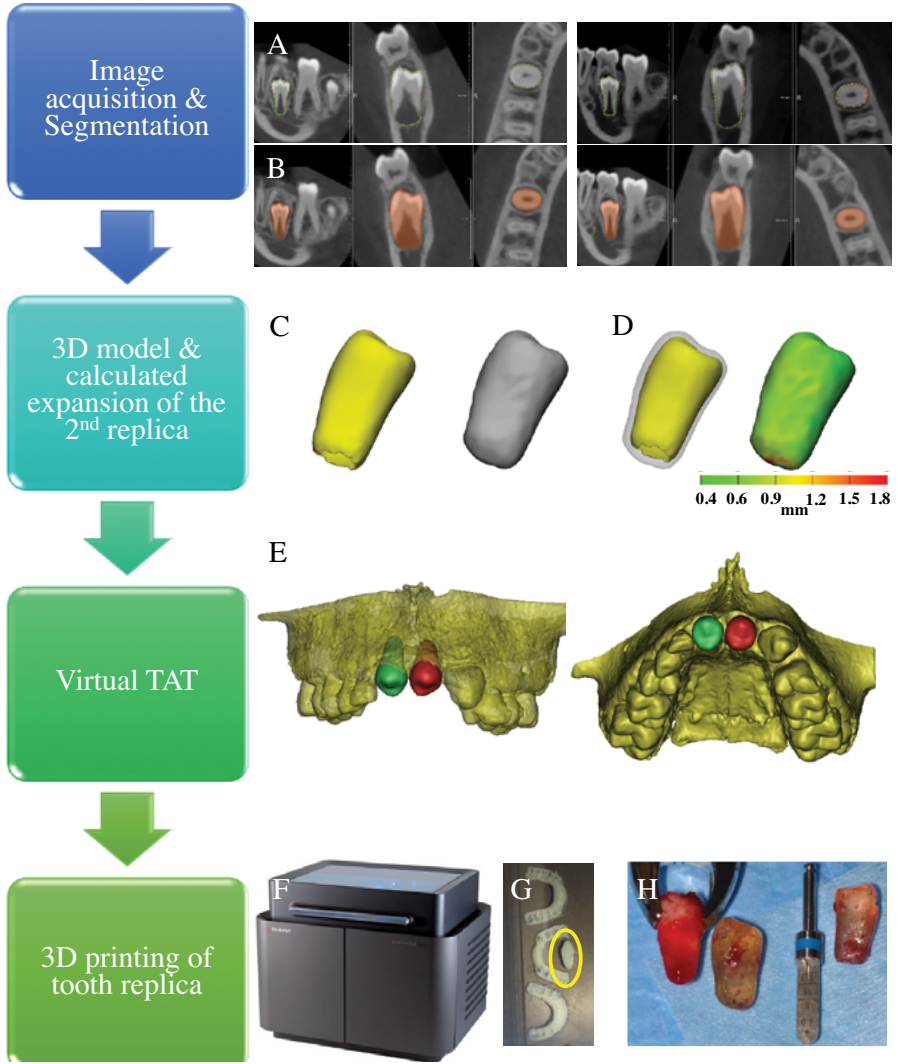


Figure 1: Work flow for the pre-operative procedure (A) CBCT acquisition, (B) donor tooth segmentation, (C) 3D model for the segmented donor tooth, yellow actual size and grey expanded model accounting for soft tissue and time interval between CBCT and surgery, (D) 2nd replica expansion ranging between 400 μ m to 1,8 mm at the apical part , (E) virtual TAT for the lower left second premolar (green) to the site of the upper right maxillary central incisor and the lower right second premolar (red) to the site of the upper left maxillary central incisor, (F&G) 3D printing of replica and guides in the in-house 3D printer, (I) the use of 2 replicas during surgery

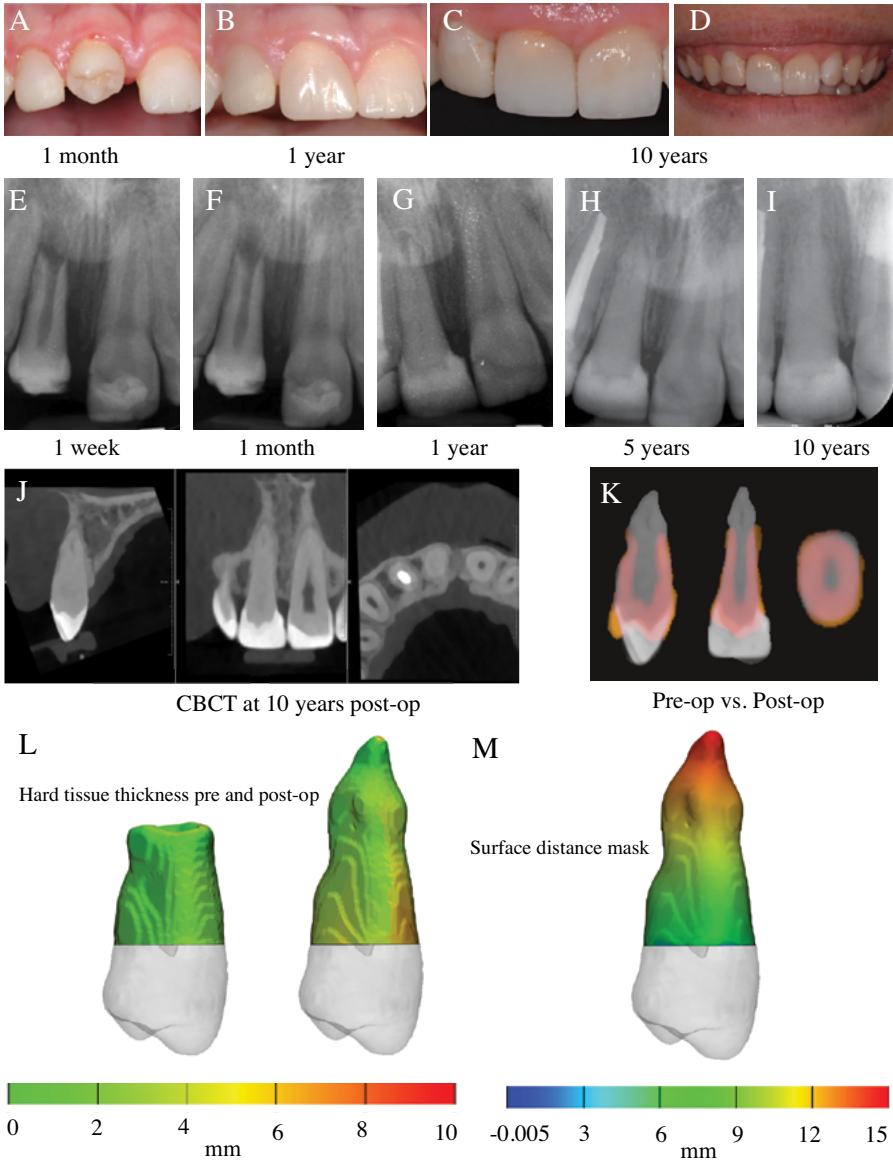
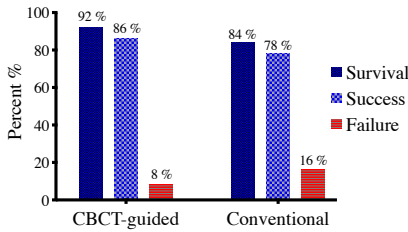


Figure 2: Outcomes CBCT-guided vs. Conventional TAT. (A) Distribution of patients in CBCT and conventional group, (B) overall survival, success and failure distribution, (B) TAT survival probability over time (baseline to 10 years)

A

Groups	Type		Number (%)	Stage of root development		
	Donor Tooth	Recipient site		<1/2	1/2-3/4	>3/4
CBCT-guided	Premolar	Incisor	32 (64%)	2	20	10
	Premolar	Premolar	18 (36%)	0	18	0
Conventional	Premolar	Incisor	32 (64%)	3	20	9
	Premolar	Premolar	18 (36%)	0	17	1

B



C

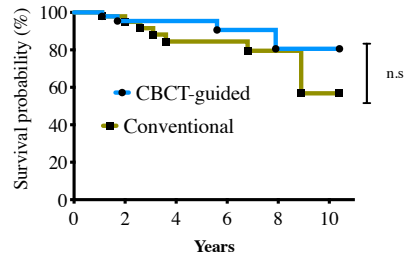


Figure 3: Long-term outcome after TAT, lower left second mandibular premolar to the site of the maxillary right central incisor. Clinical and esthetic outcome at 1 month (A), 1 year (B), and at 10 years (C & D), (E, F, G, H, & I) radiographic follow-up and successful outcome at 10 years, (J&K) CBCT at 10 years post-op, (L) 3D analysis of the hard tissue thickness, pre-op: maximum dentin thickness= 4.1mm [mean=1.7mm (±0.5)], post-op: maximum dentin thickness= 5.9mm [mean=3.1mm (±1.4)], (M) Surface distance mask representing tissue change post-op

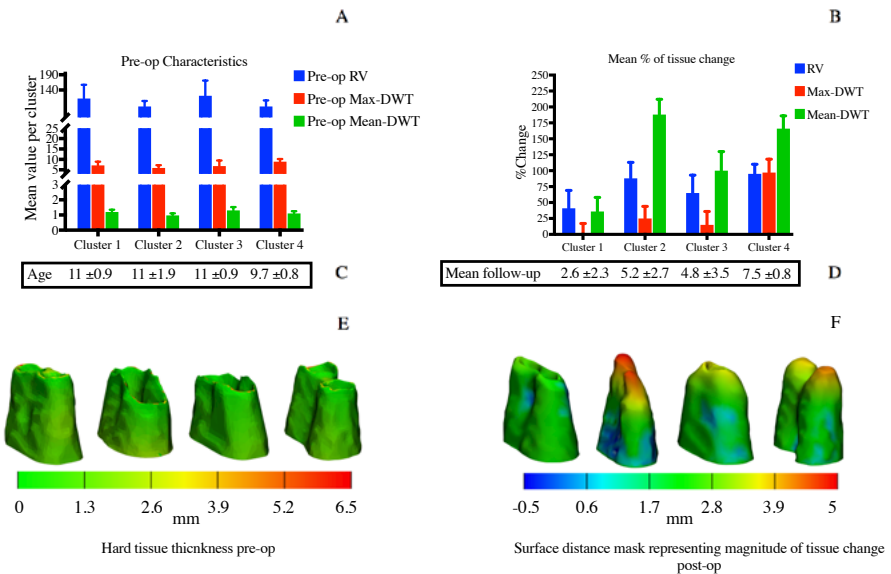


Figure 5: Different patterns of healing after TAT. (A) The pre-operative characteristics for the four clusters identified showing homogenous values for RV, Max-DWT and Mean-DWT, (B) different patterns of tissue change between the four clusters post-operatively, (C) similar mean age between the clusters pre-operatively, (D) mean follow-up period for the four clusters, (E) color coded map for the hard tissue thickness, for one example from each cluster, showing the similarities, (F) surface distance mask representing the magnitude of tissue change post-operatively, clearly showing the different patterns of healing and remodelling after TAT

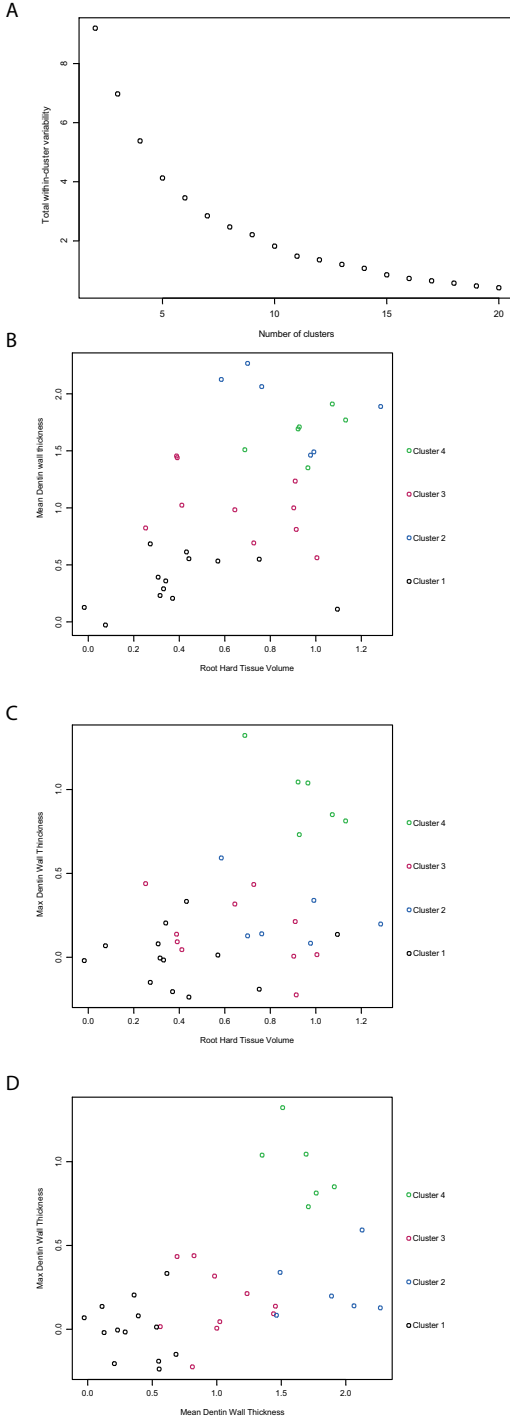


Figure 4: Cluster analysis. (A) For obtaining the optimal number of clusters, the elbow method is used. It is a graphical method where the total within cluster variability is plotted versus the number of clusters. The steepness of the plotted line changed at the number of clusters 5, thus initially a cluster analysis with 5 clusters was performed then optimized to 4 clusters. (B & C) Mean dentin wall thickness (Mean-DWT) was the variable differentiating the groups the best into horizontal bands with clusters 2 and 4 showing a strong overlap. (D) Clusters 2 and 4 can be separated using the maximum dentin wall thickness (Max-DWT)

to examine related to the overall success and survival because of the censored nature of the data.

Cluster analysis applied to the variables chosen by the PCA revealed that the CBCT-group could be classified into 4 distinct clusters (C1=37.2%, C2=17.1%, C3=28.6%, C4=17.1%) (Fig. 4). Analyzing cluster characteristics showed no differences pre-operatively (Fig. 5A, C & E), but different patterns of tissue change post-operatively (Fig. 5B, D & F). The change in Mean-DWT was the parameter mainly distinguishing between the clusters as follows: C1 increase by 36% (± 22), C2 increase by 188% (± 34), C3 increase by 100% (± 30), and C4 increase by 166% (± 20) (Fig. 5B). While clusters 2 and 4 showed overlap (Fig. 4B) they could be differentiated using the change in the Max-DWT (Fig. 4D) with C2 showing an increase by 25% (± 19) and C4 97% (± 21). Examining the influence of the mean follow-up period showed only significant differences ($P < 0.05$) between C1 2.6 (± 2.3) years and C4 7.5 (± 0.8) years (Fig. 5D).

DISCUSSION

Application of computer aided surgical planning and transfer technique combined with 3D-printing of tooth replica and surgical templates for TAT (CBCT-guided) aims to examine the surgical feasibility, plan the ideal position for the donor tooth in relation to the neighboring teeth and recipient site, and enhance esthetics and function (12). The use of tooth replica intends to reduce the extra-alveolar time, provide a passive adaptability for the donor tooth through bone contouring. Leading to preserving the periodontal membrane and pulp vitality, and reducing the risk of necrosis and resorption (11, 12, 20, 21). The current study provides results on an intermediate to long-term TAT follow-up comparing CBCT-guided to the conventional approach, focusing on immature premolars in children.

Available data in the literature on conventional TAT reflect comparable long-term survival rates (22). Kafourou et al. reported an overall survival and success rates of 94.4% and 85.4%, respectively, for conventional TAT in children and adolescents after a mean follow-up period of 2.6 (± 1.8) years (23). In the current study, CBCT-guided TAT showed slightly higher success and survival rates when compared to the conventional approach (Fig 2B). Generally, the differences between the two groups were not statistically significant. Nevertheless, such differences are significant for the individual patient. Looking at the survival curves (Fig 2C), it can be noticed that at longer follow-up periods the survival probability for the CBCT-group stays well above 80%, while it drops below 60% for the conventional group.

70 Interestingly, not only the number of failures was halved (Fig 2B), but also the types of failure were different. The main reason for failure for the CBCT-group was ankylosis accompanied by RR, while this was of inflammatory nature for the conventional approach. Repeated repositioning attempts and extended extra-alveolar times will damage the periodontal membrane and reduce the chances of pulp revascularization (8, 24), thus explaining the inflammatory nature of complications in the conventional group. On the other hand, the ankylosis followed by RR in the CBCT-group might be due to a tight fit of the donor tooth at the recipient site. One possible explanation is that the donor tooth will be larger than the replica when the time interval between the CBCT acquisition and the surgery exceeds 2-4 months. This complication can be avoided by accounting for the root growth, apical papilla, and PDL membrane by creating a second replica with calculated root expansion (Fig. 1C & D).

Root canal obliteration and continued root development after TAT of immature teeth are signs of pulp revitalization and treatment success (24-27). This study applied a novel method based on 3D-imaging to analyze the pattern of hard tissue formation and subsequent healing after TAT. Our results suggest four radiographic patterns of healing after TAT of immature premolars. These patterns have a 4D nature: change in Mean-DWT, RV, and Max-DWT influenced by the time factor. Change in Mean-DWT and RV appeared to plateau after the first 3-4 years, while the change in the Max-DWT appeared to have a gradual increase during the follow-up period (Fig 5B, D & F). One possible interpretation is that the change in Max-DWT describes the slower tissue remodeling on the external root surface at the tooth root, PDL-bone interface. On the other hand, change in Mean-DWT and RV describes the faster tissue deposition on the internal root surface and overall root maturation. This information would assist the clinicians during the follow-up in understating what is observed in the radiographic examination. Future work will focus on expanding this concept based on studies with larger sample size.

With the rapid advances in stem cell biology, biomaterials, bio-fabrication and tissue engineering strategies, tooth regeneration seems to be possible sooner than expected (28-32). TAT represents a unique biological treatment option that offers not only a solution for tooth loss in children and adolescents, but also insights for future bio-engineered tooth transplants. The design of a bio-engineered tooth root can apply lessons regarding scaffold dimensions, the most suitable developmental stage for transplantation, and expected healing patterns. Moreover, TAT appears to be a more predictable approach with the aid of 3D-planning and 3D-printing of tooth replica and surgical guides.

It is fair to mention that this study has its limitations. It was not possible to design the study as a randomized clinical trial and allocate new patients in the prospective arm to the conventional group for ethical reasons. Moreover, 3D imaging was not available for the conventional group pre-operatively, therefore a direct comparison of the healing patterns between the CBCT and conventional groups was not possible. The number of failures was limited; therefore, it was not possible to draw conclusions regarding the risk factors or prognostic variables. However, the data presented in this study are unique. This study has provided an intermediate to long-term follow-up on CBCT-guided TAT compared to the conventional approach. Moreover, meaningful parameters were identified for the 3D analysis and reporting of the treatment outcome, in addition to suggesting four patterns for the radiographic healing after TAT. Furthermore, the 3D parameters identified can be extended to studying the regenerative endodontic procedures (REP) (16, 33) in order to obtain insights into the patterns of healing and determinants of success. Future studies should focus on gaining a deeper understanding for the biology-based procedures such as TAT and REP in order to preserve the natural dentition and maximize the benefits for the patient.

CONCLUSION

TAT is a viable option for permanent tooth replacement in children and adolescents. The CBCT-guided approach simplified the surgery and increased the predictability of the treatment. The 3D analysis provided insights into the patterns of healing. CBCT-guided TAT could be adopted as an alternative for the conventional approach.

AUTHOR CONTRIBUTIONS

M. EzEldeen, J. Wyatt, R. Jacobs contributed to conception, design, data acquisition, analysis, and interpretation, drafted and critically revised the manuscript; E. Shaheen, W. Coucke, contributed to data acquisition, analysis, and interpretation, critically revised the manuscript; A. Al-Rimawi, contributed to data acquisition, analysis, critically revised the manuscript; I. Lambrichts, G. Willems, C. Politis, contributed to conception and design, critically revised the manuscript. All authors gave final approval and agree to be accountable for all aspects of the work.

ACKNOWLEDGMENTS

Supported by FWO Vlaanderen (Fonds Wetenschappelijk Onderzoek) (grant no. G089213N). The authors deny any conflicts of interest related to this study.

REFERENCES

1. Czochrowska EM, Stenvik A, Album B, Zachrisson BU. Autotransplantation of premolars to replace maxillary incisors: a comparison with natural incisors. *Am J Orthod Dentofacial Orthop.* 2000;118(6):592-600.
2. Zachrisson BU, Stenvik A, Haanaes HR. Management of missing maxillary anterior teeth with emphasis on autotransplantation. *Am J Orthod Dentofacial Orthop.* 2004;126(3):284-8.
3. Paulsen HU, Andreasen JO, Schwartz O. Tooth loss treatment in the anterior region: autotransplantation of premolars and cryopreservation. *World J Orthod.* 2006;7(1):27-34.
4. Petti S, Glendor U, Andersson L. World traumatic dental injury prevalence and incidence, a meta-analysis-One billion living people have had traumatic dental injuries. *Dent Traumatol.* 2018;34(2):71-86.
5. Sharma AB, Vargervik K. Using implants for the growing child. *J Calif Dent Assoc.* 2006;34(9):719-24.
6. Kanavakis G, Ludwig B, Rosa M, Zachrisson B, Hourfar J. Clinical outcomes of cases with missing lateral incisors treated with the 'T'-Mesialslider. *J Orthod.* 2014;41 Suppl 1:S33-8.
7. Becker K, Wilmes B, Grandjean C, Vasudavan S, Drescher D. Skeletally anchored mesialization of molars using digitized casts and two surface-matching approaches : Analysis of treatment effects. *J Orofac Orthop.* 2018;79(1):11-8.
8. Andreasen JO, Paulsen HU, Yu Z, Schwartz O. A long-term study of 370 autotransplanted premolars. Part III. Periodontal healing subsequent to transplantation. *Eur J Orthod.* 1990;12(1):25-37.
9. Kallu R, Vinckier F, Politis C, Mwalili S, Willems G. Tooth transplantations: a descriptive retrospective study. *Int J Oral Maxillofac Surg.* 2005;34(7):745-55.
10. Denys D, Shahbazian M, Jacobs R, Laenen A, Wyatt J, Vinckier F, et al. Importance of root development in autotransplantations: a retrospective study of 137 teeth with a follow-up period varying from 1 week to 14 years. *Eur J Orthod.* 2013;35(5):680-8.
11. Shahbazian M, Jacobs R, Wyatt J, Willems G, Pattijn V, Dhoore E, et al. Accuracy and surgical feasibility of a CBCT-based stereolithographic surgical guide aiding autotransplantation of teeth: in vitro validation. *J Oral Rehabil.* 2010;37(11):854-9.
12. Shahbazian M, Jacobs R, Wyatt J, Denys D, Lambrichts I, Vinckier F, et al. Validation of the cone beam computed tomography-based stereolithographic surgical guide aiding autotransplantation of teeth: clinical case-control study. *Oral Surg Oral Med Oral Pathol Oral Radiol.* 2013;115(5):667-75.
13. Loubele M, Bogaerts R, Van DE, Pauwels R, Vanheusden S, Suetens P, et al. Comparison between effective radiation dose of CBCT and MSCT scanners for dentomaxillofacial applications. *Eur J Radiol.* 2009;71(3):461-8.
14. EzEldeen M, Stratis A, Coucke W, Codari M, Politis C, Jacobs R. As Low Dose as Sufficient Quality: Optimization of Cone-beam Computed Tomographic Scanning Protocol for Tooth Autotransplantation Planning and Follow-up in Children. *J Endod.* 2017;43(2):210-7.
15. Andreasen JO, Paulsen HU, Yu Z, Ahlquist R, Bayer T, Schwartz O. A long-term study of 370 autotransplanted premolars. Part I. Surgical procedures and standardized techniques for monitoring healing. *Eur J Orthod.* 1990;12(1):3-13.

16. EzEldeen M, Van Gorp G, Van Dessel J, Vandermeulen D, Jacobs R. 3-dimensional analysis of regenerative endodontic treatment outcome. *J Endod.* 2015;41(3):317-24.
 17. Barrett WA, Mortensen EN. Interactive live-wire boundary extraction. *MedImage Anal.* 1997;1(4):331-41.
 18. Heckel F, Konrad O, Karl Hahn H, Peitgen H-O. Interactive 3D medical image segmentation with energy-minimizing implicit functions. *Computers & Graphics.* 2011;35(2):275-87.
 19. Maes F, Collignon A, Vandermeulen D, Marchal G, Suetens P. Multimodality image registration by maximization of mutual information. *IEEE Trans Med Imaging.* 1997;16(2):187-98.
 20. Keightley AJ, Cross DL, McKerlie RA, Brocklebank L. Autotransplantation of an immature premolar, with the aid of cone beam CT and computer-aided prototyping: a case report. *Dent Traumatol.* 2010;26(2):195-9.
 21. Jang Y, Choi YJ, Lee SJ, Roh BD, Park SH, Kim E. Prognostic Factors for Clinical Outcomes in Autotransplantation of Teeth with Complete Root Formation: Survival Analysis for up to 12 Years. *J Endod.* 2016;42(2):198-205.
 22. Akhlef Y, Schwartz O, Andreasen JO, Jensen SS. Autotransplantation of teeth to the anterior maxilla: A systematic review of survival and success, aesthetic presentation and patient-reported outcome. *Dent Traumatol.* 2018;34(1):20-7.
 23. Kafourou V, Tong HJ, Day P, Houghton N, Spencer RJ, Duggal M. Outcomes and prognostic factors that influence the success of tooth autotransplantation in children and adolescents. *Dent Traumatol.* 2017;33(5):393-9.
 24. Andreasen JO, Paulsen HU, Yu Z, Bayer T, Schwartz O. A long-term study of 370 autotransplanted premolars. Part II. Tooth survival and pulp healing subsequent to transplantation. *Eur J Orthod.* 1990;12(1):14-24.
 25. Andreasen JO, Paulsen HU, Yu Z, Bayer T. A long-term study of 370 autotransplanted premolars. Part IV. Root development subsequent to transplantation. *Eur J Orthod.* 1990;12(1):38-50.
 26. Czochrowska EM, Stenvik A, Bjercke B, Zachrisson BU. Outcome of tooth transplantation: Survival and success rates 17-41 years posttreatment. *Am J Orthod Dentofacial Orthop.* 2002;121(2):110-9.
 27. Tsukiboshi M. Autotransplantation of teeth: requirements for predictable success. *Dent-Traumatol.* 2002;18(4):157-80.
 28. Wei F, Song T, Ding G, Xu J, Liu Y, Liu D, et al. Functional Tooth Restoration by Allogeneic Mesenchymal Stem Cell-Based Bio-Root Regeneration in Swine. *Stem Cells Dev.* 2013;22(12):1752-62.
 29. Obregon F, Vaquette C, Ivanovski S, Huttmacher DW, Bertassoni LE. Three-Dimensional Bioprinting for Regenerative Dentistry and Craniofacial Tissue Engineering. *J Dent Res.* 2015;94(9 Suppl):143S-52S.
 30. Hilkens P, Bronckaers A, Ratajczak J, Gervois P, Wolfs E, Lambrechts I. The Angiogenic Potential of DPSCs and SCAPs in an In Vivo Model of Dental Pulp Regeneration. *Stem Cells Int.* 2017;2017:2582080.
 31. Lambrechts I, Driesen RB, Dillen Y, Gervois P, Ratajczak J, Vanganswinkel T, et al. Dental Pulp Stem Cells: Their Potential in Reinnervation and Angiogenesis by Using Scaffolds. *J Endod.* 2017;43(9S):S12-S6.
 32. Smith EE, Angstadt S, Monteiro N, Zhang W, Khademhosseini A, Yelick PC. Bioengineered Tooth Buds Exhibit Features of Natural Tooth Buds. *J Dent Res.* 2018;97(10):1144-51.
 33. Meschi N, EzEldeen M, Torres Garcia AE, Jacobs R, Lambrechts P. A Retrospective Case Series in Regenerative Endodontics: Trend Analysis Based on Clinical Evaluation and 2- and 3-dimensional Radiology. *J Endod.* 2018.
-

Appendix Table 1: List of abbreviations

Abbreviations	
TAT	Tooth autotransplantation
TDIs	Traumatic dental injuries
CBCT	Cone-beam computed tomography
3D	Three-dimensional
PDL	Periodontal ligament
AFA	Apical foramen area
RV	Root hard tissue volume
RL	Root length
CEJ	Cement enamel junction
Mean-DWT	Mean dentin wall thickness
Max-DWT	Maximum dentin wall thickness
PCA	Principle component analysis
C1	Cluster 1
C2	Cluster 2
C3	Cluster 3
C4	Cluster 4

Appendix: CBCT scanning parameters*Pre-operative scanning:*

Patients underwent CBCT imaging using a low-dose protocol using one of the following protocols:

- 1 — the Scanora 3D (Soredex, Tuusula, Finland) with voxel size 0.2 mm (field of volume 75 x 100 mm), tube voltage of 85 kV, current of 8 mA, and exposure time of 3.7 s.
- 2 — the Accuitomo 170 (J Morita MFG CORP, Kyoto, Japan) was used, operated with a voxel size of 0.16 mm (field of volume 80 x 80 mm), a tube voltage of 90 kV, a tube current of 5 mA, and a scanning time of 17.5 s.
- 3 — the NewTom VGI evo (QR Verona, Verona, Italy) was used, operated with a voxel size of 0.20 mm (field of volume 80 x 80 mm), a tube voltage of 110 kV, tube current modulation function, and a scanning time of 12.0 s.

Post-operative scanning:

Patients underwent CBCT imaging using a low-dose protocol using one of the following protocols:

- 1 — the Accuitomo 170 (J Morita MFG CORP, Kyoto, Japan), operated with a voxel size of 0.125 mm (field of volume 60 x 60 mm), a tube voltage of 90 kV, a tube current of 5 mA, and a scanning time of 17.5 s.
- 2 — the NewTom VGI evo (QR Verona, Verona, Italy) was used, operated with a voxel size of 0.20 mm (field of volume 50 x 50 mm), a tube voltage of 110 kV, tube current modulation function, and a scanning time of 12.0 s.

Appendix: Variables regression models

Variables included in Frailty regression models to examine if any factors had an influence on the survival of TAT

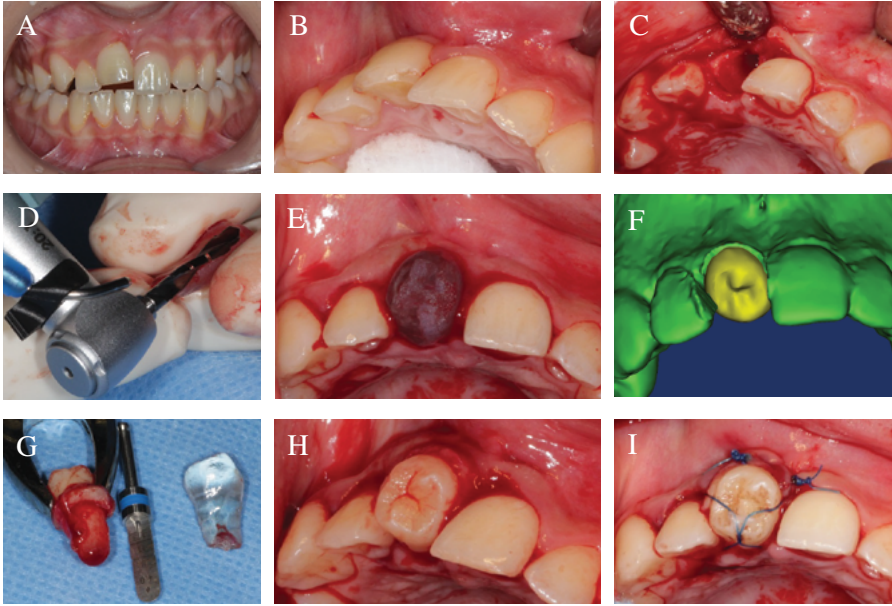
Pre-operative variables included;

- Age at TAT
- Gender
- Tooth type
- Eruption status
- Stage of root development
- Apex development
- Recipient site (incisor region or premolar)
- Tooth root shape descriptors (variables from the 3D analysis measured from the Cementoenamel junction up to the apex)
 - Apical area
 - Root hard tissue volume
 - Mean dentin thickness
 - Maximum dentin wall thickness
 - Root Length

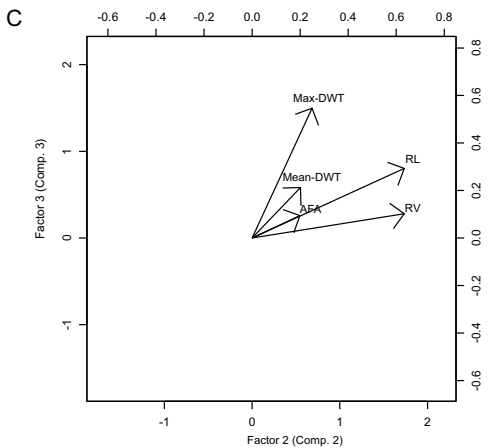
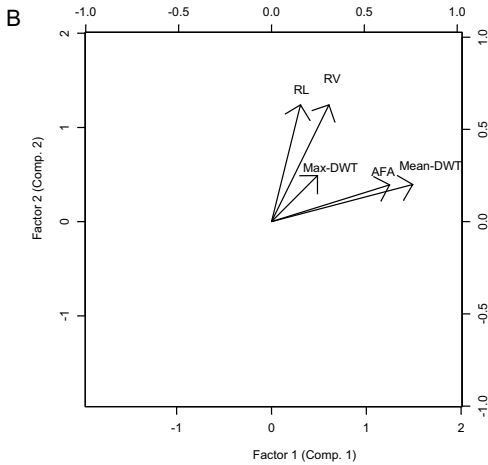
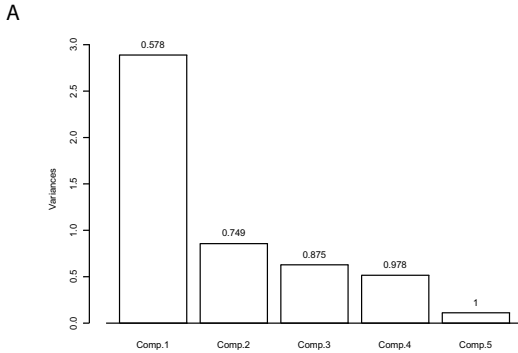
Intraoperative variables

- Extra-alveolar time of the donor tooth
- Number of repositioning attempts
- Total surgery time
- Surgical complications or difficulty

76



Appendix Figure 1: Surgery. (A&B) Clinical picture pre-op showing ankylosis of the maxillary right central incisor, (C) clinical image during the surgery after atraumatic extraction and maintenance of the buccal bone plate, (D&E) the use of the replica during the surgery, (F) planned position for the donor tooth, (G) accuracy of the replica and atraumatic extraction of the donor tooth, (H&I) realized position after TAT and flexible fixation.



Appendix Figure 2: Principle component analysis.

(A) Scree plot for the visualisation of the extent of variable reduction that is possible by principal component analysis. The first component describes the most important aspect of variability, successive components describe each time a smaller and smaller aspect of the variability. In this case, the first principal component describes 57.8% of the variability. The first three components together describe >80% of the whole information. A total of 80% is considered as acceptable. Therefore, it is decided to reduce the 5dimensional space, in which every variable makes up one dimension of the space, towards a 3dimensional space. A dimension reduction is performed using the varimax factor analysis (visualised using biplots). Variables that have a close relation with the factors (components) are identified by looking at their position with respect to the factors in the biplots.

(B) Factor analysis to identify the variables related to the 1st factor (component), mean dentin wall thickness (Mean-DWT) and apical foramen area (AFA) identified as variables related to the 1st component.

(C) Factor analysis to identify the variables related to the 2nd factor (component), root hard tissue volume (RV) and root length (RL) are identified as variables related to the 2nd component, while maximum dentin wall thickness (Max-DWT) is identified as the variable related to the 3rd component.

CHAPTER 4

This chapter is based on the following publication

EzEldeen, M., Al-Rimawi, A., Shaheen, E., Jacobs, R. Influence of Different 3D printing Technologies on Accurate Tooth Replica Fabrication Intended for CBCT-guided Tooth Autotransplantation. In preparation.

- (A) OMFS IMPATH Research Group, Faculty of Medicine, Department of Imaging and Pathology, KU Leuven and Oral and Maxillofacial Surgery, University Hospitals Leuven, Kapucijnenvoer 33, 3000 Leuven, Belgium
- (B) Department of Oral Health Sciences, KU Leuven and Paediatric Dentistry and Special Dental Care, University Hospitals Leuven, Kapucijnenvoer 33, 3000 Leuven, Belgium
- (C) Department of Dental Medicine, Karolinska Institute, Stockholm, Sweden

Influence of Different 3D Printing Technologies on Accurate Tooth Replica Fabrication Intended for CBCT-Guided Tooth Autotransplantation

M. EzEldeen (A,B), A. Al-Rimawi (A), E. Shaheen (A), R. Jacobs (A,C)

ABSTRACT

Aims — This study aimed to assess the influence of different 3D printing technologies on the accuracy of tooth replica fabrication.

Materials and Methods — Four dry human skulls and four dry human mandibles were scanned using CBCT to create 3D models for 15 premolars. The models were 3D printed using PolyJet and DLP (digital light processing) 3D printers. The accuracy of the 3D printed models was evaluated using physical volume comparison and morphological surface comparison.

Results — Physical volume measurements and morphological surface comparison (surface deviation of 3D printed replicas vs natural tooth) showed a significant effect for 3D printing technology on the accuracy of tooth replica fabrication. DLP consistently underestimated the volume of the replicas ($P < 0.05$), in contrast to PolyJet ($P > 0.05$).

Conclusion — Disease indication-specific validation and optimization of 3D printing technologies are needed before clinical application.

KEY WORDS

Computed tomography, Digital imaging/radiology, CAD, 3D printing, CBCT-guided tooth autotransplantation

INTRODUCTION

Permanent teeth loss or agenesis in children is confronting the dentist with challenging therapeutical problems mainly related to the ongoing dentoalveolar development. While implant placement is not a viable option and should be withheld until the completion of dentoalveolar development (1), tooth auto-transplantation (TAT) offers a biological approach to tooth replacement in children. It enables preservation of the alveolar ridge and allows for periodontal healing and preserving the possibility of function and growth (2-9). A low dose CBCT-guided surgical planning and transfer technique has been developed to enhance the outcome predictability of the TAT procedure (10). The procedure involves donor tooth selection and stereolithographic tooth replica fabrication (8, 11, 12). CBCT-based surgical planning aids the clinician in seeking answers regarding surgical feasibility and the best new position for the donor tooth meanwhile maximizing aesthetics and function (8). The use of stereolithographic tooth replica provides individualized bone adaptability and reduces the extra-alveolar time for the donor tooth. This process of CBCT-guided TAT mainly aims to preserve the periodontal ligament and pulp vitality, reducing the risk for necrosis and resorption (13).

Computer-aided design/ computer-aided manufacturing (CAD/CAM) in dentistry started in the early nineties with subtractive manufacturing (14, 15). Recently additive manufacturing technology, three dimensional (3D) printing, is progressing rapidly and is applied in many fields of dentistry (16), such as fabrication of surgical guides for the placement of dental implants (17-20), guides for endodontic access and apical surgeries (21, 22), fabrication of surgical guides and tooth replicas for tooth autotransplantation (TAT) (10, 23, 24), construction of physical models for orthodontics (25), manufacturing of dental implants (26), and study models, splints, guides in orthognathic surgeries (27-29).

The process of 3D printing in dentistry goes through three stages, starting with data acquisition using low dose cone-beam computed tomography (CBCT) (30, 31), followed by processing and designing using dedicated software tools, and finally printing (10, 32-34). Different 3D printing technologies are being used in dentistry, which can be technically classified into fused deposition modelling (FDM), stereolithography (SLA), PolyJet printing, MultiJet printing, ColorJet printing, selective laser sintering, and digital light processing (DLP) (16, 34).

As aforementioned, CAD/CAM and 3D printing technology are already being applied in tooth autotransplantation (TAT) procedures (10, 23). This study aimed to assess the influence of two different 3D printing technologies (DLP and PolyJet) on the accuracy of tooth replica fabrication for CBCT-guided tooth autotransplantation.

MATERIALS AND METHODS

Image acquisition

Four dry human skulls and four dry human mandibles were scanned using a CBCT machine NewTom VGI EVO (QR Verona, Verona, Italy). Ethical approval was obtained from the Ethical Review Board of the University Hospitals Leuven (S55619 ML9535, University Hospitals Leuven). Scanning parameters were set for a standard mode, 360° rotation, 200 µm voxel size and a field of view 80 x 80 mm at 110 kV (x-ray tube voltage) and automatic tube current modulation. All data sets were exported using the Digital Imaging and Communications in Medicine (DICOM) file format with an isotropic voxel size of 200 µm, a slice interval and thickness of 200 µm.

Segmentation protocol

CBCT scans were imported into MeVisLab (MeVis Medical Solutions AG, Bremen, Germany). Regions of interest, including the single-rooted 1st or 2nd premolar, were selected. All regions of interest images were normalized using an intensity windowing filter and then a median filter to suppress any noise and decrease confounding variables between the images.

All single-rooted premolars were then segmented using a dedicated tool developed in MeVisLab and validated for accurate tooth/root canal space segmentation as described (35) (Fig. 1 A). The tool applies interactive livewire boundary extraction to create a set of orthogonal contours around the tooth of interest. Livewire allows for a semi-interactive segmentation of structures with prominent edge image features (36). Internally, the module generates a graph representation of the image to work on; the graph's nodes represent image pixels, and edges connect neighbouring pixels. The edges are weighted based on the cost function (image gradient magnitude). If starting and ending points are defined on such a graph, the shortest path (minimal cost path) is computed using dynamic programming (F* algorithm) (37). This was followed by a variational interpolation algorithm that reconstructs the surface of an object with energy-minimizing, smooth, and implicit functions to create a 3D mask of the tooth surface (Fig. 1 A) (38).

After segmentation, the 3D triangle-based surfaces of the 15 premolars (four skulls: seven premolars, four mandibles: eighth premolars) were reconstructed and saved as STL files.

3D-printing of tooth replicas

The 3D models of the veneers and assigned premolars were exported to two different 3D printers: 1- Raydent (RAM500, RayMedical, Seoul, South-Korea) DLP 3D printer, and 2- Objet Connex™ 350 (Eden Prairie, United States) PolyJet 3D printer. Both printers were loaded with their own specific biocompatible resin material.

The printed replicas from the DLP printer the replicas were cleaned in an ultrasonic bath using IPA 90% (Isopropyl alcohol) to remove residual resin and then post-cured with the curing Unit (RPC500, RayMedical, Seoul, South-Korea). The replicas from the PolyJet printer were cleaned in an ultrasonic bath with sodium hydroxide 15% to remove all support material. Examples of the 3D printed replicas are shown in Figure 1.

3D model accuracy assessment

Physical volumetric measurements using Archimedes' Principle

To assess accuracy, dimensional differences between the natural teeth and the printed models from the DLP and PolyJet printers, each tooth and replica was immersed individually in a graduated cylinder containing water and the water displacement was recorded.

Optical scanning

An optical scanner (Activity™ 885, Smart Optics, Bochum, Germany) was used in this study to image the 3D surfaces of the teeth and respective replicas. Each tooth was scanned in one step using an orthodontic bracket (bounded on the buccal cusp of the crown) to releasably connect teeth and respective replicas on a silicon clay, hence reducing stitching errors resulting from the conventional 2-step scanning procedure. Natural teeth and replicas were sprayed before the scanning procedure.

3D reconstruction and morphologic surface analysis

For each premolar, the overall volume of the reconstructed 3D models obtained from the segmentation and 3D surface scans of the teeth and their respective replicas were recorded. Then all models were spatially aligned using a surface-based registration algorithm in 3-matic (Materialise; Leuven, Belgium), using the 3D model of the natural tooth as the reference image. Further, a signed morphologic surface comparison between the 3D model for each replica

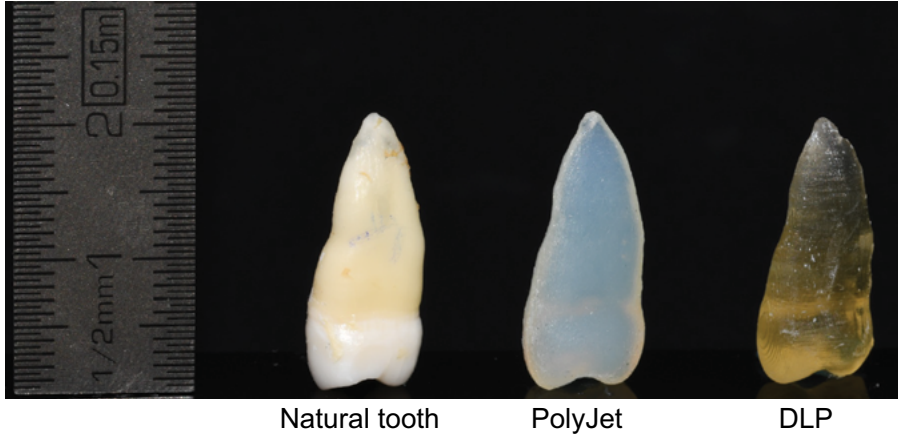


Figure 1: Examples of the 3D printed replicas versus the natural tooth.

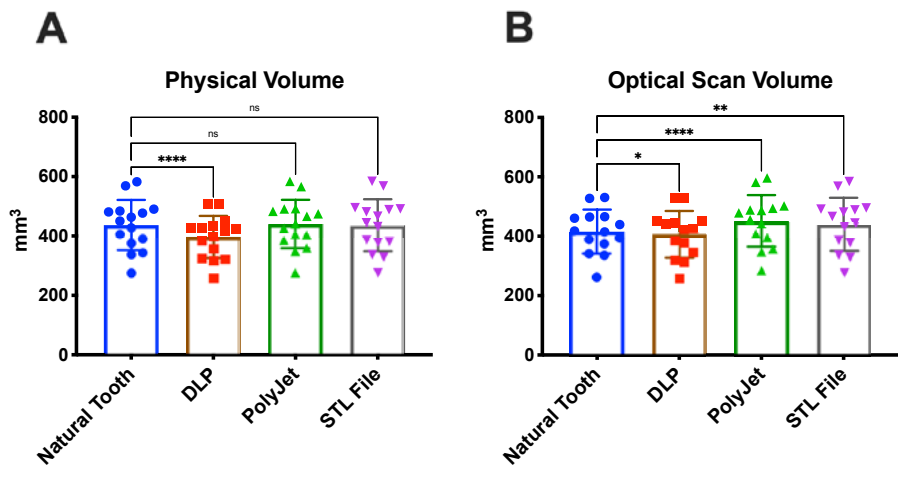


Figure 2: Effect for the 3D printing technology on the accuracy of the tooth replica fabrication. (A) Physical volume evaluation, (B) optical scanning evaluation. ns: not significant, *: significant

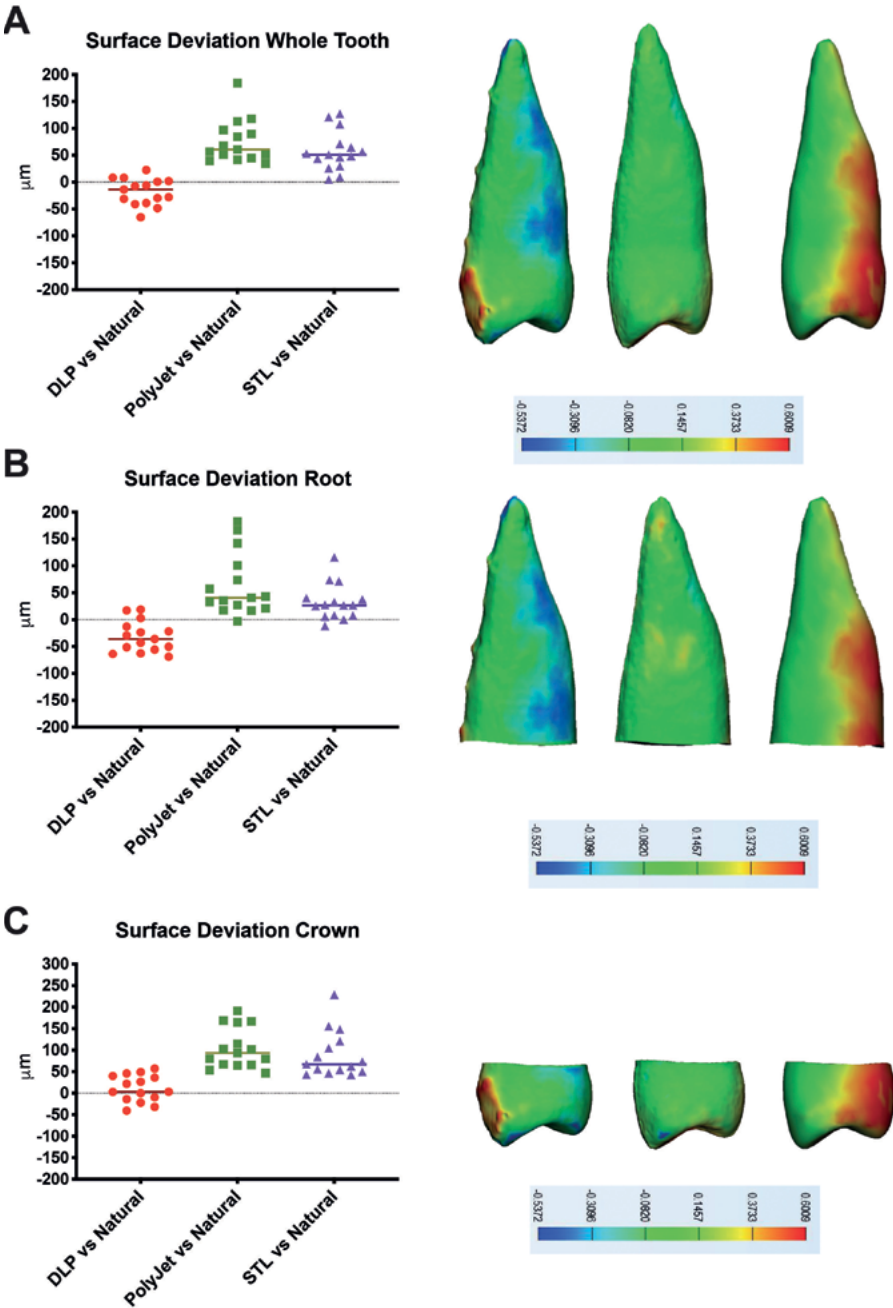


Figure 3: Morphological surface deviations of the 3D printed replicas from the natural tooth. (A) Whole tooth, (B) Crown, (C) Root.

versus the 3D model from the natural tooth, allowing for positive and negative differentiation with regard to the reference image. Measurements were calculated for the overall tooth as well as for crown and root separately.

STATISTICAL ANALYSIS

Statistical analysis was performed using GraphPad Prism for MacOS, version 9.0. (GraphPad Software, La Jolla California, USA). Volumetric variations from the natural tooth for the replicas printed using the two 3D printers (DLP and PolyJet) and the digital 3D models obtained from the segmentations were analysed using a one-way analysis of variance (ANOVA) with Dunnett's correction for multiple comparisons. Statistical differences were set at $P < 0.05$. The systematic volume deviation from the natural tooth was evaluated using the method of Bland and Altman (39).

RESULTS

There was a significant effect for the 3D printing technology at the $p < 0.05$ on the accuracy of the tooth replica fabrication when evaluated physically [$F(1.39, 19.5) = 49.0, p < 0.0001$] and with optical scanning [$F(1.48, 19.2) = 51.1, p < 0.0001$] (Figure 2). Post hoc comparisons using Dunnett's test indicated that the mean physical replica volume fabricated using the DLP printer was significantly different from physical natural tooth volume. The differences in the physical volume were not significant for the PolyJet printer and the digital 3D model obtained from the segmentation. Moreover, post hoc comparisons using Dunnett's test indicated that the volumes of the replicas from both printers and the digital 3D models were significantly different from the natural teeth when measured with optical scanning.

The deviation in tooth replica volumes fabricated using DLP technology was evaluated using the Bland-Altman method showing a systematic underestimation of the overall volume by 9.3% when evaluated physically and by 2.5% when assessed by optical scanning. For the Polyjet technology, this was a systematic overestimation by 0.9% when evaluated physically and by 8.0% when assessed by optical scanning. The digital 3D model obtained by segmentation slightly underestimated the tooth volume by 0.3% when the natural teeth were measured physically and overestimated the tooth volume by 5.2% when evaluated by optical scanning.

Figure 3 summarizes the morphological surface comparisons. Overall surface deviation maps showed an average median deviation from the natural tooth of $-14\mu\text{m}$, $61\mu\text{m}$, and $51\mu\text{m}$ for the DLP, Polyjet and the 3D digital

86 models, respectively. For the tooth crown, the deviations were $3.3\mu\text{m}$, $93.7\mu\text{m}$, and $67.1\mu\text{m}$ for the DLP, Polyjet and the 3D digital model, respectively. For the tooth root, the deviations were $-36.0\mu\text{m}$, $40.7\mu\text{m}$, and $26.5\mu\text{m}$ for the DLP, Polyjet and the 3D digital model, respectively.

DISCUSSION

The pre-operative process for CBCT-guided TAT includes image acquisition, donor tooth segmentation and 3D printing of tooth replica (10, 13, 24). This process has a cumulative error requiring the optimization and the validation of each step. We have previously optimized the CBCT scan protocols (30), and the segmentation method (35) specifically for TAT. CBCT-guided TAT showed a 92% survival rate compared to an 84% survival rate for conventional TAT (13). The main reason for failure for the CBCT-group was ankylosis accompanied by replacement resorption, while this was of inflammatory nature for the conventional approach. Repeated repositioning attempts and extended extra-alveolar times will damage the periodontal membrane and reduce the chances of pulp revascularization (4, 5), thus explaining the inflammatory nature of complications in the conventional group. On the other hand, the ankylosis followed by replacement resorption in the CBCT-group might be due to a tight fit of the donor tooth at the recipient site. One possible explanation is that the donor tooth will be larger than the replica when the time interval between the CBCT acquisition and the surgery exceeds 2-4 months, or that the fabricated replica is slightly smaller than what it should be. Therefore, there is a need to validate the accuracy of the 3D printing technologies before clinical application.

In the current study, DLP printing technology showed a systematic underestimation of the tooth dimensions concentrated at the root surface. While PolyJet technology showed an overestimation. Considering a $200\mu\text{m}$ thickness for the periodontal membrane, one can argue that for the TAT application a slight overestimation is desirable while an underestimation is considered unfavourable. An underestimated tooth root surface would result in a smaller recipient site preparation and will lead to micro-traumas to the periodontal membrane upon transplantation compromising the survival rates.

Finally, once a certain 3D printing technology is validated for a specific application, slight errors can be compensated for during the digital file preparation (STL file), by accounting for the root growth, apical papilla, and PDL membrane by creating a second replica with calculated root expansion.

CONCLUSION

Disease indication-specific validation and optimization of 3D printing technologies are needed before clinical application.

REFERENCES

1. Sharma AB, Vargervik K. Using implants for the growing child. *J Calif Dent Assoc.* 2006;34(9):719-24.
2. Andreasen JO, Paulsen HU, Yu Z, Ahlquist R, Bayer T, Schwartz O. A long-term study of 370 autotransplanted premolars. Part I. Surgical procedures and standardized techniques for monitoring healing. *Eur J Orthod.* 1990;12(1):3-13.
3. Andreasen JO, Paulsen HU, Yu Z, Bayer T. A long-term study of 370 autotransplanted premolars. Part IV. Root development subsequent to transplantation. *Eur J Orthod.* 1990;12(1):38-50.
4. Andreasen JO, Paulsen HU, Yu Z, Bayer T, Schwartz O. A long-term study of 370 autotransplanted premolars. Part II. Tooth survival and pulp healing subsequent to transplantation. *Eur J Orthod.* 1990;12(1):14-24.
5. Andreasen JO, Paulsen HU, Yu Z, Schwartz O. A long-term study of 370 autotransplanted premolars. Part III. Periodontal healing subsequent to transplantation. *Eur J Orthod.* 1990;12(1):25-37.
6. Czochrowska EM, Stenvik A, Album B, Zachrisson BU. Autotransplantation of premolars to replace maxillary incisors: a comparison with natural incisors. *Am J Orthod Dentofacial Orthop.* 2000;118(6):592-600.
7. Czochrowska EM, Stenvik A, Bjercke B, Zachrisson BU. Outcome of tooth transplantation: Survival and success rates 17-41 years posttreatment. *American Journal of Orthodontics and Dentofacial Orthopedics.* 2002;121(2):110-9.
8. Shahbazian M, Jacobs R, Wyatt J, Denys D, Lambrichts I, Vinckier F, et al. Validation of the cone beam computed tomography-based stereolithographic surgical guide aiding autotransplantation of teeth: clinical case-control study. *Oral SurgOral MedOral PatholOral Radiol.* 2013;115(5):667-75.
9. Tsukiboshi M. Autotransplantation of teeth: requirements for predictable success. *Dent-Traumatol.* 2002;18(4):157-80.
10. Shahbazian M, Jacobs R, Wyatt J, Willems G, Pattijn V, Dhoore E, et al. Accuracy and surgical feasibility of a CBCT-based stereolithographic surgical guide aiding autotransplantation of teeth: in vitro validation. *J Oral Rehabil.* 2010;37(11):854-9.
11. Shahbazian M, Jacobs R, Wyatt J, Willems G, Pattijn V, Dhoore E, et al. Accuracy and surgical feasibility of a CBCT-based stereolithographic surgical guide aiding autotransplantation of teeth: in vitro validation. *J Oral Rehabil.* 2010;37(11):854-9.
12. Jang Y, Choi YJ, Lee SJ, Roh BD, Park SH, Kim E. Prognostic Factors for Clinical Outcomes in Autotransplantation of Teeth with Complete Root Formation: Survival Analysis for up to 12 Years. *J Endod.* 2016;42(2):198-205.
13. EzEldeen M, Wyatt J, Al-Rimawi A, Coucke W, Shaheen E, Lambrichts I, et al. Use of CBCT Guidance for Tooth Autotransplantation in Children. *J Dent Res.* 2019;98(4):406-13.
14. Duret F, Preston JD. CAD/CAM imaging in dentistry. *Curr Opin Dent.* 1991;1(2):150-4.
15. Miyazaki T, Hotta Y, Kunii J, Kuriyama S, Tamaki Y. A review of dental CAD/CAM: current status and future perspectives from 20 years of experience. *Dent Mater J.* 2009;28(1):44-56.
16. Torabi K, Farjood E, Hamedani S. Rapid Prototyping Technologies and their Applications in Prosthodontics, a Review of Literature. *J Dent (Shiraz).* 2015;16(1):1-9.
17. Van Assche N, Verbruggen M, Coucke W, Teughels W, Jacobs R, Quirynen M. Accuracy of computer-aided implant placement. *Clin Oral Implants Res.* 2012;23 Suppl 6:112-23.

18. Vercruyssen M, Coucke W, Naert I, Jacobs R, Teughels W, Quirynen M. Depth and lateral deviations in guided implant surgery: an RCT comparing guided surgery with mental navigation or the use of a pilot-drill template. *Clin Oral Implants Res.* 2015;26(11):1315-20.
19. Vercruyssen M, van de Wiele G, Teughels W, Naert I, Jacobs R, Quirynen M. Implant- and patient-centred outcomes of guided surgery, a 1-year follow-up: An RCT comparing guided surgery with conventional implant placement. *J Clin Periodontol.* 2014;41(12):1154-60.
20. Colombo M, Mangano C, Mijiritsky E, Krebs M, Hauschild U, Fortin T. Clinical applications and effectiveness of guided implant surgery: a critical review based on randomized controlled trials. *BMC Oral Health.* 2017;17(1):150.
21. Krastl G, Zehnder MS, Connert T, Weiger R, Kuhl S. Guided Endodontics: a novel treatment approach for teeth with pulp canal calcification and apical pathology. *Dent Traumatol.* 2016;32(3):240-6.
22. Torres A, Shaheen E, Lambrechts P, Politis C, Jacobs R. Microguided Endodontics: a case report of a maxillary lateral incisor with pulp canal obliteration and apical periodontitis. *Int Endod J.* 2018.
23. Lee SJ, Jung IY, Lee CY, Choi SY, Kum KY. Clinical application of computer-aided rapid prototyping for tooth transplantation. *Dent Traumatol.* 2001;17(3):114-9.
24. Shahbazian M, Jacobs R, Wyatt J, Denys D, Lambrichts I, Vinckier F, et al. Validation of the cone beam computed tomography-based stereolithographic surgical guide aiding autotransplantation of teeth: clinical case-control study. *Oral Surg Oral Med Oral Pathol Oral Radiol.* 2013;115(5):667-75.
25. Kim SY, Shin YS, Jung HD, Hwang CJ, Baik HS, Cha JY. Precision and trueness of dental models manufactured with different 3-dimensional printing techniques. *Am J Orthod Dentofacial Orthop.* 2018;153(1):144-53.
26. Dawood A, Marti Marti B, Sauret-Jackson V, Darwood A. 3D printing in dentistry. *Br Dent J.* 2015;219(11):521-9.
27. Shaheen E, Alhelwani A, Van De Castele E, Politis C, Jacobs R. Evaluation of Dimensional Changes of 3D Printed Models After Sterilization: A Pilot Study. *Open Dent J.* 2018;12:72-9.
28. Shaheen E, Coopman R, Jacobs R, Politis C. Optimized 3D virtually planned intermediate splints for bimaxillary orthognathic surgery: A clinical validation study in 20 patients. *J Craniomaxillofac Surg.* 2018;46(9):1441-7.
29. Shaheen E, Sun Y, Jacobs R, Politis C. Three-dimensional printed final occlusal splint for orthognathic surgery: design and validation. *Int J Oral Maxillofac Surg.* 2017;46(1):67-71.
30. EzEldeen M, Stratis A, Coucke W, Codari M, Politis C, Jacobs R. As Low Dose as Sufficient Quality: Optimization of Cone-beam Computed Tomographic Scanning Protocol for Tooth Autotransplantation Planning and Follow-up in Children. *J Endod.* 2017;43(2):210-7.
31. Loubele M, Bogaerts R, Van Dijk E, Pauwels R, Vanheusden S, Suetens P, et al. Comparison between effective radiation dose of CBCT and MSCT scanners for dentomaxillofacial applications. *Eur J Radiol.* 2009;71(3):461-8.
32. Stanley M, Paz AG, Miguel I, Coachman C. Fully digital workflow, integrating dental scan, smile design and CAD-CAM: case report. *BMC Oral Health.* 2018;18(1):134.
33. Joda T, Zarone F, Ferrari M. The complete digital workflow in fixed prosthodontics: a systematic review. *BMC Oral Health.* 2017;17(1):124.
34. Kim GB, Lee S, Kim H, Yang DH, Kim YH, Kyung YS, et al. Three-Dimensional Printing: Basic Principles and Applications in Medicine and Radiology. *Korean J Radiol.* 2016;17(2):182-97.
35. EzEldeen M, Van Gorp G, Van Dessel J, Vandermeulen D, Jacobs R. 3-dimensional analysis of regenerative endodontic treatment outcome. *J Endod.* 2015;41(3):317-24.
36. Barrett WA, Mortensen EN. Interactive live-wire boundary extraction. *MedImage Anal.* 1997;1(4):331-41.
37. Suetens P. *Fundamentals of Medical Imaging.* 2nd ed: New York: Cambridge University Press; 2009. 264 p.

38. Heckel F, Konrad O, Karl Hahn H, Peitgen H-O. Interactive 3D medical image segmentation with energy-minimizing implicit functions. *Computers & Graphics*. 2011;35(2):275-87.
 39. Bland JM, Altman DG. Statistical methods for assessing agreement between two methods of clinical measurement. *The Lancet*. 1986;1:307-10.
-

CHAPTER 5

This chapter is based on the following publication

Al-Rimawi, A., EzEldeen, M., Schneider, D., Politis, C., Jacobs, R. (2019). 3D Printed Temporary Veneer Restoring Autotransplanted Teeth in Children: Design and Concept Validation Ex Vivo. International Journal of Environmental Research and Public Health, 16(3).
(Shared first authorship)

- (A) OMFS IMPATH research group, Department of Imaging and Pathology, Faculty of Medicine, University of Leuven and Oral & Maxillofacial Surgery, University Hospitals Leuven, Leuven, Belgium
- (B) Department of Dentistry, Royal Medical Services, Jordanian Armed Forces, Jordan
- (C) Department of Oral Health Sciences, KU Leuven and Paediatric Dentistry and Special Dental Care, University Hospitals Leuven, Leuven
- (D) Department of Dental Medicine, Karolinska Institute, Stockholm, Sweden

* These authors contributed equally to this work

3D Printed Temporary Veneer Restoring Autotransplanted Teeth in Children: Design and Concept Validation Ex Vivo

A. Al-Rimawi (A,B)*, M. EzEldeen (A,C)*, D. Schneider (A), C. Politis (A), R. Jacobs (A,D)

ABSTRACT

Introduction — Three-dimensional printing is progressing rapidly and is applied in many fields of dentistry. Tooth autotransplantation offers a viable biological approach to tooth replacement in children and adolescents. Restoring or reshaping the transplanted tooth to the anterior maxilla should be done as soon as possible for psychological and aesthetic reasons. However, to avoid interfering with the natural healing process, reshaping of transplanted teeth is usually delayed 3-4 months after transplantation. This delay creates a need for a simple indirect temporary aesthetic restoration for autotransplanted teeth. The aim of this study was to develop and validate a digital solution for temporary restoration of autotransplanted teeth using 3D printing.

KEY WORDS

CBCT, CAD/CAM, 3D printing, DLP, Tooth Autotransplantation

Methods — Four dry human skulls and four dry human mandibles were scanned using cone beam computed tomography to create 3D models for 15 premolars. Digital impression of the maxillary arch of one of the skulls was captured by intra oral scanner. Digital work-flow for the design and fabrication of temporary veneers is presented. The seating and adaptation of the 3D printed veneers were evaluated using stereomicroscopy and micro-computed tomography.

Results — Evaluation of veneer seating using stereomicroscopy showed that the mean marginal gap at all sides was below the cut-off value of 200 μm . The overall mean marginal gap was $99.9 \pm 50.7 \mu\text{m}$ [median: 87.8 (IQR 64.2-133 μm)]. Internal adaptation evaluation using micro-computed tomography showed an average median gap thickness of 152.5 ± 47.7 (IQR 129-149.3 μm).

Conclusion — The present concept of using temporary veneers, designed and fabricated with CAD/CAM technology using DLP printer may present a viable treatment option for restoration of autotransplanted teeth.

Computer-aided design/ computer-aided manufacturing (CAD/CAM) use in dentistry started in the early nineties with subtractive manufacturing (1, 2). Recently additive manufacturing technology, three dimensional (3D) printing, is progressing rapidly and is applied in many fields of dentistry (3) such as: fabrication of surgical guides for placement of dental implants (4-7) , guides for endodontic access and apical surgeries (8, 9), fabrication of surgical guides and tooth replicas for tooth autotransplantation (TAT) (10-12), construction of physical models for orthodontics (13), manufacturing of dental implants (14), and study models, splints, guides in orthognathic surgeries (15-17).

The process of 3D printing in dentistry goes through three stages starting with data acquisition using low dose cone beam computed tomography (CBCT) (18, 19) and/or intraoral scanner (IOS) (20, 21), followed processing and designing using dedicated software tools, and finally printing (12, 22-24) .

Different 3D printing technologies are being used in dentistry, which can be technically classified into: fused deposition modelling (FDM), stereolithography (SLA), PolyJet printing, Multijet printing, ColorJet printing, selective laser sintering, and digital light processing (DLP) (3, 24).

As aforementioned, CAD/CAM and 3D printing technology are already being applied in tooth autotransplantation (TAT) procedures (10, 12). TAT offers a viable biological approach to tooth replacement in children and adolescents after traumatic dental injuries (TDIs), agenesis, developmental anomalies or specific orthodontic problems (25-29). The treatment options available, for example implant placement, are limited by the ongoing dentoalveolar development (30) while, orthodontic tooth alignment is challenging unless skeletal anchorage is applied (31, 32). TAT allows for periodontal healing and enables preservation of the alveolar ridge maintaining the possibility of function and growth (25, 33-35). Restoring or reshaping the transplanted tooth to the anterior maxilla should be done as soon as possible for psychological and aesthetic reasons (36). However, to avoid interfering with the natural healing process (33, 37), reshaping of transplanted teeth is usually delayed 3-4 months after transplantation (38). This delay creates a need for a simple indirect temporary aesthetic restoration for TAT, which so far has not yet been reported.

The aim of this study was to develop and validate a digital solution for temporary restoration of autotransplanted teeth using 3D printing technology.

MATERIALS AND METHODS

Image acquisition

Four dry human skulls and four dry human mandibles were scanned using a CBCT machine NewTom VGI EVO (QR Verona, Verona, Italy). Ethical approval obtained from the Ethical Review Board of the University Hospitals Leuven (S55619 ML9535, University Hospitals Leuven). Scanning parameters were set for a standard mode, 360° rotation, 200 µm voxel size and a field of view 80 x 80 mm at 110 kV (x-ray tube voltage) and automatic tube current modulation. All data sets were exported using the Digital Imaging and Communications in Medicine (DICOM) file format with an isotropic voxel size of 200 µm, a slice interval and thickness of 200 µm.

Segmentation protocol

CBCT scans were imported into MeVisLab (MeVis Medical Solutions AG, Bremen, Germany). Regions of interest including the single rooted 1st or 2nd premolar were selected. All regions of interest images were normalized using an intensity windowing filter and then a median filter to suppress any noise and decrease confounding variables between the images.

All single rooted premolars were then segmented using a dedicated tool developed in MeVisLab and validated for accurate tooth/root canal space segmentation as described (39) (Fig. 1 A). The tool applies interactive livewire boundary extraction to create a set of orthogonal contours around the tooth of interest. Livewire allows for a semi-interactive segmentation of structures with prominent edge image features (40). Internally, the module generates a graph representation of the image to work on; the graph's nodes represent image pixels, and edges connect neighbouring pixels. The edges are weighted based on the cost function (image gradient magnitude). If starting and ending points are defined on such a graph, the shortest path (minimal cost path) is computed using dynamic programming (F* algorithm) (41). This was followed by a variational interpolation algorithm that reconstructs the surface of an object with energy-minimizing, smooth, and implicit functions in order to create a 3D mask of the tooth surface (Fig. 1 A) (42).

After segmentation, the 3D triangle-based surfaces of the 15 premolars (four skulls: seven premolars, four mandibles: eighth premolars) were reconstructed and saved as STL files.

Digital impression of the maxillary arch of one of the skulls was captured by Trios IOS (Trios® 3 Cart wired, 3Shape, Copenhagen, Denmark).

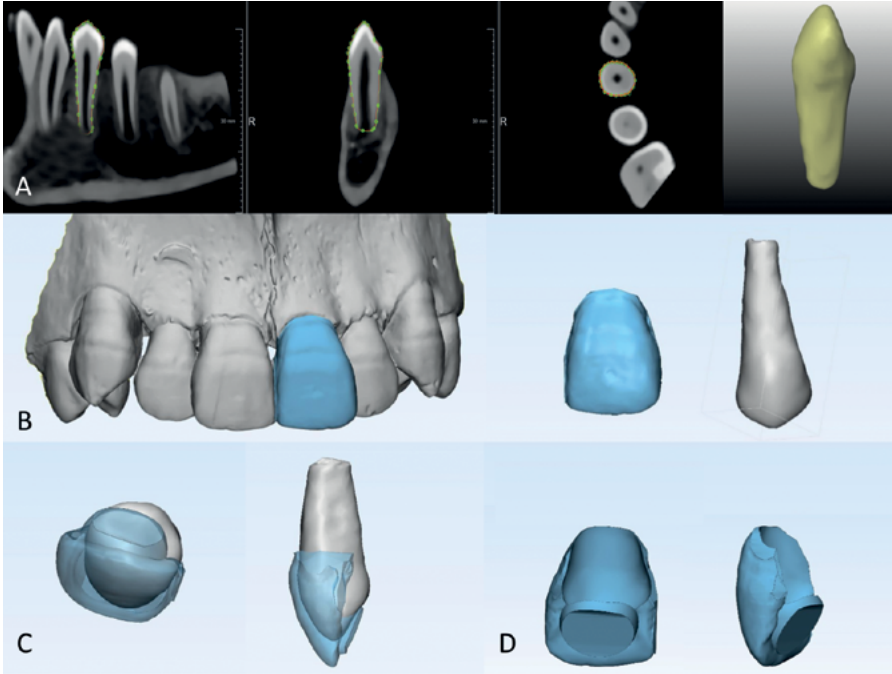


Figure 1: Digital flow for temporary veneer preparation. A: Premolar segmentation, B: designing temporary veneer based on the shape of the contralateral incisor (to mimic the clinical situation where one maxillary central incisor will be lost, a mirror image of the contralateral maxillary incisor was used to design the temporary veneer that will fit the transplanted premolar), C: checking veneer thickness to ensure optimal printing, D: final veneer design: removing undercuts, beveling the edges (green arrow) and inspecting the surface thickness is done to avoid print failure spots.

Designing of temporary veneers

The steps of veneer designing are illustrated in Figure 1. The digital 3D model of the maxillary central incisors acquired using the Trios intra-oral scanner and the 3D models of the segmented premolars were imported to 3-matic version 12.0 (Materialise; Leuven, Belgium) (Fig. 1 B & C).

To mimic the clinical situation where one maxillary central incisor will be lost, a mirror image of the contralateral maxillary incisor was used to design the temporary veneer that will fit the transplanted premolar (Fig. 1B). The crown of the central incisor was isolated from the 3D model created by the intra-oral scanner (Fig. 1C) then moved to overlap the crown of the premolar. The transparency of the central incisor was then changed into medium transparency in order to control the thickness of the desired veneer during the design process (Fig. 1C).

Subsequently, the 3D model of the premolar was subtracted from the 3D model of the maxillary central incisor (Fig. 1D). The generated subtraction object represented the temporary veneer design, the design was further optimized then exported as STL file ready for printing (Fig 1D).

This process was repeated for the 15 3D models of the segmented premolars using the same maxillary central incisor. As a result, 15 digital models of temporary veneers were generated.

Three-dimensional printing of temporary veneers

The 3D models of the veneers and assigned premolars were exported to the Raydent studio software, and printed in a Raydent (RAM500, RayMedical, Seoul, South-Korea) DLP 3D printer. The printer utilizes liquid crystal planar solidification technology and was loaded with its specific resin material (crown and bridge resin).

The printed veneers were cleaned in an ultrasonic bath using IPA 90% (Isopropyl alcohol) to remove residual resin, and then post cured with the Curing Unit (RPC500, RayMedical, Seoul, South-Korea). Figure 2A presents an example for the 3D printed temporary veneer.

Evaluation of veneer seating and marginal adaptation

All premolars were removed from the skulls and mandibles. Then each veneer was seated onto its corresponding tooth. To ensure the correct seating of each veneer, corresponding to the designed position, a special holder was designed using in 3-matic version 12.0 (Materialise; Leuven, Belgium), and 3D printed using the Connex printer (Object 360, Stratasys, Minnesota, USA).

The cervical, mesial, and distal veneer margins were examined under a stereomicroscope (Olympus, Singapore) (Fig. 2B). For each side, digital images for detected gaps were captured at 50x magnification. Six measurements were made at each image resulting in 18 readings for each veneer.

Evaluation of internal adaptation using micro-computed Tomographic Imaging *Image acquisition*

To check internal adaptation the fitted veneers were scanned with the SkyScan 1172 micro-computed tomographic (μ CT) system (Bruker, Antwerp, Belgium) (Fig. 2C). The μ CT parameters were 12.8 μ m voxel size, 40 kVp, 250 mA, 0.5 mm

96 aluminum filter, angular rotation step of 0.7° , 360° scanning, and exposure time of 0.295 seconds with a total scan duration of 22.5 minutes.

The x-ray projections were reconstructed using volumetric reconstruction software (SkyScan, Nrecon), beam hardening correction of 2% and ring artefact correction were used for the reconstruction. Reconstructed slices were exported as DICOM files.

Segmentation protocol, 3D reconstruction and Quantitative Analysis of Gap Thickness

To assess the internal adaptation, the gap between the veneer and the tooth was segmented using an indirect protocol applying logical operations. DICOM files of reconstructed images were imported into a dedicated tool developed in MeVisLab (MeVis Medical Solutions AG, Bremen, Germany).

The gap and enamel were segmented together as a single entity, and then saved as binary image, and as intensity image. The intensity image was loaded, then the enamel was thresholded and saved as a separate binary image. The segmented binary images of the gap and enamel, and the enamel separately were used to reconstruct two 3D models. The enamel 3D model was then subtracted from the 3D model of the gap and enamel resulting in the 3D model of the gap (3matic, Materialise; Leuven, Belgium). The thickness of the resulting gap 3D model was then analyzed and expressed as color-coded map (Fig 2D).

Statistical analysis

Statistical analysis and graph plotting were performed using the statistical software package GraphPad Prism 7.00 (GraphPad Software, La Jolla California USA). One-way way ANOVA was used to test for statistical differences at $P < 0.05$.

RESULTS

The resulting 3D printed temporary veneer is presented in Figure 2A. Evaluation of veneer seating using stereomicroscopy showed that the mean marginal gap at all sides was below the cut-off value of $200\ \mu\text{m}$ (Fig. 3A). The overall mean marginal gap was $99.9 \pm 50.7\ \mu\text{m}$ [median: 87.8 (IQR 64.2 - $133\ \mu\text{m}$)]. Cervically, the mean marginal gap was $92.4 \pm 48.1\ \mu\text{m}$ [median: 87.8 (IQR 50.2 - $133\ \mu\text{m}$)]. On the mesial side, the mean marginal gap was $111 \pm 59.2\ \mu\text{m}$ [median: 89.1 (IQR 81.8 - $155\ \mu\text{m}$)] and on the distal side, the mean marginal gap was $96 \pm 44.9\ \mu\text{m}$ [median: 89.8 (IQR 63.4 - $140\ \mu\text{m}$)] (Fig. 3A). Differences

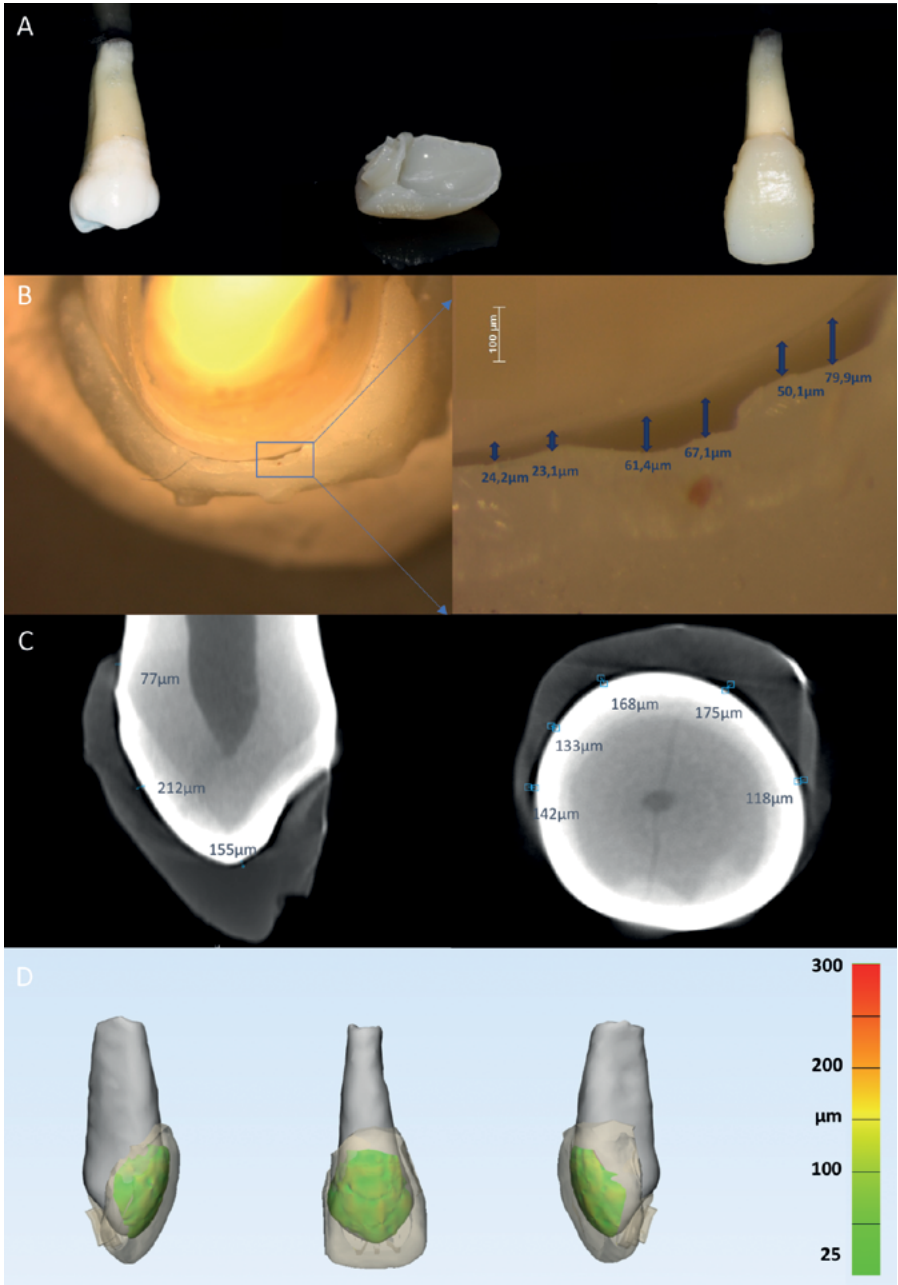


Figure 2: 3D printed veneer and evaluation methods. A: 3D printed veneer and fitting to premolar, B: evaluation of veneer seating using stereomicroscopy, C: internal gap evaluation using micro-computed tomography, D: quantitative analysis of gap thickness.

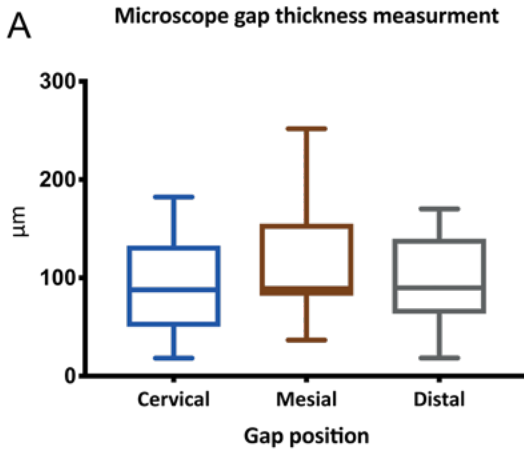
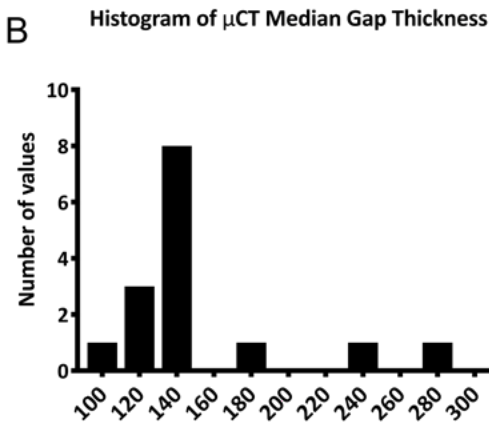


Figure 3: A: stereomicroscopy gap measurements, B: distribution of the gap thickness between the veneer and the tooth.



between the gap thickness measured at different positions did not show any statistically significant differences ($P > 0.05$).

Internal adaptation evaluation using μ CT showed an average median gap thickness of 152.5 ± 47.7 (IQR 129-149.3 μm). Figure 2D presents a color-coded map for 3D gap thickness analysis demonstrating the homogenous thickness below the cut-off value of 200 μm . Moreover, the overall distribution of the gap thickness between the veneer and the tooth was below the cut-off value of 200 μm in the majority of the samples.

DISCUSSION

Tooth autotransplantation TAT offers a viable biological approach to tooth replacement in children and adolescents after traumatic dental injuries (TDIs), agenesis, developmental anomalies or specific orthodontic problems (25-29). In a recent systematic review, Akhlef et al., (28) reported an overall survival rates for conventional TAT ranging between 93% and 100% (weighted mean: 96.7%, median: 100%) after 9 months to 22 years of observation (median: 8.75 years). The survival rates for conventional TAT of teeth with incomplete root formation was reported to be 97.4, 97.8, and 96.3%, after 1, 5, and 10 years, respectively (29). Studies reporting on the aesthetic results after TAT are limited (28). Czochrowska et al., (38) reported a clinical assessment of reshaped auto-transplanted tooth using composite build-ups compared to natural contralateral tooth according to objective parameters. The authors reported a 59% match, 27% deviation and 14% mismatch with the natural contralateral tooth (38).

While restoring or reshaping transplanted teeth to the anterior maxilla is essential for psychological and aesthetic reasons (36), reshaping of transplanted teeth is usually delayed 3-4 months after transplantation to avoid interfering with the natural healing process (28, 29, 38, 43). This interval could be bridged using a simple indirect temporary aesthetic restoration for autotransplanted teeth.

The current report proposes a digital technique for designing and fabricating temporary veneers for autotransplanted teeth via chair side 3D printing technology, namely DLP. Simultaneously the accuracy of this printing technology was validated by examining the marginal and internal adaptation of these temporary veneers.

Precise fit is an essential requirement for any dental restoration or prostheses. Ill-fitting prostheses will result in damage for the periodontium, tooth structure, and the prosthesis itself (23, 44, 45). This study applied two methods for evaluating the adaptation of the veneers: direct view with microscope to measure the marginal fit, and μ CT to evaluate the internal adaptation. Although there is no consensus about the best method to examine the marginal adaptation of fixed dental prosthesis, direct view method is the most used method and with most reproducible results. In the present study, marginal gaps were measured by stereomicroscopy (direct viewing method), resulting in a mean of marginal gap of 100 μ m, which is below the clinically acceptable value of marginal gaps of 120 μ m (46, 47).

To assess internal adaptation, μ CT scans of the maxillary central incisor shaped veneers fitted on premolars, simulating the clinical situation, were used. The majority of the studies where μ CT was used to assess internal adap-

100 tation performed two dimensional measurements of the internal gaps on cross sectional slides (48, 49), while in this study three-dimensional evaluation of the internal gap was applied. The average median thickness of internal gaps in the present study was 152 μm which is within the accepted values (50-52).

In a 2-years follow-up study on the use of 3D printed veneers, values of internal adaptation of porcelain laminate veneers ranged from 195 to 202 μm which are higher than our values, while clinical performance was rated 100% satisfactory over the 2-years period (52).

One of the potential limitations of the suggested protocol is the use of one specific 3D printing technology and one specific printing material. Future studies are needed to study different 3D printing technologies other than DLP, while using other printing materials.

With the development of 3D printing technology and new resin materials, developed specifically for dental restorations, it is expected that the use of this technique could be expanded for applications in other than autotransplanted teeth, especially in clinical situations where treatment should be done in short time for example dental treatment under general anesthesia, trauma and uncooperative children.

CONCLUSION

The present concept of using temporary veneers, designed and fabricated with CAD/CAM technology using DLP printer may present a viable treatment option for restoration of autotransplanted teeth. For the current design, values of marginal and internal adaptation were found within clinically the acceptable ranges.

REFERENCES

-
1. Duret F, Preston JD. CAD/CAM imaging in dentistry. *Curr Opin Dent.* 1991;1(2):150-4.
 2. Miyazaki T, Hotta Y, Kunii J, Kuriyama S, Tamaki Y. A review of dental CAD/CAM: current status and future perspectives from 20 years of experience. *Dent Mater J.* 2009;28(1):44-56.
 3. Torabi K, Farjood E, Hamedani S. Rapid Prototyping Technologies and their Applications in Prosthodontics, a Review of Literature. *J Dent (Shiraz).* 2015;16(1):1-9.
 4. Van Assche N, Vercruyssen M, Coucke W, Teughels W, Jacobs R, Quirynen M. Accuracy of computer-aided implant placement. *Clin Oral Implants Res.* 2012;23 Suppl 6:112-23.
 5. Vercruyssen M, Coucke W, Naert I, Jacobs R, Teughels W, Quirynen M. Depth and lateral deviations in guided implant surgery: an RCT comparing guided surgery with mental navigation or the use of a pilot-drill template. *Clin Oral Implants Res.* 2015;26(11):1315-20.

6. Vercruyssen M, van de Wiele G, Teughels W, Naert I, Jacobs R, Quirynen M. Implant- and patient-centred outcomes of guided surgery, a 1-year follow-up: An RCT comparing guided surgery with conventional implant placement. *J Clin Periodontol.* 2014;41(12):1154-60.
7. Colombo M, Mangano C, Mijiritsky E, Krebs M, Hauschild U, Fortin T. Clinical applications and effectiveness of guided implant surgery: a critical review based on randomized controlled trials. *BMC Oral Health.* 2017;17(1):150.
8. Krastl G, Zehnder MS, Connert T, Weiger R, Kuhl S. Guided Endodontics: a novel treatment approach for teeth with pulp canal calcification and apical pathology. *Dent Traumatol.* 2016;32(3):240-6.
9. Torres A, Shaheen E, Lambrechts P, Politis C, Jacobs R. Microguided Endodontics: a case report of a maxillary lateral incisor with pulp canal obliteration and apical periodontitis. *Int Endod J.* 2018.
10. Lee SJ, Jung IY, Lee CY, Choi SY, Kum KY. Clinical application of computer-aided rapid prototyping for tooth transplantation. *Dent Traumatol.* 2001;17(3):114-9.
11. Shahbazian M, Jacobs R, Wyatt J, Denys D, Lambrichts I, Vinckier F, et al. Validation of the cone beam computed tomography-based stereolithographic surgical guide aiding autotransplantation of teeth: clinical case-control study. *Oral Surg Oral Med Oral Pathol Oral Radiol.* 2013;115(5):667-75.
12. Shahbazian M, Jacobs R, Wyatt J, Willems G, Pattijn V, Dhoore E, et al. Accuracy and surgical feasibility of a CBCT-based stereolithographic surgical guide aiding autotransplantation of teeth: in vitro validation. *J Oral Rehabil.* 2010;37(11):854-9.
13. Kim SY, Shin YS, Jung HD, Hwang CJ, Baik HS, Cha JY. Precision and trueness of dental models manufactured with different 3-dimensional printing techniques. *Am J Orthod Dentofacial Orthop.* 2018;153(1):144-53.
14. Dawood A, Marti Marti B, Sauret-Jackson V, Darwood A. 3D printing in dentistry. *Br Dent J.* 2015;219(11):521-9.
15. Shaheen E, Alhelwani A, Van De Castelee E, Politis C, Jacobs R. Evaluation of Dimensional Changes of 3D Printed Models After Sterilization: A Pilot Study. *Open Dent J.* 2018;12:72-9.
16. Shaheen E, Coopman R, Jacobs R, Politis C. Optimized 3D virtually planned intermediate splints for bimaxillary orthognathic surgery: A clinical validation study in 20 patients. *J Craniomaxillofac Surg.* 2018;46(9):1441-7.
17. Shaheen E, Sun Y, Jacobs R, Politis C. Three-dimensional printed final occlusal splint for orthognathic surgery: design and validation. *Int J Oral Maxillofac Surg.* 2017;46(1):67-71.
18. EzEldeen M, Stratis A, Coucke W, Codari M, Politis C, Jacobs R. As Low Dose as Sufficient Quality: Optimization of Cone-beam Computed Tomographic Scanning Protocol for Tooth Autotransplantation Planning and Follow-up in Children. *J Endod.* 2017;43(2):210-7.
19. Loubele M, Bogaerts R, Van Dijk E, Pauwels R, Vanheusden S, Suetens P, et al. Comparison between effective radiation dose of CBCT and MSCT scanners for dentomaxillofacial applications. *Eur J Radiol.* 2009;71(3):461-8.
20. Albdour EA, Shaheen E, Vranckx M, Mangano FG, Politis C, Jacobs R. A novel in vivo method to evaluate trueness of digital impressions. *BMC Oral Health.* 2018;18(1):117.
21. Mangano F, Gandolfi A, Luongo G, Logozzo S. Intraoral scanners in dentistry: a review of the current literature. *BMC Oral Health.* 2017;17(1):149.
22. Stanley M, Paz AG, Miguel I, Coachman C. Fully digital workflow, integrating dental scan, smile design and CAD-CAM: case report. *BMC Oral Health.* 2018;18(1):134.
23. Joda T, Zarone F, Ferrari M. The complete digital workflow in fixed prosthodontics: a systematic review. *BMC Oral Health.* 2017;17(1):124.
24. Kim GB, Lee S, Kim H, Yang DH, Kim YH, Kyung YS, et al. Three-Dimensional Printing: Basic Principles and Applications in Medicine and Radiology. *Korean J Radiol.* 2016;17(2):182-97.

25. Czochrowska EM, Stenvik A, Album B, Zachrisson BU. Autotransplantation of premolars to replace maxillary incisors: a comparison with natural incisors. *Am J Orthod Dentofacial Orthop.* 2000;118(6):592-600.
26. Day P, Duggal M. Autotransplantation for failing and missing anterior teeth. *Pediatr Dent.* 2008;30(4):286-7; author reply 7.
27. Paulsen HU, Andreasen JO, Schwartz O. Tooth loss treatment in the anterior region: autotransplantation of premolars and cryopreservation. *World J Orthod.* 2006;7(1):27-34.
28. Akhlef Y, Schwartz O, Andreasen JO, Jensen SS. Autotransplantation of teeth to the anterior maxilla: A systematic review of survival and success, aesthetic presentation and patient-reported outcome. *Dent Traumatol.* 2018;34(1):20-7.
29. Rohof ECM, Kerdijk W, Jansma J, Livas C, Ren Y. Autotransplantation of teeth with incomplete root formation: a systematic review and meta-analysis. *Clin Oral Investig.* 2018;22(4):1613-24.
30. Sharma AB, Vargervik K. Using implants for the growing child. *J Calif Dent Assoc.* 2006;34(9):719-24.
31. Kanavakis G, Ludwig B, Rosa M, Zachrisson B, Hourfar J. Clinical outcomes of cases with missing lateral incisors treated with the T'-Mesialslider. *J Orthod.* 2014;41 Suppl 1:S33-8.
32. Becker K, Wilmes B, Grandjean C, Vasudavan S, Drescher D. Skeletally anchored mesialization of molars using digitized casts and two surface-matching approaches : Analysis of treatment effects. *J Orofac Orthop.* 2018;79(1):11-8.
33. Andreasen JO, Paulsen HU, Yu Z, Schwartz O. A long-term study of 370 autotransplanted premolars. Part III. Periodontal healing subsequent to transplantation. *Eur J Orthod.* 1990;12(1):25-37.
34. Kallu R, Vinckier F, Politis C, Mwalili S, Willems G. Tooth transplantations: a descriptive retrospective study. *Int J Oral Maxillofac Surg.* 2005;34(7):745-55.
35. Denys D, Shahbazian M, Jacobs R, Laenen A, Wyatt J, Vinckier F, et al. Importance of root development in autotransplantations: a retrospective study of 137 teeth with a follow-up period varying from 1 week to 14 years. *Eur J Orthod.* 2013;35(5):680-8.
36. Day PF, Kindelan SA, Spencer JR, Kindelan JD, Duggal MS. Dental trauma: part 2. Managing poor prognosis anterior teeth--treatment options for the subsequent space in a growing patient. *J Orthod.* 2008;35(3):143-55.
37. Andreasen JO, Paulsen HU, Yu Z, Bayer T, Schwartz O. A long-term study of 370 autotransplanted premolars. Part II. Tooth survival and pulp healing subsequent to transplantation. *Eur J Orthod.* 1990;12(1):14-24.
38. Czochrowska EM, Stenvik A, Zachrisson BU. The esthetic outcome of autotransplanted premolars replacing maxillary incisors. *Dent Traumatol.* 2002;18(5):237-45.
39. EzEldeen M, Van Gorp G, Van Dessel J, Vandermeulen D, Jacobs R. 3-dimensional analysis of regenerative endodontic treatment outcome. *J Endod.* 2015;41(3):317-24.
40. Barrett WA, Mortensen EN. Interactive live-wire boundary extraction. *MedImage Anal.* 1997;1(4):331-41.
41. Suetens P. *Fundamentals of Medical Imaging.* 2nd ed: New York: Cambridge University Press; 2009. 264 p.
42. Heckel F, Konrad O, Karl Hahn H, Peitgen H-O. Interactive 3D medical image segmentation with energy-minimizing implicit functions. *Computers & Graphics.* 2011;35(2):275-87.
43. Zachrisson BU, Stenvik A, Haanæs HR. Management of missing maxillary anterior teeth with emphasis on autotransplantation. *American Journal of Orthodontics and Dentofacial Orthopedics.* 2004;126(3):284-8.
44. Bader JD, Rozier RG, McFall WT, Ramsey DL. Effect of crown margins on periodontal conditions in regularly attending patients. *J Prosthet Dent.* 1991;65(1):75-9.
45. Bergenholtz G, Cox CF, Loesche WJ, Syed SA. Bacterial leakage around dental restorations: its effect on the dental pulp. *J Oral Pathol.* 1982;11(6):439-50.

46. Fransson B, Oilo G, Gjeitanger R. The fit of metal-ceramic crowns, a clinical study. *Dent Mater.* 1985;1(5):197-9.
 47. McLean JW, von Fraunhofer JA. The estimation of cement film thickness by an in vivo technique. *Br Dent J.* 1971;131(3):107-11.
 48. Borba M, Cesar PF, Griggs JA, Della Bona Á. Adaptation of all-ceramic fixed partial dentures. *Dent Mater.* 2011;27(11):1119-26.
 49. Pelekanos S, Koumanou M, Koutayas SO, Zinelis S, Eliades G. Micro-CT evaluation of the marginal fit of different In-Ceram alumina copings. *Eur J Esthet Dent.* 2009;4(3):278-92.
 50. Harasani MH, Isidor F, Kaaber S. Marginal fit of porcelain and indirect composite laminate veneers under in vitro conditions. *Scand J Dent Res.* 1991;99(3):262-8.
 51. Tetsuya A, Ryunosuke K, Takashi O, Masayoshi F. Adaptation of laminate veneer restorations fabricated with the CEREC 3 system. *Adhesive Dentistry.* 2006; 24(3):179-84.
 52. Yuce M, Ulusoy M, Turk AG. Comparison of Marginal and Internal Adaptation of Heat-Pressed and CAD/CAM Porcelain Laminate Veneers and a 2-Year Follow-Up. *J Prosthodont.* 2017.
-

CHAPTER 6

This chapter is based on the following publication

EzEldeen, M., Pedano, S., Driesen, R., Wyatt, J., Van Gorp, G., Meschi, N., Van Meerbeek, B., Lambrichts, I., Jacobs R. Multi-modality imaging for the characterization of the patterns of dental pulp healing after Tooth autotransplantation and Regenerative Endodontic Treatment.
In preparation.

- (A) OMFS IMPATHResearch Group, Faculty of Medicine, Department of Imaging and Pathology, KU Leuven and Oral and Maxillofacial Surgery, University Hospitals Leuven, Kapucijnenvoer 33, 3000 Leuven, Belgium
- (B) Department of Oral Health Sciences, KU Leuven and Paediatric Dentistry and Special Dental Care, University Hospitals Leuven, Kapucijnenvoer 33, 3000 Leuven, Belgium
- (C) Department of Oral Health Sciences, Endodontology, University Hospitals Leuven, KU Leuven, Leuven, Belgium
- (D) Biomedical Research Institute, HasseltUniversity, Campus Diepenbeek, Agoralaan Building C, B-3590 Diepenbeek, Belgium
- (E) KU Leuven (University of Leuven), Department of Oral Health Sciences, BIOMAT -Biomaterials Research group & UZ Leuven, University Hospitals Leuven, Dentistry, Kapucijnenvoer 33, 3000 Leuven, Belgium
- (F) Department of Dental Medicine, Karolinska Institute, Stockholm, Sweden

Multi-modality Imaging for the Characterization of the Patterns of Dental Pulp Healing After Tooth Autotransplantation and Regenerative Endodontic Treatment

M. EzEldeen (A,B), M. N. Simon Pedano De Piero (C), R. B. Driesen (D), J. Wyatt (B), G. Van Gorp (B), N. Meschi (C), B. Van Meerbeek (E), I. Lambrichts (D), R. Jacobs (A,F)

ABSTRACT

Introduction — Understanding dental pulp healing after tooth autotransplantation (TAT) and regenerative endodontic treatment (RET) of immature teeth is interesting from a clinical and a scientific point of view. The knowledge regarding dental pulp healing after TAT originates from studies of tooth replantation in large and small animal models with almost non-existing data from transplanted human teeth. RET has been associated with highly variable outcomes and mainly related to the formation of reparative tissue. This study aimed to characterize the pattern of dental pulp healing in human teeth that underwent TAT and RET using state-of-the-art multimodality imaging.

KEY WORDS

Tooth autotransplantation, Regenerative endodontic treatment, pulp healing/regeneration

Materials and Methods — Two premolars that underwent TAT showing pulp healing and needed to be extracted because of ankylosis after one year (case 1) and two years (case 2). One central incisor that suffered from a dentoalveolar trauma received RET and was extracted after three years (case 3) because of orthodontic reasons. The three samples were imaged using nanofocus x-ray computed tomography and then were processed for histological and immunohistochemical characterization. General tissue architecture and patterns of collagen deposition were examined using label-less laser scanning confocal second harmonic generation imaging (SHG). A maturity-matched premolar extracted for orthodontic reasons was used as a negative control for the histological and SHG characterization.

Results — Analysis of the three cases revealed different patterns of dental pulp healing. Observed similarities were the progressive obliteration of the root canal space encapsulating an interconnected root canal system. Striking loss of typical pulp architecture was observed in the TAT cases, while a pulp-like tissue was observed in the RET case. Odontoblast-like cells were observed in cases 1 & 3.

Conclusion — The current study provided insights into the patterns of dental pulp healing after TAT and RET. SHG imaging analysis shed the light on patterns of collagen deposition during reparative dentin formation.

Tooth autotransplantation (TAT) and regenerative endodontic treatment (RET) are two biology-based treatments for dental tissue loss, mainly in children. The clinical evidence of pulp healing and continued root development after immature TAT has been repeatedly demonstrated (1-5). These regenerative/repairative properties of the pulp/dentin complex after dental caries, attrition, restorative procedures, traumatic injuries (TDIs) and TAT (2, 6) have contributed to the discovery of stem/stromal cells in the dental pulp (7) well as the emergence of the idea of RET. From a tissue engineering point of view, TAT can be considered a model for stem/stromal cell transplantation (8-11), while RET can be regarded as a model for stem/stromal cell homing (12, 13).

Existing knowledge regarding pulp-dentin complex healing after TAT originates mainly from the pioneering work of Andreasen et al., and Skoglund et al., in the late seventies and the early eighties on replanted and transplanted teeth in monkeys up to 9 months (14) and dogs for periods up to 6 months (15-17). Dental Pulp healing after tooth replantation was also studied in mice and rat models up to 28 days, and these studies provided valuable insights into the immediate pulp response (18-21). To the authors knowledge, only 1 study reported on the pulp response in humans after intentional tooth replantation of premolars and this study was followed up to 6 months (22). Despite these studies' important contributions, information is still lacking regarding the outcomes at longer periods, the reestablishment of innervation, and comprehensive characterization of the pulp response in an actual clinical situation where the tooth was transplanted to a different site.

RET has been associated with highly variable outcomes (23-25). The histologic studies from animal and human teeth suggest that true pulp regeneration using the current protocol is difficult to achieve (25-27).

Therefore, the main aim of the current study was to report on the outcomes of 2 cases of TAT and 1 case with RET after 1, 2 and 3 years, respectively. Moreover, we used state-of-the-art nano-focus computed tomography, histological, immune-histochemical, and label-less confocal second harmonic generation to gain insights into the different patterns of dental pulp healing.

MATERIALS AND METHODS

Case description

Control tooth

A mandibular left first premolar (tooth 34) removed for orthodontic reasons was retrieved after obtaining informed (parental) consent from an 11 years-old girl, while visiting the department of Paediatric Dentistry, University Hospitals Leuven. This tooth served as control for histological, immunohistochemical staining and label-less confocal second harmonic generation (SHG).

Case 1: Tooth autotransplantation to a dentoalveolar trauma site

A 10 years-old girl was referred to the department of paediatric dentistry at UZ Leuven because of an ankylotic maxillary right central incisor (tooth 11) after dentoalveolar trauma and root canal treatment one year earlier (Figure 1A & B). Cone-beam computed tomography (CBCT) imaging showed replacement resorption at the palatal side (Figure 1C, D & E). After case discussion within the tooth autotransplantation team, it was decided to extract tooth 11 due to poor prognosis and to transplant, the maxillary left second premolar (tooth 25) to the central incisor region (Figure 1F). CBCT-guided tooth autotransplantation (TAT) was performed eight months after the initial consultation based on the stage of root development (Figure 1F-I) and following the procedure described previously (28). The transplanted tooth showed initial periodontal and pulp healing for 3 months (Figure 1J & K), and orthodontic treatment started.

Three months after the start of the orthodontic treatment (6 months post-TAT), the transplanted tooth was not responding to the orthodontic forces and stayed almost in its original position (Figure 1L). The presence of a metallic sound on percussion, suggesting the start of ankylosis. A low-dose CBCT scan with a small field of view was acquired to examine the periodontal ligament space all around. The CBCT scan showed signs of replacement resorption at the buccal side (Figure 1M). After discussion with the patient and parents, it was decided to use higher orthodontic forces to save the transplant. However, after six months (1-year post TAT), the transplant still did not respond. It stayed in its position (Figure 1N), necessitating the transplant extraction, and resorting to orthodontic mesialisation of the maxillary upper right lateral incisor. Therefore, one year post-transplant, the tooth was extracted due to ankylosis. However, the transplant showed clear signs of pulp healing demonstrated in the root canal obliteration and continued root development (Figure 1M). Therefore, after informed consent from the patient and parents, the extracted transplant was directly fixed in 4% paraformaldehyde to be examined using

108 nano-focus computed tomography and histologically to gain insights into the treatment outcome.

Case 2: Tooth autotransplantation to an agenesis site

A 10 years-old girl was referred to the department of paediatric dentistry at UZ Leuven due to multiple agenesis, mandibular right second premolar (tooth 45), mandibular left first premolar (tooth 34) and mandibular left second premolar (35) (Figure 2A). After case discussion within the tooth autotransplantation team, it was decided to transplant the maxillary right second premolar (tooth 15) to the mandibular left premolar region, where there were two missing premolars to facilitate the orthodontic treatment (Figure 2B & C). Orthodontic treatment started six months post-transplantation. The transplanted tooth showed periodontally and pulp healing up to 1-year post-transplantation (Figure 2D-H).

At 20 months post-TAT, the transplanted tooth did not show full bodily movement (Figure 2I), and a metallic sound on percussion, suggesting the start of ankylosis. A low-dose CBCT scan with a small field of view was acquired to examine the periodontal ligament space. The CBCT scan showed progressive replacement resorption at multiple sites on the root surface (Figure 2J & K). After discussion, it was decided to maintain the transplant serving as a bone anchor. Later it was extracted 24 months post-transplantation, and after informed consent, the extracted transplant was immediately fixed in 4% paraformaldehyde for further studies.

Case 3: Regenerative endodontic treatment in a tooth with dentoalveolar trauma

An eight-year-old girl presented to the emergency clinic of the department of paediatric dentistry at UZ Leuven with a dentoalveolar trauma. Clinical and radiological examination showed a luxated maxillary left central incisor (tooth 21) combined with an enamel dentin fracture without pulp exposure and an avulsed maxillary right central incisor (tooth 11) (Figure 3A). Tooth 11 was repositioned in the socket and splinted with a flexible splint (Figure 3B). Two weeks after the trauma, regenerative endodontic treatment (RET) of both central incisors was initiated by cleaning and disinfecting the root canal. The RET treatment was finalized a month later according to the protocol previously described (23). This report will focus on the RET outcome for tooth 21. Clinical and radiographic follow-up 2.5 years post RET showed a successful treatment outcome as demonstrated by the absence of any signs of inflammation and the progressive obliteration of the root canal space (Figure 3 A-J).

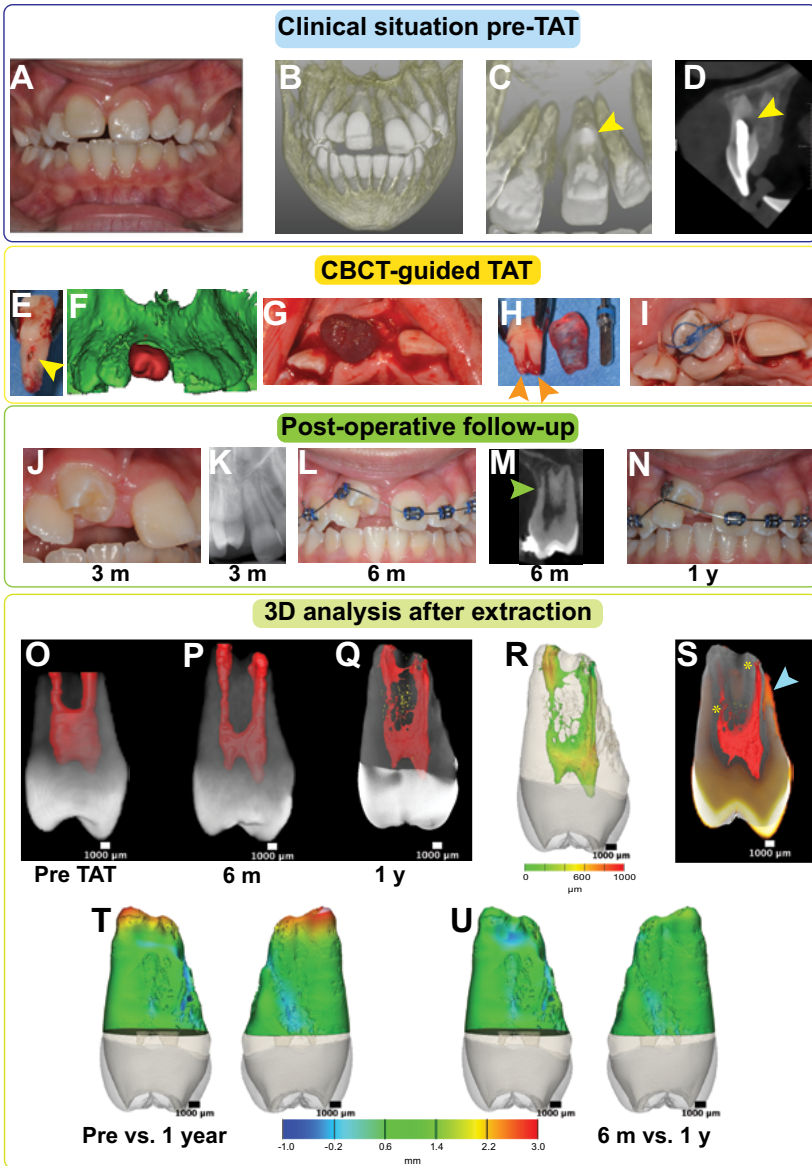


Figure 1: Case 1 (TAT), (A, B) clinical and radiological presentation of ankylotic tooth 11, (C, D) root resorption at the palatal surface (yellow arrowheads), (E) confirmation of the resorption lesion after extraction, (F-I) the surgical process of CBCT-guided TAT, (H) intact apical papilla at TAT (orange arrowheads), (J-N) clinical and radiological follow-up till 1-year post-TAT, (M) detection of ankylosis and replacement resorption at 6 months post-TAT, (O-Q) 3D reconstruction of the transplanted tooth from CBCT scans pre-TAT (O), at 6 months post-TAT (P), and from the nano-CT scan at 1-year post-TAT. (R) colour coded map for the root canal system thickness (mean= 269.4 $\mu\text{m} \pm 381.7$), (S) superimposition of the pre-TAT image (in orange colour) on the nano-CT image 1-year post-TAT (in grey values) showing the extent of root resorption (blue arrowhead) and highlighting the newly formed dentin post-TAT (yellow asterisks), (T, U) surface distance maps for root tissue change post-TAT.

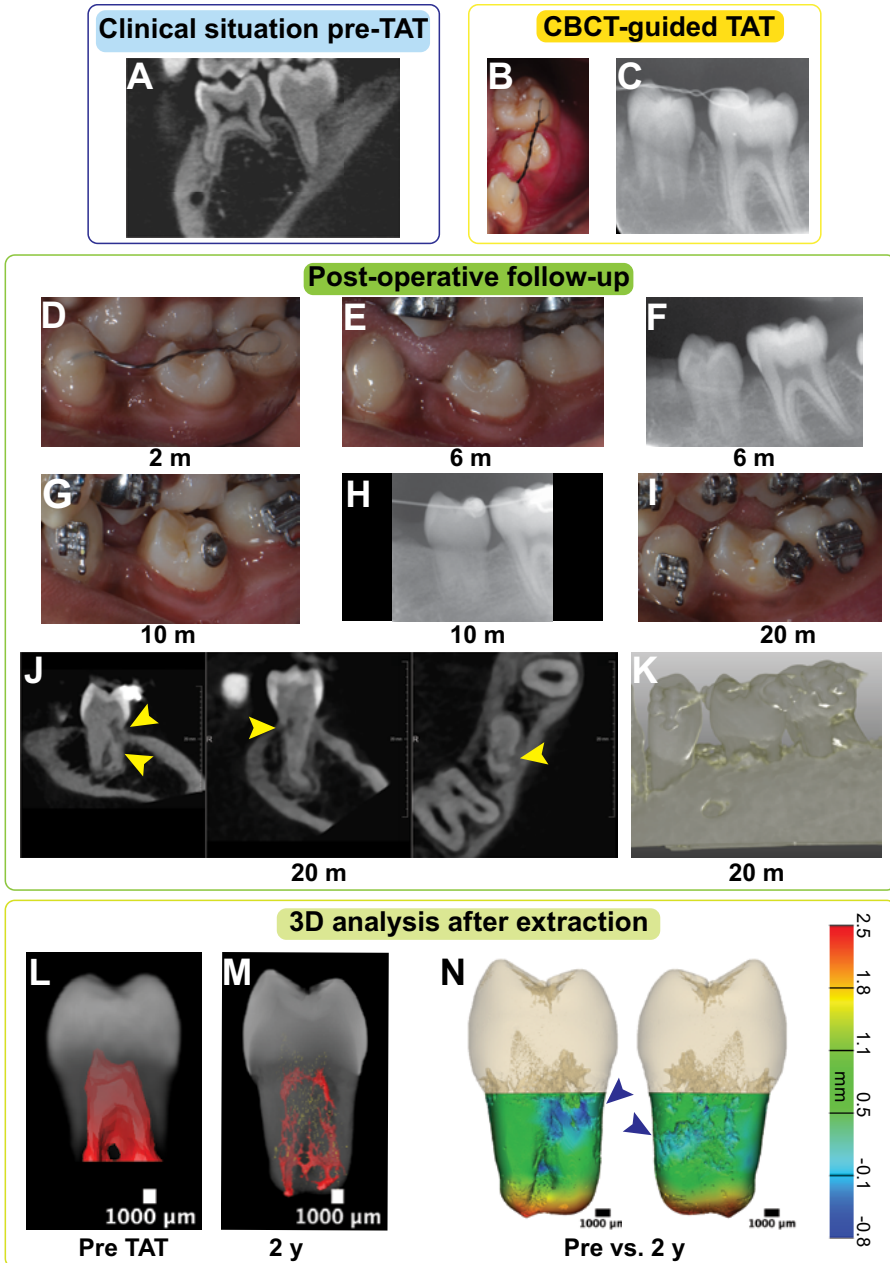


Figure 2: Case 2 (TAT), (A) a 10 years-old girl with agenesis of the 2 premolars, (B-C) directly after TAT of tooth 15 to the site of tooth 35, (D-I) clinical and radiological follow-up till 20 months post-TAT, (J, K) detection of ankylosis and replacement resorption at 20 months post-TAT, (L, M) 3D reconstruction of the transplanted tooth and root canal system from CBCT scans pre-TAT (L), and from the nano-CT scan at 2 years post-TAT, (N) surface distance maps for root tissue change post-TAT.

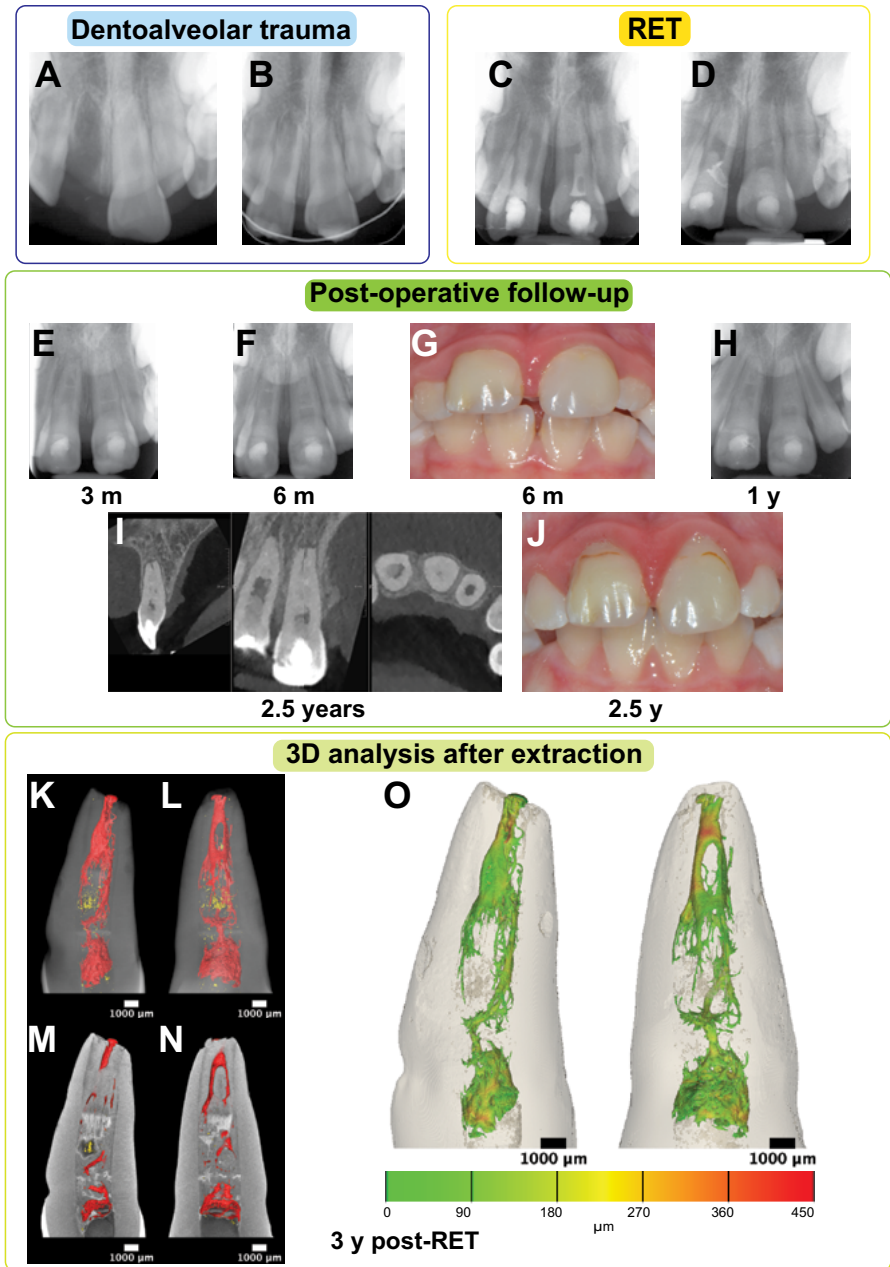


Figure 3: Case 3 (RET), (A, B) an 8 years-old girl presenting with a dentoalveolar trauma on teeth 11 & 21. (C, D) RET, (E-J) clinical and radiological follow-up of tooth 21 till 2.5 years post-RET, (K, L) 3D reconstruction of tooth 21 from the nano-CT scan at 3 years post-RET, note the 3D interconnected root canal system (in red) and the porosity inside newly formed tissue (in yellow), (M, N) longitudinal sections are highlighting the newly formed tissue post-RET, (O) colour-coded map for the root canal system thickness (mean= 82.1 μm \pm 63.3).

- 112 Three years post-RET, within the orthodontic treatment, it was decided to extract the two maxillary central incisors in addition to two lower premolars. After informed consent, the extracted tooth 21 was immediately fixed in 4% paraformaldehyde for further studies.

Nanofocus X-ray computed tomography

CT images were acquired on a submicrometric resolution CT device (Nanotom, GE Phoenix, Blomberg, Germany). Samples were positioned on a sample holder on the rotary table, ensuring that the longitudinal axis coincided with the rotary axis. Scanning was performed over 360° with a step size of 0.7°. All scans were obtained using a tungsten target applying an operating voltage of 65 kV and a current of 320 mA during a 500 ms exposure time. A 0.5 mm aluminium filter was used, and an isotropic voxel size of 8.5 µm could be reached. The projected radiographs were reconstructed in cross-sectional images in a commercial software package (Phoenix datosx, GE Phoenix, Germany).

Image processing and 3D analysis

Pre-operative cone-beam computed tomography (CBCT) scans and nano-CT scans were imported into MeVisLab (MeVis Medical Solutions AG, Bremen, Germany). All teeth were then segmented using a dedicated tool developed in MeVisLab and validated for accurate tooth/root canal space segmentation as described (23) to create a mask image including hard tissue and root canal space. For each tooth, the segmented nano-CT image was then spatially aligned to the segmented pre-operative CBCT image using the dentin-enamel and the cement-enamel junctions as alignment landmarks and maximization of mutual information as a registration metric (29). All segmented images were normalized using a non-local means filter to suppress any noise and decrease confounding variables between the images. Two segmentation algorithms were applied to separate tooth hard tissue and root canal space. The first step applied interval thresholding for the segmentation of the hard tissue and porosity within the dentin and was performed in Amira image analysis software (Amira, Thermo Fisher Scientific, USA). The second step applied semi-automatic user-guided 3D active contour segmentation using level-set methods (30), available in the ITK-SNAP tool kit (www.itksnap.org) (30) for the segmentation of the root canal space. In the first step, a probability map was computed by applying a one-sided smooth threshold once for the root canal space. In a second step, the segmentation was initialized by placing one or more spherical seeds in the region of interest (root canal). The last step was specifying the weights of the various terms in the active contour evolution partial differential equation (PDE) and running the evolution interactively (30). The 3D triangle-based sur-

face of both hard tissue and the root canal space was reconstructed. The root hard tissue volume (RV) was calculated by measuring from the cement-enamel junction (CEJ) to the apex at different time points. Morphological quantification was performed in 3matic (Materialise; Leuven, Belgium).

Histological processing

The chemically fixed teeth were demineralized (4–6 weeks) with 10% formic acid (Chem-Lab Analytical, Zedelgem, Belgium) with the decalcifying solution refreshed every three days. The decalcification endpoint was determined by dental radiography (MINRAY, Soredex, Tuusula, Finland) and visual/tactile evaluation. After decalcification, the teeth were immersed in water for 24 h and then dehydrated in ascending concentrations of ethanol (70% for 12 h, 80%, 95% and 100% for two h each), followed by xylene (VWR) clearance. The teeth were next immersed in liquid paraffin (56 °C melting point; Paraclean, Klinipath, Duiven, The Netherlands) for 24 h before being embedded in paraffin blocks. Serial paraffin sections were cut with a thickness of 5–7 µm using a microtome (Microm HM 360 Microtome, Hyland Scientific, Stanwood, WA, USA). For every ten sequential sections, two sections were selected for staining. One section with Gill'sIII hematoxylin (Leica Microsystems, Diegem, Belgium) and with 1% aqueous eosin solution (Leica Microsystems), while the other section was stained with Masson trichrome staining. The stained sections were examined using light microscopy (Axio Imager M2, Carl Zeiss Microscopy, Germany).

Immunostaining

Nestin immunostaining was performed using a mouse monoclonal antibody to nestin (ab22035, Abcam, UK) at 1/200 concentration. The signal was revealed using the BOND polymer refine detection system kit (Leica). Diaminobenzidine (DAB) immunostaining was performed for neurofilament (NF) (2f11, Dako, Agilent USA) at 1/500, and CD 90 (ab181469, Abcam, UK) at 1/200.

Second-harmonic generation imaging

To examine the structure of the pulp-dentin complex and the patterns of collagen deposition, Z-stacks of fixed, demineralized, unstained sections were acquired on a laser scanning confocal microscope (LSM 780, AxioObserver, Carl Zeiss Microscopy, Germany) using a water-immersion 25x objective (NA 0.8, Carl Zeiss Microscopy, Germany). A tunable Mai Tai DeepSee Titanium-Sapphire femtosecond laser (680-1050 nm; Spectra-Physics) was used for 2-photon-autofluorescence (2PAF) imaging and second harmonic generation

114 (SHG) imaging with an excitation wavelength of 850 nm. 2PAF was detected at 500-550 nm (green channel), the forward SHG signal was detected at 380-430 nm (yellow channel), the backward SHG signal was detected at 420-480 nm (red channel). Images were acquired with BiG (GaAsP) non-descanned detectors (Carl Zeiss Microscopy, Germany), in the forward and backward detection beam paths, respectively. An air condenser (NA 0.55) was used for recording the second harmonic signals. Extended depth of focus (maximum projections) was performed in Zen desk software (Carl Zeiss Microscopy, Germany). Images were adjusted for brightness and contrast.

RESULTS

Figure 4 shows the typical morphology of the pulp-dentin complex. The core of the pulp consisting of loose connective tissue free of inflammation, with abundant cells and neurovascular bundles (Figure 4A). At the interface with the dentin, an aligned layer of odontoblasts extending their processes into tubules running uninterruptedly through predentin into the dentin (Figure 4A-D). The pulp-dentin complex's architecture and collagen deposition pattern can be appreciated using SHG imaging (Figure 4B, E & I). The pattern of nestin staining in a normal pulp is shown in (Figure 4C). Masson trichrome staining (MTC) highlights the numerous neurovascular bundles inside the pulp (Figure 4G & H). The appearance of neurofilament (NF) staining is shown in Figure 4F. The pattern of CD90+ staining in a normal pulp is shown in Figure 4J-L, note the presence of CD90+ cells only in the vicinity of the vasculature.

Case 1

The 3D analysis for the hard tissue change showed a net hard tissue gain of 54.5 mm³ (33.5 %) at 1-year post-TAT (Figure 1O & Q). From 6 months to 1-year post-TAT, the net hard tissue gain was 1.1 mm³ (0.5%) (Figure 1P & Q). Mapping root surface changes showed that at 1-year vs pre-TAT, the root surface resorption extended to -853.5 μm and the hard tissue gain extended to 3238.6 μm (mean= 333.5 μm) (Figure 1T). At 1-year vs six months, the root surface resorption extended to -1289.1 μm and the hard tissue gain extended to 1276.1 μm (mean= -26.4 μm) (Figure 1U). These measurements suggest that the bulk of root canal space obliteration and root maturation occurred in the first 6 months post-TAT, while the bulk of root surface resorption occurred in the last 6 months before the extraction. Finally, at 1-year post TAT, the average thickness of the root canal system was 269.4 μm (SD: 381.7) (Figure 1R).

Dentin formation post-TAT is marked with a calciotraumatic line visible on the nano-CT scan and the histological sections (Figure 5A-C). A striking

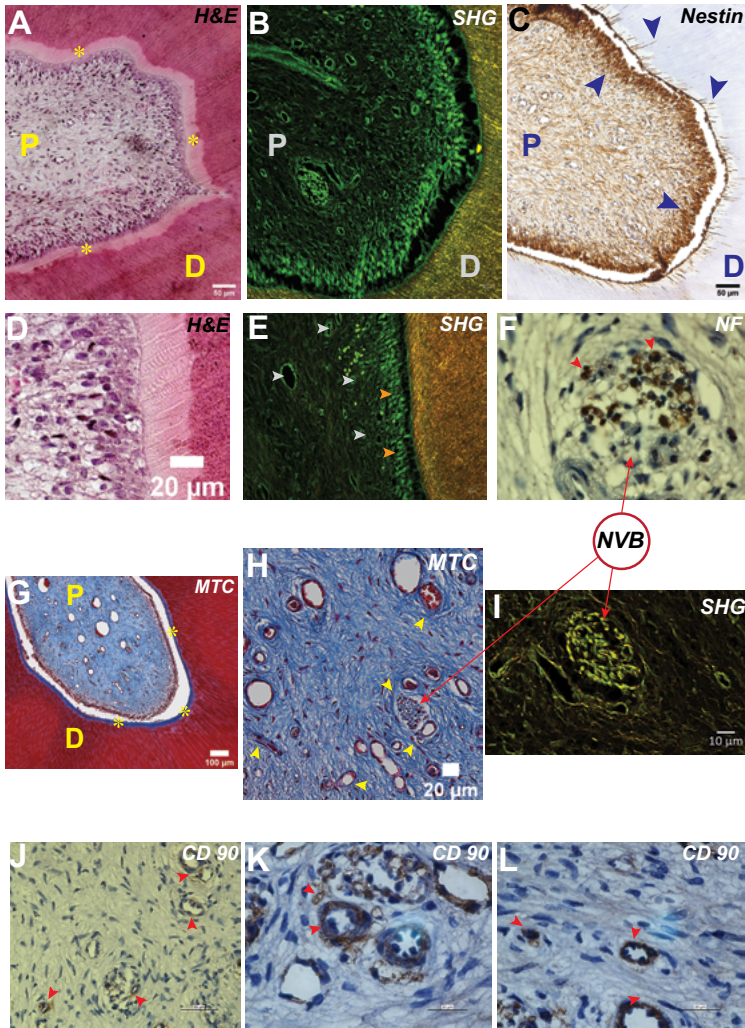


Figure 4: Morphology of the pulp-dentin complex from a maturity matched premolar as seen in different stains and imaging modalities, (A) hematoxylin and eosin (H&E) staining, dentin (D), pulp (P), and predentin (yellow asterisks), (B) second harmonic generation (SHG) label-less visualization of collagen and general tissue architecture, yellow is forward SHG signal indicating mainly collagen I showing an intense signal corresponding to intertubular dentin, red is backward SHG signal, green is 2-photon autofluorescence showing the fibrous architecture of the pulp, (C) nestin immunostaining showing an typical intense brown staining at the odontoblast layer as well as the processes that are extending through the predentin into the dentin (blue arrowheads), (D) H&E staining showing the organization of the odontoblasts, (E) SHG imaging showing the organization of the odontoblasts (orange arrowheads), extending their processes into the dentinal tubules that are surrounded by intertubular collagen (yellow & red color), while supported by a network of blood vessels in different sizes (grey arrows), (F) neurofilament (NF) immunostaining, (G) Masson's trichrome (MTC) staining, dentin (D), pulp (P), and predentin (yellow asterisks), (H) MTC staining highlighting the neurovascular bundles (yellow arrowheads) inside the dental pulp, (I) SHG imaging showing a neurovascular bundle inside the dental pulp, (J-L) CD90 immunostaining. Note the morphology of the neurovascular bundle (NVB) can be recognized clearly on MTC and SHG corresponding to NF immunostaining.

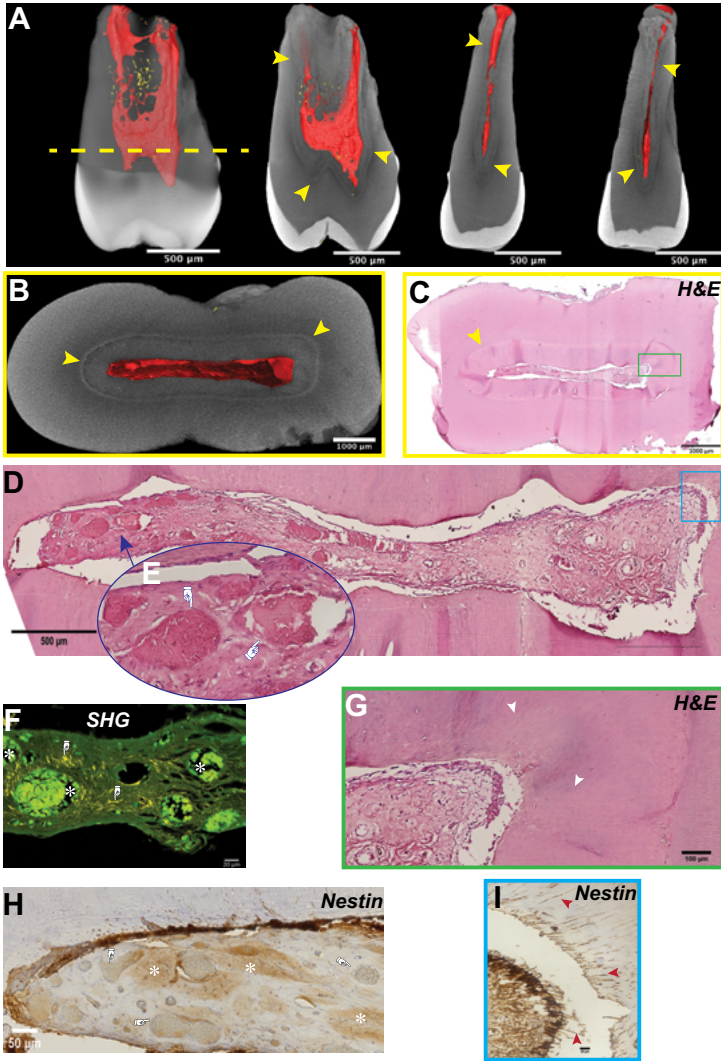


Figure 5: Case 1 (TAT), multimodality imaging for the pattern of pulp healing 1-year post-TAT. (A) 3D reconstruction of the transplanted tooth from the nano-CT scan 1 year post-TAT, and longitudinal sections showing the calciotraumatic line defining dentin formation post-TAT (yellow arrowheads), (B) nano-CT cross-section at the coronal third of the root corresponding to the dashed yellow line in (A), newly formed dentin originated from the canal walls (yellow arrowheads) towards the center of the pulp, (C) H&E stained section corresponding to (B), (D) healed pulp tissue 1 year post-TAT, (E) magnification for the section in D (blue arrow) showing progressive mineralization within the pulp, (F) SHG imaging for an area corresponding to (E & H) showing that the mineralization foci have a low collagen content (white asterisks), while patches of dense collagen are seen scattered over the pulp (pointing hand). (G) magnification for the green rectangle in (C) showing the structure of the healed pulp and the newly formed tubular reparative dentin (white arrow heads), (H) nestin immunostaining in an area corresponding to (E) showing patches of nestin positive staining (white asterisks), while the mineralization foci are weakly stained for nestin (pointing hand), (I) nestin immunostaining in an area corresponding to the blue rectangle in (D) showing a nestin positive functional odontoblast layer with processes extending into the dentin (red arrowheads).

loss of the typical pulp architecture is observed at the coronal third of the root (Figure 5D). The cell-rich connective tissue at the core of the pulp (Figure 4A, B & G) is replaced by a cell-poor vascularized fibrous connective tissue (dense collagen organization) (Figure 5D). Newly formed dentin is tubular dentin resembling reparative (tertiary) dentin (Figure 5G & I). Predentin is not present, and a nestin-positive odontoblast-like cell layer lines the interface between dentin and the pulp tissue (Figure 5H & I). Despite the presence of a nestin-positive odontoblast layer, the pattern of nestin staining diverges from the expected (Figure 4C). The distinct pattern of nestin decreasing gradient starting from the odontoblast layer to the core of the pulp (Figure 4C) is replaced by random patches of positive and negative nestin staining (Figure 5H).

Moreover, the mineralization foci are weakly stained for nestin (Figure 5H). These mineralization foci contain cells and seem to originate from the blood vessels walls (Figure 5D, E & H). This is further observed in the SHG imaging (Figure 5F) as they are characterized by a strong two-photon autofluorescence signal typical for cells. Interestingly the collagen I SHG forward signal is weak inside these foci and is seen as random patches in their vicinity (Figure 5F) corresponding to the nestin-positive tissue parts (Figure 5H).

The middle third of the root, at the transition from the primary dentin to the reparative (tertiary) dentin is atubular dentin with cell-containing lacune-like structures (Figure 6B-E). The pattern and direction of collagen deposition shifts at the transition from primary to newly formed dentin (Figure 6D & E). SHG imaging showed that dense unorganised collagen patches are observed at the transition and around the lacunes, followed by an intertubular collagen deposition pattern in a different orientation compared to the primary dentin (Figure 6E). The pulp is vascularized with very few cells (Figure 6F & G), with zones of dense fibres rich in collagen I resembling dentin (Figure 6F). Odontoblasts are present at the interface with odontoblast processes extending into the dentin without a predentin layer (Figure 6H & I).

At the beginning of the apical third of the root, two different patterns of dentin deposition are observed (Figure 7A-C). In the buccal root, a more organized reparative dentin (Figure 7F) and healed pulp tissue with a dense fibrous collagen network (Figure 7D & E) and an odontoblast-like cell layer is observed (Figure 7H). Within the palatal root, hard tissue resembling less organized atubular dentin with higher porosity is visualized (Figure 7 B & C). The healed pulp tissue within the buccal root shows two different zones as well, a zone with more cells and less dense collagen organization (Figure 7D & E) showing the highest nestin staining gradient at the odontoblast layer (Figure 7H). Remnants of peripheral nerve can be observed in (Figure 7G). Few cells within the

- 118 extracellular matrix (ECM) of the pulp show a weak CD90+ immunostaining. Further, periodontal tissue infiltration into the resorption lacunes is visible at this level (Figure 7B & C).

Case 2

The 3D analysis for the hard tissue change showed that there was a net hard tissue gain of 47.9 mm^3 (46.4%) at 2-years post-TAT (Figure 2L & M). Mapping root surface changes showed that at 2-year vs pre-TAT, the root surface resorption extended to $794.6 \text{ }\mu\text{m}$ and the hard tissue gain extended to $2523.4 \text{ }\mu\text{m}$ (mean= $280.0 \text{ }\mu\text{m}$) (Figure 2N). The average thickness of the root canal system was $102.8 \text{ }\mu\text{m}$ (SD: 82.2) (Figure 8D).

Tissue formation post-TAT is marked with a calciotraumatic line visible on the nano-CT scan and the histological sections (Figure 8B, C & F). The root canal space was filled with porous bone-like tissue (Figure 8A-E) with cells containing lacunes (Figure 8E) at the coronal and middle thirds. SHG imaging for the interface between the primary root dentin and the newly formed tissue showed a highly disordered collagen organization with cell-containing lacunes (Figure 8G).

At the apical third, traces of the root canal system can be found containing pulp tissue with several fibroblasts at its core and neurovascular bundles with surrounding reparative dentin showing dentinal tubules (Figure 8H & I). Further at the apex, the cells lining the dentin wall seem parallel to the dentin and not perpendicular to it (Figure 8J).

Case 3

Nano-CT images showed that the root canal space was filled with newly formed hard tissue three years post-RET (Figure 3M & N). A thin but interconnected 3D root canal system (pulp space) was observed within this newly formed hard tissue thanks to the segmentation strategy applied (Figure 3K & L). The average thickness of this root canal system was $82.1 \text{ }\mu\text{m}$ (SD: 63.3) (Figure 3O). Patches of dense mineralized tissue accompanied by well-defined porosities not connected to the root canal system were observed within the newly formed tissue starting from the middle third of the root down to the calcium silicate cement (Figure 9A).

Hard tissue formation post-RET is marked with a calciotraumatic line visible on the nano-CT images and the histological sections (Figure 9 A-C). At the transition from the primary dentin to the newly formed tissue, mineralized tis-

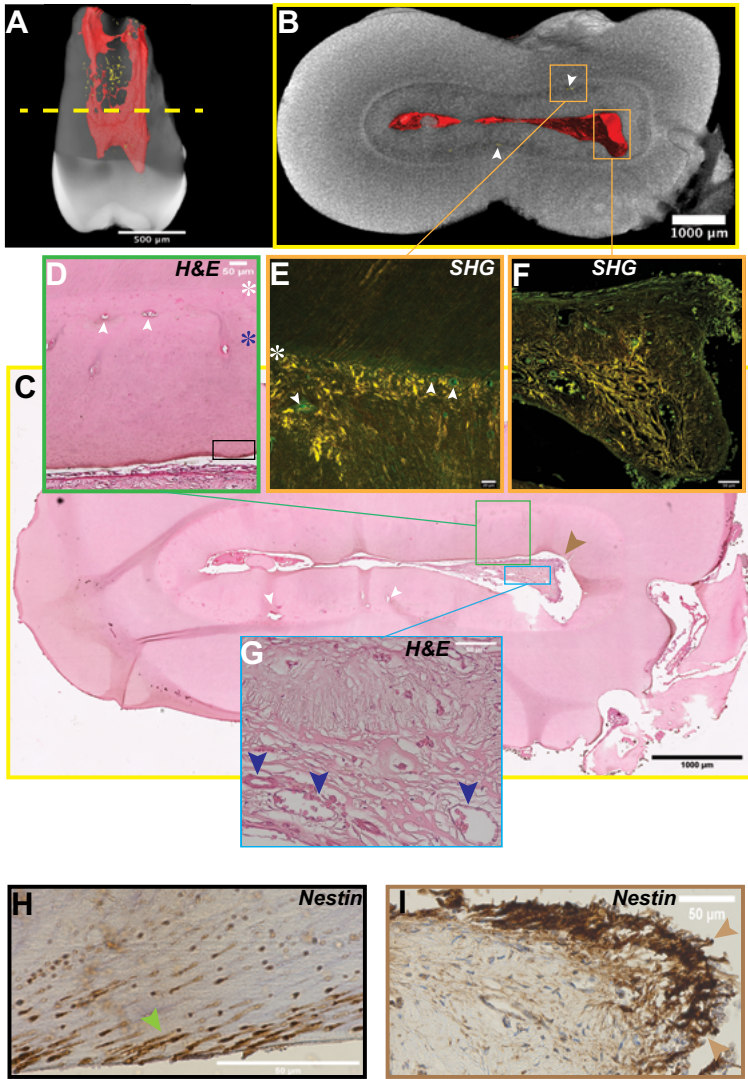


Figure 6: Case 1 (TAT), (A) 3D reconstruction of the transplanted tooth from the nano-CT scan 1-year post-TAT, (B) nano-CT cross-section at the middle third of the root corresponding to the dashed yellow line in (A), porosities at the transition from primary to newly formed dentin (white arrowheads), (C) H&E stained section corresponding to (B), (D) the transition from primary tubular dentin to atubular reparative dentin (white asterisk) then the transition to tubular reparative dentin (blue asterisk) running to the pulp, (E) SHG imaging for the interface between primary and reparative dentin showing cell containing lacunes (white arrowheads) at the transition (white asterisk) surrounded by patches of non-uniform collagen deposition (intense yellow signal) in contrast to an organized collagen deposition in the tubular reparative dentin zone, (F) SHG imaging showing the architecture of the healed pulp and dense collagen I deposition at the centre (intense forward SHG signal in yellow color), (G) vascularization within the core of the pulp (blue arrowheads), (H) magnification of the black rectangle in (D) showing positive nestin staining inside the dentinal tubules (green arrowhead), (I) pattern of nestin immunostaining in the healed pulp in area corresponding to the brown arrowhead in (C), note the positive stained odontoblast processes (brown arrowheads).

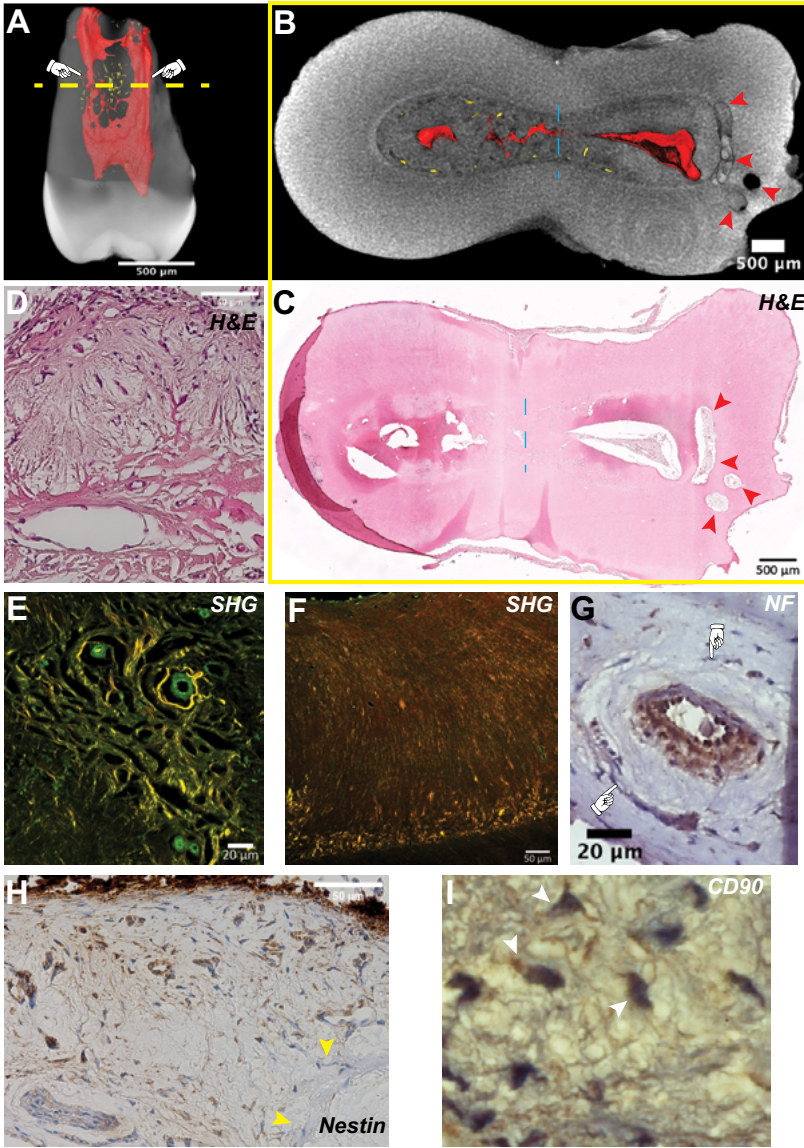


Figure 7: Case 1 (TAT), (A) 3D reconstruction of the transplanted tooth from the nano-CT scan 1-year post-TAT showing a different pattern of hard tissue deposition between the two roots (pointing hand), (B) nano-CT cross-section at the start of the apical third of the root corresponding to the dashed yellow line in (A), (C) H&E stained section corresponding to (B), the different pattern of hard tissue deposition marked by the dashed blue line in (B & C), and resorption lacunae are visible at this level (red arrowheads) (B & C), (D) different tissue organization within the healed pulp, (E) SHG imaging showing the dense fibrous collagen I structure within the core of the pulp (intense forward SHG signal in yellow color), (F) pattern of collagen deposition in the full width of the newly formed dentin, note the prominent appearance of the backward SHG signal (red colour) indicative of immature collagen, (G) remnants of peripheral nerve within the healed pulp tissue, (H) pattern of nestin immunostaining within the healed pulp, note that the signal almost vanishes in the area close to the dense fibrous collagen deposits (yellow arrowheads), (I) weak CD90⁺ staining for cells within the ECM of the pulp (white arrowheads).

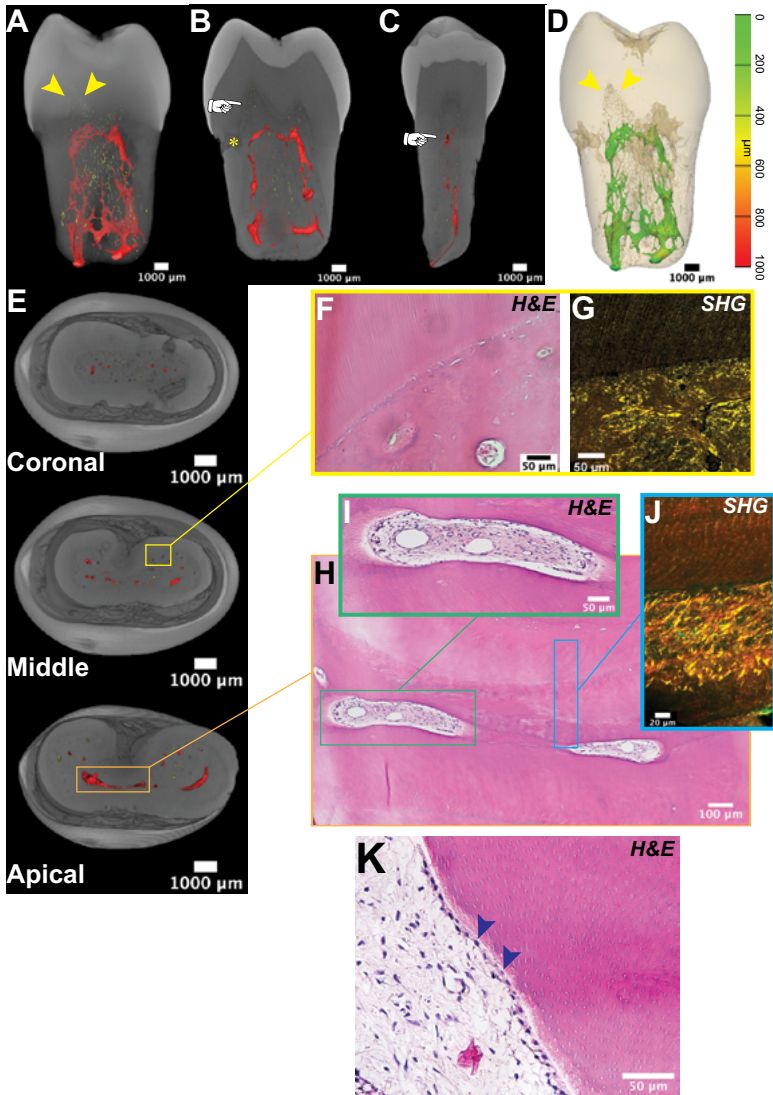


Figure 8: Case 2 (TAT), multimodal imaging for the pattern of pulp healing 2 years post-TAT, (A) 3D reconstruction of the transplanted tooth from the nano-CT scan 2 years post-TAT, original pulp chamber outline (yellow arrowheads), (B, C) longitudinal sections showing the calcitropic line defining dentin formation post-TAT (pointing hand), and resorption lacunes (yellow asterisk), (D) color coded map for the root canal system thickness (mean= 102.8 μm ±82.2), newly formed hard tissue is marked by high porosity (yellow arrowheads), (E) nano-CT cross-sections from the coronal, middle and apical thirds of the root demonstrating the nature of the newly formed hard tissue, (F) the interface between primary dentin and newly formed hard tissue, (G) SHG imaging for the interface showing the difference in the collagen deposition pattern, (H) traces of the root canal system at the apical third, (I) loose connective pulp-like tissue within the canal in the apical third, (J) different patterns of collagen deposition varying between organized inter-tubular collagen to un-organized dense collagen deposits surrounding cell containing lacunes, (K) pulp-like tissue at the apex, note the parallel orientation of the cells lining the dentin wall (blue arrows).

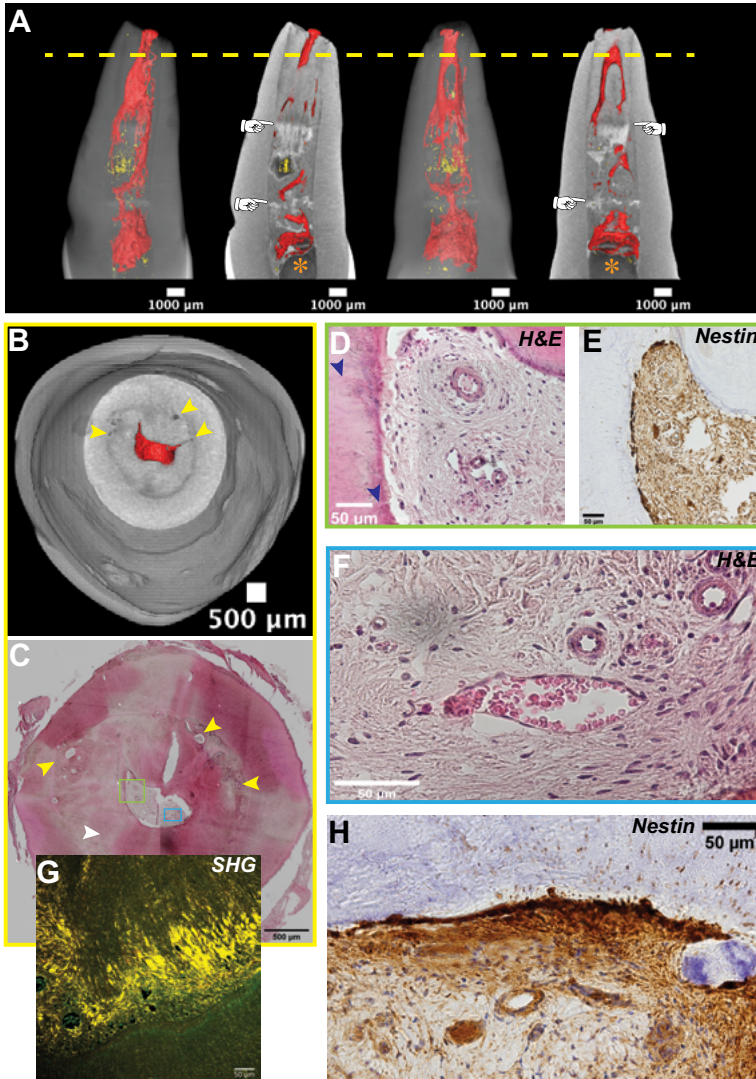


Figure 9: Case 3 (RET), multimodality imaging for the pattern of pulp healing 3 years post-RET, (A) 3D reconstruction of the transplanted tooth from the nano-CT scan 3 year post-RET, and longitudinal sections showing the calciotraumatic line defining hard tissue formation post-RET showing zones of different intensities and porosities (pointing hands), (B) nano-CT cross-section at the apical third of the root corresponding to the dashed yellow line in (A), (C) H&E stained cross-section corresponding to (B), showing different patterns of hard tissue deposition (yellow and white arrowheads), (D) magnification for the green square in (C) showing vascularized pulp-like tissue lined by tubular reparative dentin (blue arrowheads), (E) nestin immunostaining for an area corresponding to (D) showing nestin positive odontoblast-like cells lining the newly formed dentin, (F) magnification for the blue rectangle in (C) showing neurovascular bundles in different sizes and fibroblasts within the core of the newly formed pulp tissue, (G) SHG imaging for the interface between primary dentin and reparative dentin showing cell containing lacunes surrounded with dense collagen deposition followed by inter-tubular collagen deposition that has a similar deposition direction to the collagen in the primary dentin, (H) pattern of nestin immunostaining within the newly formed pulp, note the absence of the predentin.

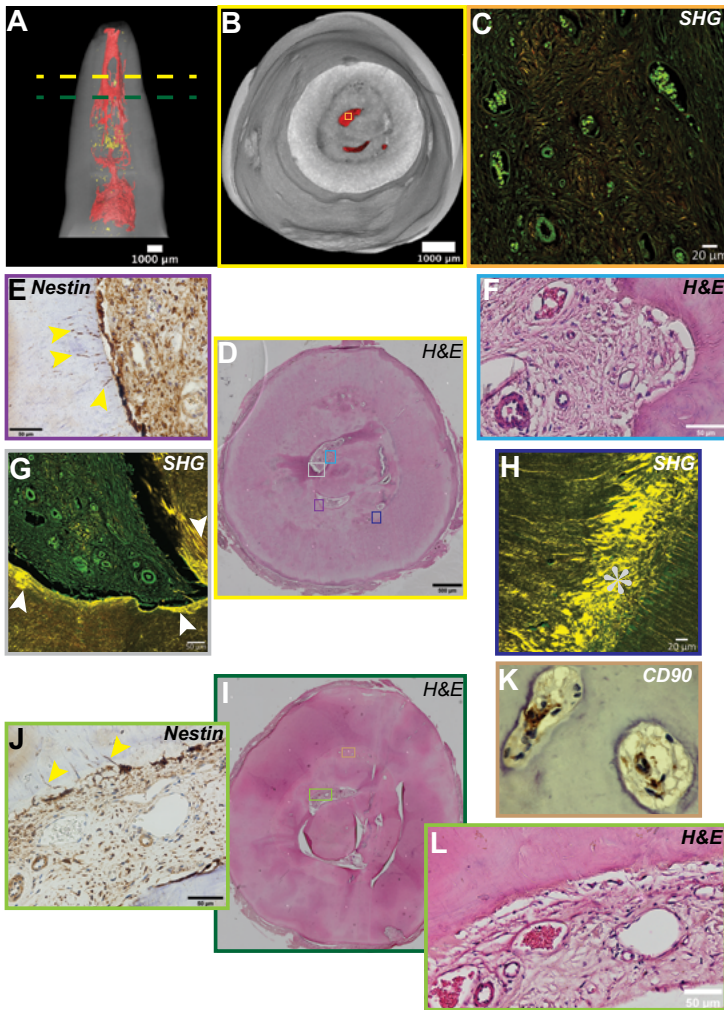


Figure 10: Case 3 (RET), (A) 3D reconstruction of the nano-CT scan 3-year post-RET, (B) nano-CT cross-section of the root corresponding to the dashed yellow line in (A) showing the calciotraumatic line defining hard tissue formation post-RET, (C) SHG imaging of the pulp core of an area corresponding to the orange square in (B), showing the architecture of the newly formed pulp tissue with several neurovascular bundles and areas of dense collagen I deposition (forward SHG signal in yellow colour), (D) H&E stained cross-section corresponding to (B), (E) nestin immunostaining for an area corresponding to the purple rectangle in (D), showing an odontoblast-like layer with processes extending into the newly formed dentin, (F) magnification of the blue rectangle in (D) showing a loose connective tissue rich in cells, with cells lining tubular dentin (yellow arrowhead), (G) SHG of an area corresponding to the grey rectangle in (D) showing a dense collagen deposition parallel to the root canal wall (white arrowheads), (H) SHG of an area corresponding to the blue rectangle in (D) showing dense collagen deposition at the transition from primary to newly formed dentin (white asterisk), (I) H&E stained cross-section corresponding to the dashed green line in (A), (J) nestin immunostaining for an area corresponding to the green rectangle in (I), showing a functional odontoblast-like cell layer with processes extending into the newly formed dentin and a nestin staining pattern very similar to normal, (K) magnification of the orange rectangle in (I), showing the presence of CD90⁺ cells, (L) magnification of the green rectangle in (I), showing the architecture of the newly formed tissue.

124 sue with lacune like structures was observed (Figure 9 B, C & G). SHG showed very dense collagen deposits surrounding these cells containing lacunes (Figure 9G). Moving towards the root canal space, another transition can be observed to tubular dentin like tissue (Figure 9C &G) originating from the root canal space (Figure 9D). The direction of collagen deposition deviates slightly from the primary dentin (Figure 9G). Inside the root canal space, a de-novo pulp-like tissue (Figure 9D) consists of connective tissue free of inflammation, with cells and neurovascular bundles (Figure 9D & F). At the newly formed dentin interface, a layer of nestin positive odontoblast-like cells, extending their processes into tubules running into the dentin were observed (Figure 9E). The cells lining the newly formed dentin seem to have an almost parallel, not perpendicular orientation to the dentin (Figure 9 D & E). The gradient of nestin staining in the de-novo pulp tissue (Figures 9E & G) resembles the control tooth (Figure 4C).

Figure 10 shows sections towards the middle third of the root. Similar hard tissue formation patterns to the apical third are observed (Figure 10B, D & I). At the root canal space, de-novo pulp-like tissue can be observed with numerous neurovascular bundles (Figure 10C, F, G & L). Although fewer than in a normal pulp, nestin positive odontoblast like cells can be observed lining the newly formed tissue with extended processes into the tubules (Figure 10E & J). The cell containing lacunes at the transition from primary to reparative dentin contain CD90+ cells. SHG imaging showed that at the transition from primary dentin to the newly formed dentin dense unorganized collagen patches are observed, followed by an intertubular collagen deposition almost in the same direction as the primary dentin collagen (Figure 10H). Moreover, a dense collagen layer can be observed lining the root canal walls (Figure 10G).

Discussion

The healing capacity of the pulp-dentin complex is a fascinating process that is not yet fully understood. For TAT, the mainstream theory is that the pulp tissue will undergo a process of sterile necrosis followed by replacement by new tissue (15). The healing process could also involve invading periodontal ligament (PDL)-derived stromal cells accompanied by cementum deposition on the root canal walls or even bone invasion (14, 16, 31). This process is supported by revascularization, reaching the entire length of the pulp 30 days post-replantation or transplantation (17). However, it was not shown when this process starts precisely. The exact mechanism of this revascularization is highly speculative, and end-to-end anastomoses were hypothesized (17). Moreover, this process should involve the immune system through the infiltration of neutrophils followed by macrophages to eliminate the dead cells and be followed by a shift from inflammation to repair/regeneration to reach a healed pulp. The

mechanism of new pulp tissue formation and the source of cells repopulating the pulp was not fully explained in the pioneer's (15-17).

With the current knowledge regarding the apical papilla, it was shown to be the driving force behind tooth root growth and maturation. Stem cells of the apical papilla (SCAPs) show the capacity to differentiate into odontoblasts and adipocytes. Moreover, SCAPs have shown a higher proliferative, migratory, and mineralized matrix deposition compared to dental pulp stem/stromal cells (DPSCs) (32). It is hypothesized that SCAPs might be the source of primary odontoblasts that form primary dentin of the tooth root (33), while DPSCs are the source of the cells replacing odontoblasts and producing reparative dentin (7). Therefore, in the mainstream hypothesis that all cells within the pulp are replaced by new cells, these new cells might be originating from the apical papilla.

A second hypothesis, originating from tooth replantation studies in small animal models, suggests the involvement of immunocompetent cells in replacing the degenerated odontoblast layer to form odontoblast-like cells capable of producing reparative dentin (34, 35). Class II major histocompatibility complex (MHC) antigen-presenting cells present in the dental pulp play a significant role in response to stress or bacterial invasion (36). MHC antigen-presenting cells are in the sub-odontoblast layer and the vicinity of the blood vessels in the pulp (34-36). Heat shock protein (HSP) 25, highly expressed in the odontoblasts (19), is thought to be released upon stress conditions such as hypoxia, typical after TAT, recruiting antigen-presenting cells to the site of injury (34). Furthermore, evidence from the *ex-vivo* tooth model studies suggests that DPSCs survive up to 4 weeks inside the pulps of extracted immature wisdom molars when suspended in a culture medium (37). After an induced injury to the odontoblasts, DPSCs migrated from the vicinity of the blood vessels to form reparative dentin (38-40). Therefore, it might be possible that not all cells inside the pulp will degenerate after TAT. Other cell populations such as immune cells or dental pulp stromal cells could be migrating from their niches to form a *de-novo* odontoblast layer along the root canal walls.

In the current report, the pulp healing patterns within the two TAT cases were different. In the first case, the reparative dentin formation appeared to originate from the canal walls towards the centre of the pulp with the presence of an odontoblast like cell layer at the interface with the pulp tissue. In the second case, the healing can be described as lamellar arranged cellular hard tissue along the dentinal wall and progressively filling the root canal up to the apical third without an odontoblast-like layer. In the first case, loss of typical pulp architecture can be observed with mineralization foci that seem to be

126 originating from the core of the pulp from the blood vessels. In the second case, pulp-like tissue could be observed at the most apical part of the root. It is possible that the difference is related to the period post-TAT (1 year vs 2 years) and that the pulp of case 1 will resemble case 2 at the coronal and middle thirds when it is completely obliterated at 2 years. Our observations are in line with the observations from the replantation and transplantation studies in large animal models (14, 16). Skoglund et al., observed a pulp with a typical morphologic structure only in 2 teeth out of 15 teeth 6 months post-replantation/transplantation of dogs' incisors (16). In the other 13 teeth, the pulp was described as connective tissue deficient in cells and blood vessels and devoid of odontoblasts.

Furthermore, the pulp space contained large cells containing hard tissue deposits in addition to the accumulation of macrophages (16). However, it must be noted that no immunostaining was performed in that study. In the current report, a nestin-positive odontoblast-like cell layer was observed at the boundary of the pulp. Nestin is expressed only in functional and differentiated odontoblasts (41, 42). Moreover, nestin expression is upregulated in odontoblasts surrounding injury sites to respond by laying down reparative dentin (38, 39, 41). Either these cells migrated from the apical papilla, immunocompetent cells or DPSCs migrating from the core of the pulp, they have differentiated into functional odontoblasts and secreted dentin. Fiane et al., reported histological outcomes of replanted immature and mature premolars in humans (22). In both immature and mature premolars, an initial degeneration of the odontoblast layer and loss of vasculature and typical pulp structure was observed after 3 weeks.

Further, in the immature teeth, revascularization and reparative dentin formation were evident after 6 weeks. After 6 months, complete pulp obliteration in the coronal part was observed with traces of pulp tissue with a typical architecture, including a predentin layer (22). In our study, we did not observe a predentin layer.

Kristerson et al., reported extensive dentin formation after revascularization of replanted incisors in monkeys after 9 months. The average daily dentin formation was 4 μ m as measured from histology sections (14). The current report observed a 34% and 48% gain in root hard tissue volume starting from the cemento-enamel junction after 1 year and 2 years, respectively. It was hypothesized that this accelerated dentin production is because of a loss of pulp tissue's autonomic and/or sensory nervous control (14, 31).

The RET-treated tooth in case 3 demonstrated a successful clinical outcome at 3 years. Nano-CT analysis showed that the newly formed tissue consisted of regions of different intensities and porosities (Figure 3M &N), suggesting a heterogeneous nature of the formed tissue. This is in contrast with previous reports on RET using μ CT imaging, where the newly formed tissue had a similar appearance to the native dentin (27). Our studies using H&E, SHG, and immunostaining showed that the newly formed tissues in case 3 represented osteodentin tissue, and dentin-like tissue with a distinct organization. The osteodentin was formed at the interface with the primary dentin, followed by a de-novo reparative tubular dentin towards the pulp.

Moreover, the newly formed dentin was lined with functional odontoblast-like cells. The core of the newly formed pulp showed a well-established vasculature. This is a unique finding as most of the previous reports on RET showed the formation of cementum-like tissue and un-organized mineralized tissue along the walls of the root canal with fibrous connective tissue without odontoblast-like cells (43-45). Austah et al., showed the presence of odontoblast-like cells lining the newly formed dentin (27). However, this was slightly different from the current report as the newly formed dentin was continuous with the primary dentin and had similar density and organization of tubules. In our study, the newly formed dentin resembled tertiary reparative dentin with fewer tubules and aligned odontoblasts.

The cells involved in pulp healing/regeneration in RET are thought to originate from the apical papilla, under the condition that it will survive the initial insult causing pulp necrosis (12, 46). Conditioning the root canal walls to release the growth factors trapped in the dentin and induction of bleeding into the root canal is hypothesized to provide a blood clot scaffold enriched with growth factors to induce SCAPs migration and subsequent differentiation into odontoblasts (12, 13, 27, 44, 46). Although the RET outcomes are highly variable clinically (23, 24, 47) and histologically (25, 27, 43-45, 48-51), they provide us with valuable insights into the mechanisms of pulp repair and regeneration.

The progressive root canal obliteration and the non-uniform tissue formation after RET may be result from the lack of an exogenous scaffold providing the appropriate guidance for cell/tissue organization (27). However, the same progressive obliteration is observed after TAT, where a nature-engineered pulp scaffold is present. Therefore, it seems that more profound research into the molecular mechanisms controlling odontogenesis and the healing of the pulp-dentin complex is needed. The application of RNA and single-cell sequencing in well-designed animal studies and tissue samples might unravel

128 novel key molecules involved in the process. Finally, from a clinical point of view, such pulp healing outcomes as reported in the current study are highly desirable, and result in a more robust tooth root structure with a close to normal dental pulp. Moreover, they bring us one step closer to the inspired aim of a biological tissue engineering-based treatment modality.

CONCLUSION

The current study provided insights into the patterns of dental pulp healing after TAT and RET. SHG imaging shed light on the patterns of collagen deposition during reparative dentin formation.

ACKNOWLEDGMENTS

The authors would like to thank Prof. Ghislain Opdenakker for his critical reading and correcting the manuscript. A special thanks to Mr. Tobie Martens for his assistance with the SHG imaging, and to Dr. Kathleen Van den Eynde, and Miss Eef Allegaert for their assistance with the nestin immunostaining.

REFERENCES

1. Akhlef Y, Schwartz O, Andreasen JO, Jensen SS. Autotransplantation of teeth to the anterior maxilla: A systematic review of survival and success, aesthetic presentation and patient-reported outcome. *Dent Traumatol.* 2018;34(1):20-7.
2. Andreasen JO, Hjørting-Hansen E. Replantation and autotransplantation of teeth. *Trans Int Conf Oral Surg.* 1970:430-3.
3. Czochrowska EM, Stenvik A, Albus B, Zachrisson BU. Autotransplantation of premolars to replace maxillary incisors: a comparison with natural incisors. *Am J Orthod Dentofacial Orthop.* 2000;118(6):592-600.
4. Denys D, Shahbazian M, Jacobs R, Laenen A, Wyatt J, Vinckier F, et al. Importance of root development in autotransplantations: a retrospective study of 137 teeth with a follow-up period varying from 1 week to 14 years. *Eur J Orthod.* 2013;35(5):680-8.
5. Kafourou V, Tong HJ, Day P, Houghton N, Spencer RJ, Duggal M. Outcomes and prognostic factors that influence the success of tooth autotransplantation in children and adolescents. *Dent Traumatol.* 2017;33(5):393-9.
6. Andreasen JO, Hjørting-Hansen E. Replantation of teeth. II. Histological study of 22 replanted anterior teeth in humans. *Acta Odontol Scand.* 1966;24(3):287-306.
7. Gronthos S, Mankani M, Brahmi J, Robey PG, Shi S. Postnatal human dental pulp stem cells (DPSCs) in vitro and in vivo. *Proc Natl Acad Sci U S A.* 2000;97(25):13625-30.
8. Andreasen JO, Paulsen HU, Yu Z, Bayer T. A long-term study of 370 autotransplanted premolars. Part IV. Root development subsequent to transplantation. *Eur J Orthod.* 1990;12(1):38-50.
9. Andreasen JO, Paulsen HU, Yu Z, Bayer T, Schwartz O. A long-term study of 370 autotransplanted premolars. Part II. Tooth survival and pulp healing subsequent to transplantation. *Eur J Orthod.* 1990;12(1):14-24.
10. Andreasen JO, Paulsen HU, Yu Z, Schwartz O. A long-term study of 370 autotransplanted premolars. Part III. Periodontal healing subsequent to transplantation. *Eur J Orthod.* 1990;12(1):25-37.

11. Shahbazian M, Jacobs R, Wyatt J, Denys D, Lambrichts I, Vinckier F, et al. Validation of the cone beam computed tomography-based stereolithographic surgical guide aiding autotransplantation of teeth: clinical case-control study. *Oral SurgOral MedOral PatholOral Radiol.* 2013;115(5):667-75.
12. Hargreaves KM, Diogenes A, Teixeira FB. Treatment options: biological basis of regenerative endodontic procedures. *J Endod.* 2013;39(3 Suppl):S30-43.
13. Hargreaves KM, Giesler T, Henry M, Wang Y. Regeneration potential of the young permanent tooth: what does the future hold? *J Endod.* 2008;34(7 Suppl):S51-6.
14. Kristerson L, Andreassen JO. Autotransplantation and replantation of tooth germs in monkeys: Effect of damage to the dental follicle and position of transplant in the alveolus. *Int J Oral Surg.* 1984;13(4):324-33.
15. Skoglund A, Hasselgren G, Tronstad L. Oxidoreductase activity in the pulp of replanted and autotransplanted teeth in young dogs. *Oral SurgOral MedOral PatholOral Radiol.* 1981;52(2):205-9.
16. Skoglund A, Tronstad L. Pulpal changes in replanted and autotransplanted immature teeth of dogs. *J Endo.* 1981;7(7):309-16.
17. Skoglund A, Tronstad L, Wallenius K. A microangiographic study of vascular changes in replanted and autotransplanted teeth of young dogs. *Oral SurgOral MedOral PatholOral Radiol.* 1978;45(1):17-28.
18. Lee Y, Go EJ, Jung HS, Kim E, Jung IY, Lee SJ. Immunohistochemical analysis of pulpal regeneration by nestin expression in replanted teeth. *Int Endod J.* 2012;45(7):652-9.
19. Ohshima H, Nakakura-Ohshima K, Yamamoto H, Maeda T. Alteration in the expression of heat shock protein (Hsp) 25-immunoreactivity in the dental pulp of rat molars following tooth replantation. *Arch Histol Cytol.* 2001;64(4):425-37.
20. Panzarini SR, Okamoto R, Poi WR, Sonoda CK, Pedrini D, da Silva PE, et al. Histological and immunohistochemical analyses of the chronology of healing process after immediate tooth replantation in incisor rat teeth. *Dent Traumatol.* 2013;29(1):15-22.
21. Takamori Y, Suzuki H, Nakakura-Ohshima K, Cai J, Cho SW, Jung HS, et al. Capacity of dental pulp differentiation in mouse molars as demonstrated by allogenic tooth transplantation. *J Histochem Cytochem.* 2008;56(12):1075-86.
22. Fiane JE, Breivik M, Vandevska-Radunovic V. A histomorphometric and radiographic study of replanted human premolars. *Eur J Orthod.* 2014;36(6):641-8.
23. EzEldeen M, Van Gorp G, Van Dessel J, Vandermeulen D, Jacobs R. 3-dimensional analysis of regenerative endodontic treatment outcome. *J Endod.* 2015;41(3):317-24.
24. Meschi N, EzEldeen M, Torres Garcia AE, Jacobs R, Lambrechts P. A Retrospective Case Series in Regenerative Endodontics: Trend Analysis Based on Clinical Evaluation and 2- and 3-dimensional Radiology. *J Endod.* 2018;44(10):1517-25.
25. Meschi N, Hilkens P, Van Gorp G, Strijbos O, Mavridou A, Cadenas de Llano Perula M, et al. Regenerative Endodontic Procedures Posttrauma: Immunohistologic Analysis of a Retrospective Series of Failed Cases. *J Endod.* 2019;45(4):427-34.
26. Huang GT, Garcia-Godoy F. Missing Concepts in De Novo Pulp Regeneration. *J Dent Res.* 2014;93(8):717-24.
27. Austah O, Joon R, Fath WM, Chrepa V, Diogenes A, Ezeldeen M, et al. Comprehensive Characterization of 2 Immature Teeth Treated with Regenerative Endodontic Procedures. *J Endod.* 2018;44(12):1802-11.
28. EzEldeen M, Wyatt J, Al-Rimawi A, Coucke W, Shaheen E, Lambrichts I, et al. Use of CBCT Guidance for Tooth Autotransplantation in Children. *J Dent Res.* 2019;98(4):406-13.
29. Maes F, Collignon A, Vandermeulen D, Marchal G, Suetens P. Multimodality image registration by maximization of mutual information. *IEEE Trans Med Imaging.* 1997;16(2):187-98.
30. Yushkevich PA, Piven J, Hazlett HC, Smith RG, Ho S, Gee JC, et al. User-guided 3D active contour segmentation of anatomical structures: significantly improved efficiency and reliability. *Neuroimage.* 2006;31(3):1116-28.

31. Kristerson L, Andreasen JO. Influence of root development on periodontal and pulpal healing after replantation of incisors in monkeys. *Int J Oral Surg.* 1984;13(4):313-23.
32. Sonoyama W, Liu Y, Fang D, Yamaza T, Seo BM, Zhang C, et al. Mesenchymal stem cell-mediated functional tooth regeneration in swine. *PLoS One.* 2006;1:e79.
33. Volponi AA, Sharpe PT. The tooth -- a treasure chest of stem cells. *Br Dent J.* 2013;215(7):353-8.
34. Nakakura-Ohshima K, Watanabe J, Kenmotsu S, Ohshima H. Possible role of immunocompetent cells and the expression of heat shock protein-25 in the process of pulpal regeneration after tooth injury in rat molars. *J Electron Microsc (Tokyo).* 2003;52(6):581-91.
35. Rungvechvuttivittaya S, Okiji T, Suda H. Responses of macrophage-associated antigen-expressing cells in the dental pulp of rat molars to experimental tooth replantation. *Arch Oral Biol.* 1998;43(9):701-10.
36. Sotirovska Ivkowska A, Zabokova-Bilbilova E, Georgiev Z, Bajraktarova Valjakova E, Ivkovski L. Immunohistochemical study on antigen-presenting cells in healthy and carious human teeth. *Bratisl Lek Listy.* 2018;119(4):249-53.
37. Pedano MS, Li X, Jeanneau C, Ghosh M, Yoshihara K, Van Landuyt K, et al. Survival of human dental pulp cells after 4-week culture in human tooth model. *J Dent.* 2019;86:33-40.
38. Pedano MS, Li X, Camargo B, Hauben E, De Vleeschauwer S, Yoshihara K, et al. Injectable phosphopullulan-functionalized calcium-silicate cement for pulp-tissue engineering: An in-vivo and ex-vivo study. *Dent Mater.* 2020;36(4):512-26.
39. Téclès O, Laurent P, Aubut V, About I. Human tooth culture: A study model for reparative dentinogenesis and direct pulp capping materials biocompatibility. *Journal of Biomedical Materials Research Part B: Appl Biomater.* 2008;85B(1):180-7.
40. Téclès O, Laurent P, Zygouritsas S, Burger A-S, Camps J, Dejou J, et al. Activation of human dental pulp progenitor/stem cells in response to odontoblast injury. *Arch Oral Biol.* 2005;50(2):103-8.
41. About I, Laurent-Maquin D, Lendahl U, Mitsiadis TA. Nestin Expression in Embryonic and Adult Human Teeth under Normal and Pathological Conditions. *The Am J Pathol.* 2000;157(1):287-95.
42. Quispe-Salcedo A, Ida-Yonemochi H, Nakatomi M, Ohshima H. Expression patterns of nestin and dentin sialoprotein during dentinogenesis in mice. *Biomed Res.* 2012;33(2):119-32.
43. Lei L, Chen Y, Zhou R, Huang X, Cai Z. Histologic and Immunohistochemical Findings of a Human Immature Permanent Tooth with Apical Periodontitis after Regenerative Endodontic Treatment. *J Endo.* 2015;41(7):1172-9.
44. Meschi N, Hilkens P, Lambrichts I, Van den Eynde K, Mavridou A, Strijbos O, et al. Regenerative endodontic procedure of an infected immature permanent human tooth: an immunohistological study. *Clin Oral Investig.* 2016;20(4):807-14.
45. Torabinejad M, Faras H. A clinical and histological report of a tooth with an open apex treated with regenerative endodontics using platelet-rich plasma. *J Endod.* 2012;38(6):864-8.
46. Galler KM, Krastl G, Simon S, Van Gorp G, Meschi N, Vahedi B, et al. European Society of Endodontology position statement: Revitalization procedures. *Int Endod J.* 2016;49(8):717-23.
47. Chrepa V, Joon R, Austah O, Diogenes A, Hargreaves KM, Ezeldeen M, et al. Clinical Outcomes of Immature Teeth Treated with Regenerative Endodontic Procedures-A San Antonio Study. *J Endod.* 2020;46(8):1074-84.
48. Lui JN, Lim WY, Ricucci D. An Immunofluorescence Study to Analyze Wound Healing Outcomes of Regenerative Endodontics in an Immature Premolar with Chronic Apical Abscess. *J Endod.* 2020;46(5):627-40.
49. Martin G, Ricucci D, Gibbs JL, Lin LM. Histological findings of revascularized/revitalized immature permanent molar with apical periodontitis using platelet-rich plasma. *J Endod.* 2013;39(1):138-44.

50. Nosrat A, Kolahdouzan A, Hosseini F, Mehrizi EA, Verma P, Torabinejad M. Histologic Outcomes of Uninfected Human Immature Teeth Treated with Regenerative Endodontics: 2 Case Reports. *J Endod.* 2015;41(10):1725-9.
 51. Shimizu E, Ricucci D, Albert J, Alobaid AS, Gibbs JL, Huang GT, et al. Clinical, radiographic, and histological observation of a human immature permanent tooth with chronic apical abscess after revitalization treatment. *J Endod.* 2013;39(8):1078-83.
-

PART III

**The role of COAM in a chemokine-mediated
dental tissue regeneration**

CHAPTER 7

This chapter is based on the following publication

EzEldeen,M., Toprakhisar,B., Murgia,D., Smisdom,N., Deschaume,O., Bartic,C., Van Oosterwyck,H., Pereira,R.V.S., Opendakker,G., Lambrechts,I., Bronckaers,A., Jacobs,R., Patterson J. (2021). Chlorite oxidized oxyamylose differentially influences the microstructure of fibrin and self assembling peptide hydrogels as well as dental pulp stem cell behavior. Scientific Reports.

- (A) OMFS IMPATH Research Group, Faculty of Medicine, Department of Imaging and Pathology, KU Leuven and Oral and Maxillofacial Surgery, University Hospitals Leuven, Kapucijnenvoer 33, 3000 Leuven, Belgium
- (B) Department of Oral Health Sciences, KU Leuven and Paediatric Dentistry and Special Dental Care, University Hospitals Leuven, Kapucijnenvoer 33, 3000 Leuven, Belgium
- (C) Stem Cell Institute, KU Leuven, University of Leuven, Leuven, Belgium
- (D) Department of Surgical, Oncological and Oral Sciences, University of Palermo, Via Liborio Giuffrè 5, 90127 Palermo, Italy
- (E) Biomedical Research Institute, Hasselt University, Campus Diepenbeek, Agoralaan Building C, B-3590 Diepenbeek, Belgium
- (F) Soft-Matter Physics and biophysics section, KU Leuven, University of Leuven, Leuven, Belgium
- (G) Biomechanics Section, Department of Mechanical Engineering, KU Leuven, University of Leuven, Leuven, Belgium
- (H) Department of Microbiology, Immunology and Transplantation, Rega Institute for Medical Research, KU Leuven, University of Leuven, Leuven, Belgium
- (I) Department of Dental Medicine, Karolinska Institute, Stockholm, Sweden
- (J) IMDEA Materials Institute, Tecnogetafe, Calle Eric Kandel, 2, 28906 Getafe, Madrid, Spain
- (K) Prometheus Division of Skeletal Tissue Engineering, KU Leuven, University of Leuven, Leuven, Belgium

* Correspondence to Mostafa EzEldeen

+ These authors share senior authorship

Chlorite Oxidized Oxyamylose Differentially Influences the Microstructure of Fibrin and Self Assembling Peptide Hydrogels as Well as Dental Pulp Stem Cell Behavior

M. EzEldeen (A,B)*, B. Toprakhisar (C, G), D. Murgia (A,D), N. Smisdom (E), O. Deschaume (F), C. Bartic (F), H. Van Oosterwyck (G, K), R. Vaz Sousa Pereira (H), G. Opendakker (H), I. Lambrichts (E), A. Bronckaers (E), R. Jacobs (A,I)*, J. Patterson (A,J)*

ABSTRACT

Tailored hydrogels mimicking the native extracellular environment could help overcome the high variability in outcomes within regenerative endodontics. This study aimed to evaluate the effect of the chemokine-binding and antimicrobial polymer, chlorite-oxidized oxyamylose (COAM), on the microstructural properties of fibrin and self-assembling peptide (SAP) hydrogels. A further goal was to assess the influence of the microstructural differences between the hydrogels on the *in vitro* behavior of human dental pulp stem/stromal cells (hDPSCs). Structural and mechanical characterization of the hydrogels with and without COAM was performed by atomic force microscopy and scanning electron microscopy to characterize their microstructure (roughness and fiber length, diameter, straightness, and alignment) and by nanoindentation to measure their stiffness (elastic modulus). Then, hDPSCs were encapsulated in hydrogels with and without COAM. Cell viability and circularity were determined using confocal microscopy, and proliferation was determined using DNA quantification. Inclusion of COAM did not alter the microstructure of the fibrin hydrogels at the fiber level while affecting the SAP hydrogel microstructure (homogeneity), leading to fiber aggregation. The stiffness of the SAP hydrogels was 7-fold higher than the fibrin hydrogels. The viability and attachment of hDPSCs were significantly higher in fibrin hydrogels than in SAP hydrogels. The DNA content was significantly affected by the hydrogel type and the presence of COAM. The microstructural stability after COAM inclusion and the favorable hDPSCs' response observed in fibrin hydrogels suggest this system as a promising carrier for COAM and application in endodontic regeneration.

KEY WORDS

Dental pulp cells, dental pulp tissue engineering, fibrin hydrogels, self-assembling peptide hydrogels, atomic force microscopy

INTRODUCTION

Oral health plays an essential role in our daily lives, contributing to good overall health and wellbeing. Yet, impaired oral conditions have a high prevalence, affecting almost half of the world population (1). Dental pulp necrosis due to caries, trauma, or developmental anomalies is standardly treated by filling the root canal space with bio-inert plastic-like materials, thus depriving the tooth of vascularization, an immune response, and innervation. Immature teeth with pulp necrosis are rendered fragile even after treatment, and the roots fail to reach complete development.

While the classical regenerative medicine approach employs a combination of cells with biomaterials to promote tissue regeneration, the economic and regulatory hurdles associated with cell-based therapies have also led to the proliferation of cell-free biomaterial approaches, which stimulate the activity of endogenous stem cells. Therefore, regenerative endodontics can be approached either in a cell-free or cell-based manner (2-4) and has attracted attention attempting to restore tooth vitality (5). A cell-free clinical protocol intended to reestablish the pulp-dentin complex has been developed, which is known under the synonyms pulp revitalization, root-canal revascularization, or regenerative endodontic treatment (RET) (6-8). Nevertheless, RET has been associated with highly variable outcomes (9-11), and histologic studies have shown that true pulp regeneration using the current protocol is challenging to achieve (7, 11, 12).

Furthermore, a cell-based RET approach would utilize human dental pulp stem/stromal cells (hDPSCs), stem cells from human exfoliated deciduous teeth (SHED), or stem cells of the apical papilla (SCAPs). hDPSCs, SHED, and SCAPs are mesenchymal stem/stromal cells that possess the potential to differentiate into numerous cell types *in vitro*, including odontoblasts, osteoblasts, chondroblasts, adipocytes, and neuronal cells (13-15). The relative ease of accessibility from extracted wisdom molars or exfoliated primary teeth (16) renders them a valuable tool for studying and exploring tissue regeneration possibilities in the dentoalveolar and craniofacial regions.

Polymeric hydrogels are suitable candidates for tissue engineering and regenerative medicine (TERM) approaches, including dental pulp regeneration (17). The use of tailored hydrogels closely mimicking the native extracellular environment could help overcome the high variability in the RET outcomes. Many recent studies have demonstrated that cell behavior is strongly influenced by the cell microenvironment (18), which is dictated by the hydrogels' composition and microstructure (19, 20). Polymeric hydrogels can be natural (biopolymers), synthetic, or hybrids of the two (21, 22), with several advan-

tages and disadvantages related to each class (23). Fibrin is a typical natural hydrogel, and it has been extensively used as a biomaterial for different TERM and clinical applications (17, 22-24). Fibrin is a tailorable hydrogel system utilizing fibrinogen, thrombin, and Factor XIIIa. Fibrinogen, a soluble 340-kDa clotting factor, is enzymatically converted, in the presence of Ca^{2+} , into fibrin monomers by the protease thrombin (25). These fibrin monomers undergo self-assembly and lateral aggregation to form protofibrils that are packed into fibers forming branched fibrous networks (25). Factor XIIIa promotes the formation of covalent bonds between fibrinogen peptides to form a mesh network of fibrin fibers (22). The fibrous network and mechanical properties of fibrin can be tuned by altering the composition (26). For instance, higher concentrations of factor XIIIa result in increasing the stiffness of fibrin by catalyzing fibrin covalent crosslinking and compacting fibers (27). Moreover, fiber diameter and length are inversely proportional to thrombin concentration (22), whereas increasing factor XIIIa concentrations lead to increased packing of protofibrils within the fibers (27). Self-assembling peptide (SAP) hydrogels belong to the synthetic class and are produced using amino acids (28). These peptides self-assemble to form nanofibrous hydrogels in physiological conditions. This self-assembly depends on the specific amino acid sequence of the peptide. These scaffolds consist of >99% water, with fibers thought to be around 10 nm in diameter and 5 – 200 nm pores, closely mimicking the natural extracellular matrix (ECM) (28). Arginine-alanine-aspartic acid-alanine-16 (RADA-16) is a member of the self-assembling peptide family, consisting of 16 residues, and can undergo self-assembly to form nanofibers by forming stable β -sheet structures in physiological saline, which in turn form an interwoven nanofibrous hydrogel (29). The SAP (RADA-16) hydrogel has been used in several dental pulp tissue engineering studies with variable degrees of success (17, 30, 31).

This study aimed to evaluate the effect of the inclusion of a novel macromolecule, chlorite-oxidized oxyamylose (COAM), on the microstructural properties of tailored fibrin and SAP hydrogels. COAM is a polyanionic polysaccharide derivative that acts as an antibacterial (32) and antiviral agent (33, 34) and as an immunomodulator by interference with glycosaminoglycan (GAG) binding of chemokines (35). Further goals were to assess the influence of the microstructural differences between the hydrogels on the *in vitro* behavior of hDPSCs and to identify the most suitable hydrogel for further *in vivo* experiments.

MATERIALS AND METHODS

COAM synthesis, hydrogel composition, and preparation

Chlorite-oxidized oxyamylose (COAM) was synthesized by two-step oxidation of amylose, purified, and fractionated according to molecular weight (MW) as described previously (33, 36). COAM was endotoxin-free and used as MW mixture (corresponding to protein molecular equivalent weights exceeding 100 kDa).

Fibrin hydrogels were prepared by mixing fibrinogen and thrombin components in equal volumes (pH = 6.6), as described previously (22). Plasminogen-depleted fibrinogen (Enzyme Research Laboratories, USA), derived from human plasma, was dissolved in 20 mM HEPES and 150 mM NaCl (fibrinogen buffer). Sterile stock solutions of thrombin (Sigma, USA), derived from human plasma, and factor XIII (Fibrogammin, CSL Behring, Germany) were prepared in 20 mM HEPES, 150 mM NaCl, 40 mM CaCl₂, and 0.1% BSA (thrombin buffer). Thrombin and factor XIII were mixed with the thrombin buffer and were kept in a water bath at 37 °C for 30 min to activate factor XIII to factor XIIIa. The control fibrin hydrogels were prepared at 3.5 mg/ml fibrinogen, 0.1 U/ml thrombin, and 0.1 U/ml factor XIII, whereas the test fibrin hydrogels were prepared at 3.5 mg/ml fibrinogen, 0.1 U/ml thrombin, 0.1 U/ml factor XIII, and 1 mg/ml COAM.

SAP RADA-16 hydrogels were prepared according to the manufacturer's instructions by mixing the peptide solution (PuraMatrix Peptide Hydrogel, BD Biosciences, USA) with 20% sucrose solution followed by adding an equal amount of phosphate-buffered saline (PBS) for gelation. The control SAP hydrogels were prepared at 3.5 mg/ml RADA-16 peptide, whereas the test SAP hydrogels were prepared at 3.5 mg/ml RADA-16 peptide and 1 mg/ml COAM.

Structural and Mechanical Characterization

Atomic force microscopy (AFM)

AFM imaging was performed to characterize the microstructure of the different hydrogels at the fiber level. A 100 µl sample from each hydrogel composition (n=3) was deposited on a silica sample holder and incubated at 37 °C for 30 min. After gelation, the hydrogel's top surface was carefully removed using gentle air blowing/drying to allow the imaging of the internal network. Agilent 5500 with MAC III controller and JPK Nanowizard 3 AFM systems were used for morphological imaging in intermittent contact mode in air. A sharp microlever probe MSNL-F (f = 120 kHz, k = 0.6 N/m, tip radius of curvature < 12 nm) was used. The AFM topography images were leveled, line-corrected,

and measured (height and roughness profiles) using Gwyddion (37). A fiber extraction algorithm, ct-FIRE (38), was applied to the AFM images to characterize the fiber diameter, length, straightness, and alignment.

Scanning electron microscopy (SEM)

A 100 μl sample from each hydrogel composition ($n=3$) was prepared then fixed using 4% glutaraldehyde in PBS for 30 min. This was followed by drying in an ethanol series for the fibrin hydrogels and freeze-drying for the SAP hydrogels because the SAP hydrogels disintegrated in ethanol. Subsequently, the samples were attached to aluminum stubs and sputter-coated with a 5 nm thick platinum layer under vacuum. The microstructure was then observed using an XL30 FEG scanning electron microscope (Philips, Panama).

Evaluation of hydrogel stiffness

The stiffness of hydrogels of each composition ($n=3$) was determined using a Chiaro Nanoindenter (Optics11, the Netherlands) by applying serial indentations with a spherical glass probe ($r = 24.5 \mu\text{m}$) attached to a flexible cantilever ($k = 0.063 \text{ N/m}$). Loading and unloading velocities of the probe were set to 2 $\mu\text{m/s}$, with 2 s of holding period in between. For each sample, matrix scans (5×5 points) from three random locations were obtained. Load vs. displacement curves were extracted individually for each indentation point, and the Elastic Modulus (E) was calculated by using a Hertzian Contact Model (Poisson's ratio = 0.5) with Piuma Dataviewer Software (Optics11, the Netherlands), using equation (1):

$$F = \frac{4}{3} * E * \sqrt{R} * h^{3/2} * (1 - \nu^2) \quad (1)$$

where F is the applied force, E is the elastic modulus, R is the radius of the probe, h is the indentation depth, and ν is Poisson's ratio.

Biological Characterization

Primary cell cultures

Dental pulp tissues were acquired with informed consent from patients (15–20 years of age, male and female) undergoing extraction of third molars for therapeutic or orthodontic reasons as described previously (39). Written informed consent was obtained from the patients or their parents, as approved by the medical ethical committee of Hasselt University, Belgium (protocol 13/0104U). The dental pulp tissue was harvested with forceps after mechanically fractur-

140 ing the disinfected tooth with surgical chisels. Pulp tissues were then rinsed and transported at 37 °C in Eagle's Minimal Essential Medium, alpha modification (α MEM, Sigma-Aldrich, USA) supplemented with 2 mM L-glutamine (Sigma-Aldrich), 100 U/ml penicillin (Sigma-Aldrich), 100 μ g/ml streptomycin (Sigma-Aldrich), and 10% fetal bovine serum (FBS, Gibco, Thermo Fisher Scientific, USA). human dental pulp stem/stromal cells hDPSCs were isolated according to the explant method and expanded in culture as described previously (39). Cells were cultured in α -MEM, enriched with 10% heat-inactivated FBS (Biowest, Nuaille, France), 2 mM L-glutamine, 100 U/mL penicillin, and 100 μ g/mL streptomycin (Sigma-Aldrich). Only mycoplasma negative cells, screened with the Plasmotest kit (InvivoGen), were used. All hDPSC cultures were tested for the expression of the following (stem) cell markers at the protein level by means of flow cytometry as described previously (39): positive for CD29, CD73, CD90, and CD105 and negative for CD31, CD34, and CD45. hDPSCs were used as a mixed population without sorting.

Evaluation of hDPSC viability

To obtain enhanced green fluorescent protein (eGFP) labeled cells, pooled hDPSCs from three donors were transduced with a lentiviral vector encoding eGFP and a blasticidin resistance cassette. The selection was performed with blasticidin (10 μ g/mL, InvivoGen, Toulouse, France). Stem cells were used until passage 15. These labeled hDPSCs at 1×10^6 cells/ml seeding density were encapsulated in 100 μ l hydrogels (n=9) with and without COAM and deposited in a glass-bottom 96 well plate (CELLview Slide, Greiner, Austria). After gelation, an equal amount of maintenance culture medium was added (α MEM supplemented with 2 mM L-glutamine, 100 U/ml penicillin, 100 μ g/ml streptomycin, and 1% FBS). Tranexamic acid at 0.5 mg/ml (Exacyl, Eumedica, Belgium) was added to the medium of fibrin hydrogels to prevent fibrin degradation. After 1, 4, and 7 days in culture, the nucleus of the cells was labeled with Hoechst 33342 (Invitrogen, USA), and the dead hDPSCs were labeled using the nucleic acid dye propidium iodide (PI) (Invitrogen) according to the manufacturer's instructions using an incubation time of 15 min at 37 °C. The images were collected using laser scanning confocal microscopy (LSM 880, ZEISS, Germany) using a 20 \times objective (EC Plan-Neofluar 20 \times /0.50 M27). The fluorescence excitation/emission was measured at 490/552, 597/695, and 410/490 nm for GFP, PI, and Hoechst 33342, respectively. The number of live cells and dead cells were analyzed from 5 different regions per well (425 μ m \times 425 μ m \times 10 μ m) in Fiji (Image J, National Institutes of Health, USA) (40). Viability was calculated as a percent of live cells among the total number of live and dead cells.

Evaluation of hDPSC circularity (shape analysis)

Live cells from 5 different regions per well ($425 \mu\text{m} \times 425 \mu\text{m} \times 10 \mu\text{m}$) were segmented using a combination of watershed segmentation, thresholding, and manual contour correction for cell boundaries. Shape (circularity) of segmented cells per region, excluding cells on the image edges, was analyzed using the particle analysis plug-in in Fiji (Image J, National Institutes of Health, USA) (40). The circularity score was averaged for each well, yielding a final circularity score ranging between 0 and 1, where the closer the score to 1, the closer the shape to a circle, which would indicate low cellular attachment.

*Evaluation of hDPSC proliferation
(PicoGreen/Quant-iT DNA Quantification)*

hDPSCs at 5×10^5 cells/ml seeding density were encapsulated in 100 μl hydrogels ($n=3$ per gel and per time point) with and without COAM and deposited in a 96 well plate coated with 50 μl of the same hydrogel devoid of cells or COAM (TPP Tissue Culture Plates, Sigma-Aldrich). Hydrogels were prepared devoid of cells as blank replicates. In addition, 2D controls of 5×10^3 cells were seeded in a 96 well plate. After gelation an equal amount of serum-free mesenchymal stem cell (MSC) medium (MesenCult-ACF Plus Medium, Stem Cell Technologies, Canada) supplemented with 2 mM L-glutamine, 100 U/ml penicillin, and 100 $\mu\text{g/ml}$ streptomycin was added to each well. At baseline (day 0) and after 1, 2, 3, and 7 days in culture, a PicoGreen/Quant-iT kit (Invitrogen) was used to investigate the effect of different hydrogels on cellular proliferation. The DNA content of three hydrogels per condition and per time point was calculated for three independent experiments. Fibrin hydrogels were first digested in a buffer composed of 50 FU/ml nattokinase in 5mM EDTA in PBS for 2 h at 37 °C. SAP hydrogels were digested in a buffer composed of 1 mg/ml Pronase (Thermo Fisher Scientific) in PBS for 2 h at 37 °C. The cells seeded in the control wells were released using Trypsin-EDTA. The contents of the wells were collected, and cell pellets were retrieved by centrifugation. Retrieved cell pellets were then lysed to extract DNA using 100 μl cell lysis buffer composed of 0.029% Sodium EDTA, 0.112% Sodium pyrophosphate decahydrate, 0.88% Sodium chloride, 0.315% Tris HCl, 1% Triton-X-100, 0.038% EGTA, 0.0001% Leupeptin, 0.019% Sodium orthovanadate, 0.0216% β -glycerophosphate and 1mM PMSF (ab152163, Abcam) and centrifuged at 14000 rpm at 4°C to collect the supernatant. A 200 μl working solution representing each well (hydrogel) was prepared and aliquoted directly into black 96-well plates (Chimney well, Fluotrac, Greiner, Austria), according to the manufacturer's instructions, and incubated for 5 min protected from light at room temperature. The fluorescence excitation/emission was measured at 481/520 nm using a microplate

142 reader (Varioskan, Thermo Fisher Scientific). A standard curve was performed with λ DNA, provided with the kit, and treated equally to the sample plates. The standards ranged from 10 ng/ml to 1 μ g/ml λ DNA and were used to calculate the final DNA content per ml of the sample.

Statistical analysis

Statistical analysis was performed using the statistical software package GraphPad Prism 8.00 (GraphPad Software, La Jolla California USA). Comparison of the fiber measurements from AFM images was performed using a one-way analysis of variance (ANOVA). Comparison of the stiffness of the hydrogels was performed using a two-way ANOVA. The influence of the different experimental conditions and the time factor on cell viability, shape, and DNA quantity was modeled using a three-way ANOVA. All ANOVA tests were followed by Tukey's correction for multiple comparisons. Statistical significance was determined at $p < 0.05$. Descriptive statistics are represented as mean and standard deviation (SD), or standard error of the mean (\pm), where appropriate.

RESULTS

COAM did not modify fibrin microstructure but affected SAP hydrogels leading to fiber aggregation

The inclusion of COAM did not alter the microstructure of the fibrin hydrogel at the fiber level as demonstrated by atomic force microscopy (AFM) images (Figure 1A-D) and quantitative analysis (Table 1). However, SAP hydrogel microstructure (homogeneity) at the fiber level was affected by the inclusion of COAM (Figure 1E-H), leading to fiber aggregation (visible in Figure 1F, H). SEM images further confirmed the microstructural stability of the fibrin hydrogels (Figure 1I&J). In contrast, the effect of COAM inclusion on the morphology of the SAP hydrogels was not detected by SEM (Figure 1K&L). The fiber height distribution showed no significant impact of COAM inclusion on fibrin hydrogels when comparing those without COAM (Figure 2A&B) to those with COAM (Figure 2C&D). SAP hydrogels without COAM (Figure 2E&F) showed a distinct fiber height distribution with three peaks between 1 and 5 nm. After COAM inclusion (Figure 2G&H), those three peaks disappeared, confirming aggregation at the fiber level.

Topographic and quantitative microstructural analysis for the AFM images showed that both fibrin and SAP hydrogels have a nanofibrous structure at different scales (Table 1). The roughness average (Ra) was 8.1 (SD: 1.6) nm for fibrin hydrogels and 1.2 (SD: 0.1) nm for the SAP hydrogels. The inclusion of

Table 1: AFM image analysis using ctFIRE Fiber Extraction Algorithm

Parameter	Fibrin	Fibrin COAM	SAP	SAP COAM
Roughness average (Ra)	8.1 nm (SD: 1.6)	16.9 nm (SD: 7.5)	1.2 nm (SD: 0.1)	3.0 nm* (SD: 0.4)
Fiber diameter	146.6 nm** (± 1.1)	156.6 nm** (± 1.2)	73.3 nm** (± 0.3)	NA
Fiber length	1136.7 nm (± 50.2)	1077.7 nm (± 49.0)	1369.9 nm (± 24.7)	NA
Fiber straightness	0.93 (± 0.003)	0.93 (± 0.002)	0.80 (± 0.003)	NA
Fiber alignment	0.05	0.06	0.06	NA

SD: Standard deviation ±: Standard Error of Mean *: measured on the aggregated fibers **: approximately overestimated by 15 nm because of tip diameter

COAM in fibrin hydrogels increased the Ra to 16.9 (SD: 7.5) nm. However, this increase was not statistically significant ($p > 0.05$). The mean fiber diameters for the fibrin hydrogels were 146.6 ± 1.1 nm without COAM and 156.6 ± 1.2 nm with COAM ($p > 0.05$). The mean fiber diameter for the SAP hydrogels 73.2 ± 0.3 nm. For the SAP hydrogels with COAM, the fiber measurements were unreliable due to fiber aggregation (Figure 1F&H); therefore, these measurements were not reported.

Effect of COAM inclusion on fibrin and SAP hydrogel stiffness

The elastic modulus for fibrin hydrogels at 3.5 mg/ml fibrinogen concentration was 752 ± 13 Pa before and 683 ± 6 Pa after the inclusion of COAM (Figure 3). Furthermore, for the SAP hydrogels at 3.5 mg/ml RADA-16 concentration, the elastic modulus was 5425 ± 295 Pa before and 4821 ± 386 Pa after the inclusion of COAM (Figure 3). The stiffness of the SAP hydrogels was 7-fold higher than the fibrin hydrogels ($p < 0.05$). The inclusion of COAM did not alter the stiffness of the fibrin and SAP hydrogels ($p > 0.05$).

hDPSCs show higher viability and better attachment in fibrin hydrogels

According to an ANOVA analysis, we observed a significant effect on hDPSC viability in the maintenance medium for both the hydrogel type [F (1, 22) = 438.6, $p < 0.0001$] and the time period of the experiment [F (2, 22) = 9.9, $p = 0.0008$] (Figure 4A-E). Post hoc comparisons using the Tukey test showed that viability did not significantly decrease over time for either the fibrin hydrogels without COAM or the fibrin hydrogels with COAM ($p > 0.05$). On the contrary, cell viability declined significantly in the SAP hydrogels without COAM from day 1 (66.9%) until day 7 (54.1%) and in the SAP hydrogels with COAM from day 1 (68.3%) until day 7 (53.9%) ($p < 0.05$) (Figure 4E). The average hDPSC viability in the fibrin hydrogels was 91.3% without COAM and 89.9% with COAM over the 7-day test period ($p > 0.05$).

In addition, ANOVA analysis showed a significant effect on hDPSC circularity for the hydrogel type [F (1, 48) = 102.9, $p < 0.0001$] (Figure 4F). hDPSCs adopted a spread morphology, indicated by a lower circularity value, in the fibrin hydrogels both with and without COAM (Figure 4A-B). In contrast, hDPSCs remained rounded in the SAP hydrogels, again for the hydrogels both with and without COAM (Figure 4C-D). These results indicate superior cell attachment in the fibrin hydrogels (Figure A-D & F). Furthermore, the hDPSC morphology did not change significantly with time for any of the treatment conditions (Figure 4F). The average circularity scores were 0.25 ± 0.05 in the fibrin hydrogels without COAM and 0.26 ± 0.02 in the fibrin hydrogels with COAM over the 7-day test period. The average circularity scores were 0.76 ± 0.01 in the SAP hydrogels without COAM and 0.74 ± 0.02 in the SAP hydrogels with COAM over the 7-day test period.

DNA quantification to measure cell proliferation

According to an ANOVA analysis, there was a significant effect on the amount of DNA for both the hydrogel type [F (1, 49) = 89.85, $p < 0.0001$] and the presence of COAM [F (1, 49) = 12.47, $p = 0.0009$]. Post hoc comparisons using the Tukey test showed a significantly higher DNA content in response to the fibrin hydrogels with and without COAM compared to the SAP hydrogels with and without COAM ($p < 0.05$). hDPSCs showed a proliferative pattern in the fibrin hydrogels with an average 1.3-fold increase in DNA content at day 7 compared to day 0 for fibrin without COAM ($p > 0.05$) and a significant 2.1-fold increase for fibrin with COAM ($p < 0.05$).

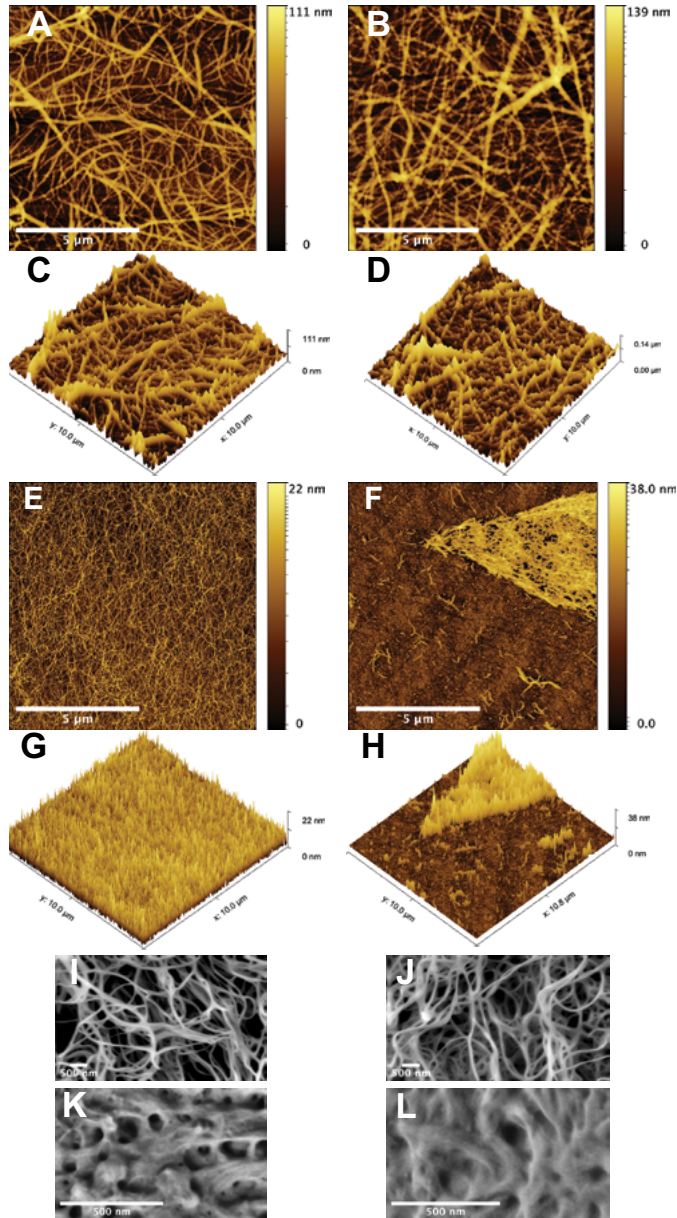


Figure 1: Hydrogel microstructure: Topographic atomic force microscopy (AFM) images of (A) fibrin hydrogel without COAM and (B) fibrin hydrogel with COAM. 3D AFM images of (C) fibrin hydrogel without COAM and (D) fibrin hydrogel with COAM. Topographic AFM images of (E) SAP hydrogel without COAM and (F) SAP hydrogel with COAM. 3D AFM images of (G) SAP hydrogel without COAM and (H) SAP hydrogel with COAM. Scanning electron microscopy (SEM) micrographs of (I) fibrin hydrogel without COAM, (J) fibrin hydrogel with COAM, (K) SAP hydrogel without COAM, and (L) SAP hydrogel with COAM. Color code scale in AFM images (A-H) represents fiber height. Scale bars in A, B, E & F = 5 μm, and in I, J, K & L = 500 nm.

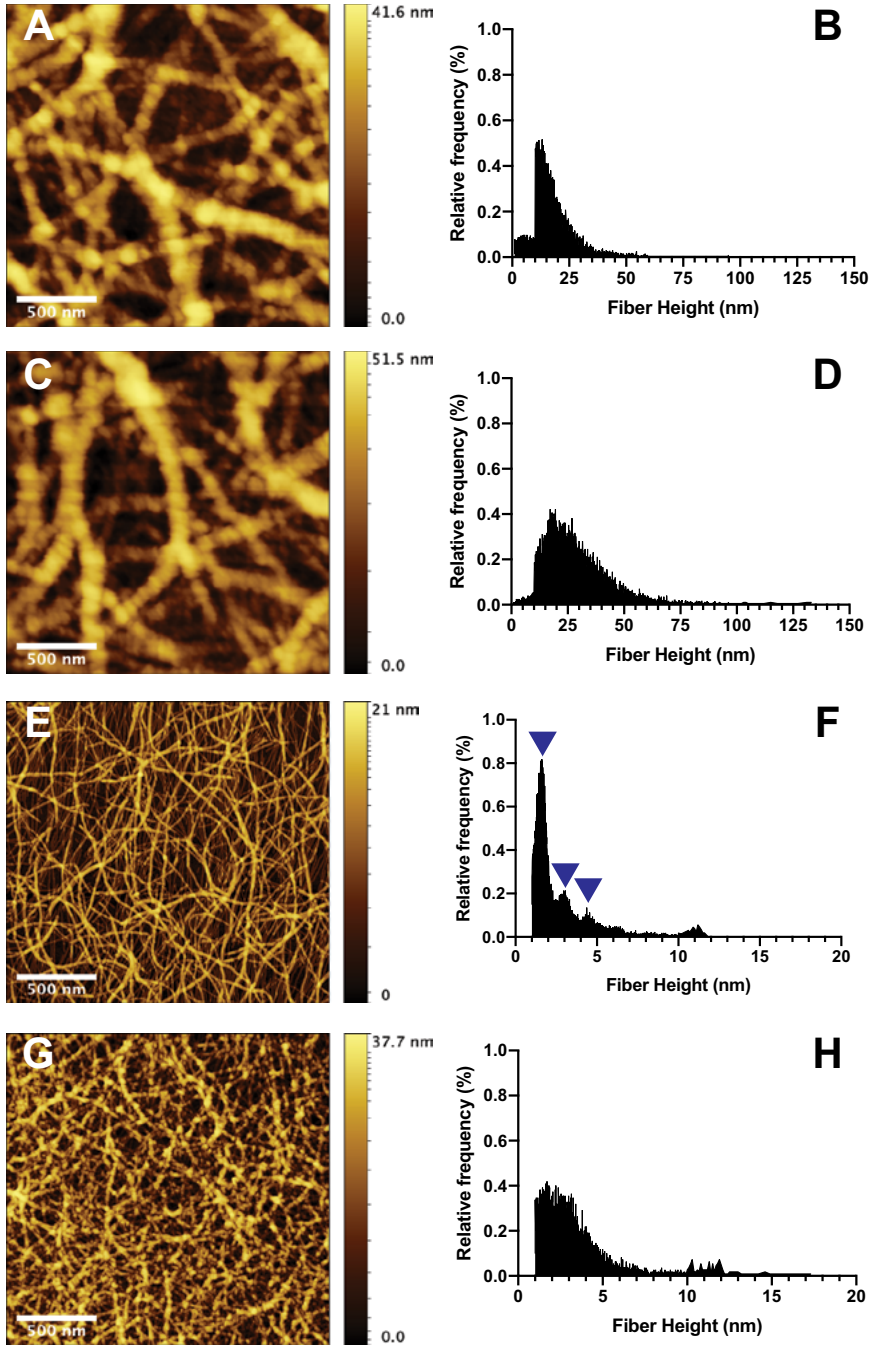


Figure 2: High-resolution atomic force microscopy (AFM) and quantitative fiber height distribution: (A & B) fibrin hydrogels without COAM, (C & D) fibrin hydrogels with COAM, (E & F) SAP hydrogels without COAM and with distinct peaks indicated by blue arrowheads, and (G & H) SAP hydrogels with COAM.

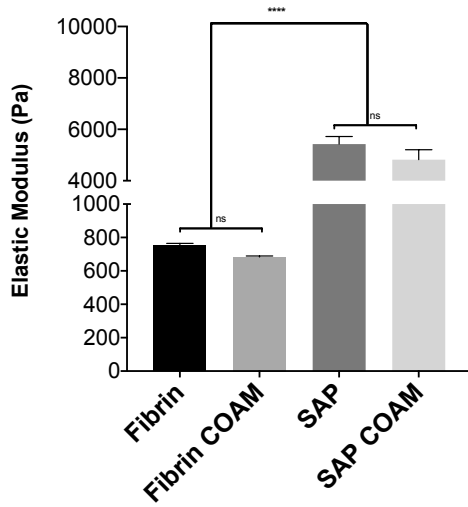


Figure 3: Hydrogels stiffness: The elastic modulus for fibrin hydrogels at 3.5 mg/ml fibrinogen concentration and SAP hydrogels at 3.5 mg/ml RADA-16 concentration. Results are presented as mean \pm SEM; ns refers to not significant, * significant differences.

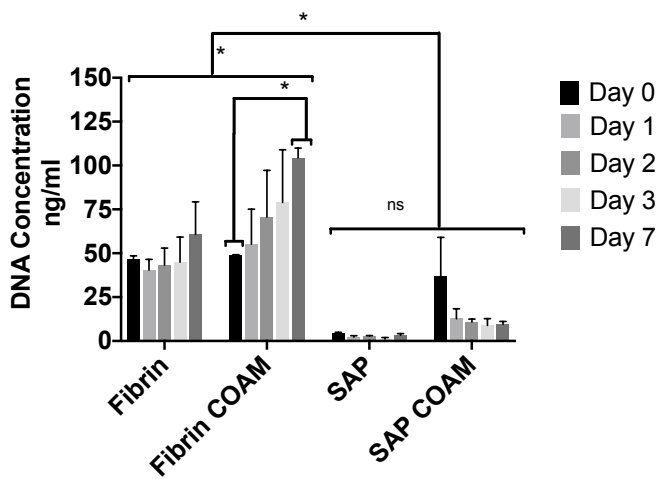


Figure 5: DNA content of cell-laden hydrogels: Results are presented as mean \pm SEM, ns refers to not significant, * significant differences.

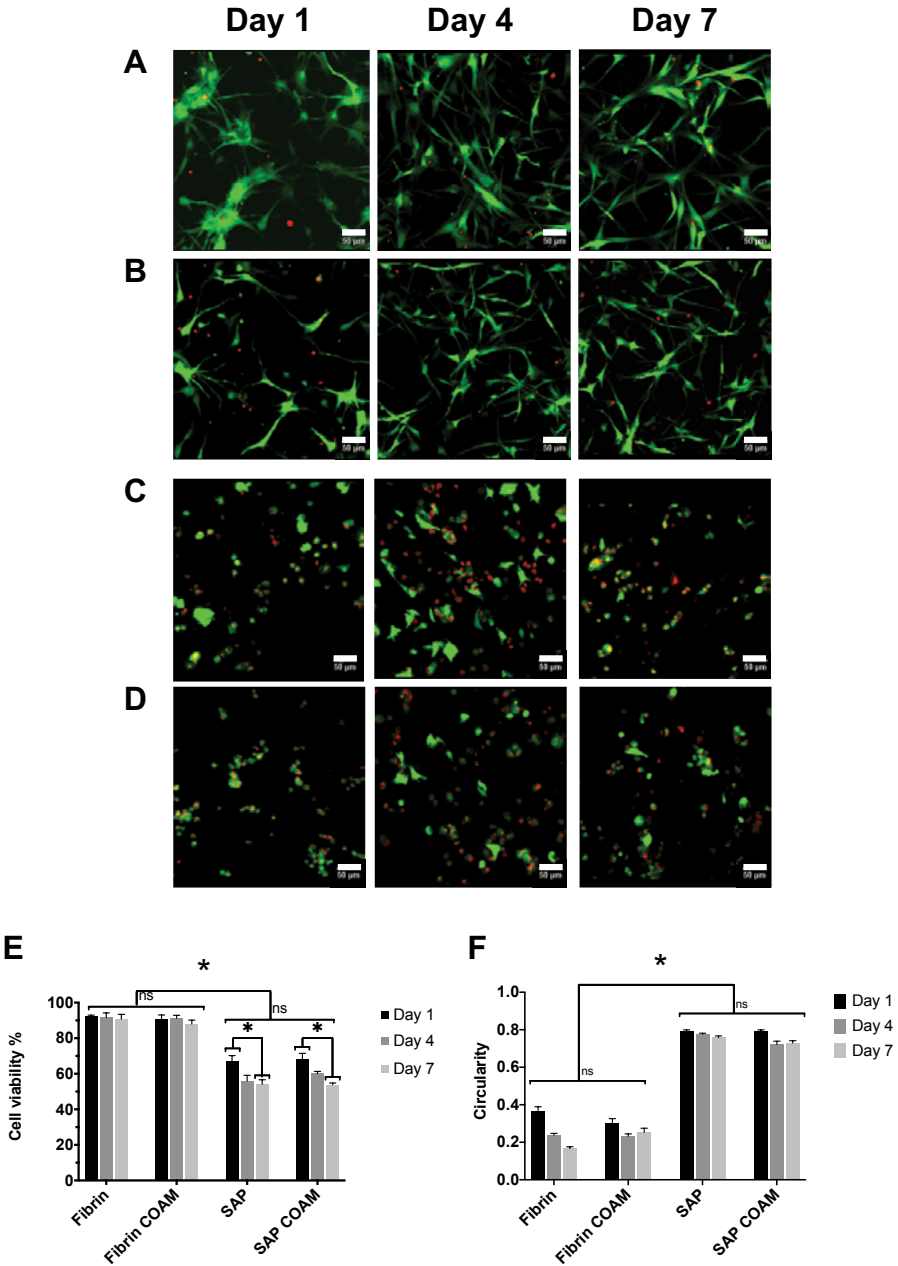


Figure 4: Cell viability (hDPSCs) in cell-laden hydrogels: Representative Live/Dead images of hDPSCs encapsulated up to 7 days in (A) fibrin hydrogels without COAM, (B) fibrin hydrogels with COAM, (C) SAP hydrogels without COAM, and (D) SAP hydrogels with COAM. (E) Quantification of cell viability from Live/Dead images. (F) Cell shape (circularity) analysis from Live/Dead images using ImageJ. Green shows live cells, and red shows dead cells. Scale bars = 50 μ m. Results are presented as mean \pm SEM. ns refers to not significant, * significant differences.

A low DNA content was observed in the SAP hydrogels without COAM at day 0 with 10-fold and 8-fold lower DNA content compared to the fibrin hydrogels without COAM ($p < 0.05$) and SAP hydrogels with COAM ($p > 0.05$), respectively. SAP hydrogels with COAM showed higher DNA content than SAP hydrogels without COAM ranging between 5-fold higher at day 1 and 3-fold higher at day 7. However, these differences were not statistically significant ($p > 0.05$). Moreover, the DNA content was stable in both SAP hydrogels from day 1 up to day 7 (Figure 5).

DISCUSSION

In this study, we characterized the structural and mechanical characteristics of selected compositions of fibrin and SAP hydrogels. Nano- to micro-scale structural and mechanical cues are associated with biological responses in both native ECM and synthetic constructs (18). Although the understanding of the association between the surface topography and the cellular response is still limited, it has been suggested that the nano-topography enhances cellular communication, such as in neural cell networks (41), and protein adsorption, thus affecting the modulation of cellular interactions (42). In this study, the nanoscale topographical features of fibrin and SAP hydrogels were different. The roughness average of the fibrin surface was 7-fold higher than that of the SAP hydrogel, along with a 2-fold increase in the average fiber diameter. Other features, such as fiber straightness and alignment, were comparable. Fibrin hydrogels showed structural stability after the inclusion of our experimental macromolecule, COAM, while SAP hydrogels were affected, leading to fiber aggregation. The effect of COAM inclusion on the morphology of the SAP hydrogels was not observed in the SEM images, which could be due to the sample preparation procedure that resulted in drying artifacts.

The measured stiffness of fibrin hydrogels, with the composition tested in the current study, was in the range of the stiffness of the native pulp tissue, which has previously been reported to be 800 Pa (43). In addition, the stiffness of SAP hydrogels was found to be 7-fold higher than the fibrin hydrogels. hDPSCs are mesenchymal stem/stromal cells (MSCs) that pose the potential to differentiate into numerous cell types *in vitro*, including odontoblasts/osteoblasts, chondroblasts, adipocytes, and neuronal-like cells (13-15). MSCs have been shown to specify lineage and commit to phenotypes with extreme sensitivity to tissue-level elasticity, as soft matrices induced neurogenic differentiation and stiffer matrices were osteogenic (44). The current mechanical characterization results might aid in explaining previous observations of mineralized tissue formation within SAP (RADA-16) hydrogels encapsulating hDPSCs when they were implanted in an ectopic mouse model for 12 weeks (30). Future studies

150 should explore to which extent differences in matrix stiffness would affect hDPSC differentiation profiles *in vivo*.

The current study showed higher hDPSC survival in fibrin hydrogels compared to in SAP hydrogels. This agrees with the data reported previously (17), where hDPSCs in fibrin hydrogels prepared at 10 mg/ml showed higher viability compared to hDPSCs in SAP (RADA-16) hydrogels when they were evaluated using an MTT assay. Moreover, other authors (45) reported hDPSCs' survival at day 4 to be just above 60% in SAP (RADA-16) hydrogels at 1.5 mg/ml, reflecting the cell viability data reported in the current study. The higher cell survival in fibrin hydrogels can be likely explained by the presence of natural cell adhesion motifs (46) facilitating cell attachment and elongated cellular morphology, which was demonstrated in the current study. In contrast, SAP hydrogels lack these cell adhesion motifs. Future studies could explore the possibility of improving cellular attachment to SAP hydrogels by conjugating bioactive short peptide motives such as the integrin-binding arginine-glycine-aspartic acid (RGD) to the C-terminus of the RADA-16 peptide. Another possible explanation for the low cell survival in SAP hydrogels could be the initial acidic pH (3.0) that is only neutralized after adding medium to induce gelation. The DNA quantification results confirmed differences in cell viability, with a 10-fold lower DNA content measured at day 0 for SAP hydrogels compared to fibrin hydrogels. The DNA content in SAP hydrogels with COAM was 8-fold and 5-fold higher compared to SAP hydrogels without COAM at day 0 and day 1, respectively, suggesting an initial protective influence for COAM that needs to be further investigated. The hDPSC viability and the DNA content for the SAP hydrogels with and without COAM were then relatively stable over the remaining period of the experiments, strengthening the hypothesis that this drop in viability is related to the low attachment and the pH conditions at the time of encapsulation.

One interesting outcome was the effect of COAM on the increase of the DNA content, suggesting that the hDPSCs were proliferating more. Such effect for the presence of COAM may be explained in terms of a biological influence since no effect was observed for COAM inclusion on the structural and mechanical properties of the fibrin hydrogels. COAM is a polyanionic polysaccharide derivative with antibacterial properties (32) and broad-spectrum antiviral activity that acts as an immunomodulator (33, 34). In previous studies, COAM has been shown to induce and bind chemokines such as granulocyte chemoattractant protein-2 (GCP-2), leading to significant recruitment of myeloid cells in mice (47). Furthermore, it has been demonstrated that COAM competes with GAGs for binding and recruitment of chemokines (35). This COAM-chemokine binding complex influenced chemokine localization and the selectivity of

leukocyte responses and migration (35). hDPSCs and MSCs produce a plethora of soluble factors, cytokines, and chemokines influencing cellular growth, proliferation, migration, differentiation, and immune responses (48, 49). For example, insulin-like growth factor-1 (IGF-1), a cytokine produced by hDPSCs, was found to stimulate hDPSC proliferation in serum-free culture medium (50). Moreover, hDPSCs overexpressing the chemokine stromal-derived factor-1 alpha (SDF-1a/CXCL12) showed higher cell proliferation compared to wild-type hDPSCs (51). Therefore, one possible explanation for the higher DNA content in fibrin hydrogels with COAM could be the formation of a binding complex, increasing the availability of factors and chemokines involved in cellular proliferation inside the 3D hydrogel microenvironment. This is in line with preliminary experiments, in which we found that COAM binds SDF-1a/CXCL12, both on solid phase and in solution (unpublished data).

Finally, the current study presents a comprehensive structural and mechanical characterization for two promising biomaterials for dental pulp tissue engineering in combination with an analysis of biological features such as cell viability, shape, and proliferation. Future research will explore the influence of different hydrogel properties such as matrix stiffness on hDPSC migration and differentiation. Furthermore, the molecular mechanisms underlying the effect of COAM on hDPSC proliferation need to be investigated in detail in order to obtain insight to optimize their use in tissue engineering.

CONCLUSION

The microstructural stability after the inclusion of COAM as well as the preservation of cell viability, elongated morphology, and higher DNA content observed in the fibrin hydrogels suggest this system as a promising carrier for COAM and application in endodontic regeneration.

ACKNOWLEDGMENTS

Supported by the Fund for Scientific Research-Flanders (FWO-Vlaanderen) grant number (G089213N), Research Council of KU Leuven grant numbers (C24/18/068), (C14/17/111), and KU Leuven equipment grant (KA/16/084). The authors deny any conflicts of interest related to this study.

AUTHOR CONTRIBUTIONS

M.E., B.T., R.J., and J.P. contributed to the conception, design, data acquisition, analysis, and interpretation for the overall study and drafted and critically revised the manuscript; D.M., O.D., G.O., I.L., and A.B. contributed to the data

152 acquisition, analysis, and interpretation of individual experiments and critically revised the manuscript; N.S., C.B., H.V., and R.P. contributed to the conception and design of specific experiments and critically revised the manuscript. All authors gave final approval and agreed to be accountable for all aspects of the study.

REFERENCES

1. Kassebaum NJ, Smith AGC, Bernabe E, Fleming TD, Reynolds AE, Vos T, et al. Global, Regional, and National Prevalence, Incidence, and Disability-Adjusted Life Years for Oral Conditions for 195 Countries, 1990-2015: A Systematic Analysis for the Global Burden of Diseases, Injuries, and Risk Factors. *J Dent Res.* 2017;96(4):380-7.
2. Ansari S, Freire M, Choi MG, Tavari A, Almohaimeed M, Moshaverinia A, et al. Effects of the orientation of anti-BMP2 monoclonal antibody immobilized on scaffold in antibody-mediated osseous regeneration. *J Biomater Appl.* 2015;30(5):558-67.
3. Freire MO, You HK, Kook JK, Choi JH, Zadeh HH. Antibody-mediated osseous regeneration: a novel strategy for bioengineering bone by immobilized anti-bone morphogenetic protein-2 antibodies. *Tissue Eng Part A.* 2011;17(23-24):2911-8.
4. Kim K, Lee CH, Kim BK, Mao JJ. Anatomically shaped tooth and periodontal regeneration by cell homing. *J Dent Res.* 2010;89(8):842-7.
5. Galler KM, D'Souza RN. Tissue engineering approaches for regenerative dentistry. *Regen Med.* 2011;6(1):111-24.
6. Chueh LH, Huang GT. Immature teeth with periradicular periodontitis or abscess undergoing apexogenesis: a paradigm shift. *J Endod.* 2006;32(12):1205-13.
7. Huang GT, Garcia-Godoy F. Missing Concepts in De Novo Pulp Regeneration. *J Dent Res.* 2014;93(8):717-24.
8. Chueh LH, Ho YC, Kuo TC, Lai WH, Chen YH, Chiang CP. Regenerative endodontic treatment for necrotic immature permanent teeth. *J Endod.* 2009;35(2):160-4.
9. EzEldeen M, Van Gorp G, Van Dessel J, Vandermeulen D, Jacobs R. 3-dimensional analysis of regenerative endodontic treatment outcome. *J Endod.* 2015;41(3):317-24.
10. Meschi N, EzEldeen M, Torres Garcia AE, Jacobs R, Lambrechts P. A Retrospective Case Series in Regenerative Endodontics: Trend Analysis Based on Clinical Evaluation and 2- and 3-dimensional Radiology. *J Endod.* 2018;44(10):1517-25.
11. Meschi N, Hilkens P, Van Gorp G, Strijbos O, Mavridou A, Cadenas de Llano Perula M, et al. Regenerative Endodontic Procedures Posttrauma: Immunohistologic Analysis of a Retrospective Series of Failed Cases. *J Endod.* 2019;45(4):427-34.
12. Austah O, Joon R, Fath WM, Chrepa V, Diogenes A, Ezeldeen M, et al. Comprehensive Characterization of 2 Immature Teeth Treated with Regenerative Endodontic Procedures. *J Endod.* 2018;44(12):1802-11.
13. Bronckaers A, Hilkens P, Fanton Y, Struys T, Gervois P, Politis C, et al. Angiogenic properties of human dental pulp stem cells. *PLoS One.* 2013;8(8):e71104.
14. Bronckaers A, Hilkens P, Martens W, Gervois P, Ratajczak J, Struys T, et al. Mesenchymal stem/stromal cells as a pharmacological and therapeutic approach to accelerate angiogenesis. *Pharmacol Ther.* 2014;143(2):181-96.
15. Ratajczak J, Hilkens P, Gervois P, Wolfs E, Jacobs R, Lambrechts I, et al. Angiogenic Capacity of Periodontal Ligament Stem Cells Pretreated with Deferoxamine and/or Fibroblast Growth Factor-2. *PLoS One.* 2016;11(12):e0167807.
16. Hilkens P, Driesen RB, Wolfs E, Gervois P, Vanganswinkel T, Ratajczak J, et al. Cryopreservation and Banking of Dental Stem Cells. *Adv Exp Med Biol.* 2016;951:199-235.

17. Galler KM, Brandl FP, Kirchof S, Widbiller M, Eidt A, Buchalla W, et al. Suitability of Different Natural and Synthetic Biomaterials for Dental Pulp Tissue Engineering. *Tissue Eng Part A*. 2018;24(3-4):234-44.
18. Betancourt BAP, Florczyk SJ, Simon M, Juba D, Douglas JF, Keyrouz W, et al. Effect of the scaffold microenvironment on cell polarizability and capacitance determined by probabilistic computations. *Biomed Mater*. 2018;13(2):025012.
19. Lin S, Sangaj N, Razafiarison T, Zhang C, Varghese S. Influence of physical properties of biomaterials on cellular behavior. *Pharm Res*. 2011;28(6):1422-30.
20. Man AJ, Davis HE, Itoh A, Leach JK, Bannerman P. Neurite outgrowth in fibrin gels is regulated by substrate stiffness. *Tissue Eng Part A*. 2011;17(23-24):2931-42.
21. Galler KM, Hartgerink JD, Cavender AC, Schmalz G, D'Souza RN. A customized self-assembling peptide hydrogel for dental pulp tissue engineering. *Tissue Eng Part A*. 2012;18(1-2):176-84.
22. Leonidakis KA, Bhattacharya P, Patterson J, Vos BE, Koenderink GH, Vermant J, et al. Fibrin structural and diffusional analysis suggests that fibers are permeable to solute transport. *Acta Biomater*. 2017;47:25-39.
23. Yuan Z, Nie H, Wang S, Lee CH, Li A, Fu SY, et al. Biomaterial selection for tooth regeneration. *Tissue Eng Part B Rev*. 2011;17(5):373-88.
24. Sierra DH. Fibrin sealant adhesive systems: a review of their chemistry, material properties and clinical applications. *J Biomater Appl*. 1993;7(4):309-52.
25. Weisel JW, Litvinov RI. Mechanisms of fibrin polymerization and clinical implications. *Blood*. 2013;121(10):1712-9.
26. Litvinov RI, Weisel JW. Fibrin mechanical properties and their structural origins. *Matrix Biol*. 2017;60-61:110-23.
27. Kurniawan NA, Grimbergen J, Koopman J, Koenderink GH. Factor XIII stiffens fibrin clots by causing fiber compaction. *J Thromb Haemost*. 2014;12(10):1687-96.
28. Cui H, Webber MJ, Stupp SI. Self-assembly of peptide amphiphiles: from molecules to nanostructures to biomaterials. *Biopolymers*. 2010;94(1):1-18.
29. Gelain F, Horii A, Zhang S. Designer self-assembling peptide scaffolds for 3-d tissue cell cultures and regenerative medicine. *Macromol Biosci*. 2007;7(5):544-51.
30. Hilkens P, Bronckaers A, Ratajczak J, Gervois P, Wolfs E, Lambrichts I. The Angiogenic Potential of DPSCs and SCAPs in an In Vivo Model of Dental Pulp Regeneration. *Stem Cells Int*. 2017;2017:2582080.
31. Mangione F, EzEldeen M, Bardet C, Lesieur J, Bonneau M, Decup F, et al. Implanted Dental Pulp Cells Fail to Induce Regeneration in Partial Pulpotomies. *J Dent Res*. 2017;96(12):1406-13.
32. Zi Y, Zhu M, Li X, Xu Y, Wei H, Li D, et al. Effects of carboxyl and aldehyde groups on the antibacterial activity of oxidized amylose. *Carbohydr Polym*. 2018;192:118-25.
33. Li S, Martens E, Dillen C, Van den Steen PE, Opendakker G. Virus entry inhibition by chlorite-oxidized oxyamylose versus induction of antiviral interferon by poly(I:C). *Biochem Pharmacol*. 2008;76(7):831-40.
34. Opendakker G, Li S, Berghmans N, Damme JV. Applications of glycobiology: biological and immunological effects of a chemically modified amylose-derivative. *Carbohydrate Chemistry*. *Carbohydrate Chemistry* 2012. p. 1-12.
35. Li S, Pettersson US, Hoorelbeke B, Kollackowska E, Schelfhout K, Martens E, et al. Interference with glycosaminoglycan-chemokine interactions with a probe to alter leukocyte recruitment and inflammation in vivo. *PLoS One*. 2014;9(8):e104107.
36. Claes P, Billiau A, De Clercq E, Desmyter J, Schonne E, Vanderhaeghe H, et al. Polyacetal carboxylic acids: a new group of antiviral polyanions. *J Virol*. 1970;5(3):313-20.
37. Nečas D, Klapetek P. Gwyddion: an open-source software for SPM data analysis. *Open Physics*. 2012;10(1).

38. Bredfeldt JS, Liu Y, Pehlke CA, Conklin MW, Szulczewski JM, Inman DR, et al. Computational segmentation of collagen fibers from second-harmonic generation images of breast cancer. *J Biomed Opt.* 2014;19(1):16007.
 39. Hilkens P, Gervois P, Fanton Y, Vanormelingen J, Martens W, Struys T, et al. Effect of isolation methodology on stem cell properties and multilineage differentiation potential of human dental pulp stem cells. *Cell Tissue Res.* 2013;353(1):65-78.
 40. Schindelin J, Arganda-Carreras I, Frise E, Kaynig V, Longair M, Pietzsch T, et al. Fiji: an open-source platform for biological-image analysis. *Nat Methods.* 2012;9(7):676-82.
 41. Onesto V, Cancedda L, Coluccio ML, Nanni M, Pesce M, Malara N, et al. Nano-topography Enhances Communication in Neural Cells Networks. *Sci Rep.* 2017;7(1):9841.
 42. Lord MS, Foss M, Besenbacher F. Influence of nanoscale surface topography on protein adsorption and cellular response. *Nano Today.* 2010;5(1):66-78.
 43. Erisken C, Kalyon DM, Zhou J, Kim SG, Mao JJ. Viscoelastic Properties of Dental Pulp Tissue and Ramifications on Biomaterial Development for Pulp Regeneration. *J Endod.* 2015;41(10):1711-7.
 44. Engler AJ, Sen S, Sweeney HL, Discher DE. Matrix elasticity directs stem cell lineage specification. *Cell.* 2006;126(4):677-89.
 45. Dissanayaka WL, Hargreaves KM, Jin L, Samaranyake LP, Zhang C. The interplay of dental pulp stem cells and endothelial cells in an injectable peptide hydrogel on angiogenesis and pulp regeneration in vivo. *Tissue Eng Part A.* 2015;21(3-4):550-63.
 46. Li Y, Meng H, Liu Y, Lee BP. Fibrin gel as an injectable biodegradable scaffold and cell carrier for tissue engineering. *Sci. World J.* 2015;2015:685690.
 47. Li S, Starckx S, Martens E, Dillen C, Lamerant-Fayel N, Berghmans N, et al. Myeloid cells are tunable by a polyanionic polysaccharide derivative and co-determine host rescue from lethal virus infection. *J Leukoc Biol.* 2010;88(5):1017-29.
 48. Joo KH, Song JS, Kim S, Lee HS, Jeon M, Kim SO, et al. Cytokine Expression of Stem Cells Originating from the Apical Complex and Coronal Pulp of Immature Teeth. *J Endod.* 2018;44(1):87-92 e1.
 49. Lavoie JR, Rosu-Myles M. Uncovering the secrets of mesenchymal stem cells. *Biochimie.* 2013;95(12):2212-21.
 50. Onishi T, Kinoshita S, Shintani S, Sobue S, Ooshima T. Stimulation of proliferation and differentiation of dog dental pulp cells in serum-free culture medium by insulin-like growth factor. *Arch Oral Biol.* 1999;44(4):361-71.
 51. Zhu L, Dissanayaka WL, Zhang C. Dental pulp stem cells overexpressing stromal-derived factor-1alpha and vascular endothelial growth factor in dental pulp regeneration. *Clin Oral Investig.* 2019;23(5):2497-509.
-

CHAPTER 8

This chapter is based on the following publication

EzEldeen, M., Pereira, R. V. S., Pedano, S., Martens, E., Murgia, D., Van Meerbeek, B., Lambrichts, I., Jacobs, R., Opendakker, G. Application of COAM as a novel strategy for hydrogel functionalisation with chemokines: towards chemokine-mediated dental tissue regeneration.
In preparation.

- (A) OMFS IMPATH Research Group, Faculty of Medicine, Department of Imaging and Pathology, KU Leuven and Oral and Maxillofacial Surgery, University Hospitals Leuven, Kapucijnenvoer 33, 3000 Leuven, Belgium
- (B) Department of Oral Health Sciences, KU Leuven and Paediatric Dentistry and Special Dental Care, University Hospitals Leuven, Kapucijnenvoer 33, 3000 Leuven, Belgium
- (C) Department of Microbiology, Immunology and Transplantation, Rega Institute for Medical Research, KU Leuven, University of Leuven, Leuven, Belgium
- (D) Department of Oral Health Sciences, Endodontology, University Hospitals Leuven, KU Leuven, Leuven, Belgium
- (E) Department of Surgical, Oncological and Oral Sciences, University of Palermo, Via Liborio Giuffrè 5, 90127 Palermo, Italy
- (F) KU Leuven (University of Leuven), Department of Oral Health Sciences, BIOMAT -Biomaterials Research group & UZ Leuven, University Hospitals Leuven, Dentistry, Kapucijnenvoer 33, 3000 Leuven, Belgium
- (G) Biomedical Research Institute, Hasselt University, Campus Diepenbeek, Agoralaan Building C, B-3590 Diepenbeek, Belgium
- (H) Department of Dental Medicine, Karolinska Institute, Stockholm, Sweden

Application of COAM as a Novel Strategy for Hydrogel Functionalization with Chemokines: Towards Chemokine-Mediated Dental Tissue Regeneration

M. EzEldeen (A,B), R. Vaz Sousa Pereira (C), M. N. Simon Pedano De Piero (D), E. Martens (C),
D. Murgia (A,E), B. Van Meerbeek (F), I. Lambrichts (G), R. Jacobs (H), G. Opendakker (C)

ABSTRACT

Introduction — Unlike salamanders, humans cannot regenerate tissues, particularly infected tissues. The regenerative capacity is gradually reduced in humans after birth, co-incidentally with the development of the immune system. Nevertheless, tissue repair and regeneration and the cells that guide the immune system can be modulated. In this study, we aimed to evaluate the effect of the chemokine-binding and antimicrobial polymer, chlorite-oxidized oxyamylose (COAM), in the delivery of chemokines for dental pulp repair and regeneration.

KEY WORDS

*COAM, chemokine,
SDF-1/CXCL12,
Dental pulp cells*

Materials and Methods — Chemokine (SDF-1/CXCL12 and MCP-1/CCL2) binding to COAM was investigated using gel filtration chromatography. The release of COAM of chemokines from fibrin hydrogels was evaluated by enzyme-linked immunosorbent assay (ELISA). The effect of 3D encapsulation in fibrin hydrogels on the immunophenotype of dental pulp stromal cells (hDPSCs) was performed with flow cytometry analysis (FACS). The influence of encapsulation and the presence of COAM and SDF-1/CXCL12 on hDPSCs proliferation was evaluated by FACS. An *ex-vivo* tooth model was used to investigate the dental pulp reaction to functionalized hydrogels.

Results — In gel chromatography analysis COAM formed a strong binding complex with SDF-1/CXCL12, while this was not observed for MCP-1/CCL2. The formation of this binding complex influenced the patterns of SDF-1/CXCL12 release from fibrin hydrogels. hDPSCs maintained their phenotype after seven days of encapsulation. However, a CD34+ population emerged in all experimental groups. The presence of COAM and SDF-1/CXCL12 did not affect the proliferation pattern of encapsulated.

Conclusion — COAM formed a binding complex with SDF-1/CXCL12 leading to it delayed chemokine release from fibrin hydrogels. Although COAM also has the benefits of a broad antimicrobial agent, the application of COAM as a pharmacological agent in dental tissue regeneration is challenged.

INTRODUCTION

The classical regenerative medicine approach employs a combination of cells with biomaterials to induce tissue regeneration. The economic and regulatory hurdles associated with cell-based therapies have also led to the proliferation of cell-free biomaterial approaches, which stimulate the activity of endogenous stem cells. Therefore, regenerative medicine can be approached either in a cell-free or in a cell-based manner. Immune-modulated tissue regeneration techniques can be applied as an independent cell-free approach or adjunct for cell-based approaches (1).

Chemokines are small, secreted proteins that signal through G protein-coupled receptors (2, 3). By quickly mobilizing blood cells, chemokines are involved in various biological processes such as innate immune defence, neural development, atherosclerosis, angiogenesis, inflammation, and viral pathogenesis (3-6). Further, signalling by specific chemokines promotes cell survival, proliferation and provides directional guidance to migrating cells (3, 4, 6-12).

Chemokines generally play a pivotal role in (stem) cell homing (7) and differentiation (13). Mesenchymal stromal cells (MSCs) express chemokine receptors CCR1, CCR3, and CXCR4 and exhibit significant chemotaxis induced by macrophage inflammatory protein 1-alpha (MIP-1a or CCL3), a ligand of CCR1, and by stromal cell-derived factor-1 (SDF-1 or CXCL12), the natural ligand for CXCR4 (5). Especially for tissue repair and regeneration, the latter ligand/receptor pair (SDF-1/CXCR4) has attracted much attention for the migration of hematogenic stem cells and progenitor cells, such as dental pulp stem/stromal cells (DPSCs) (8) to the site of injury. This contribute to tissue repair and regeneration. This ligand and receptor pair play pivotal roles in the mobilization, migration, homing, proliferation and differentiation of CD34⁺ haematopoietic stem cells (HPCs) (7). Moreover, odontoblastic differentiation was stimulated by SDF-1 activation and repressed by SDF-1/CXCR4 inhibition (13). Additionally, the monocyte chemoattractant protein-1 (MCP-1 or CCL2) discovered as a monocyte/macrophage chemokine, was shown to play an important role in inducing the so called M2 macrophage differentiation and subsequent tissue regeneration (14).

Nevertheless, challenges exist for the use of chemokines and other small proteins in tissue engineering and regenerative medicine (TERM). These include their short half-lives, rapid diffusion through the extracellular matrix (ECM), the difficulty of appropriate dosing, sensitivity to proteases and instant deactivation in an inflammatory environment (such as found in almost every dental condition) (15, 16). Although local delivery of specific chemotactic fac-

tors to drive stem cell recruitment into injured tissues represents a potentially innovative approach to regeneration, some critical factors for practical and reliable use of chemokines are the release in a sustained manner and the protection from the external environment to prevent the degradation (17, 18). In addition, the crucial role played by the binding of chemokines to glycosaminoglycans (GAG) on chemokine functions is well established (10, 19). SDF-1/CXCL12 binds selectively to the sulphated regions of heparan sulphate (HS), a GAG found ubiquitously at the cell surface and in the extracellular matrix (ECM), and to heparin (a chemically related GAG). This binding enhances the local concentration of chemokines in the vicinity of the G-protein-coupled receptor or provides a haptotactic gradient of the protein along cell surfaces. Moreover, it has been suggested that HS could protect chemokines from the enzymatic degradation by dipeptidyl peptidase 4 (DPP4) (19).

Chlorite-oxidized oxyamylose (COAM) is a polyanionic polysaccharide derivative that acts as an antiviral (20), antibacterial (21), and as an immunomodulator by interference with glycosaminoglycan (GAG) binding of chemokines (22). The binding potential has varying affinities to a multitude of chemokines in mice (22). Therefore, it was concluded that COAM formed a binding complex with chemokines that influenced chemokine localization and selectivity of leukocyte responses and migration (22). Furthermore, its antimicrobial actions constitute a bonus for conditions in which infections are eminent.

In this study we aimed to investigate the binding of COAM to human SDF-1/CXCL12 and MCP-1/CCL2 and explore its potential role in chemokine delivery in the context of dental pulp tissue engineering.

MATERIALS AND METHODS

Reagents

Recombinant human stromal-cell derived factor-1 (SDF-1/CXCL12), and recombinant human monocyte chemotactic protein (MCP-1/CCL2) were purchased from Peprotech (Peprotech, USA). Heparan sulphate fraction was purchased from Iduron (Iduron, UK). Enzyme-linked immunosorbent assay (ELISA) kits were purchased from R&D Systems (R&D Systems, UK). Antibodies for flow cytometry were purchased as follows: PE/Cyanine7 CD34 antibody, APC CD73 antibody, Brilliant Violet 785™ CD90 antibody, PE/Cyanine5 CD29 antibody, Brilliant Violet 421™ CD184 (CXCR4) antibody, and Zombie Aqua™ fixable viability kit (Biolegend Europe, Amsterdam), PE-STRO1 antibody (Abcam, UK), BU395 CD31 antibody, APC-R700 CD45 (BD Bioscience, USA). Bromodeoxyuridine (BrdU) was purchased from ThermoFisher (ThermoFisher,

160 USA). Monoclonal Anti-BrdU antibody was purchased from Sigma-Aldrich (Sigma-Aldrich, USA).

COAM synthesis

Chlorite-oxidized oxyamylose (COAM) was synthesised by two-step oxidation of amylose, purified, and fractionated according to molecular weight (MW) as described previously (20, 23). COAM was endotoxin-free and used as MW mixture (corresponding to protein molecular equivalent weights exceeding 100 kDa). Fluorescent labelling of COAM was performed to examine the release of COAM from the hydrogels. COAM was fluorescently labelled with Alexa Fluor™ 488 (Invitrogen). After labelling, the free dye was removed by gel filtration chromatography on a PD10 column (GE Healthcare, Sweden).

Chemokine-binding assay

Gel Filtration Chromatography

SDF-1/CXCL12 alone (MW ~ 8kDa), the mixture of high MW COAM (>200 kDa) and SDF-1/CXCL12, the mix of heparan sulfate (MW ~ 40kDa) and SDF-1/CXCL12, MCP-1/CCL2 alone (MW ~ 8kDa), the mixture of high MW COAM and MCP-1/CCL2, or the mixture of heparan sulfate and MCP-1/CCL2 were applied consecutively on a Superdex 200 10/300 GL column (GE Healthcare, Sweden) in 0.1 M NH_4CO_3 , pH 7.8, and fractionated at a flow rate of 0.3 ml/min. A 100 ng of each chemokine was used while 400 μg of COAM or heparan sulfate was added. Calibration of the chromatography columns was with a protein mixture containing thyroglobulin (669 kDa), IgG (150 kDa), BSA (67 kDa), and cytochrome c (13 kDa), all purchased from Sigma-Aldrich. All fractions were analysed by enzyme-linked immunosorbent assay (ELISA) assay for the presence of SDF-1/CXCL12 and MCP-1/CCL2.

Hydrogel composition and preparation

Fibrin hydrogels were prepared by mixing fibrinogen and thrombin components in equal volumes, as described previously (24). Plasminogen-depleted fibrinogen (Enzyme Research Laboratories, USA), derived from human plasma, was dissolved in 20 mM HEPES and 150 mM NaCl (fibrinogen buffer). Sterile stock solutions of thrombin (Sigma, USA), derived from human plasma, and factor XIII (Fibrogammin, CSL Behring, Germany) were prepared in 20 mM HEPES, 150 mM NaCl, 40 mM CaCl_2 , and 0.1% BSA (thrombin buffer). Thrombin and factor XIII were mixed with the thrombin buffer and were kept in a water bath at 37 °C for 30 min to activate factor XIII to factor XIIIa. The control fibrin hydrogels were prepared at 3.5 mg/ml fibrinogen, 0.1 U/ml thrombin,

and 0.1 U/ml factor XIII, whereas the test fibrin hydrogels were prepared at 3.5 mg/ml fibrinogen, 0.1 U/ml thrombin, 0.1 U/ml factor XIII, and 1 mg/ml COAM (Fibrin-COAM hydrogel), or 2 µg SDF-1/CXCL12 with 1mg/ml COAM (Fibrin-SDF-1 hydrogel).

Chemokine release and release kinetics

Fibrin hydrogels, 100 µl each with 3.5 mg/ml fibrinogen were prepared in 96 well plates as follows: 1- devoid of molecules (negative control), 2- encapsulating SDF-1/CXCL12 at 2 µg/ml alone, or 3- SDF-1/CXCL12 at 2 µg/ml and COAM at 1 mg/ml. The hydrogels were left to polymerise for 30 minutes at 37 °C, and they were immersed in PBS and placed in a shaker incubator at 37 °C. At 30 minutes, 2 hours, 1 day, 4, 7, 10, and 14 days, 200 µl of supernatant from each well was collected and immediately frozen at -80 °C, and fresh PBS was added to replace the removed volume. COAM content was directly quantified in the supernatant at an excitation-emission wavelength of 499-520 nm. SDF-1/CXCL12 content in the supernatant was quantified using an ELISA assay. The following mathematical models (zero-order, first-order, Higuchi, Korsmeyer-Peppas or Peppas-Salin) were fit to explore the chemokine release kinetics from the hydrogels.

Primary cell cultures and flow cytometry characterisation

Dental pulp tissues were acquired with informed consent from patients (15–20 years of age, male and female) undergoing extraction of third molars for therapeutic or orthodontic reasons. Written informed consent was obtained from the patients and their parents, as approved by the Commission for Medical Ethics of KU Leuven (file number S54254). Pulp tissue was obtained with forceps after mechanically fracturing the extracted and disinfected tooth with surgical chisels. Pulp tissue was rinsed and transported at 37 °C in αMEM supplemented with 2 mM L-glutamine, 100 U/ml penicillin, 100 µg/ml streptomycin and 10% fetal bovine serum (FBS). According to the explant method, human dental pulp stromal cells (hDPSCs) were isolated and expanded in culture as described previously (25). Cells were cultured in serum-free mesenchymal stem cells (MSCs) medium (MesenCult-ACF plus medium, Stem Cell Technologies, Canada) supplemented with 2 mM L-glutamine. Only mycoplasma negative cells, screened with the Plasmotest™ kit (InvivoGen), were used. All hDPSCs cultures were tested for the expression of the following mesenchymal cell markers at the protein level by flow cytometry (FACS) for CD29, CD73, CD90, STRO-1, CD184 (CXCR4), CD31, CD34 and CD45. Cells were used in the experiments at passage 5.

162 **Effect of encapsulation on dental pulp stromal cell phenotype**

At baseline, the phenotype of hDPSCs was characterized using FACS for the following markers: CD29, CD73, CD90, STRO-1, CXCR4, CD31, CD34 and CD45. hDPSCs at 1×10^6 cells/ml seeding density were encapsulated in 200 μ l hydrogels ($n=4$ per group and time point) of the three groups described above (hydrogel preparation) and deposited in a 48 well plate (TPP Tissue Culture Plates, Sigma-Aldrich). After gelation, 500 μ l of serum-free mesenchymal stem cell (MSC) medium (MesenCult-ACF Plus Medium, Stem Cell Technologies, Canada) supplemented with 2 mM L-glutamine was added to each well. After 7 days in culture, fibrin hydrogels were digested in a 50 FU/ml nattokinase buffer in 5mM EDTA in PBS for 2 h at 37 °C, and the cells were retrieved for FACS analysis.

Effect of encapsulation on dental pulp stromal cell proliferation in vitro

hDPSCs in culture were incubated with CellTrace™ violet at 5 μ M in phosphate-buffered saline (PBS) for 20 minutes at 37 °C. hDPSCs at 1×10^6 cells/ml seeding density were encapsulated in 200 μ l hydrogels ($n=4$ per group and time point) of the three groups described above (hydrogel preparation) and deposited in a 48 well plate (TPP Tissue Culture Plates, Sigma-Aldrich). After gelation, 500 μ l of serum-free mesenchymal stem cell (MSC) medium (MesenCult-ACF Plus Medium, Stem Cell Technologies, Canada) supplemented with 2 mM L-glutamine, was added to each well. After 7 days in culture, fibrin hydrogels were digested in a 50 FU/ml nattokinase buffer in 5mM EDTA in PBS for 2 h at 37 °C, and the cells were retrieved for FACS analysis.

Flow Cytometry Analysis

Flow cytometry was used to identify and quantify hDPSCs markers before encapsulation and after culture within the hydrogels with the different formulations. For baseline characterisation, hDPSCs seeded in 175-cm² culture flasks were harvested by trypsinisation. For characterisation after encapsulation, the cells were harvested according to the protocol described above. To remove any hydrogel debris, cells were filtered through a 40- μ m cell strainer (BD Falcon, Corning, NY, USA). Harvested cells were counted with NucleoCounter®. For each staining, 0.5×10^5 cells were washed once with PBS containing 2% FBS and 2 mM ethylenediaminetetraacetic acid (EDTA) (FACS buffer). They were incubated for 30 min at room temperature in FACS buffer to allow re-expression of receptor proteins at the cell surface. Then, the cells were incubated in FACS blocking buffer for 15 mins at room temperature to prevent non-specific stain-

ing. The following groups were established: negative control (no staining), live/dead (1:1, and stained with Zombie Acqua), panel 1 (multi-staining, including cells labelled with CellTrace™), panel 2 (multi-staining without CellTrace™). The cells were then incubated with fluorescently labelled antibody cocktails (see Table 1) for 30 mins at 4 °C. As a final step, the cells were washed and resuspended in 300µl FACS buffer. Flow cytometry was performed using a BD LSRFortessa X-20 (BD Bioscience). A compensation matrix was established based on single-stained beads and negative controls to ensure proper gating and identification of the different cell populations of interest. FACS data were analysed with FlowJo software (version 10, FlowJo LLC, USA). Proliferation modelling was performed in FlowJo software (version 10, FlowJo LLC, USA).

Dental pulp cell response to functionalised hydrogels in an *ex-vivo* human tooth model

Teeth sampling and culturing

The samples were gathered after approval by the Commission for Medical Ethics of KU Leuven (file number S54254) and following informed consent from the donors. Fully impacted immature human third molars were collected immediately after extraction from seven healthy young patients (15-22 years old). A total of 16 teeth were used in the experiment. In the surgery room, the teeth were placed immediately after extraction in 50 ml centrifuge tubes (VWR, Leuven, Belgium), containing Dulbecco's Modified Eagle Medium (DMEM; Gibco, Merelbeke, Belgium) supplemented with 10% Fetal Bovine Serum (FBS; Gibco), 1% penicillin-streptomycin (Gibco) and 1% amphotericin B (Gibco)

Table 1: Panels and antibodies used for flow cytometry

Panel number	Antibody	Label	Laser	Concentration
1	CD31	BUV395	355nm	1:100
1	Proliferation marker	CellTrace violet	405nm	5µM
1	CD34	PE/Cy7	561nm	1:100
1	STRO-1	PE	561nm	1:100
1	CD73	APC	640nm	1:1000
1	Viability marker	Zombie Acqua	405nm	1:4000
2	CD90	BV786	405nm	1:200
2	CD184 (CXCR4)	BV421	405nm	1:100
2	CD29	PE/Cy5	561nm	1:1000
2	CD45	APC-700	640nm	1:100
2	Viability marker	Zombie Acqua	405nm	1:4000

164 (tooth-culture medium). The samples were brought to the cell-culture room within 2 h to proceed with the cell culture experiments.

Once in the cell culture room, all teeth were rinsed with sterile Phosphate Buffered Saline (PBS; Sigma Aldrich, St. Louis, MO, USA) for 1 min, upon which they were then placed in the tooth-culture medium until further processed. The periodontal ligament was removed with a sterile #15 scalpel blade (Swann Morton, Sheffield, UK). After cleaning, the teeth were handled with sterile gauzes (Yibon Medical, Kuurne, Belgium) soaked in a tooth-culture medium to avoid desiccation.

Ex-vivo human tooth-culture pulp-capping assay

Figure 1 shows an example of the process. Sixteen teeth from seven different patients were gathered and handled as described above. Once the teeth were cleaned, a pulp-capping procedure was performed in a sterile condition. A class-I cavity was cut using a sterile bur (1.1 mm in diameter; Endo Access Bur Size 1, A 0164 300 001 00, Dentsply Sirona, Ballaigues, Switzerland) under high-speed copious irrigation with sterile saline (Fresenius Kabi, Bad Homburg, Germany). At low speed, the pulp was exposed with a round carbide bur (1.0 mm in diameter; H1SE.205.010, Komet, Lemgo, Germany) with abundant irrigation. Afterwards, the cavity was cleaned with sterile saline and gently dried with sterile cotton pellets.

The teeth were divided into four groups depending on the pulp-capping procedure carried out: (1) application of fibrin hydrogel (negative control), (2) application of pure calcium hydroxide (positive control), (3) application of fibrin-COAM hydrogel, and (4) application of fibrin-COAM-SDF-1 hydrogel.

The cavity was restored with glass-ionomer cement (Fuji triage Capsules, GC). Next, flowable composite (G-aenial Flo, GC) was applied on the occlusal surface, in which a sterilised stainless steel orthodontic wire (M form; ORM-CO, Orange, CA, USA) was seated, followed by 40-s light-curing of the flowable composite using a light-curing unit with a light output of 1200 mW/cm² (Bluephase 20i, Ivoclar Vivadent, Schaan, Liechtenstein). The teeth were immediately hanged (Figure 1D) using the wire in separate wells of 24-well culture plates (Costar, Cambridge, MA, USA), each containing 1.5 ml of tooth-culture medium containing 1 mg/mL bromodeoxyuridine (BrdU) for the first 24 hours to label the proliferating cells and ensure exposure of the pulp tissue to the medium. The teeth were then further cultured in the same medium without BrdU. The medium was refreshed every day, and after 1 day and 14 days, the wire was removed, and the teeth (n=3 per time point and hydrogel) were immediately placed in 4% PFA for two weeks to fix the tissue properly.

Ex-vivo human tooth-culture model- histology

The chemically fixed teeth were demineralised (4–6 weeks) with 10% formic acid (Chem-Lab Analytical, Zedelgem, Belgium) with the decalcifying solution refreshed every 3 days. The decalcification endpoint was determined by dental radiography (MINRAY, Soredex, Tuusula, Finland) and visual/tactile evaluation. After decalcification, the glass ionomer and composite restorations were manually removed, upon which the teeth were subsequently immersed in water for 24 h and then dehydrated in ascending concentrations of ethanol (70% for 12 h, 80%, 95% and 100% for 2 h each), followed by xylene (VWR) clearance. The teeth were next immersed in liquid paraffin (56°C melting point; Paraclean, Klinipath, Duiven, The Netherlands) for 24 h before being embedded in paraffin blocks. Serial paraffin sections were cut with a thickness of 7-9 μm using a microtome (Microm HM 360 Microtome, Hyland Scientific, Stanwood, WA, USA), this from the level where the interaction of the pulp-capping agent and the pulp tissue first appeared until any interaction was no longer visible. Every six sequential sections, two sections were selected for staining with Gill's III hematoxylin (Leica Microsystems, Diegem, Belgium) and with 1% aqueous eosin solution (Leica Microsystems). The stained sections were examined using light microscopy (Axio Imager M2, Carl Zeiss Microscopy, Jena, Germany).

Statistical analysis

Statistical analysis was performed using GraphPad Prism for MacOS, version 9.0. (GraphPad Software, La Jolla California, USA). The effect of COAM presence on the release of SDF-1/CXCL12 from fibrin hydrogels was tested with the use of a one-way Analysis of Variance (ANOVA) and area under the curve analysis (AUC). All ANOVA tests were followed by Tukey's correction for multiple comparisons. Statistical significance was determined at $p < 0.05$. Descriptive statistics are represented as the mean and standard deviation (\pm).

RESULTS**COAM binds efficiently SDF-1/CXCL12
but less MCP-1/CCL2 in solution**

Gel chromatography showed that COAM forms a strong binding complex with SDF-1 (Figure 2A), while this was not observed for MCP-1 (Figure 2B). The recovery of SDF-1, when added with COAM, was 9-fold and 36-fold higher than heparan sulphate and the control, respectively. Almost all SDF-1 immunoreactivity was observed in the region corresponding to the high molecular weight of COAM (Figure 2A). As a contrast MCP-1 recovery when added with

166 COAM was 3-fold and 1-fold higher than heparan sulphate and the control, respectively. The MCP-1 immunoreactivity in the region corresponding to the molecular weight COAM was not different from immunoreactivity in the region of the free MCP-1 (Figure 2B). Therefore, it was concluded that COAM did not form a binding complex with MCP-1 in solution even though it showed the highest recovery rates. Based on these results, only SDF-1 was used in the following experiments.

COAM-SDF-1 binding affects the pattern of SDF-1 release

The *in-vitro* release of SDF-1 from fibrin hydrogels with or without COAM was investigated with the use of ELISA for up to 14 days. The formulations exhibited similar overall release trends with differences in the rate (Figure 3A). There was a significant effect on SDF-1 release at the $p < 0.05$ level for the time [F (6, 70) = 87.09, $p < 0.0001$] and the interaction between time and COAM [F (6, 70) = 27.63, $p < 0.0001$]. The presence of COAM resulted in shifting the peak of SDF-1 release from 2h to 24h (Figure 3A). This observation was confirmed with the post hoc comparisons using the Tukey test, showing that the SDF-1 release was significantly reduced in the presence of COAM at 30 min and 2h ($p < 0.05$) and increased at D1 and D4 ($p < 0.05$) (Figure 3A). The release pattern of SDF-1 from the fibrin hydrogels with COAM closely resembled the release pattern of COAM (Figure 3B), confirming further the formation of a binding complex.

Furthermore, the initial fast release phase was followed by a second slow release phase characterised by decreased release rate, and the average cumulative maximum release reached near-constant after 96 h (Figure 3C). The release percentage of the dose resulted in 0.028% and 0.025% for SDF-1 alone and with COAM, respectively. AUC analysis for SDF-1 cumulative release showed a higher fractional release from simple fibrin hydrogels ($p < 0.05$) and suggested COAM involvement in SDF-1 retention (Figure 3D). The best fitting of release kinetics model, especially for SDF-1/COAM, was achieved with the Korsmeyer-Peppas model (Figure 3E). The exponent value of SDF-1/COAM (0.658) was between $0.45 < B < 0.89$ (Figure 3F), suggesting the non-Fickian models or anomalous transport, thus a mechanism of drug release governed by diffusion and swelling with comparable rates.

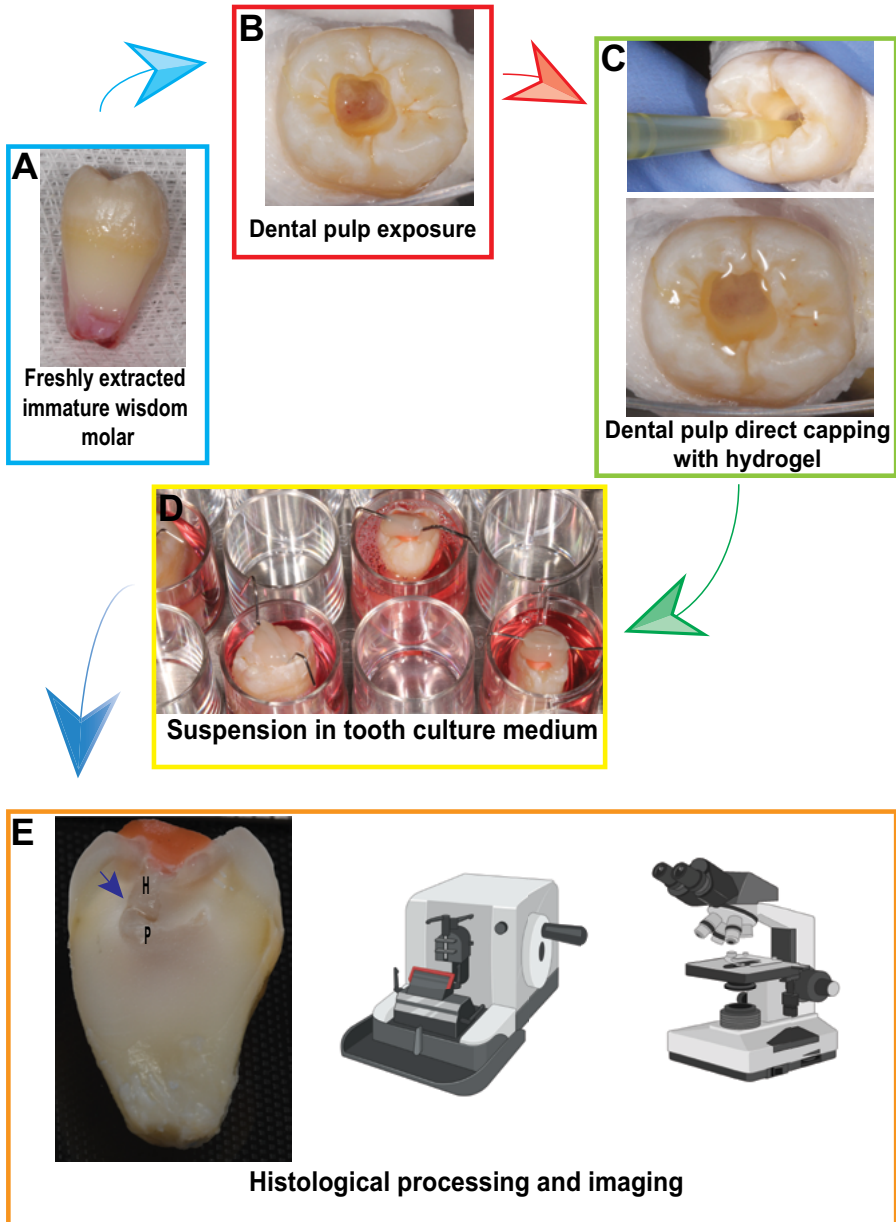


Figure 1: *Ex-vivo* human tooth-culture-pulp-capping assay. (A) Fresh extracted immature wisdom molar after cleaning and removal of the periodontal ligaments, (B) dental pulp exposure, (C) filling the cavity with fibrin hydrogel in contact with the pulp tissue, (D) restoring the tooth and suspension in tooth culture medium, (E) collecting the teeth and preparation for histology, note the contact between the hydrogel (H) and the pulp tissue (P) at the blue arrow.

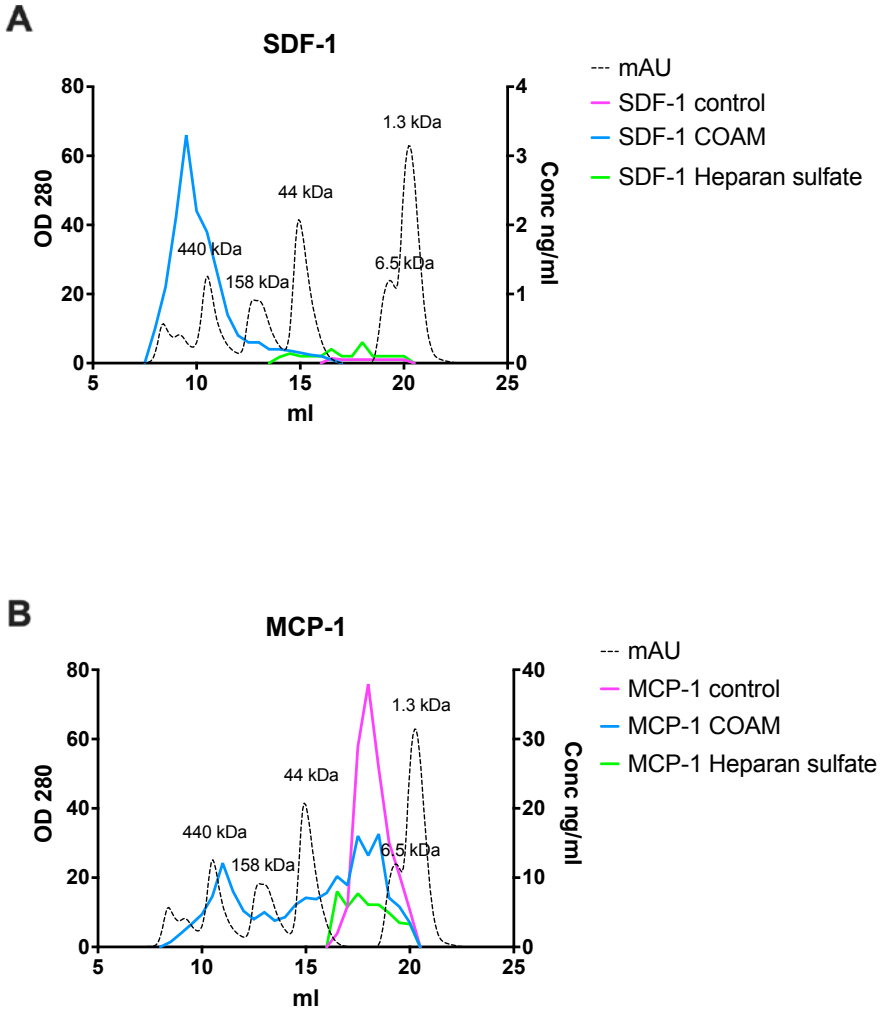


Figure 2: Chemokine binding assay. (A) Formation of a binding complex between COAM and SDF-1/CXCL12 is characterized by a peak at the region of high molecular weight (blue peak), (B) the absence of a binding complex between COAM and MCP-1/CCL2 as well as heparan sulphate.

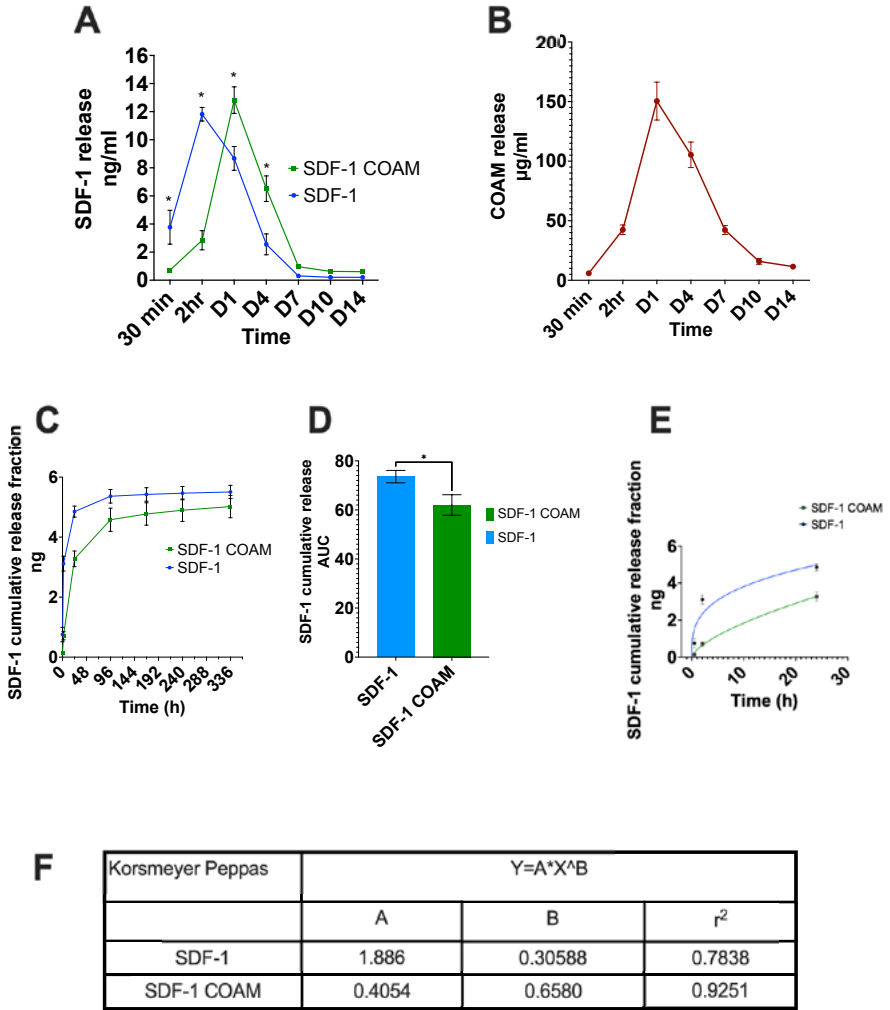


Figure 3: SDF-1/CXCL12 and COAM release patterns from fibrin hydrogel. (A) SDF-1/CXCL12 release from fibrin hydrogels with and without COAM up to 14 days, (B) COAM release from fibrin hydrogels, (C) cumulative release of SDF-1/CXCL12 release from fibrin hydrogels with and without COAM up to 14 days, (D) area under the curve (AUC) for (C), (E & F) release kinetics model fit to release up to 24h.

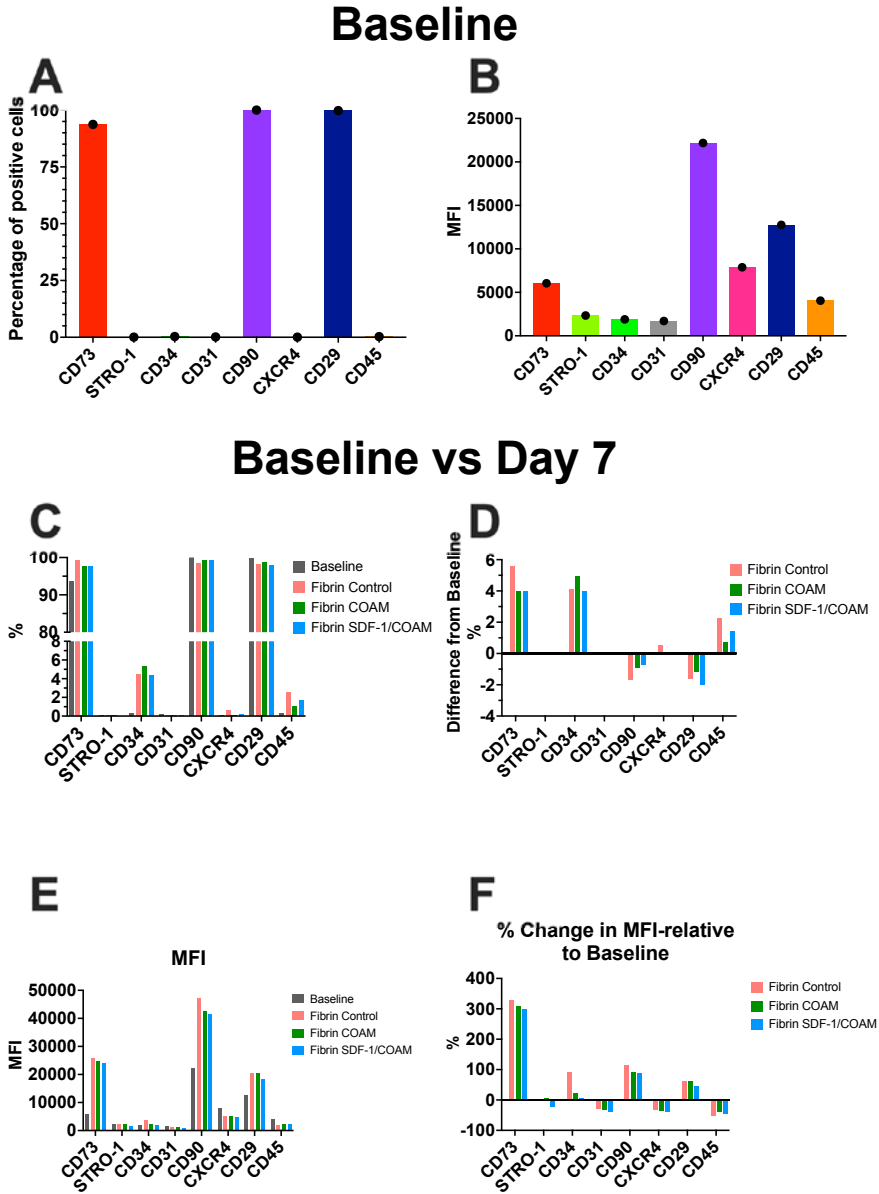


Figure 4: Flowcytometry characterization and analysis. (A) Percentage of positive cells for the corresponding antibodies, (B) median fluorescent intensity (MFI) as expressed at baseline, (C-F) phenotype characterization after harvesting the cells at D7 from the hydrogels compared to baseline.

Effect of encapsulation on dental pulp stromal cells phenotype

At baseline, hDPSCs showed a typical mesenchymal stromal cell (MSCs) phenotype. hDPSCs were positive for CD73, CD90, CD29, and CD105 and negative for CD34, CD31, CD45 (Figure 4A & B). hDPSCs characterised in this study were also negative for STRO-1 and CXCR4 (Figure 4A).

After 7 days of encapsulation, hDPSCs from the different experimental groups still stained positive for CD73, CD90, CD29 and negative for CD31. A change in CD45 and CD34 staining was observed by the emergence of small positively stained populations in the 3 experimental groups (Figure 4C & D). The percentage of CD45⁺ populations was around 2% which may be neglected. However, after 7 days the CD34⁺ populations increased from 0.3% to 4.4%, 5.3%, and 4.3% for fibrin control, fibrin COAM and fibrin SDF-1/COAM, respectively (Figure 4C & D). Moreover, the median fluorescent intensity (MFI) increased by 91.1%, 20.9%, and 4.7% for fibrin control, fibrin COAM and fibrin SDF-1/COAM, respectively (Figure 4E & F).

In vitro proliferation modelling for encapsulated hDPSCs

Harvested hDPSCs labelled with CellTrace™ were analyzed with FACS at day 7 to evaluate the effects of 3D encapsulation in fibrin hydrogels with different formulations on cell proliferation. A proliferation model was fit to the distributions of the signal of the cells harvested from the three groups while defining the cells' signal at baseline in addition to the background autofluorescence signal (Figure 5A-D). hDPSCs in the fibrin control hydrogels showed the highest percent of divided cells of 71.5%, followed by 70.3% for fibrin SDF-1/COAM and 64.1% for fibrin COAM. The average number of divisions that all responding cells have undergone since the initiation of the encapsulation is described using the proliferation index (PI). The PIs were 2.6, 2.3, and 2.5 for control, COAM, and SDF-1/COAM groups. The parameters derived from the proliferation models are listed in Table 2.

Table 2: Parameters derived from the proliferation models

Parameter	Fibrin control	Fibrin COAM	Fibrin SDF-1/COAM
Percent Divided	71.5	64.1	70.3
Proliferation Index	2.6	2.3	2.5
Division Index	1.9	1.5	1.8
Expansion Index	7.3	5.3	6.4
Replication Index	9.8	7.7	8.8

Dental pulp cells response to functionalised hydrogels in an *ex-vivo* human tooth model

Preliminary results for the pulp response at day 14 from H&E staining are presented in Figure 6. Pure calcium hydroxide cement (CaOH₂) elected a defensive mineralization response within the pulp evident from the mineralization foci observed (Figure 6A). Very few cells are observed within the core of the pulp with signs of pulp tissue disintegration (Figure 6A). The pulp cells appeared not to react to the fibrin hydrogel without COAM or SDF-1 (Figure 6B). Further, in the teeth treated with fibrin SDF-1/COAM several blood vessels in the vicinity of the exposure/hydrogel area can be observed (Figure 6D).

DISCUSSION

The chemokine system together with the chemo-attracted cells play a central role in tissue repair and regeneration. Not only differentiated immune effector cells in the fight against infections but also bone-marrow-derived hematogenic precursor cells are playing a role in regeneration. Therefore, the immune response to tissue injury is critical in determining the rate and the outcome of the healing process, including the extent of repair and the restoration of function (18). Modulating immune components through biomaterials and drug delivery systems have become attractive approaches in tissue engineering and regenerative medicine (TERM), especially since therapies based on stem cells and growth factors have not yet proven to be widely practical or effective in the clinic (17, 18, 26). For the design of immunomodulatory biomaterials or drug delivery systems one needs to consider the physicochemical properties of the biomaterials and the inclusion of pro-inflammatory and anti-inflammatory modulators to guide the tissue through the inflammation phase into the resolution phase leading to tissue regeneration (17, 18, 27).

In the current study, we tested the application of COAM in a biomaterial drug delivery system intended for dental pulp tissue engineering. COAM is a polyanionic polysaccharide derivative with antimicrobial properties (21, 28, 29) that acts as an immunomodulator by interference with glycosaminoglycan (GAG) binding of chemokines (22). In previous work, we have demonstrated the compatibility of COAM with a tailored fibrin hydrogel in addition to the characterization of several physicochemical properties of the hydrogel system and the biocompatibility of COAM with hDPSCs (24). In the present study, we focused on the binding and delivery characteristics of two chemokines of interest, namely SDF-1/CXCL12 and MCP-1/CCL2. We showed that COAM forms a binding complex with SDF-1/CXCL12, while this was not the case for MCP-1/CCL2. Moreover, with the gel chromatography data we showed that human

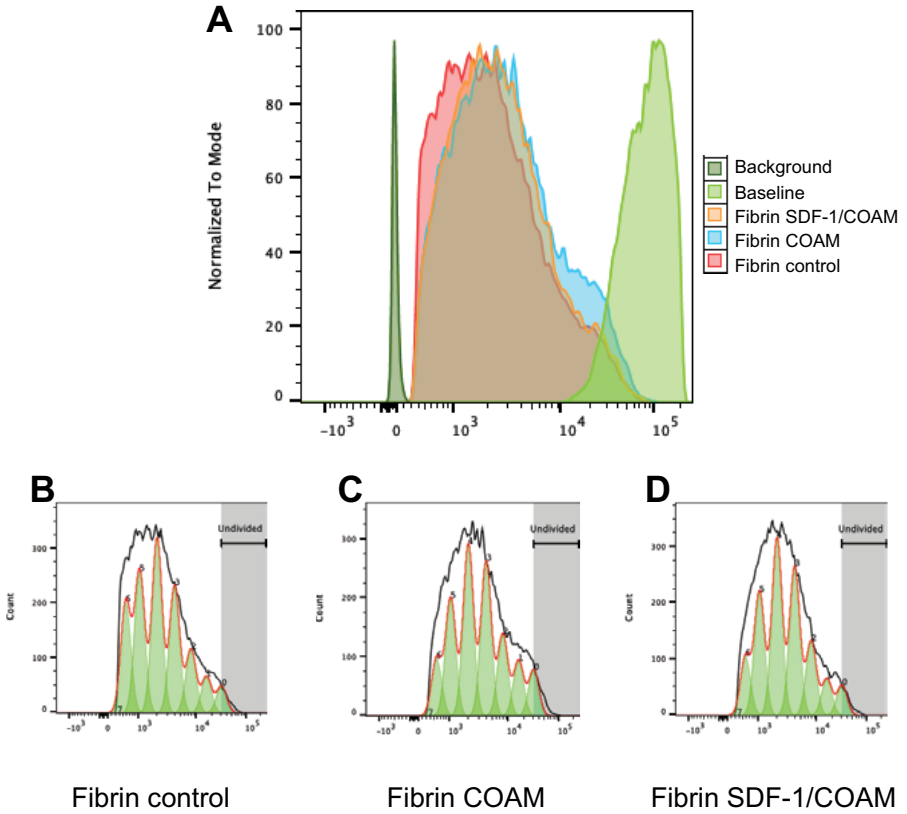


Figure 5: Effect of encapsulation and different hydrogel formulations on hDPSCs proliferation, (A) Distribution of signal intensity for labelled cells at baseline, the three experimental groups and un-labelled cells (autofluorescence background signal), (B) proliferation model for cells harvested from fibrin control hydrogels at D7, (C) proliferation model for cells harvested from fibrin COAM hydrogels at D7, (D) proliferation model for cells harvested from SDF-1/COAM hydrogels at D7.

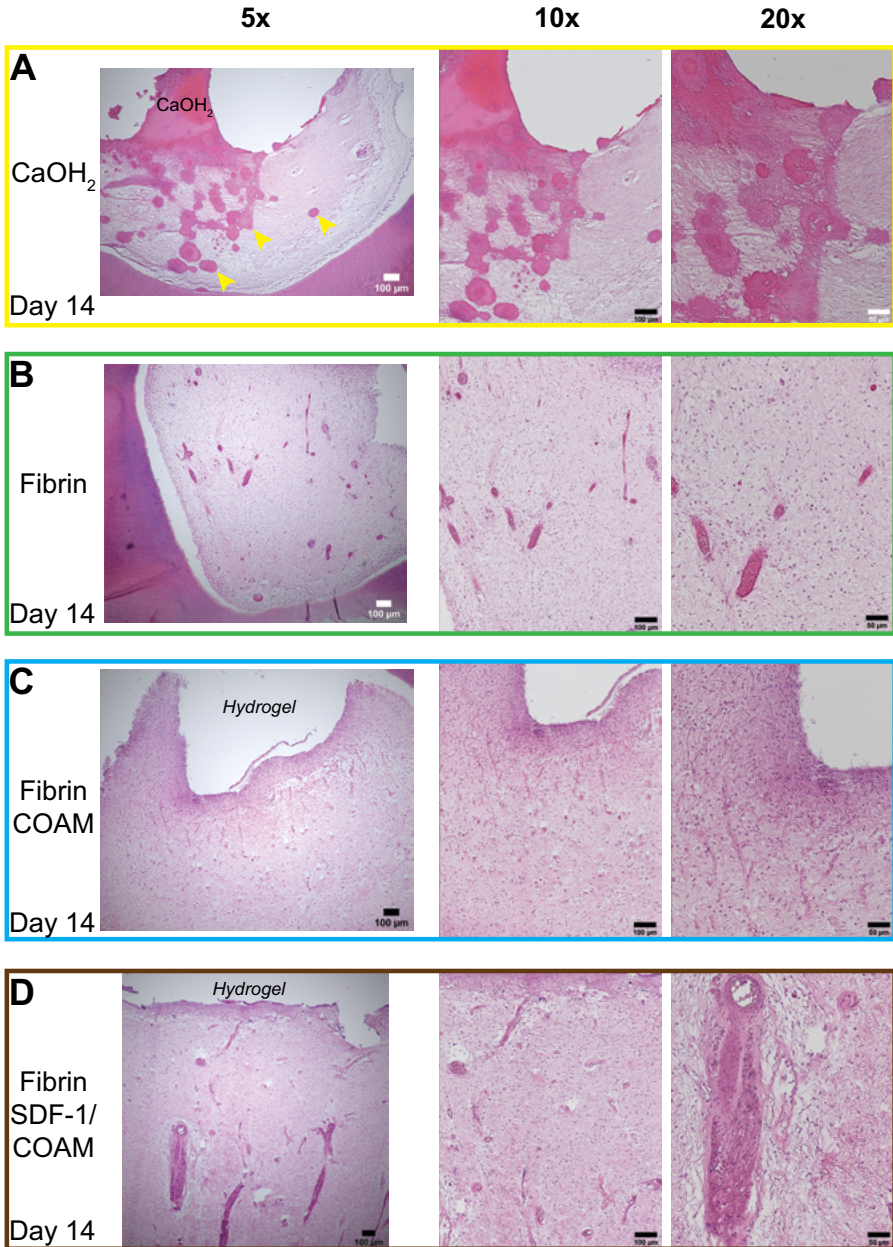


Figure 6: Dental pulp cells response to functionalised hydrogels after 14 days (H&E staining), (A) response to pure calcium hydroxide cement. Note the formation of mineralization foci (yellow arrowheads) and the loss of cellularity, (B, C & D) pulp cells do not respond by forming mineralization foci to fibrin hydrogels

SDF-1/CXCL12 formed a binding complex to COAM and not to the GAG heparan sulphate (HS). MCP-1/CCL2 was found not to bind to either COAM or heparan sulphate, in line with previously published data using surface plasmon resonance technology (22). Indeed, with previous work we demonstrated that COAM forms a binding complex with mouse CXCL6 with a higher affinity than HS and chondroitin sulphate (28). COAM has GAG-mimetic functions by binding CXCL1, CXCL2, CXCL6, CXCL10, CXCL11, and CCL5 (22).

Farges et al., reported seventeen chemokine genes to be expressed in the dental pulp (30). The most frequently expressed in their study were SDF-1/CXCL12, MCP-1/CCL2, CXCL9, CX3CL1, CCL8, CXCL10, CCL16, and CCL5 (30). In the same study, 9 receptor genes were expressed in the dental pulp. The most frequently expressed were CXCR4, CCR1, CCRL1, CXCR6 (30). Moreover, CXCR4 is expressed perivascularly in the apical papilla (31), and in cells isolated from the apical papilla (SCAPs) (32). Therefore, the SDF-1/CXCR4 axis is a potential therapeutic target for dental pulp repair and regeneration.

GAGs are present in the ECM, forming a negatively charged matrix that allows interaction with positively charged protein structures such as chemokines (10). This binding enhances the local concentration of chemokines in the vicinity of the G-protein-coupled receptor or provides a haptotactic gradient of the protein along cell surfaces (10). Furthermore, it has been suggested that interaction of SDF-1/CXCL12 with GAGs is critical for its *in vivo* function because this interaction protects SDF-1/CXCL12 from NH₂-terminal truncation and inactivation by dipeptidyl peptidase 4 (DPP4) (CD26) (19, 33, 34). Therefore, based on the data presented, GAG-mimetic binding through COAM could mimic the presentation of SDF-1/CXCL12 in the ECM and provide protection against instant deactivation through proteases. Future work will focus on gaining a deeper understanding of the mechanism and kinetics of COAM binding to SDF-1/CXCL12 through surface plasmon resonance technology. Furthermore, we will investigate if COAM will protect SDF-1/CXCL12 from NH₂-terminal truncation and inactivation by CD26.

The release data demonstrated that the formation of the binding complex between COAM and SDF-1/CXCL12 affected the pattern of SDF-1/CXCL12 release from fibrin hydrogels. Moreover, the release pattern confirmed the binding data as the SDF-1/CXCL12 release pattern matched that of COAM. COAM binding resulted in a delayed-release and retention of SDF-1/CXCL12. Considering the water-soluble behavior of SDF-1, its release should mainly be governed by a diffusion process. The study of drug release kinetic fitting of the most common mathematical models (zero-order, first-order, Higuchi, Korsmeyer-Peppas or Peppas-Salin) finds some limitations due to the low dose per-

176 centage released that could be related to the experimental set-up and the rapid reaching of the plateau in the cumulative release. Nevertheless, the following analysis approach was tried, considering just the initial portion of the graph. The best fitting, especially for SDF-1/COAM, was achieved with the Korsmeyer-Peppas model. Since this model could be applied to fit the data until the 60% release of the initial dose and the presented data are far from that point, further considerations should be intended as hypotheses. The power law is a semi-empirical equation used to describe drug release from polymeric systems and is based on an exponential relationship between the release and the time. It is used when more than one mechanism is involved in the release process and, depending on the exponent value, it is possible to observe behaviors governed by Fickian or Non-Fickian models. In particular, the exponent value of SDF-1/COAM (0.658) was between $0.45 < B < 0.89$, suggesting the non-Fickian models or anomalous transport, thus a mechanism of drug release governed by diffusion and swelling with comparable rates. The rearrangement of polymeric chains occurring slowly and the diffusion process simultaneously cause the time-dependent anomalous effects (35).

Heparin-based polyethylene glycol (PEG) hydrogels were used for the sustained delivery of SDF-1/CXCL12 and to successfully attract circulating pro-angiogenic cells (36). PEG-heparin hydrogels were prepared, then soaked in a solution containing fluorescent labelled SDF-1/CXCL12 and observed using laser scanning confocal microscopy up to 24 hours. It was then concluded that successful loading was related to the presence of heparin (36). In our study, we observed SDF-1/CXCL12 release from fibrin hydrogels suggesting that SDF-1/CXCL12 can be loaded in simple hydrogels. However, the main issue is the sustained, controlled release and most importantly the protection from enzymatic degradation. Moreover, in the study by Porokoph et al., the release rate of SDF-1/CXCL12 at 2.5 µg/ml from PEG-heparin hydrogels (36) was similar to the fibrin hydrogels without COAM in the current study, with the release peak in the first hours. Moreover, the preparation of MMP-cleavable hydrogels only increased the fraction of release but not the rate (36). In the current study, the presence of COAM resulted in a delayed release of SDF-1/COAM up to day 4. Our experimental setup did not allow for hydrogel degradation that resulted in a low release fraction. Future work will evaluate the application of the proposed chemokine delivery system in vivo.

Dental pulp stem/stromal cells (DPSCs) are classified as mesenchymal stem/stromal cells (MSCs) and subsequently inherited a terminology issue; are they stem cells or multipotent stromal cells? The International Society of Cellular Therapies recommended the terminology "multipotent mesenchymal stromal cells" instead, defining these as clonogenic, multipotent, self-renew-

ing cells that express CD105, CD73, and CD90, but not CD45, CD34, CD14, CD11b, CD79 α , or HLA-DR, and are capable of osteogenic, chondrogenic and adipogenic differentiation (37). Nevertheless, these cells are still referred to as dental pulp stem cells throughout the literature as this issue continues to be discussed. In the current study, hDPSCs are used as a heterogeneous population without sorting, and therefore they are considered dental pulp stromal cells. One of the aims of the current study was to assess the influence of encapsulation in fibrin hydrogels with different formulations on the phenotype of hDPSCs. Overall, hDPSCs maintained their phenotype except for the emergence of a small CD34⁺ population. CD34 is a transmembrane phosphoglycoprotein, first identified on hematopoietic stem and progenitor cells (38). CD34 is mainly regarded as a marker of hematopoietic stem cells (HSCs) and hematopoietic progenitor cells. However, CD34 has been suggested as a marker of several other nonhematopoietic cell types, including vascular endothelial progenitors and embryonic fibroblasts (38). In fact, CD34⁺ MSCs exhibit a high proliferative capacity compared to CD34⁻ MSCs (39). Moreover, CD34⁺/CD90⁺ adipose-derived stem cells (ASCs) could form capillary-like structures and produce high levels of vascular endothelial growth factor (VEGF) when encapsulated in methylcellulose scaffolds (40). Future work will focus on understanding if this CD34⁺ population already exist in the heterogenous hDPSCs or whether it is a result of the encapsulation in fibrin hydrogels.

The SDF-1/CXCR4 pair plays a pivotal role in the homing, proliferation and differentiation of CD34⁺ haematopoietic stem cells (HSCs) (7). The effects of SDF-1/CXCL12 on DPSCs have been reported by several authors. Odontoblastic differentiation was stimulated by SDF-1 activation and repressed by SDF-1/CXCR4 inhibition (13). SDF-1/CXCL12 promoted cell migration and odontoblastic differentiation *in vitro* and had a slight effect on proliferation when added to the culture medium (41). hDPSCs overexpressing SDF-1/CXCL12 showed higher cell proliferation compared to wild-type hDPSCs (42). In the current study, we investigated the effect of the presence of SDF-1/CXCL12 in a 3D microenvironment on the proliferation of hDPSCs while cultured in a serum-free MSCs medium using a flow cytometric assay based on the dilution of carboxyfluorescein diacetate succinimidyl ester. hDPSCs encapsulated in fibrin hydrogels with SDF-1/CXCL12 had a similar proliferation pattern to cells encapsulated in the control hydrogels. However, hDPSCs encapsulated in the control and SDF-1/CXCL12 fibrin gels had a slightly higher percentage of divided cells and proliferation index compared to the hydrogels with only COAM. Previous studies relied on cell counting assays as a measure of proliferation (42). However, cell counting assays cannot be used to determine the precursor frequency nor the distribution of the number of divisions that responding cells underwent (43). Thus, cell counting assays might not be suitable to describe proliferation rather than a measure of cellular viability.

178 Evidence from the *ex-vivo* tooth model studies suggest that DPSCs survive up to 4 weeks inside the pulps of extracted immature wisdom molars when suspended in culture medium (44). Moreover, after induced injury to the odontoblasts, DPSCs migrated from the vicinity of the blood vessels to form reparative dentin (45-47). Therefore, the hypothesis in the current study was that DPSCs would react to a chemokine gradient formed by the release of COAM of SDF-1/COAM binding complex into the pulp exposure area. The results shown are preliminary, as immunostaining for BrdU and CXCR4 is still in progress.

In future experiments we will investigate the expression of CXCR4 and STRO-1 in DPSCs with western blot and immunostaining. Further, the migration of DPSCs and SCAPs towards hydrogels functionalized with SDF-1/CXCL12 will be investigated *in vitro*.

CONCLUSION

COAM formed a binding complex with SDF-1/CXCL12 leading to its delayed release from fibrin hydrogels. Although COAM also has the benefits of a broad antimicrobial agent, the application of COAM as a pharmacological agent in dental tissue regeneration is challenged.

ACKNOWLEDGMENTS

The authors would like to thank Dr. Kathleen Van den Eynde, Bo Corbeels, and Sarah Cumps for their technical assistance with the histological staining and BrdU immunostaining.

REFERENCES

1. Freire MO, You HK, Kook JK, Choi JH, Zadeh HH. Antibody-mediated osseous regeneration: a novel strategy for bioengineering bone by immobilized anti-bone morphogenetic protein-2 antibodies. *Tissue Eng Part A*. 2011;17(23-24):2911-8.
2. Rollins BJ. Chemokines. *Blood*. 1997;90(3):909-28.
3. Wang J, Knaut H. Chemokine signaling in development and disease. *Development*. 2014;141(22):4199-205.
4. Lapidot T, Dar A, Kollet O. How do stem cells find their way home? *Blood*. 2005;106(6):1901-10.
5. Takano T, Li YJ, Kukita A, Yamaza T, Ayukawa Y, Moriyama K, et al. Mesenchymal stem cells markedly suppress inflammatory bone destruction in rats with adjuvant-induced arthritis. *Lab Invest*. 2014;94(3):286-96.
6. Wu Y, Zhao RC. The role of chemokines in mesenchymal stem cell homing to myocardium. *Stem Cell Revi*. 2012;8(1):243-50.
7. Lataillade JJ, Domenech J, Le Bousse-Kerdiles MC. Stromal cell-derived factor-1 (SDF-1)\CXCR4 couple plays multiple roles on haematopoietic progenitors at the border between the old cytokine and new chemokine worlds: survival, cell cycling and trafficking. *Eur Cytokine Net*. 2004;15(3):177-88.

8. Suzuki T, Lee CH, Chen M, Zhao W, Fu SY, Qi JJ, et al. Induced migration of dental pulp stem cells for in vivo pulp regeneration. *J Dent Res.* 2011;90(8):1013-8.
9. De Buck M, Gouwy M, Proost P, Struyf S, Van Damme J. Identification and characterization of MIP-1alpha/CCL3 isoform 2 from bovine serum as a potent monocyte/dendritic cell chemoattractant. *Biochem Pharmacol.* 2013;85(6):789-97.
10. Janssens R, Struyf S, Proost P. The unique structural and functional features of CXCL12. *Cell Mol Immunol.* 2018;15(4):299-311.
11. Loos T, Opdenakker G, Van Damme J, Proost P. Citrullination of CXCL8 increases this chemokine's ability to mobilize neutrophils into the blood circulation. *Haematologica.* 2009;94(10):1346-53.
12. Ruytinx P, Proost P, Van Damme J, Struyf S. Chemokine-Induced Macrophage Polarization in Inflammatory Conditions. *Front Immunol.* 2018;9:1930.
13. Kim DS, Kim YS, Bae WJ, Lee HJ, Chang SW, Kim WS, et al. The role of SDF-1 and CXCR4 on odontoblastic differentiation in human dental pulp cells. *Int Endod J.* 2014;47(6):534-41.
14. Zhuang Z, Yoshizawa-Smith S, Glowacki A, Maltos K, Pacheco C, Shehabeldin M, et al. Induction of M2 Macrophages Prevents Bone Loss in Murine Periodontitis Models. *J Dent Res.* 2019;98(2):200-8.
15. Krieger JR, Ogle ME, McFaline-Figueroa J, Segar CE, Temenoff JS, Botchwey EA. Spatially localized recruitment of anti-inflammatory monocytes by SDF-1 α -releasing hydrogels enhances microvascular network remodeling. *Biomaterials.* 2016;77:280-90.
16. Shen X, Zhang Y, Gu Y, Xu Y, Liu Y, Li B, et al. Sequential and sustained release of SDF-1 and BMP-2 from silk fibroin-nanohydroxyapatite scaffold for the enhancement of bone regeneration. *Biomaterials.* 2016;106:205-16.
17. Browne S, Pandit A. Biomaterial-mediated modification of the local inflammatory environment. *Front Bioeng Biotechnol.* 2015;3:67.
18. Julier Z, Park AJ, Briquez PS, Martino MM. Promoting tissue regeneration by modulating the immune system. *Acta Biomater.* 2017;53:13-28.
19. Sadir R, Imberty A, Baleux F, Lortat-Jacob H. Heparan sulfated/heparin oligosaccharides protect stromal cell-derived factor-1 (SDF-1)/CXCL12 against proteolysis induced by CD26/dipeptidyl peptidase IV. *J Biol Chem.* 2004;279(42):43854-60.
20. Li S, Martens E, Dillen C, Van den Steen PE, Opdenakker G. Virus entry inhibition by chlorite-oxidized oxyamylose versus induction of antiviral interferon by poly(I:C). *Biochem Pharmacol.* 2008;76(7):831-40.
21. Zi Y, Zhu M, Li X, Xu Y, Wei H, Li D, et al. Effects of carboxyl and aldehyde groups on the antibacterial activity of oxidized amylose. *Carbohydr Polym.* 2018;192:118-25.
22. Li S, Pettersson US, Hoorelbeke B, Kolarczkowska E, Schelfhout K, Martens E, et al. Interference with glycosaminoglycan-chemokine interactions with a probe to alter leukocyte recruitment and inflammation in vivo. *PLoS One.* 2014;9(8):e104107.
23. Claes P, Billiau A, De Clercq E, Desmyter J, Schonhe E, Vanderhaeghe H, et al. Polyacetal carboxylic acids: a new group of antiviral polyanions. *J Virol.* 1970;5(3):313-20.
24. EzEldeen M, Toprakhisar B, Murgia D, Smisdorn N, Deschaume O, Bartic C, et al. Chlorite oxidized oxyamylose differentially influences the microstructure of fibrin and self assembling peptide hydrogels as well as dental pulp stem cell behavior. *Sci Rep.* 2021;11(1):5687.
25. Pedano MS, Li X, Jeanneau C, Ghosh M, Yoshihara K, Van Landuyt K, et al. Survival of human dental pulp cells after 4-week culture in human tooth model. *J Dent.* 2019;86:33-40.
26. Sridharan R, Cameron AR, Kelly DJ, Kearney CJ, O'Brien FJ. Biomaterial based modulation of macrophage polarization: a review and suggested design principles. *Materials Today.* 2015;18(6):313-25.
27. Selders GS, Fetz AE, Radic MZ, Bowlin GL. An overview of the role of neutrophils in innate immunity, inflammation and host-biomaterial integration. *Regen Biomater.* 2017;4(1):55-68.
28. Li S, Starckx S, Martens E, Dillen C, Lamerant-Fayel N, Berghmans N, et al. Myeloid cells are tunable by a polyanionic polysaccharide derivative and co-determine host rescue from lethal virus infection. *J Leukoc Biol.* 2010;88(5):1017-29.

29. Claes P, Billiau A, De Clercq E, Desmyter J, Schonne E, Vanderhaeghe H, et al. Polyacetal carboxylic acids: a new group of antiviral polyanions. *J Virol.* 1970;5(3):313-20.
 30. Farges JC, Keller JF, Carrouel F, Durand SH, Romeas A, Bleicher F, et al. Odontoblasts in the dental pulp immune response. *J Exp Zool B Mol Dev Evol.* 2009;312B(5):425-36.
 31. Liu JY, Chen X, Yue L, Huang GT, Zou XY. CXC Chemokine Receptor 4 Is Expressed Paravascularly in Apical Papilla and Coordinates with Stromal Cell-derived Factor-1alpha during Transmigration of Stem Cells from Apical Papilla. *J Endod.* 2015;41(9):1430-6.
 32. Driesen RB, Hilkens P, Smisdom N, Vangansewinkel T, Dillen Y, Ratajczak J, et al. Dental Tissue and Stem Cells Revisited: New Insights From the Expression of Fibroblast Activation Protein-Alpha. *Front Cell Dev Biol.* 2019;7:389.
 33. Metzemaekers M, Van Damme J, Mortier A, Proost P. Regulation of Chemokine Activity - A Focus on the Role of Dipeptidyl Peptidase IV/CD26. *Front Immunol.* 2016;7:483.
 34. Mortier A, Gouwy M, Van Damme J, Proost P, Struyf S. CD26/dipeptidylpeptidase IV-chemokine interactions: double-edged regulation of inflammation and tumor biology. *J Leukoc Biol.* 2016;99(6):955-69.
 35. Bruschi ML. Mathematical models of drug release. Strategies to Modify the Drug Release from Pharmaceutical Systems 2015. p. 63-86.
 36. Prokoph S, Chavakis E, Levental KR, Zieris A, Freudenberg U, Dimmeler S, et al. Sustained delivery of SDF-1alpha from heparin-based hydrogels to attract circulating pro-angiogenic cells. *Biomaterials.* 2012;33(19):4792-800.
 37. Dominici M, Le Blanc K, Mueller I, Slaper-Cortenbach I, Marini F, Krause D, et al. Minimal criteria for defining multipotent mesenchymal stromal cells. The International Society for Cellular Therapy position statement. *Cytotherapy.* 2006;8(4):315-7.
 38. Sidney LE, Branch MJ, Dunphy SE, Dua HS, Hopkinson A. Concise review: evidence for CD34 as a common marker for diverse progenitors. *Stem Cells.* 2014;32(6):1380-9.
 39. Simmons PJ, Torok-Storb B. CD34 expression by stromal precursors in normal human adult bone marrow. *Blood.* 1991;78(11):2848-53.
 40. De Francesco F, Tirino V, Desiderio V, Ferraro G, D'Andrea F, Giuliano M, et al. Human CD34/CD90 ASCs are capable of growing as sphere clusters, producing high levels of VEGF and forming capillaries. *PLoS One.* 2009;4(8):e6537.
 41. Wen Q, Zhao YM, Wang YY, Wang X, Ling L, Ge LH. [Effects of stromal cell-derived factor-1 on proliferation, migration, and odontoblastic differentiation of human dental pulp stem cells]. *Beijing Da Xue Xue Bao Yi Xue Ban.* 2016;48(1):23-9.
 42. Zhu L, Dissanayaka WL, Zhang C. Dental pulp stem cells overexpressing stromal-derived factor-1alpha and vascular endothelial growth factor in dental pulp regeneration. *Clin Oral Investig.* 2019;23(5):2497-509.
 43. Roederer M. Interpretation of cellular proliferation data: avoid the panglossian. *Cytometry A.* 2011;79(2):95-101.
 44. Pedano MS, Li X, Jeanneau C, Ghosh M, Yoshihara K, Van Landuyt K, et al. Survival of human dental pulp cells after 4-week culture in human tooth model. *J Dent.* 2019;86:33-40.
 45. Pedano MS, Li X, Camargo B, Hauben E, De Vleeschauwer S, Yoshihara K, et al. Injectable phosphopullulan-functionalized calcium-silicate cement for pulp-tissue engineering: An in-vivo and ex-vivo study. *Dent Mater.* 2020;36(4):512-26.
 46. Téclès O, Laurent P, Aubut V, About I. Human tooth culture: A study model for reparative dentinogenesis and direct pulp capping materials biocompatibility. *Journal of Biomedical Materials Research Part B: Applied Biomaterials.* 2008;85B(1):180-7.
 47. Téclès O, Laurent P, Zygouritsas S, Burger A-S, Camps J, Dejou J, et al. Activation of human dental pulp progenitor/stem cells in response to odontoblast injury. *Arch Oral Biol.* 2005;50(2):103-8.
-

CHAPTER 9

This chapter is based partially on the following publication

EzEldeen, M., Moroni, L., Nejad, Z., Jacobs, R., Mota, C.

Biofabrication of engineered dento-alveolar tissue. *Frontiers in Bioengineering and Biotechnology*, submitted

- (A) OMFS IMPATH Research Group, Faculty of Medicine, Department of Imaging and Pathology, KU Leuven and Oral and Maxillofacial Surgery, University Hospitals Leuven, Kapucijnenvoer 33, 3000 Leuven, Belgium
- (B) Department of Oral Health Sciences, KU Leuven and Paediatric Dentistry and Special Dental Care, University Hospitals Leuven, Kapucijnenvoer 33, 3000 Leuven, Belgium
- (C) Institute for technology-inspired Regenerative Medicine, Department of Complex Tissue Regeneration, Maastricht University, Maastricht, the Netherlands
- (D) Biomaterials research group, Department of Nanotechnology and Advance Materials, Materials and Energy Research Center, P.O. Box: 31787-316, Karaj, Alborz, Iran
- (E) Department of Dental Medicine, Karolinska Institute, Stockholm, Sweden

Discussion and Future Perspectives

M. EzEldeen (A,B), L. Moroni (C), Z. M. Nejad (A,D), R. Jacobs (A,E), C. Mota (C)

DISCUSSION

This final chapter will discuss the main results obtained in **Parts I-III** and highlight the link between the three parts. This work aimed mainly to bridge the gap between the clinic and the laboratory for the ultimate goal of tooth tissue engineering. Therefore, the future perspectives section will focus on how we can apply the tools developed and lessons learned from this work to a clinically feasible tooth root engineering concept.

Beyond cone-beam computed tomography

There is no doubt that the introduction of dental cone beam computed tomography (CBCT) has revolutionized dentistry and maxillofacial surgery at the levels of diagnosis, treatment planning, and intervention (1, 2). Amongst daily clinical interventions relying on CBCT are 3D-guided implant surgery (3), guided-endodontics and apical surgeries (4, 5) CBCT-based planning and fabrication of donor teeth replicas and surgical guides for successful tooth auto-transplantation (TAT) (6), digital orthodontic applications (7) and virtual orthognathic surgery planning (8). One standard procedure in the digital workflow of all the applications mentioned above is image segmentation. Image segmentation is a process of dividing an image into different meaningful regions and is utilized in structural identification and quantitative assessment of dental structures for various imaging modalities (9, 10). Therefore, tooth segmentation is vital for accurate diagnosis, treatment planning and surgical interventions.

Teeth segmentation on CBCT is a labour-intensive task that is directly affected by image quality and resolution. In contrast to conventional computed tomography (CT), where image segmentation relies on well-defined Hounsfield units (HUs), CBCT has no HUs but grey values instead (11). Moreover, the limited differential contrast between cementum, dentin, and bone with only 200 μm -wide periodontal ligament space renders any attempt of segmentation by relying solely on intensity variation of CBCT images unreliable (7).

Part I tackled the issue of tooth segmentation, image quality and associated radiation dose. **Chapter 1** focused on developing an image segmentation tool that is independent of the intensity variations of CBCT. The tool utilized already existing algorithms available in MeVisLab® (MeVis Research, Bremen,

184 Germany). Briefly, the imaging analysis tool applied semi-interactive livewire boundary extraction (12) to create a set of orthogonal contours, followed by a variational interpolation algorithm that reconstructs the surface of an object with energy-minimizing, smooth, and implicit functions (13). Further, **chapter 2** aimed at the optimization of the CBCT scanning protocols to reduce the paediatric radiation dose while maintaining sufficient image quality for clinical applications involving teeth segmentation. **We succeeded in reaching the goals defined in Part I**, as the tool developed offered the advantages of increasing the accuracy and reducing the working time. The segmentation time was reduced to 7 mins on average compared to >1 hour using the available commercial software (14). Moreover, the paediatric effective radiation dose for large field of view (FOV) protocols was reduced to the range of 74-158 μSv , while maintaining sufficient image quality for accurate 3D planning and surgical replica fabrication. Moreover, the dose for the small FOV protocols, could be reduced to the range of 24-42 μSv . This work was performed with the clinical applications in sight, as **chapter 1** demonstrated the use and usefulness of the tool in the analysis of the regenerative endodontic treatment (RET) outcomes providing valuable insights. In addition, **chapter 2** focused on CBCT-guided tooth autotransplantation (TAT) and optimized the CBCT protocols for pre-operative planning and post-operative follow-up.

The rapid advancements in the fields of Deep Learning (DL) and Artificial intelligence (AI), offered us the possibility to build on the developed tool in **chapter 1** and develop it further into an AI-based teeth segmentation tool achieving a segmentation time of 30 seconds (15). Moreover, **chapter 2** coined the concept of indication-oriented optimization of CBCT protocols aiming at minimizing the dose and maximizing the benefits for the patient (16, 17). Finally, the results of **Part I** were directly applied in **Part II** for the pre-surgical procedure of CBCT-guided TAT and 3D analysis of the outcomes.

Tooth transplantation: old dog new tricks

The earliest evidence of dentistry can be traced back to 7500 B.C., where the Egyptians used replacement teeth instead of lost ones (18). The biological basis of tooth autotransplantation (TAT) was established by the pioneering work of Andreasen et al., and Skoglund et al., in the late seventies and the early eighties on replanted and transplanted teeth in monkeys (19) and in dogs (20-22). Moreover, Andreasen et al., then established the surgical procedure (conventional TAT) and demonstrated the feasibility of TAT as a routine clinical practice (23-26). TAT offers a viable biological approach to tooth replacement in children. It enables preservation of the alveolar ridge and allows for periodontal and pulp healing and preserving the possibility of function and growth (23-30).

To enhance outcome predictability of the TAT procedure, a low dose CBCT-based surgical planning and transfer technique has been developed in Leuven, involving donor tooth selection and tooth replica fabrication (3D printing) (29, 31, 32). CBCT-based surgical planning may aid the clinician seeking answers regarding surgical feasibility and best new position for the donor tooth meanwhile maximizing esthetics and function (29). The use of stereolithographic tooth replica provides individualized bone adaptability and reduces extra-alveolar time for the donor tooth. It may thus help to preserve the periodontal ligament and pulp vitality, reducing the risk for necrosis and resorption (29, 30).

Part II focused on all aspects of CBCT-guided TAT, including long-term clinical outcomes (**chapter 3**), evaluating the accuracy of 3D-printing of tooth replica (**chapter 4**), suggesting a new-concept for TAT restoration (**chapter 5**), and in-depth histological and immunohistochemical characterization of the patterns of pulp-dentin complex healing (**chapter 6**).

The accuracy of CBCT-guided TAT procedure (**as described in chapter 3**) is cumulative starting with image acquisition (**chapter 2**), and segmentation (**chapter 1**). Followed by 3D printing of the tooth replica (**chapter 4**) that will be used during the surgery (**chapter 3**). One of the highlights of this thesis is the development, optimization, and validation of every step along the CBCT-guided TAT trajectory. Moreover, the results are immediately translated to the clinic, which is a unique feature for the TAT-team inside UZ Leuven. Such meticulous work is a clinical necessity because there are more than 279 CBCT models available in the market with wide variations in features and technical specifications (1), affecting the accuracy of tooth segmentation (33, 34). In addition, a wide range of 3D printing technologies and materials are available, affecting the accuracy of the 3D printed objects (35-38). This was demonstrated by the results in **chapter 4**, as digital light processing (DLP) printing technology consistently underestimated the dimensions of the root in the tooth replica. Our findings have an important clinical significance for TAT and highlight the need for indication specific validation of newly available technologies and products.

Chapters 3 & 6 combined, presented unique insights into the clinical, radiological, and histological patterns of healing following TAT. Root canal obliteration and continued root development after TAT of immature teeth are signs of pulp revitalization and treatment success (24, 25, 28, 30). In **chapter 3** we applied a novel method based on 3D-imaging to analyze the pattern of hard tissue formation and subsequent healing after TAT. The results in chapter 3 suggest four radiographic patterns of healing after TAT of immature premolars. These patterns have a 4D nature: change in Mean-DWT, RV, and Max-DWT influenced by the time factor. Change in Mean-DWT and RV appeared to plateau

186 after the first 3-4 years, while the change in the Max-DWT appeared to have a gradual increase during the follow-up period. One possible interpretation is that the change in Max-DWT describes the slower tissue remodeling on the external root surface at the tooth root, PDL-bone interface. While change in Mean-DWT and RV describes the faster tissue deposition on the internal root surface and overall root maturation. In **chapter 6** we examined the nature of this progressive obliteration and showed that healing of the pulp-dentin complex post TAT is of a reparative nature rather than a regenerative one, at least in the studied cases. Moreover, it was clear that there are still gaps in our knowledge regarding the molecular mechanisms controlling odontogenesis, and the healing of the pulp-dentin complex.

Future work will focus on linking the results from clinical, radiological, histological, and RNA sequencing data from well-designed animal studies and tissue samples to gain a comprehensive understanding of the process. Analysis, interpretation, and linking these data sets is beyond the commonly applied statistical methods and is only possible using the emerging technologies of deep learning and *in silico* modelling (39-41).

The role of COAM in a chemokine-mediated dental tissue regeneration

Part III was concerned by exploring a potential role of COAM in a chemokine-mediated dental tissue regeneration. COAM is a polyanionic polysaccharide derivative with antimicrobial properties (42, 43) that acts as an immunomodulator by interference with glycosaminoglycan (GAG) binding of chemokines (44). Furthermore, its antiviral (42) and antibacterial (43), actions constitute a bonus for conditions in which infections are eminent. The application of COAM was approached in a systematic fashion. In **chapter 7**, we evaluated the effect of COAM inclusion on the microstructural properties of fibrin and self-assembling peptide (SAP) hydrogels to select the appropriate delivery system. Moreover, we assessed the influence of the microstructural differences between the hydrogels on the *in vitro* behavior of human dental pulp stromal/stem cells (hDPSCs). The results of **chapter 7** demonstrated the compatibility of COAM with a tailored fibrin hydrogel as well as the biocompatibility of COAM with hDPSCs. Further, the measured stiffness of the fibrin hydrogels (with and without COAM), with the composition tested in **chapter 7**, was in the range of the stiffness of the native pulp tissue, which has previously been reported to be 800 Pa (45). In **chapter 8**, we investigated the binding and delivery of two chemokines of interest, namely SDF-1/CXCL12 and MCP-1/CCL2. We showed that COAM forms a binding complex with SDF-1/CXCL12, while this was not the case for MCP-1/CCL2. The binding between COAM and SDF-1/CXCL12

affected the pattern of SDF-1/CXCL12 release from fibrin hydrogels. SDF-1/CXCL12 was reported as the most frequently expressed chemokine gene in the dental pulp (46). The most frequently expressed receptor was the CXCR4 (46). Moreover, CXCR4 is expressed perivascularly in the apical papilla (47), and in cells isolated from the apical papilla (SCAPs) (48). Therefore, the SDF-1/CXCR4 axis is a potential therapeutic target for dental pulp repair and regeneration. The results from **chapter 8** suggest the application of COAM as a promising strategy for hydrogel functionalization with SDF-1/CXCL12 as well as providing delayed release. An extended release could be achieved using polymeric nanoparticles encapsulating the binding complex of COAM-SDF-1/CXCL12.

Future perspectives

*From biocompatible to biological dental tissue replacement:
a needed paradigm shift in dentistry*

Dentistry has been successful to a great extent in restoring damaged dental tissue, mainly the coronal part of the teeth, utilizing a wide range of biocompatible inert materials (49-52). On the contrary, restoring the dental root and surrounding tissue (periodontium & alveolar bone) has been more challenging, eventually resulting in dento-alveolar tissue loss (53-56). To date, complete tooth loss is widely replaced with biocompatible titanium dental implants, and this is primarily limited to adult patients and by the presence of sufficient alveolar bone (57). Treatment options such as implant placement are limited for children and adolescents due to the ongoing dento-alveolar development (58).

Dentistry excels in delivering personalized care, traditionally through the fabrication of dental crowns and prostheses (59). In the last two decades, additive manufacturing (AM) techniques, also known as 3D printing techniques, have been gradually introduced in daily dental practice and are frequently used. Examples of their application are mentioned above and **demonstrated in this thesis**. These well-established tools and the use of 3D printing in dentistry facilitate the shift to 3D biofabrication of patient-specific scaffolds. Biofabrication was recently defined as “the automated generation of biologically functional products with a structural organization from living cells, bioactive molecules, biomaterials, cell aggregates such as micro-tissues, or hybrid cell-material constructs, through bioprinting or bioassembly and subsequent tissue maturation processes” (60). Within biofabrication, several AM technologies, bioprinting, and electrospinning techniques (Figure 1) have started to be used to manufacture scaffolds for diverse tissue and organ engineering applications (61). The selection of the optimal biofabrication approach and techniques depends on factors such as the materials, the cells, and the targeted tissue. As these new therapies become a reality in the lab gradually, the translation to

188 the dental clinic is still minute, with a further need to overcome all challenges and to broaden the clinical application of these alternatives. In the next section pre-clinical and clinical examples of biofabrication are highlighted as well as our vision on how tooth-root engineering could become a clinical reality.

*From bench-side to chair-side
Pre-clinical and clinical examples*

Although a rich literature exists on biofabrication for dento-alveolar tissue engineering (62-64), a limited number of these have reached the clinic. A hybrid 3D-printed polycaprolactone-hydroxyapatite (PCL-HA) scaffold filled with recombinant human platelet-derived growth factor (rhPDGF-BB) was manufactured based on the computed tomography (CT) scan of a 53 years-old male suffering from periodontitis (65). This biofabricated scaffold was inserted in a periodontal defect associated with the lower-left canine and followed up to 13-months. Despite the initial success in gaining a 3-mm clinical attachment and partial root coverage, the scaffold was exposed, inflamed, and needed to be removed at 13-months. The authors suggested that the failure might have been due to the biomaterial choice and the bulky design of the scaffold (65). Another possible explanation might be the lack of bioactivity of the scaffold as the release of the rhPDGF-BB was characterized as a burst release in the first 3 hours. For alveolar bone augmentation, HA scaffolds were fabricated using a (CNC) milling machine based on CT scans of 10 patients and inserted in alveolar bone defects in the maxilla (66). After 8-months, titanium dental implants were inserted, and bone core biopsies were obtained. Histological evaluation showed newly formed trabecular bone and residual biomaterial, mainly in the central portion. The new bone was in strict contact with the residual material. Another study used 3D-printed biphasic calcium phosphate (CaP) ceramic for alveolar bone augmentation in the maxilla, and a bone core biopsy was obtained after 7-years (67). Similar results were shown, as the CaP scaffold was almost entirely intact after 7-years; however, it was integrated into the newly formed bone.

Regarding tooth root engineering, only pre-clinical data can be found. HA/TCP cylinders containing SCAPs in the central part and surrounded by a gel foam containing periodontal ligament stem cells (PDLSCs) was able to form a functional periodontal ligament (PDL) in a mini-pig model (68). It is not clear what was the aim of using the SCAPs, as no characterization for pulp-dentin complex regeneration was performed. Moreover, it is hard to imagine that the SCAPs will survive and regenerate the pulp-dentin complex without being encapsulated in a suitable scaffold. The same group published a follow-up study using a similar concept. However, this time, there was no attempt to regenerate

the pulp-dentin complex, and the HA/TCP cylinders were coated with bi-layered cell sheets (DPSCs and PDLSCs) (69). The biofabricated constructs had similar biomechanical properties to the natural teeth (compressive strength, modulus of elasticity, and torsional force) and were able to form a PDL-like attachment. Nevertheless, the success rate was only 22% (10 of 46) when compared to titanium dental implants (100%, 9 of 9) placed as controls (69). While these results might seem negative, they demonstrate the feasibility of tooth root engineering. Applying novel concepts in biofabrication and surface functionalization, for example, applying electrospinning to fabricate the PDL interface, could improve the reproducibility and increase the success rate.

Finally, although not a biofabrication example, a recent randomized clinical trial demonstrated the potential for pulp-dentin complex regeneration using hDPSCs (SHEDs) isolated from the primary canines and transplanted as cell aggregates into necrotic immature permanent incisors (70). Therefore, one can easily imagine combining different biofabrication techniques with multipotent stromal cells isolated from primary teeth or the wisdom molars to successfully biofabricate a bio-engineered tooth root.

*CBCT-guided TAT as an inspirational clinical model
for tooth root engineering*

Although often applied, synthetic dental implants have severe shortcomings, including risk for an immune reaction, ulcers and peri-implantitis, inferior osseointegration and anchorage (which is essential given the high masticatory forces) (71). Moreover, the physiological functions of the tooth are not ad-

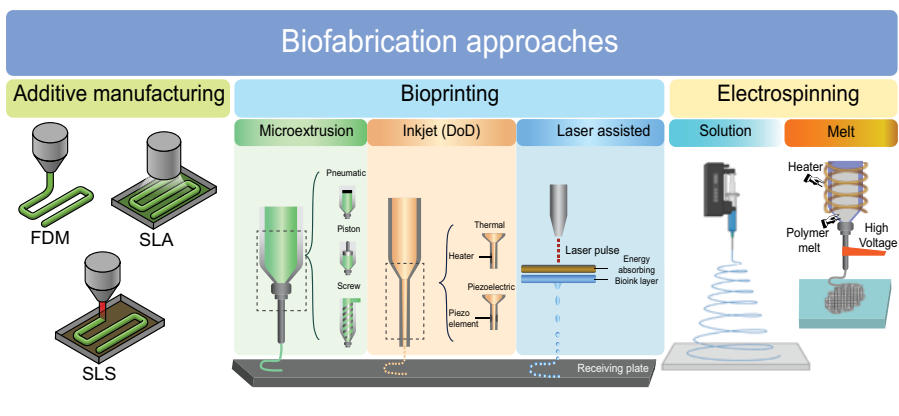


Figure 1: Biofabrication approaches. Additive manufacturing: fused depositions modeling (FDM), stereolithography (SLA), selective laser sintering (SLS). Bioprinting: microextrusion, inkjet (droplet-on-demand), and laser-assisted. Electrospinning: solution-based or melt electrowriting.

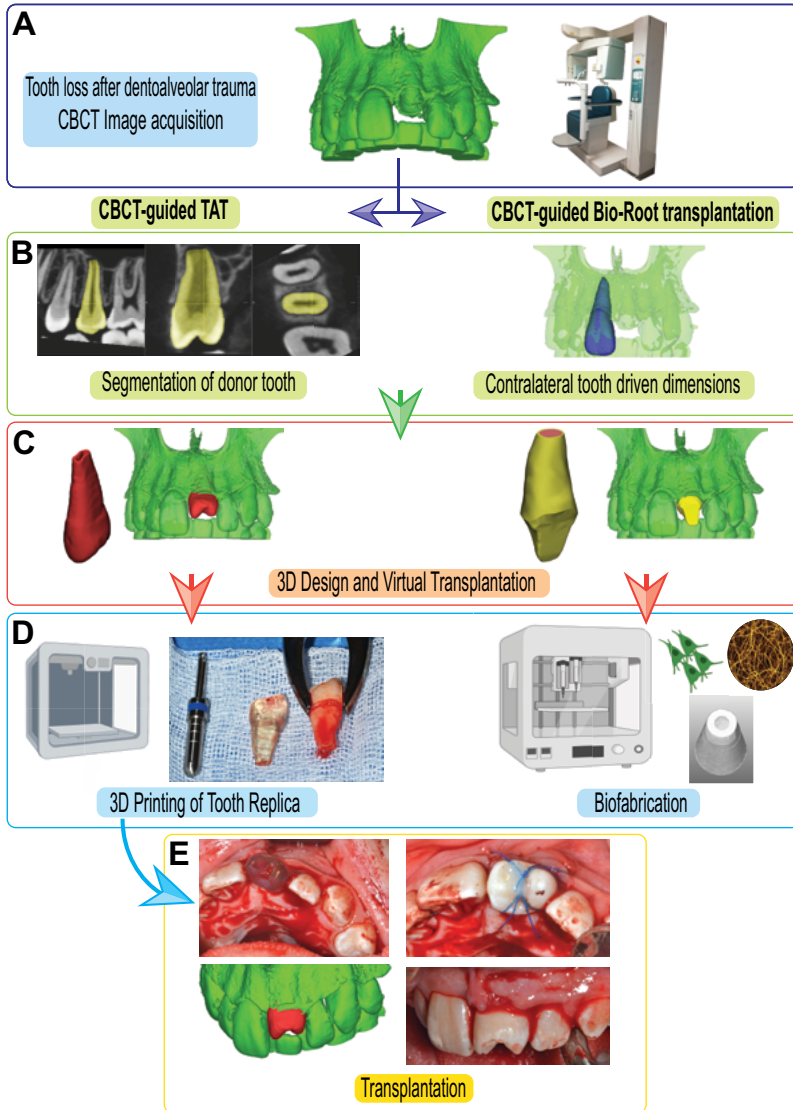


Figure 2: CBCT-guided Tooth Autotransplantation (TAT) concept adaptation for Bio-tooth root transplantation. (A) A clinical situation where 11 years-old child loses his maxillary left central incisor after dento-alveolar trauma. (B) The currently applied procedure for TAT starts with donor tooth selection and segmentation. This step could be adapted to segment the contralateral tooth (maxillary right central incisor, shown in blue) to drive the dimensions needed for Bio-Root design and fabrication. (C) Virtual transplantation is performed to examine the fit of the donor's tooth into the recipient site and plan the best new position. The adaptation will include designing the Bio-Root and planning the transplantation position. (D) 3D-printing of the tooth replica to be used during the surgery to prepare the recipient (light blue arrow). This step will correspond to the biofabrication step and assembling the Bio-Root. (E) Surgical procedure for CBCT-guided TAT showing the use of the replica during surgery to adapt the recipient site avoiding any trauma to the periodontal ligaments and reducing the surgery time. A 3D-printed replica will ensure a passive fit for the Bio-Root, enhancing the chances of cell survival and overall success of the procedure.

equately restored. For instance, implant therapy does not replace the PDL, which has vital roles in tooth support, homeostasis, and repair (72, 73).

Furthermore, the outstanding long-term clinical success, and the evidence of tissue integration/regeneration (pulp-dentin complex and periodontal ligament) after TAT (immature teeth) **(as demonstrated in this thesis), is without a doubt the most significant proof for the feasibility of tooth root engineering (bio-engineered root).**

The process of cone-beam computed tomography (CBCT)-guided TAT (Figure 2) involves: (i) the selection of the appropriate donor tooth based on the patient's CBCT scan, (ii) planning the ideal transplantation position, (iii) 3D-printing of the donor tooth replica to be used during the surgery to adapt the recipient site, (iv) atraumatic extraction and transplantation of the donor tooth (**chapter 3**). TAT is limited by the availability of a donor tooth at the appropriate developmental stage and dimensions matching the recipient site. This clinical process could be adapted to the design, fabrication, and transplantation of bio-engineered roots (Figure 2). Furthermore, 3D analysis of TAT outcomes (**chapter 3**) has revealed that specific shape descriptors of the tooth root pre-TAT (mean hard tissue thickness, root hard tissue volume and maximum hard tissue thickness) influence the pattern of tissue healing/formation post-TAT (**chapter 3**). Therefore, these parameters could be applied in the design of the bio-engineered roots to increase the chances of PDL and pulp-dentin complex integration/regeneration and offer a starting point boosting the predictability of the approach.

Ethical aspects related to biofabrication

Ethical considerations in biofabrication of dentoalveolar tissues are similar to those in regenerative medicine and other biomedical fields. These considerations can be categorized as bench-side, chair-side and societal (74). Bench-side aspects are mainly concerned with the use of both animal and human materials. In regenerative medicine, animals are used as a source of cells, or as a model to test new innovations. Nowadays, the 3Rs, or the replacement, reduction, and refinement of animal research, are widely accepted and applied (75). Therefore, proper justification of using animals for laboratory experiments is needed. Interestingly, biofabrication aids the 3Rs principle as it can produce tissue models for testing, create custom bioreactors, and fabricate organs-on-chips as alternatives (76). The use of human (stem) cells is another debate in particular the use of human embryonic and fetal tissues for research (74). In dentistry, the cell source is expected to be exfoliating primary teeth and extracted wisdom molars which is ethically and societally acceptable. However,

192 proper regulation of collection and storage is required through biobanking and obtaining the needed consents.

The translation from bench-side to chair-side in the context of tissue engineering and biofabrication requires specific refinement of the standard ethical, legal, and regulatory framework of clinical trials (74, 77, 78). The general risks of biofabricated products are that cells may exhibit a tumorigenic potential and biomaterial interactions may cause undesirable effects. Therefore, we should pay extra attention combined with thorough ethical reflection for the transition from bench-side to chair-side, as premature trials could compromise patient safety and damage public perception of the field (74). Finally, societal considerations revolve mainly around transparent communication with the public to avoid over-expectations and to maintain public trust.

Concluding remarks on future perspectives

Despite the remarkable progress utilizing biofabrication approaches to create scaffolds or tissue constructs, most of these did not translate into clinical solutions. One might reason that there is no clinical demand to drive the shift from biocompatible to biological management of dental conditions. However, this is far from true as demonstrated in this thesis, there are daily clinical situations where biofabrication is highly indicated. For example, teeth loss or agenesis in children, cleft lip and palate patients, periodontal tissue loss, and patients with bisphosphonate-related osteonecrosis of the jaw.

There are clearly several issues to overcome before biofabricated approaches reach the clinic. The first being the need to develop biomaterials specific for the dento-alveolar tissue considering its heterogeneous nature, dimensions, and the challenging environment. The next issue is the cells, there should be a new clear definition for dental stem cells and dental multipotent stromal cells. Moreover, to facilitate the transition to the clinic, attention should be paid to the culturing conditions and the use of animal-component free medium while gaining a deeper understanding into the effect on cell phenotype. Furthermore, the biofabrication approaches need to be adapted mainly to the challenging dimensions of the target tissue. At the moment, it does not seem possible to biofabricate a tooth root using a single modality and a multi-modality fabrication (Figure 1) followed by an assembly step seems to be the most viable option in the near future.

The clinical application of dento-alveolar biofabrication should start inside specialized academic centers where cells can be isolated, expanded, characterized, maintained, and combined with patient-specific constructs. On

the intermediate to long term, once regulatory and economic hurdles are overcome, bio-technology companies will emerge to take part in the daily dental workflow supplying the dentist with personalized scaffolds ready for implantation.

Finally, as attempted in this thesis, we should consider clinical models of repair/regeneration for inspiration and to fill the gaps in the current knowledge to reach the ultimate goal of the biofabrication of dento-alveolar tissue to assist a wide range of patients in need.

REFERENCES

<p>1. Gaêta-Araujo H, Alzoubi T, Vasconcelos KF, Orhan K, Pauwels R, Casselman JW, et al. Cone beam computed tomography in dentomaxillofacial radiology: a two-decade overview. <i>Dentomaxillofac Radiol.</i> 2020;49(8):20200145.</p> <p>2. Gaêta-Araujo H, Leite AF, Vasconcelos KF, Jacobs R. Two decades of research on CBCT imaging in DMFR - an appraisal of scientific evidence. <i>Dentomaxillofac Radiol.</i> 2021;50(4):20200367.</p> <p>3. Van Assche N, Vercruyssen M, Coucke W, Teughels W, Jacobs R, Quirynen M. Accuracy of computer-aided implant placement. <i>Clin Oral Implants Res.</i> 2012;23 Suppl 6:112-23.</p> <p>4. Torres A, Shaheen E, Lambrechts P, Politis C, Jacobs R. Microguided Endodontics: a case report of a maxillary lateral incisor with pulp canal obliteration and apical periodontitis. <i>Int Endod J.</i> 2019;52(4):540-9.</p> <p>5. Byun C, Kim C, Cho S, Baek SH, Kim G, Kim SG, et al. Endodontic Treatment of an Anomalous Anterior Tooth with the Aid of a 3-dimensional Printed Physical Tooth Model. <i>J Endod.</i> 2015;41(6):961-5.</p> <p>6. EzEldeen M, Wyatt J, Al-Rimawi A, Coucke W, Shaheen E, Lambrechts I, et al. Use of CBCT Guidance for Tooth Autotransplantation in Children. <i>J Dent Res.</i> 2019;98(4):406-13.</p> <p>7. Cui Z, Li C, Wang W. ToothNet: Automatic Tooth Instance Segmentation and Identification From Cone Beam CT Images. 2019 IEEE/CVF Conference on Computer Vision and Pattern Recognition (CVPR); 06/2019; Long Beach, CA, USA: IEEE; 2019. p. 6361-70.</p>	<p>8. Shaheen E, Shujaat S, Saeed T, Jacobs R, Politis C. Three-dimensional planning accuracy and follow-up protocol in orthognathic surgery: a validation study. <i>Int J Oral Maxillofac Surg.</i> 2019;48(1):71-6.</p> <p>9. EzEldeen M, Van Gorp G, Van Dessel J, Vandermeulen D, Jacobs R. 3-dimensional analysis of regenerative endodontic treatment outcome. <i>J Endod.</i> 2015;41(3):317-24.</p> <p>10. Nguyen KCT, Duong DQ, Almeida FT, Major PW, Kaipatur NR, Pham TT, et al. Alveolar Bone Segmentation in Intraoral Ultrasonographs with Machine Learning. <i>J Dent Res.</i> 2020;99(9):1054-61.</p> <p>11. Jacobs R. Dental cone beam CT and its justified use in oral health care. <i>JBR-BTR.</i> 2011;94(5):254-65.</p> <p>12. Barrett WA, Mortensen EN. Interactive live-wire boundary extraction. <i>MedImage Anal.</i> 1997;1(4):331-41.</p> <p>13. Heckel F, Konrad O, Karl Hahn H, Peitgen H-O. Interactive 3D medical image segmentation with energy-minimizing implicit functions. <i>Computers & Graphics.</i> 2011;35(2):275-87.</p> <p>14. Star H, Thevissen P, Jacobs R, Fieuws S, Solheim T, Willems G. Human dental age estimation by calculation of pulp-tooth volume ratios yielded on clinically acquired cone beam computed tomography images of monoradicular teeth. <i>J Forensic Sci.</i> 2011;56 Suppl 1:S77-82.</p> <p>15. Lahoud P, EzEldeen M, Beznik T, Willems H, Leite A, Van Gerven A, et al. Artificial Intelligence for Fast and Accurate 3-Dimensional Tooth Segmentation on Cone-beam Computed Tomography. <i>J Endod.</i> 2021;47(5):827-35.</p>
--	--

16. Belmans N, Oenning AC, Salmon B, Baselet B, Tabury K, Lucas S, et al. Radiobiological risks following dentomaxillofacial imaging: should we be concerned? *Dentomaxillofac Radiol.* 2021;50(6):20210153.
17. De Mulder D, Cadenas de Llano-Péruła M, Willems G, Jacobs R, Dormaar JT, Verdonck A. An optimized imaging protocol for orofacial cleft patients. *Clin Exp Dent Res.* 2018;4(5):152-7.
18. Forshaw RJ. The practice of dentistry in ancient Egypt. *Br Dent J.* 2009;206(9):481-6.
19. Kristerson L, Andreasen JO. Autotransplantation and replantation of tooth germs in monkeys: Effect of damage to the dental follicle and position of transplant in the alveolus. *Inter J Oral Sur.* 1984;13(4):324-33.
20. Skoglund A, Hasselgren G, Tronstad L. Oxidoreductase activity in the pulp of replanted and autotransplanted teeth in young dogs. *Oral Sur, Oral Med, Oral Pathol.* 1981;52(2):205-9.
21. Skoglund A, Tronstad L. Pulpal changes in replanted and autotransplanted immature teeth of dogs. *J End.* 1981;7(7):309-16.
22. Skoglund A, Tronstad L, Wallenius K. A microangiographic study of vascular changes in replanted and autotransplanted teeth of young dogs. *Oral Sur Oral Med Oral Pathol.* 1978;45(1):17-28.
23. Andreasen JO, Paulsen HU, Yu Z, Ahlquist R, Bayer T, Schwartz O. A long-term study of 370 autotransplanted premolars. Part I. Surgical procedures and standardized techniques for monitoring healing. *Eur J Orthod.* 1990;12(1):3-13.
24. Andreasen JO, Paulsen HU, Yu Z, Bayer T. A long-term study of 370 autotransplanted premolars. Part IV. Root development subsequent to transplantation. *Eur J Orthod.* 1990;12(1):38-50.
25. Andreasen JO, Paulsen HU, Yu Z, Bayer T, Schwartz O. A long-term study of 370 autotransplanted premolars. Part II. Tooth survival and pulp healing subsequent to transplantation. *Eur J Orthod.* 1990;12(1):14-24.
26. Andreasen JO, Paulsen HU, Yu Z, Schwartz O. A long-term study of 370 autotransplanted premolars. Part III. Periodontal healing subsequent to transplantation. *Eur J Orthod.* 1990;12(1):25-37.
27. Czochrowska EM, Stenvik A, Album B, Zachrisson BU. Autotransplantation of premolars to replace maxillary incisors: a comparison with natural incisors. *Am J Orthod Dentofacial Orthop.* 2000;118(6):592-600.
28. Czochrowska EM, Stenvik A, Bjercke B, Zachrisson BU. Outcome of tooth transplantation: Survival and success rates 17-41 years posttreatment. *American Journal of Orthodontics and Dentofacial Orthopedics.* 2002;121(2):110-9.
29. Shahbazian M, Jacobs R, Wyatt J, Denys D, Lambrechts I, Vinckier F, et al. Validation of the cone beam computed tomography-based stereolithographic surgical guide aiding autotransplantation of teeth: clinical case-control study. *Oral Surg Oral Med Oral Pathol Oral Radiol.* 2013;115(5):667-75.
30. Tsukiboshi M. Autotransplantation of teeth: requirements for predictable success. *Dent-Traumatol.* 2002;18(4):157-80.
31. Shahbazian M, Jacobs R, Wyatt J, Willems G, Pattijn V, Dhoore E, et al. Accuracy and surgical feasibility of a CBCT-based stereolithographic surgical guide aiding autotransplantation of teeth: in vitro validation. *J Oral Rehabil.* 2010;37(11):854-9.
32. Jang Y, Choi YJ, Lee SJ, Roh BD, Park SH, Kim E. Prognostic Factors for Clinical Outcomes in Autotransplantation of Teeth with Complete Root Formation: Survival Analysis for up to 12 Years. *J Endod.* 2016;42(2):198-205.
33. EzEldeen M, Stratis A, Coucke W, Codari M, Politis C, Jacobs R. As Low Dose as Sufficient Quality: Optimization of Cone-beam Computed Tomographic Scanning Protocol for Tooth Autotransplantation Planning and Follow-up in Children. *J Endod.* 2017;43(2):210-7.
34. Shaheen E, Khalil W, Ezeldeen M, Van de Castelee E, Sun Y, Politis C, et al. Accuracy of segmentation of tooth structures using 3 different CBCT machines. *Oral Surg Oral Med Oral Pathol Oral Radiol.* 2017;123(1):123-8.
35. Khalil W, EzEldeen M, Van De Castelee E, Shaheen E, Sun Y, Shahbazian M, et al. Validation of cone beam computed tomography-based tooth printing using different three-dimensional printing technologies. *Oral Surg Oral Med Oral Pathol Oral Radiol.* 2016;121(3):307-15.

36. Shaheen E, Alhelwani A, Van De Castele E, Politis C, Jacobs R. Evaluation of Dimensional Changes of 3D Printed Models After Sterilization: A Pilot Study. *Open Dent J.* 2018;12:72-9.
37. Shujaat S, da Costa Senior O, Shaheen E, Politis C, Jacobs R. Visual and haptic perceptibility of 3D printed skeletal models in orthognathic surgery. *J Dent.* 2021;109:103660.
38. Wang X, Shujaat S, Shaheen E, Jacobs R. Accuracy of desktop versus professional 3D printers for maxillofacial model production. A systematic review and meta-analysis. *J Dent.* 2021:103741.
39. Carlier A, Skvortsov GA, Hafezi F, Ferraris E, Patterson J, Koc B, et al. Computational model-informed design and bioprinting of cell-patterned constructs for bone tissue engineering. *Biofabrication.* 2016;8(2):025009.
40. Geris L, Lambrechts T, Carlier A, Papaniouni I. The future is digital: In silico tissue engineering. *Current Opinion in Biomedical Engineering.* 2018;6:92-8.
41. Gorgun C, Ceresa D, Lesage R, Villa F, Reverberi D, Balbi C, et al. Dissecting the effects of preconditioning with inflammatory cytokines and hypoxia on the angiogenic potential of mesenchymal stromal cell (MSC)-derived soluble proteins and extracellular vesicles (EVs). *Biomaterials.* 2021;269:120633.
42. Li S, Martens E, Dillen C, Van den Steen PE, Opdenakker G. Virus entry inhibition by chlorite-oxidized oxyamylose versus induction of antiviral interferon by poly(I:C). *Biochem Pharmacol.* 2008;76(7):831-40.
43. Zi Y, Zhu M, Li X, Xu Y, Wei H, Li D, et al. Effects of carboxyl and aldehyde groups on the antibacterial activity of oxidized amylose. *Carbohydr Polym.* 2018;192:118-25.
44. Li S, Pettersson US, Hoorelbeke B, Kolarczkowska E, Schelfhout K, Martens E, et al. Interference with glycosaminoglycan-chemokine interactions with a probe to alter leukocyte recruitment and inflammation in vivo. *PLoS One.* 2014;9(8):e104107.
45. Eriskin C, Kalyon DM, Zhou J, Kim SG, Mao JJ. Viscoelastic Properties of Dental Pulp Tissue and Ramifications on Biomaterial Development for Pulp Regeneration. *J Endod.* 2015;41(10):1711-7.
46. Farges JC, Keller JF, Carrouel F, Durand SH, Romeas A, Bleicher F, et al. Odontoblasts in the dental pulp immune response. *J Exp Zool B Mol Dev Evol.* 2009;312B(5):425-36.
47. Liu JY, Chen X, Yue L, Huang GT, Zou XY. CXC Chemokine Receptor 4 Is Expressed Paravascularly in Apical Papilla and Coordinates with Stromal Cell-derived Factor-1alpha during Transmigration of Stem Cells from Apical Papilla. *J Endod.* 2015;41(9):1430-6.
48. Driesen RB, Hilken P, Smisdorn N, Vanganswinkel T, Dillen Y, Ratajczak J, et al. Dental Tissue and Stem Cells Revisited: New Insights From the Expression of Fibroblast Activation Protein-Alpha. *Front Cell Dev Biol.* 2019;7:389.
49. da Veiga AM, Cunha AC, Ferreira DM, da Silva Fidalgo TK, Chianca TK, Reis KR, et al. Longevity of direct and indirect resin composite restorations in permanent posterior teeth: A systematic review and meta-analysis. *J Dent.* 2016;54:1-12.
50. Demarco FF, Collares K, Coelho-de-Souza FH, Correa MB, Cenci MS, Moraes RR, et al. Anterior composite restorations: A systematic review on long-term survival and reasons for failure. *Dent Mater.* 2015;31(10):1214-24.
51. Peumans M, De Munck J, Van Landuyt K, Van Meerbeek B. Thirteen-year randomized controlled clinical trial of a two-step self-etch adhesive in non-carious cervical lesions. *Dent Mater.* 2015;31(3):308-14.
52. Vagropoulou GI, Klifopoulou GL, Vlahou SG, Hirayama H, Michalakos K. Complications and survival rates of inlays and onlays vs complete coverage restorations: A systematic review and analysis of studies. *J Oral Rehabil.* 2018;45(11):903-20.
53. Chercoles-Ruiz A, Sanchez-Torres A, Gay-Escoda C. Endodontics, Endodontic Retreatment, and Apical Surgery Versus Tooth Extraction and Implant Placement: A Systematic Review. *J Endod.* 2017;43(5):679-86.
54. Mavridou AM, Bergmans L, Barendregt D, Lambrechts P. Descriptive Analysis of Factors Associated with External Cervical Resorption. *J Endod.* 2017;43(10):1602-10.
55. Torabinejad M, Anderson P, Bader J, Brown LJ, Chen LH, Goodacre CJ, et al. Outcomes of root canal treatment and restoration, im-

- plant-supported single crowns, fixed partial dentures, and extraction without replacement: A systematic review. *The Journal of Prosthetic Dentistry*. 2007;98(4):285-311.
56. Torabinejad M, White SN. Endodontic treatment options after unsuccessful initial root canal treatment: Alternatives to single-tooth implants. *J Am Dent Assoc*. 2016;147(3):214-20.
 57. Chatzopoulos GS, Koidou VP, Lunos S, Wolff LF. Implant and root canal treatment: Survival rates and factors associated with treatment outcome. *J Dent*. 2018;71:61-6.
 58. Sharma AB, Vargervik K. Using implants for the growing child. *J Calif Dent Assoc*. 2006;34(9):719-24.
 59. Joda T, Zarone F, Ferrari M. The complete digital workflow in fixed prosthodontics: a systematic review. *BMC Oral Health*. 2017;17(1):124.
 60. Moroni L, Boland T, Burdick JA, De Maria C, Derby B, Forgacs G, et al. Biofabrication: A Guide to Technology and Terminology. *Trends Biotechnol*. 2018;36(4):384-402.
 61. Mota C, Puppi D, Chiellini F, Chiellini E. Additive manufacturing techniques for the production of tissue engineering constructs. *J Tissue Eng Regen Med*. 2015;9(3):174-90.
 62. Park CH, Rios HF, Jin Q, Bland ME, Flanagan CL, Hollister SJ, et al. Biomimetic hybrid scaffolds for engineering human tooth-ligament interfaces. *Biomaterials*. 2010;31(23):5945-52.
 63. Obregon F, Vaquette C, Ivanovski S, Huttmacher DW, Bertassoni LE. Three-Dimensional Bioprinting for Regenerative Dentistry and Craniofacial Tissue Engineering. *J Dent Res*. 2015;94(9 Suppl):143S-52S.
 64. Visscher DO, Farre-Guasch E, Helder MN, Gibbs S, Forouzanfar T, van Zuijlen PP, et al. Advances in Bioprinting Technologies for Craniofacial Reconstruction. *Trends Biotechnol*. 2016;34(9):700-10.
 65. Rasperini G, Pilipchuk SP, Flanagan CL, Park CH, Pagni G, Hollister SJ, et al. 3D-printed Bioresorbable Scaffold for Periodontal Repair. *J Dent Res*. 2015;94(9 Suppl):153S-7S.
 66. Mangano F, Macchi A, Shibli JA, Luongo G, Iezzi G, Piattelli A, et al. Maxillary ridge augmentation with custom-made CAD/CAM scaffolds. A 1-year prospective study on 10 patients. *J Oral Implantol*. 2014;40(5):561-9.
 67. Mangano C, Giuliani A, De Tullio I, Raspanti M, Piattelli A, Iezzi G. Case Report: Histological and Histomorphometrical Results of a 3-D Printed Biphasic Calcium Phosphate Ceramic 7 Years After Insertion in a Human Maxillary Alveolar Ridge. *Front Bioeng Biotechnol*. 2021;9:614325.
 68. Sonoyama W, Liu Y, Fang D, Yamaza T, Seo BM, Zhang C, et al. Mesenchymal stem cell-mediated functional tooth regeneration in swine. *PLoS One*. 2006;1:e79.
 69. Gao ZH, Hu L, Liu GL, Wei FL, Liu Y, Liu ZH, et al. Bio-Root and Implant-Based Restoration as a Tooth Replacement Alternative. *J Dent Res*. 2016;95(6):642-9.
 70. Xuan K, Li B, Guo H, Sun W, Kou X, He X, et al. Deciduous autologous tooth stem cells regenerate dental pulp after implantation into injured teeth. *Sci Transl Med*. 2018;10(455).
 71. Giannobile WV, Lang NP. Are Dental Implants a Panacea or Should We Better Strive to Save Teeth? *J Dent Res*. 2016;95(1):5-6.
 72. Kinane DF, Stathopoulou PG, Papananou PN. Periodontal diseases. *Nat Rev Dis Primers*. 2017;3:17038.
 73. Larsson L, Decker AM, Nibali L, Pilipchuk SP, Berglundh T, Giannobile WV. Regenerative Medicine for Periodontal and Peri-implant Diseases. *J Dent Res*. 2016;95(3):255-66.
 74. Otto IA, Breugem CC, Malda J, Bredenoord AL. Ethical considerations in the translation of regenerative biofabrication technologies into clinic and society. *Biofabrication*. 2016;8(4):042001.
 75. Kirk RGW. Recovering The Principles of Humane Experimental Technique: The 3Rs and the Human Essence of Animal Research. *Sci Technol Human Values*. 2018;43(4):622-48.
 76. Arslan-Yildiz A, El Assal R, Chen P, Guven S, Inci F, Demirci U. Towards artificial tissue models: past, present, and future of 3D bioprinting. *Biofabrication*. 2016;8(1):014103.

77. Aithal AP, Bairy LK, Seetharam RN. Safety and therapeutic potential of human bone marrow-derived mesenchymal stromal cells in regenerative medicine. *Stem Cell Investig.* 2021;8:10.
 78. Habets MG, Delden JJv, Bredenoord AL. The inherent ethical challenge of first-in-human pluripotent stem cell trials. *Regenerative Medicine.* 2014;9(1):1-3.
-

"Although there exist in the world today some microbes of the soul, such as discrimination and aggression, science was and still is the core of progress for humanity and the continuity of civilization."

AHMED ZEWAAL

"The more I know, the more I know that I do not know."

SOCRATES

"Try not to become a man of success,
but rather try to become a man of value."

ALBERT EINSTEIN

The general **aim** of this PhD project was to bridge part of the gap between *in vitro* studies and the clinical application for dental tissue regeneration with the main use of a cell-free approach. This aim was approached systematically, on the one hand, through the study of two clinical models involving tissue repair and regeneration namely tooth autotransplantation (TAT) and regenerative endodontic treatment (RET). On the other hand, we explored the concept of chemokine-mediated dental tissue regeneration by applying chlorite oxidized oxyamylose (COAM).

This PhD thesis comprises the following three PhD project parts, namely **Part I**, entitled '*Developing and optimizing the tools to study regenerative dental procedures*', **Part II**, entitled '*Tooth Autotransplantation as a current solution full of future inspirations*', and **Part III**, entitled '*The role of COAM in a chemokine-mediated dental tissue regeneration*'.

In Part I (chapter 1), we focused on the development of a standardized quantitative method for the analysis of tooth tissue change based on cone beam computed tomography (CBCT) imaging. A volumetric measurement tool involving two segmentation steps was applied to extract the tooth of interest from the surrounding tissue (live-wire) and further to separate tooth hard tissue and root canal space (level-set methods). Volumetric measurements from CBCT imaging were validated against measurements from micro-computed tomography (μ CT). Furthermore, the tool was applied on a CBCT data set of a RET case series. The results showed no statistical differences and strong agreement between CBCT and μ CT volumetric measurements highlighting the accuracy of the approach. Volumetric comparison of the root hard tissue showed significant hard tissue formation [mean volume of newly formed hard tissue was 27.9 (\pm 10.5) mm³, ($p < 0.05$)]. In conclusion this work showed **the feasibility and accuracy of detailed 3D analysis of tooth root tissue change based on CBCT**. Moreover, analysis of 3D data for teeth treated with RET offered valuable insights into the treatment outcome and patterns of hard-tissue formation.

202 CBCT images overcome the limitations of 2D images such as the lack of the bucco-lingual dimension, masking of areas of interest by overlying anatomy (anatomic noise) and avoid geometrical distortion. A high spatial resolution and true volumetric information can be obtained because of the isotropic nature of CBCT images. Nevertheless, CBCT has its own limitation, the effective radiation dose delivered by CBCT devices available in the market vary enormously from around 10 μSv to 1200 μSv (which is an equivalent of 2-240 panoramic radiographs). Therefore, in **chapter 2**, we were mainly concerned about the optimization of the CBCT scanning protocols to achieve a dose as low as possible and to maintain sufficient image quality. This optimization study was indication-oriented, targeting paediatric clinical situations where image segmentation is applied either for diagnosis, treatment planning or 3D analysis of treatment outcomes. For this end, a Sectional Head Phantom (SK150) was scanned using 18 exposure protocols in 3 different CBCT machines: 3D Accutomo 170[®] (Morita, Kyoto, Japan), the ProMax[®] 3D MAX (Planmeca, Helsinki, Finland) and the NewTom[®] VGI EVO (QR Verona, Verona, Italy). Effective dose (ED) was calculated with Monte-Carlo simulation and pediatric voxel phantoms (5 & 8 years-old male, 12 years-old female). Image quality was assessed by comparing segmented teeth volumes, evaluation of the visibility of the lamina-dura, and morphological surface analysis of 3D models. A general linear mixed model was fit to combine image quality parameters and radiation effective dose for each protocol to rank and compare all the protocols examined in the study. The results showed that the ED for the pre-operative scans can be reduced to the range of 74.6-157.9 μSv with ProMax ULD-HDR 100x90 scoring highest ranking. In conclusion, **a considerable reduction in the paediatric effective radiation dose can be achieved while maintaining sufficient image quality for tooth autotransplantation planning and follow-up using the dose optimization protocols**. Finally, the optimization of the small field of view protocols has an importance extended to other indications such as (i) the diagnosis and treatment of traumatic dental injuries, (ii) guided endodontics for anomalous teeth and teeth with pulp canal calcifications, and (iii) regenerative endodontic procedures including the treatment planning and long-term follow-up.

Tooth autotransplantation (TAT) offers a viable biological approach to tooth replacement in children and adolescents. **Part II** dealt with the different aspects of CBCT-guided TAT. In **chapter 3**, we evaluated CBCT-guided TAT compared to the conventional TAT protocol and assessed the 3D patterns of healing after CBCT-guided TAT. This study included 100 autotransplanted teeth in 88 patients. Each experimental group consisted of 50 transplants in 44 patients (31 males and 19 females). The mean age at the time of surgery was 10.7 (± 1.1) years-old for the CBCT-guided group. This was 10.6 (± 1.3) years-old for the conventional-group. The mean follow-up period was 4.5 (± 3.1)

years (range 1.1-10.4 years). Overall survival rate for the CBCT-guided TAT was 92% and success rate was 86% compared to 84% survival rate and 78% success rate for the conventional-group ($P > 0.05$). The following measurements were extracted from the 3D analysis: root hard tissue volume (RV), root length (RL), apical foramen area (AFA), mean and maximum dentin wall thickness (Mean-DWT & Max-DWT). Overall, the mean percentage of tissue change was RV gain by 65.8% (± 34.6), RL gain by 37.3% (± 31.5), AFA reduction by 91.1% (± 14.9), Mean-DWT increase by 107.9% (± 67.7), and Max-DWT increase by 26.5% (± 40.1). **Principle component analysis (PCA) identified the Mean-DWT, RV and Max-DWT as the parameters best describing the tissue change after TAT. Cluster analysis applied to the variables chosen by the PCA classified the CBCT-group into 4 distinct clusters (C1=37.2%, C2=17.1%, C3=28.6%, C4=17.1%) revealing different patterns of tissue healing after TAT.** In conclusion, the CBCT-guided approach increased the predictability of the treatment. The 3D analysis provided insights into the patterns of healing post-TAT. CBCT-guided TAT could be adopted as an alternative for the conventional approach.

Chapters 4 & 5 focused on 3D printing technology serving TAT. **Chapter 4** assessed the influence of different 3D printing technologies on the accuracy of tooth replica fabrication. Physical volume measurements and morphological surface comparison (surface deviation of 3D printed replicas vs natural tooth) showed a significant effect for 3D printing technology on the accuracy of tooth replica fabrication. DLP consistently underestimated the volume of the replicas ($P < 0.05$), in contrast to PolyJet ($P > 0.05$). It was then concluded that **disease indication-specific validation and optimization of 3D printing technologies are needed before clinical application.** **Chapter 5** aimed to develop and validate a digital solution for temporary restoration of autotransplanted teeth using 3D printing. Digital workflow for the design and fabrication of temporary veneers was introduced. The evaluation of veneer seating using stereomicroscopy showed that the mean marginal gap at all sides was below the cut-off value of 200 μm . The overall mean marginal gap was $99.9 \pm 50.7 \mu\text{m}$ [median: 87.8 (IQR 64.2-133 μm)]. Internal adaptation evaluation using μCT showed an average median gap thickness of 152.5 ± 47.7 (IQR 129-149.3 μm). In conclusion, **the present concept of using temporary veneers, designed, and fabricated with CAD/CAM technology using DLP printer may present a viable treatment option for restoration of autotransplanted teeth.**

Chapter 6 characterized the pattern of dental pulp healing in human teeth that underwent TAT and RET using state-of-the-art multimodality imaging. Analysis of the cases revealed different patterns of dental pulp healing. Observed similarities were the progressive obliteration of the root canal space

204 encapsulating an interconnected root canal system. **Striking loss of typical pulp architecture was observed in the TAT cases, while a pulp-like tissue was observed in the RET case.** Odontoblast-like cells were observed in both TAT & RET cases. Odontoblast-like cells were observed in cases both TAT & RET. This chapter provided insights into the patterns of dental pulp healing after TAT and RET. **Second harmonic generation imaging analysis shed light on the different patterns of collagen deposition during reparative dentin formation.**

Finally, in **Part III** the role of COAM in a chemokine-mediated dental tissue regeneration was explored. In **chapter 7**, we evaluated the effect of the chemokine-binding and antimicrobial polymer, COAM, on the microstructural properties of tailored fibrin and self-assembling peptide (SAP) hydrogels. A further goal was to assess the influence of the microstructural differences between the hydrogels on the in vitro behavior of human dental pulp stem/stromal cells (hDPSCs). Inclusion of COAM did not alter the microstructure of the fibrin hydrogels at the fiber level while affecting the SAP hydrogel microstructure (homogeneity), leading to fiber aggregation. The stiffness of the SAP hydrogels was 7-fold higher than the fibrin hydrogels. The viability and attachment of hDPSCs were significantly higher in fibrin hydrogels than in SAP hydrogels. The DNA content was significantly affected by the hydrogel type and the presence of COAM. It was then concluded that **the microstructural stability after COAM inclusion and the favorable hDPSCs' response observed in fibrin hydrogels suggest this system as a promising carrier for COAM and application in endodontic regeneration.**

Chapter 8 evaluated the effect of COAM in the delivery of chemokines for dental pulp repair and regeneration. Gel chromatography showed that COAM forms a strong binding complex with SDF-1/CXCL12, while this was not observed for MCP-1/CCL2. The formation of this binding complex influenced the patterns of SDF-1/CXCL12 release from fibrin hydrogels. hDPSCs maintained their phenotype after seven days of encapsulation. However, a CD34⁺ population emerged in all experimental groups. The presence of COAM and SDF-1/CXCL12 did not affect the proliferation pattern of encapsulated hDPSCs. In conclusion, **COAM formed a binding complex with SDF-1/CXCL12 leading to its delayed release from fibrin hydrogels. These observations suggested a promising role for using COAM as a novel method of hydrogel functionalization with chemokines.** Although COAM also has the benefits of a broad antimicrobial agent, the application of COAM as a pharmacological agent in dental tissue regeneration was challenged so far.

Based on the abovementioned findings, the next **general conclusions** can be drawn: **205**

1. 3D analysis of TAT and RET outcomes from clinical CBCT data can offer us valuable insights into the patterns of healing and hard-tissue formation.
2. Optimized application of digital technologies such image segmentation and 3D printing based on CBCT images can improve the standard level of care.
3. TAT has outstanding long-term clinical success with evidence of periodontal ligament and pulp-dentin complex healing.
4. Important gaps are present in our knowledge regarding the healing/regeneration of the pulp-dentin complex.
5. The chemokine binding and antimicrobial properties of COAM are preambles for further studies on chemokine delivery.

Het **algemene doel** van dit doctoraatsproject was om een deel van de kloof tussen in vitro studies en de klinische toepassing voor tandweefselregeneratie te overbruggen met gebruikmaking van een celvrije benadering. Dit doel werd systematisch benaderd, enerzijds door de studie van twee klinische modellen van weefselherstel en -regeneratie, namelijk tandautotransplantatie (TAT) en regeneratieve endodontische behandeling (RET). Anderzijds werd daartoe het concept van chemokine-gemedieerde tandweefselregeneratie onderzocht, en dit via toepassing van chloriet-geoxideerde oxyamylose (COAM).

Dit proefschrift bestaat uit de volgende drie delen van het doctoraatsproject, namelijk **Deel I**, getiteld *‘Ontwikkeling en optimalisering van de hulpmiddelen om regeneratieve tandheelkundige procedures te bestuderen’*, **Deel II**, getiteld *‘Tandautotransplantatie als een huidige oplossing vol toekomstige inspiraties’*, en **Deel III**, getiteld *‘De rol van COAM in een chemokine-gemedieerde tandweefselregeneratie’*.

Deel I (hoofdstuk 1), richtte zich op de ontwikkeling van een gestandaardiseerde kwantitatieve methode voor de analyse van tandweefselverandering op basis van “cone beam computed tomography” (CBCT) beeldvorming. Een volumetrisch meetmethode met twee segmentatiestappen werd toegepast om de tand van interesse uit het omringende weefsel te extraheren (live-wire) en verder om hard tand weefsel en wortelkanaalruimte te scheiden (level-set methoden). Volumetrische metingen van CBCT-beeldvorming werden gevalideerd tegen metingen van “microcomputed tomography” (μ CT). Bovendien werd het methode toegepast op een CBCT-gegevensset van een aantal tanden die RET ondergaan. De resultaten vertoonden geen statistische verschillen en een sterke overeenkomst tussen CBCT en μ CT volumetrische metingen, wat de nauwkeurigheid van de aanpak onderstreept. Volumetrische metingen van CBCT-beeldvorming werden gevalideerd tegen metingen van microcomputed tomography (μ CT). Bovendien werd het instrument toegepast op een CBCT-gegevensset van een RET-caseserie. De resultaten vertoonden geen statistische verschillen en een sterke overeenkomst tussen CBCT en μ CT volumetrische metingen, wat de nauwkeurigheid van de aanpak onderstreept. Volumetrische

vergelijking van het harde weefsel van de wortel toonde significante vorming van hard weefsel [gemiddeld volume van nieuw gevormd hard weefsel was $27,9 (\pm 10,5) \text{ mm}^3$, ($p < 0,05$)]. Concluderend toonde dit werk **de haalbaarheid en nauwkeurigheid aan van gedetailleerde 3D analyse van tandwortelweefselverandering op basis van CBCT**. Bovendien bood de analyse van 3D-gegevens van met RET behandelde tanden waardevolle inzichten in het resultaat van de behandeling en de patronen van hard-weefselvorming.

CBCT-beelden kunnen beperkingen van 2D-beelden opvangen, zoals het ontbreken van de bucco-linguale dimensie, het maskeren van aandachtsgebieden door overliggende anatomie (anatomische ruis) en het vermijden van geometrische vervorming. Een hoge ruimtelijke resolutie en echte volumetrische informatie kunnen worden verkregen door de isotrope aard van CBCT-beelden. Toch heeft CBCT zijn eigen beperkingen, gerelateerd aan het gebruik van ioniserende straling. De effectieve stralingsdosis van huidige CBCT-toestellen op de markt varieert enorm, van ongeveer $10 \mu\text{Sv}$ tot $1200 \mu\text{Sv}$ (wat een equivalent is van 2-240 panoramische radiografieën). Daarom werd in **hoofdstuk 2** vooral aandacht besteed aan de optimalisatie van de CBCT-scan protocollen om een zo laag mogelijke dosis te bekomen en toch voldoende beeldkwaliteit te behouden. Deze optimalisatiestudie was indicatiegericht, gericht op pediatrische klinische situaties waar beeldsegmentatie wordt toegepast voor diagnose, behandelplanning of 3D analyse van behandeluitkomsten. Hiertoe werd een Sectioneel Hoofd Fantoom (SK150) gescand met 18 belichtingsprotocollen in 3 verschillende CBCT-machines: 3D Accuitomo 170® (Morita, Kyoto, Japan), de ProMax® 3D MAX (Planmeca, Helsinki, Finland) en de NewTom® VGI EVO (QR Verona, Verona, Italië). De effectieve dosis (ED) werd berekend met behulp van Monte-Carlo simulatie en pediatrische voxel fantomen (5 & 8 jaar oude man, 12 jaar oude vrouw). De beeldkwaliteit werd beoordeeld door vergelijking van de gesegmenteerde tandvolumes, evaluatie van de zichtbaarheid van de lamina dura, en morfologische oppervlakteanalyse van 3D-modellen. Een algemeen lineair gemengd model werd toegepast om de beeldkwaliteitsparameters en de effectieve stralingsdosis voor elk protocol te combineren om alle in de studie onderzochte protocollen te rangschikken en te vergelijken. De resultaten toonden aan dat de ED voor de pre-operatieve scans kan worden teruggebracht tot een bereik van $74,6\text{-}157,9 \mu\text{Sv}$, waarbij ProMax ULD-HDR 100x90 het hoogst scoorde. De ED voor de postoperatieve scan kan worden teruggebracht tot $24,2\text{-}41,5 \mu\text{Sv}$, waarbij ProMax ULD-NDR 50x55 en NewTom 50x50 standaard het hoogst scoren. Concluderend kan worden gesteld dat **een aanzienlijke vermindering van de pediatrische effectieve bestralings dosis kan worden bereikt met behoud van voldoende beeldkwaliteit voor de planning en follow-up van autotransplantaties met behulp van de protocollen voor dosisoptimalisatie**. Tenslotte is de optimalisatie van de protocollen voor kleine

208 gezichtsvelden ook van belang voor andere indicaties zoals (i) de diagnose en behandeling van traumatische tandletsels, (ii) geleide endodontie voor afwijkende tanden en tanden met pulpakanaalverkalkingen, en (iii) regeneratieve endodontische procedures met inbegrip van de planning van de behandeling en de follow-up op lange termijn.

Autotransplantatie van tanden (TAT) is een biologische benadering van tandvervanging bij kinderen en adolescenten. In **Deel II** behandelde ik de verschillende aspecten van CBCT-geleide TAT. In **Hoofdstuk 3** evalueerden wij CBCT-geleide TAT in vergelijking met het conventionele TAT-protocol en beoordeelden wij de 3D patronen van genezing na CBCT-geleide TAT. Deze studie omvatte 100 eigen getransplanteerde tanden bij 88 patiënten. Elke experimentele groep bestond uit 50 transplantaten bij 44 patiënten (31 mannen en 19 vrouwen). De gemiddelde leeftijd op het moment van de operatie was 10,7 ($\pm 1,1$) jaar voor de CBCT-geleide groep. Dit was 10,6 ($\pm 1,3$) jaar voor de conventionele groep. De gemiddelde follow-up periode was 4,5 ($\pm 3,1$) jaar (range 1,1-10,4 jaar). De totale overlevingskans voor de CBCT-geleide TAT was 92% en de succeskans 86%, vergeleken met 84% overlevingskans en 78% succeskans voor de conventionele-groep ($P > 0,005$). De volgende metingen werden geëxtraheerd uit de 3D analyse: wortelhardweefsel volume (RV), wortellengte (RL), apicaal foramen gebied (AFA), gemiddelde en maximale dentine wanddikte (Mean-DWT & Max-DWT). Globaal was er een gemiddelde weefselverandering met toename van RV met 65,8% ($\pm 34,6$), toename van RL met 37,3% ($\pm 31,5$), afname van AFA met 91,1% ($\pm 14,9$), toename van Mean-DWT met 107,9% ($\pm 67,7$), en toename van Max-DWT met 26,5% ($\pm 40,1$). **“Principle component analysis” (PCA) identificeerde de Mean-DWT, RV en Max-DWT als de parameters die de weefselverandering na TAT het best beschrijven. Clusteranalyse toegepast op de door de PCA gekozen variabelen classificeerde de CBCT-groep in 4 verschillende clusters (C1=37,2%, C2=17,1%, C3=28,6%, C4=17,1%) die verschillende patronen van weefselgenezing na TAT onthullen.** De conclusie is dat de CBCT-geleide aanpak de voorspelbaarheid van de behandeling verhoogde. De 3D analyse verschaftte inzicht in de patronen van genezing na TAT. CBCT-geleide TAT zou kunnen worden gebruikt als alternatief voor de conventionele aanpak.

Hoofdstukken 4 en 5 richtten zich op 3D-printtechnologie ten dienste van TAT. In **hoofdstuk 4** werd de invloed van verschillende 3D printtechnologieën op de nauwkeurigheid van het vervaardigen van tandreplica's beoordeeld. Fysieke volumemetingen en morfologische oppervlaktevergelijkingen (oppervlakteafwijking van 3D geprinte replica's ten opzichte van natuurlijke tanden) toonden een significant effect aan van 3D printtechnologie op de nauwkeurigheid van het vervaardigen van tandreplica's. DLP onderschatte consequent het volume van de replica's ($P < 0,05$), in tegenstelling tot PolyJet ($P > 0,05$). **Hier-**

uit werd geconcludeerd dat er een indicatie-specifieke validatie en optimalisatie van 3D printtechnologieën nodig is voor elke klinische toepassing. In **Hoofdstuk 5** hadden wij als doel het ontwikkelen en valideren van een digitale oplossing voor tijdelijke restauratie van autotransplantaat tanden met behulp van 3D printen. De digitale workflow voor het ontwerp en de fabricage van tijdelijke veneers werd geïntroduceerd. De evaluatie van de veneerplaatsing met behulp van stereomicroscopie toonde aan dat de gemiddelde marginale spleet aan alle zijden onder de drempelwaarde van 200 μm lag. De totale gemiddelde marginale spleet was $99,9 \pm 50,7 \mu\text{m}$ [mediaan: 87,8 (IQR 64,2-133 μm)]. Interne adaptatie-evaluatie met behulp van μCT toonde een gemiddelde mediane spleetdikte van $152,5 \pm 47,7$ (IQR 129-149,3 μm). Tot besluit kan **het huidige concept van tijdelijke veneers, ontworpen en vervaardigd met CAD/CAM-technologie met behulp van DLP-printer, een haalbare behandelingsoptie zijn voor de restauratie van autotransplantaat tanden.**

In **Hoofdstuk 6** karakteriseerden we het patroon van de genezing van de tandpulpa in menselijke tanden die TAT en RET ondergingen met behulp van “state-of-the-art” multimodale beeldvorming. Analyse van de patiëntengegevens onthulde verschillende patronen van genezing van de tandpulpa. Waargenomen overeenkomsten waren de progressieve vernietiging van de wortelkanaalruimte die een onderling verbonden wortelkanaalsysteem omsloot. **Opvallend verlies van de typische pulpa-architectuur werd waargenomen in de TAT gevallen, terwijl een pulpa-achtig weefsel werd waargenomen in het RET-geval.** Odontoblast-achtige cellen werden waargenomen in zowel TAT als RET gevallen. Dit hoofdstuk verschafte inzicht in de patronen van genezing van de tandpulpa na TAT en RET. **Beeldvormingsanalyse op basis van tweede harmonische generatie wierp licht op de verschillende patronen van colla-geenafzetting tijdens reparatieve dentinevorming.**

Tenslotte werd in **Deel III** de rol van COAM in een chemokine-gemedieerde regeneratie van tandweefsel onderzocht. In **hoofdstuk 7** evalueerden we het effect van het chemokine-bindende en antimicrobiële polymeer, COAM, op de microstructurele eigenschappen van op maat gemaakte fibrine en zelfsemblerende peptide (SAP) hydrogels. Een ander doel was om de invloed van de microstructurele verschillen tussen de hydrogels op het in vitro gedrag van humane tandpulp stam/stromale cellen (hDPSCs) te beoordelen. De toevoeging van COAM veranderde de microstructuur van de fibrinehydrogels niet op vezelniveau, terwijl het de SAP-hydrogelsmicrostructuur (homogeniteit) aantastte, wat leidde tot vezelaggregatie. De stijfheid van de SAP-hydrogels was 7-maal hoger dan die van de fibrinehydrogels. De levensvatbaarheid en de aanhechting van hDPSC's waren significant hoger in fibrinehydrogels dan in SAP-hydrogels. Het DNA-gehalte werd significant beïnvloed door het hydrogel type en de aanwezigheid van COAM. **De waargenomen microstructurele**

210 stabiliteit na opname van COAM en de gunstige respons van hDPSC's in fibrinehydrogels, doen vermoeden dat dit systeem als veelbelovende drager voor COAM kan gezien worden, met mogelijke toepassing in endodontische regeneratie.

In **Hoofdstuk 8** evalueerden we het effect van COAM in de toediening van chemokines voor herstel en regeneratie van de tandpulpa met behulp van gelfiltratie chromatografie toonden we aan dat COAM een sterk bindend complex vormt met SDF-1/CXCL12, terwijl dit niet werd waargenomen voor MCP-1/CCL2. De vorming van dit bindingscomplex beïnvloedde de patronen van SDF-1/CXCL12-vrijgave uit fibrinehydrogels. hDPSC's behielden hun fenotype na zeven dagen inkapseling. Er ontstond echter een CD34+ populatie in alle experimentele groepen. De aanwezigheid van COAM en SDF-1/CXCL12 had geen invloed op het proliferatiepatroon van ingekapselde hDPSC's. Concluderend, **COAM vormde een bindend complex met SDF-1/CXCL12 wat leidde tot zijn vertraagde vrijlating uit fibrinehydrogels. Deze observaties suggereerden een mogelijke rol voor het gebruik van COAM als een nieuwe methode voor hydrogel functionalisering met chemokines.** Hoewel COAM ook de voordelen heeft van een breed antimicrobieel middel, dient de toepassing van COAM als farmacologisch middel bij de regeneratie van tandweefsel nog verder onderzocht te worden.

Op basis van de bovengenoemde bevindingen kunnen de volgende **algemene conclusies** worden getrokken:

1. 3D analyse van de resultaten van TAT en RET uit klinische CBCT gegevens kan ons waardevolle inzichten bieden in de patronen van genezing en hard-weefsel vorming.
2. Geoptimaliseerde toepassing van digitale technologieën zoals beeldsegmentatie en 3D printen op basis van CBCT-beelden kan het standaard niveau van zorg verbeteren.
3. TAT heeft een uitstekend klinisch succes op lange termijn met bewijs van genezing van de parodontale ligamenten en het pulpa-dentine complex.
4. Er zijn belangrijke hiaten in onze kennis over de genezing/regeneratie van het pulpa-dentine complex.
5. De chemokinebindende en antimicrobiële eigenschappen van COAM suggereren mogelijk toepassingen bij het lokaal moduleren van chemokine-activiteiten.

This PhD thesis is written by the PhD student Mostafa EzEldeen and properly revised by the promotor Prof. Dr. Reinhilde Jacobs and the co-promotors Prof. Dr. Ivo Lambrechts and Prof. Dr. Ghislain Opendakker.

All experiments were performed by or under the supervision of the PhD candidate with the collaboration and technical support from other researchers and colleagues.

All the manuscripts from this thesis were written by the PhD candidate and revised by all co-authors.

The authors declare no potential conflicts of interest with respect to the authorship and/or publication of this work.

It is a November night, and I am writing the acknowledgements for my PhD thesis. The PhD journey is coming to an end, and I am thinking about the beginnings. What comes first to my mind is a saying that I used to hear a lot back home in Egypt "**seek knowledge even unto China**". A phrase by Prophet Mohamed that promotes the importance of study, travel, and first-hand experience in understanding the world from different perspectives. My journey brought me to Belgium, and along the road, I have met many remarkable persons who contributed to this realization and whom I will try to thank in the following lines.

My most profound sense of gratitude goes to my promotor, **Prof. Reinhilde Jacobs**. Dear **Reinhilde**, you told me once that the correct spelling is promotor. However, I still think it is a promoter because a promoter forwards, advances and encourages others or actions, which is precisely what you do. Not every PhD student has the privilege to be supervised by one of the top 2% of scientists in the field, but I have been privileged. A top scientist is just the tip of the iceberg. For me, you are the perfect supervisor because you give the space for creativity, innovation, and the possibility for each of your students to shine. You are doing so while managing successfully an enormously big research group with students from all over the world, all with different backgrounds and cultures. These merits made the OMFS-IMPACT group a new home to many, and I am proud to be one of them.

It is tough to describe by words my respect and my deep sense of appreciation to my co-promotors, **Prof. Ivo Lambrechts** and **Prof. Ghislain Opdenakker**. Both of you are beacons of light that guided me into the high seas of basic research. Dear **Ivo**, the doors of your lab at Hasselt University have been open for me since day one. I could count on you and your great team to learn about dental stem cells, histology, and microscopy. I always felt welcome and at ease coming to Hasselt. I would like to thank you for your unconditioned support and guidance. Dear **Ghislain**, as you always ask me to call you, I am always fascinated by your knowledge and insights. It all started when I came to you for advice on my project, and you said I had something for you, and then it was COAM. This steered my PhD into a different direction and introduced me to

214 the exciting world of chemokines and immune modulation. You always made time for me for discussions, and you and your fantastic team welcomed me to the Rega Institute. Therefore, I will always be grateful to you.

I would like to express my appreciation to the examining committee of this thesis. To **Prof. Paul Lambrechts** (KU Leuven) for being the sound of dentistry and his inspiring comments during the evaluation moments. To **Prof. Sofie Struyf** (KU Leuven) for being the chemokines expert and her critical remarks that affected the direction of the COAM experiments. To **Prof. Imad About** (Aix-Marseille University) and **Prof. Sarah Baatout** (Belgian Nuclear Research Centre) for their constructive remarks and key suggestions to improve this PhD manuscript. An extra thank you to **Prof. Imad About** for being the sponsor of the young scientists in the pulp biology and regeneration group at the IADR; you are an actual role model. I am also very grateful to **Prof. Tania Roskams** for chairing the public defence of my PhD dissertation.

My first home in Belgium was the Paediatric Dentistry and Special Dental Care (KU/UZ Leuven), where I received my clinical training under the supervision of **Prof. Frans Vinckier** and **Prof. Dominique Declerck**. To **Prof. Frans Vinckier**, I would like to thank you for teaching me to be a paediatric dentist. Your tremendous clinical skills are only matched with your compassion for the patients and care of your staff. Your mark is also evident in this PhD project as you were the leading surgeon performing the conventional transplantations and had the insight to shift for the CBCT-guided. I will always be grateful to **Prof. Dominique Declerck** for teaching me to be critical and a researcher. Your weekly guidance and two master theses have genuinely shaped the beginning of my research journey and put me on a solid base for what is to come. My profound appreciation goes to Paediatric Dentistry and Special Dental Care staff for their guidance and continuous support up till today. Many thanks to **Jan Wyatt**, **Veroniek Verhaeghe**, **Geertje Van Gorp**, **Griet Vansteenkiste**, **Jasmin Verschueren**, **Ludo Coelst** and **Christine Vergalle**. I would also like to thank **Shadi AlKhatib** and **Golgis Ahabab** for their friendship during my residency years. I am also grateful to all the Paediatric Dentistry residents I had the privilege to supervise; you are all brilliant. Special thanks to the nursing staff, **Marina Vanlaer**, **Marie Henriette Valkaert**, and **Eva Dehaes**, for their enormous support and help. **Jan** and **Geertje** deserve their own words of gratitude. **Jan**, thank you so much for your mentorship and friendship. I will always be proud of being your first "stagiair". Your contribution to the CBCT-guided tooth autotransplantation project is evident; it would not be possible without you. You are a true team leader. **Geertje**, you are a pioneer. Your lust for knowledge and novelty is inspiring. Thanks to **Geertje's Jan** and the family, it always felt like being with my family when you invited me to your home.

The birth of the OMFS-IMPACT group marked the arrival of **Prof. Constantinus Politis**. The changes and developments he brought were critical for the progress of my PhD. Therefore, I am very grateful for his words of encouragement and praise that always helped me move forward.

The **OMFS-IMPACT** research group is an international group of clinicians and researchers collaborating in a family environment. I have met great people from all over the world within the lab, and I owe each one of them a big thank you. However, some of them deserve special words of gratitude. **Karla**, thank you so much for being such a great friend and the person you are. **Eman**, thanks a lot for your friendship and collaboration. You never complain when I come knocking on your door with a crazy idea for analysis, design, or 3D printing. **Andres**, you are a great officemate and friend, besides being a very talented clinician and researcher. **Pierre**, thanks for your daily enthusiasm, kindness and, of course, being my most brilliant student so far. You will be the student who will exceed his mentor. **Denise & Marta**, thanks a lot for your collaboration and for helping me set up the lab's biological side. Many thanks for your friendship and support over the years: **Robin, Jeroen, Yan, Khaled, Anna, Catalina, Myrthel, Bassant, Ahmed, Ali, Mehdi, Yi, Dominique, Gabriela, and Nele**.

I want to acknowledge the help and support of the **UHasselt** team. **Prof. Annelies Bronckaers**, thanks for your help and collaboration and for teaching me everything I know about cell culture. **Dr. Nick Smisdom**, thanks for teaching me about confocal microscopy and for the support during the experiments. **Dr. Ronald Driesen**, thanks for your collaboration; your work is impressive.

The **Rega Institute** is one of the world-leading institutes in biomedical research, and I am fortunate to be remotely linked to it. I would like to express my appreciation for the whole team of Prof. Opdenakker. First, my COAM partner, **Rafaela Vaz Sousa Pereira**, thank you for the great collaboration; you are a very skillful and talented researcher. I am sure your work will have a significant impact. To **Erik Martens**, it was such a pleasure knowing you. Your skills, knowledge, and perseverance are impressive. Thanks a lot for your unconditioned help; the COAM experiments would not move forward without you. **Dr. Estefania Ugarte Berzal** and **Dr. Jennifer Vandooren**, thanks a lot for your support and for welcoming me into the group. To **Estefania**, it is such a joy talking to you every time coming to the Rega, and thanks for your invaluable advice related to the experiments.

There are two colleagues to whom I have a lot of admiration. **Dr. Simon Pedano De Piero** and **Dr. Nastaran Meschi**. **Simon**, first of all, thanks for your friendship, then for the collaboration on the histology, the ex-vivo model, and

216 the cell culture. Your support in the last year has been critical for my PhD. I hope that we will be able to continue our collaboration to achieve what we dream of. To **Nastaran**, I am privileged to collaborate with you and have my name on your important work. Also, many thanks for your friendship over the years.

As a dentist with very little knowledge of hydrogels, I was desperate for help. The help came from **Prof. Jennifer Patterson** and her team. **Jennifer**, I will always be very grateful for your hands-on assistance and guidance at the beginning of the project. I would also like to thank **Burak** and **Christian** for their collaboration and support during the experiments. I would like to thank **Dr. Olivier Deschaume** for teaching me about atomic force microscopy and **Prof. Carmen Bartic** for granting me access and collaboration. Also, special thanks to **Prof. Hans Van Oosterwyck** for the collaboration and advice related to the mechanical properties of the hydrogels.

The last two years of this PhD were marked with intensive work related to cell biology. A considerable part was done in the Oral Biology lab on the 6th floor, thanks to **Prof. Kirsten Van Landuyt** and **Prof. Wim Teughels**, who granted me access. The access alone is not enough, and without the help of **Dr. Martine Pauwels**, the ship would not have sailed. **Martine**, I really appreciate your continuous support, help, and great tips on everything related to the lab. I would also like to thank **Naira**, **Wannes**, **Chen**, and **Marko** for being excellent colleagues.

I would also like to express my appreciation to **Prof. Bart Van Meerbeek** for being a true believer in research and granting me access to Biomat to go further with the histology work. While in Biomat, you cannot miss **Benjamin Mercelis**. Thanks, **Ben**, for your friendly support, especially when the workstation of the microscope crashed two weeks before the thesis submission.

I am very proud to be a member of the tooth transplantation multi-disciplinary team in UZ Leuven. In addition to Jan, Geertje and Prof. Jacobs, I highly appreciate the contribution and expertise of **Prof. Maria Cadenas de Iliano Perula**. I would also like to thank **Prof. Guy Willems** for supporting the tooth transplantation project since the beginning.

I would like to thank **Dr. Kathleen Van den Eynde** for the excellent help and patience. I appreciate all the staff from the pathology lab who were involved in the staining of my histology samples. Many thanks to **Bo Corbeels**, **Sarah Cumps** and **Eef Allegaert**.

I used every imaging method I had access to, and one of my favorites is the second harmonic generation imaging. Like father, like son, another member of the Martens family was there for invaluable assistance. To **Tobie Martens**, thanks a lot for your enthusiasm and expertise and **Prof. Pieter Vanden Berghe** for granting me access.

My great appreciation and admiration go to **Prof. Annabel Braem**. **Annabel**, thank you for your collaboration, I have learned a lot from you, and I hope that one of our applications will be successful.

I would like to thank **Janine Kopatz** for her talented hard work in designing and editing this PhD manuscript. Thanks **Janine**, for your patience and great suggestions.

My world does not revolve only around research; being a dentist busy in three different practices besides the hospital makes things more complicated. Having great colleagues made it possible. Many thanks to **Petia Jekova**, **Veneta Toncheva** (TP Zuid), **Charbel Bou Serhal** (Silocare) and **Niels Leerdam** (MCW). I appreciate your support and understanding daily.

I must confess, I am very fortunate when it comes to friends. To my childhood friends who are still my support circle till today: **Akram**, **Mahmoud**, **Eslam**, **Ramy**, **Mo Hakim**, **Atef**, **Faby**, **Hassan**, **Mostafa**, **Helmy** and **Hassan**, thanks guys I am so proud of each one of you. I am very grateful to **Dr. Medhat Ali** for his friendship, advice, and support since I arrived in Belgium. To **Hamza Tageldin** and **Mohamed Hassan**, thanks a lot for your friendship and for keeping me linked to Egypt. To my best Belgian friend **Vincent Vanneste**, we will always share special memories from the Dagobertstraat and your visit to Egypt. You and **Griet** are like family to us.

I want to thank you, **the one who is reading these lines**. I hope that you have found something interesting. I might have forgotten someone who helped me along the road; please be sure that I am very grateful to you.

I dedicate this thesis to the most important people of my life, **my family**. To **my parents**, who taught me the value of science and raised me to be a man of value, I love you, **Mum** and **Dad**, and I hope that I make you proud. To my sister **Marwa**, you are the sweetest and the best sister anyone can have. I love you and your family: **Amr**, **Fayrooz & Yehya**. To my late **Grandmother**, I miss you a lot. I would not be here today without your support to my uncles and role models, **Dr. Medhat Abou El Asrar** and **Prof. Ahmed Abou El Asrar**. I would also like to thank my sister-in-law, **Sara**, for her help, especially with

218 Talin and for the immunology discussions from time to time. To my lovely wife **Rania**, you know the proverb, "behind every successful man is a great woman", so if this PhD is a success, it was only possible because of you. Thank you for the continuous moral support and understanding; I know that I have worked almost every weekend since we got married. Not only moral but also scientific support, how often you gave me precious advice on my experiments. You are a great scientist and life companion. I watch you every day with love, admiration, and appreciation while you are balancing family with work and holding our house together. One year ago, we were blessed with an angel who filled our lives with joy and happiness; baby **Talin**, you taught me that life has more than work. I hope to be the father you deserve.

Finally, I like to recall the words of the great Egyptian scholar Dr. Taha Hussein:

ويل لطالب العلم إن رضى عن نفسه

This can be loosely translated into the following words: "The end will begin when seekers of knowledge become satisfied with their own achievements". Just to remind me that this PhD is just the end of one journey along the path of knowledge.

Thank you, Dank U, شكرا

Mostafa EzEldeen

Born on July 19th, 1984, in Mansoura, Egypt

CURRENT JOB POSITION

- August 2014 - today **Consultant Paediatric and Special Care Dentistry**
at the Paediatric Dentistry and Special Care
Department, UZ Leuven
- August 2014 - today **PhD-researcher**
at the OMFS-IMPACT research group, KU Leuven
- August 2013 - today **Dentist at Tandartsenpraktijk Zuid,
Medisch Centrum Wijnegem, and Silocare**
(private practices, Belgium)

EDUCATION

- **PhD in Biomedical Sciences**
KU Leuven, Belgium, 2021
- **Postgraduate studies in Advanced Medical Imaging,**
KU Leuven, Belgium 2013. General grade (**Magna cum laude**)
- **Master of Paediatric Dentistry and Special Dental Care**
KU Leuven, Belgium 2012. General grade (**Cum laude**)
- **Clinical postgraduate studies in Paediatric Dentistry and Special Dental Care**
KU Leuven, Belgium 2012
- **Master of Oral Health Research**
KU Leuven, Belgium, 2010. General grade (**Magna cum laude**)

- 220
- **Postgraduate studies in General Dentistry**
KU Leuven, Belgium 2014. General grade
(Summa cum laude with congratulations of the Board of Examiners)
 - **Master in Dentistry**
KU Leuven, Belgium 2013. General grade
(Summa cum laude)
 - **Bachelor of Dental Medicine and Surgery**
Mansoura University, Faculty of Dentistry and Oral Surgery, Egypt, 2007.
General grade **(Magna cum laude)**
 - **High School,**
Mansoura Language Schools, Mansoura, Egypt, July 2001

EXPERIENCE

- Certified for performing animal experiments **FELASA B**, KU Leuven 2019
- Reviewer for **Journal of Dental Research** since June 2019
- Scientific advisory board **Journal of Endodontics** since January 2017
- **Responsible for the surgical 3D Planning for Tooth Autotransplantation and 3D Printing of Surgical Templates** at the OMFS-IMPACT, UZ Leuven, since August 2014
- **Consultant Paediatric and Special Care Dentistry** since August 2013
- **Clinical postgraduate studies in Paediatric Dentistry and Special Dental Care**, KU Leuven, Belgium 2012, (Resident at the Paediatric Dentistry and Special Care department in the period between August 2009 and August 2012)
- **Certified dentist for the use of Nitrous Oxide Sedation**, KU Leuven, U. Gent, VVT, 2011.

- 2021: **Honourable mention in the Journal of Endodontics Awards in the category of regenerative endodontics for the year 2020**
- 2018: **Foundation Albert Joachim Award**
- 2017: **IADMFR Travel Grant to attend the 2017 ICDMFR congress in Kaohsiung, Taiwan**
- 2016: **Journal of Endodontics Awards 2016 – Best clinical article in the category of clinical research for the year 2015**
- 2014: **International Association of Dental Traumatology – First place award for research presentation**

LIST OF PUBLICATIONS

List of international peer-reviewed publications

Journal articles

- **EzEldeen M**, Toprakhisar B, Murgia D, Smisdom N, Deschaume O, Bartic C, Van Oosterwyck H, Pereira R.V.S, Opdenakker G, Lambrechts I, Bronckaers A, Jacobs R, Patterson J. (2021). **Chlorite oxidized oxy-amylose differentially influences the microstructure of fibrin and self assembling peptide hydrogels as well as dental pulp stem cell behavior.** *Sci Rep.*
- **EzEldeen M**, Loos J, Mousavi Nejad Z, Cristaldi M, Murgia D, Braem A, Jacobs R. (2021). **3D-printing-assisted fabrication of chitosan scaffolds from different sources and cross-linkers for dental tissue engineering.** *Eur Cell Mater.*
- Meschi N, **EzEldeen M**, Garcia, A.E.T., Lahoud P, Van Gorp G, Coucke W, Jacobs R, Vandamme K, Teughels W, Lambrechts P. (2021) **Regenerative endodontic procedure of immature permanent teeth with leukocyte and platelet rich fibrin: a multicenter controlled clinical trial.** *Journal of Endodontics.*
- Rodrigues CT, **EzEldeen M**, Jacobs R, Lambrechts P, Alcalde MP, Hungaro Duarte MA. (2021) **Cleaning efficacy and uncontrolled removal of dentin of two methods of irrigant activation in curved canals connected by an isthmus.** *Aust Endod J.*
- Mangione F, Salmon B, **EzEldeen M**, Jacobs R, Chaussain C, Vital S. (2021). **Characteristics of Large Animal Models for Current Cell-Based Oral Tissue Regeneration.** *Tissue Eng Part B Rev.*
- Lahoud P, **EzEldeen M**, Beznik T, Willems H, Leite A, Van Gerven A, Jacobs R. (2021). **Artificial Intelligence for Fast and Accurate 3-Dimensional Tooth Segmentation on Cone-beam Computed Tomography.** *Journal of Endodontics.*
- Alqahtani K, Shaheen E, Shujaat S, **EzEldeen M**, Dormaar T, de Llano-Perula MC, et al. (2021) **Validation of a novel method for canine eruption assessment in unilateral cleft lip and palate patients.** *Clin Exp Dent Res.*

- Grisar, K., Smeets, M., **EzEldeen, M.**, Shaheen, E., De Kock, L., Politis, C., Jacobs, R. (2020). **Survival and success of autotransplanted impacted maxillary canines during short-term follow-up: A prospective case-control study.** *Orthodontics & Craniofacial Research*.
- Chrepa, V., Joon, R., Austah, O., Diogenes, A., Hargreaves, K.M., **EzEldeen, M.**, Ruparel, N.B. (2020). **Clinical Outcomes of Immature Teeth Treated with Regenerative Endodontic Procedures-A San Antonio Study.** *Journal of Endodontics*, 46 (8), 1074-1084.
- Torres, F.F E., Jacobs, R., **EzEldeen, M.**, de Faria-Vasconcelos, K., Guerreiro-Tanomaru, J.M., dos Santos, B.C., Tanomaru-Filho, M. (2020). **How image-processing parameters can influence the assessment of dental materials using micro-CT.** *Imaging Science in Dentistry*, 50 (2), 161-168.
- Ockerman, A., Braem, A., **EzEldeen, M.**, Castro, A., Coucke, B., Politis, C., Verhamme, P., Jacobs, R., Quirynen, M. (2020). **Mechanical and structural properties of leukocyte- and platelet-rich fibrin membranes: An in vitro study on the impact of anticoagulant therapy.** *Journal of Periodontal Research*.
- Torres, F.F E., Jacobs, R., **EzEldeen, M.**, Guerreiro-Tanomaru, J.M., Dos Santos, B.C., Lucas-Oliveira, E., Bonagamba, T.J., Tanomaru-Filho, M. (2020). **Micro-computed tomography high resolution evaluation of dimensional and morphological changes of 3 root-end filling materials in simulated physiological conditions.** *Journal of Materials Science-Materials in Medicine*, 31 (2).
- Boelen, G.-J., Boute, L., d'Hoop, J., **EzEldeen, M.**, Lambrichts, I., Opendakker, G. (2019). **Matrix metalloproteinases and inhibitors in dentistry.** *Clinical Oral Investigations*, 23 (7), 2823-2835.
- **EzEldeen, M.**, Wyatt, J., Al-Rimawi, A., Coucke, W., Shaheen, E., Lambrichts, I., Willems, G., Politis, C., Jacobs, R. (2019). **Use of CBCT Guidance for Tooth Autotransplantation in Children.** *Journal of Dental Research*, 98 (4), 406-413.
- Al-Rimawi, A., **EzEldeen, M.**, Schneider, D., Politis, C., Jacobs, R. (2019). **3D Printed Temporary Veneer Restoring Autotransplanted Teeth in Children: Design and Concept Validation Ex Vivo.** *International Journal of Environmental Research and Public Health*, 16 (3). (Shared first authorship)
- Austah, O., Joon, R., Fath, W.M., Chrepa, V., Diogenes, A., **EzEldeen, M.**, Couve, E., Ruparel, N.B. (2018). **Comprehensive Characterization of 2 Immature Teeth Treated with Regenerative Endodontic Procedures.** *Journal of Endodontics*, 44 (12), 1802-1811.
- Meschi, N., **EzEldeen, M.**, Garcia, A.E.T., Jacobs, R., Lambrechts, P. (2018). **A Retrospective Case Series in Regenerative Endodontics: Trend Analysis Based on Clinical Evaluation and 2-and 3-dimensional Radiology.** *Journal of Endodontics*, 44 (10), 1517-1525.
- Mangione, F., **EzEldeen, M.**, Bardet, C., Lesieur, J., Bonneau, M., Decup, F., Salmon, B., Jacobs, R., Chaussain, C., Opsahl-Vital, S. (2017). **Implanted Dental Pulp Cells Fail to Induce Regeneration in Partial Pulpotomies.** *Journal of Dental Research*, 96 (12).
- **EzEldeen, M.**, Stratis, A., Coucke, W., Codari, M., Politis, C., Jacobs, R. (2017). **As Low Dose as Sufficient Quality: Optimization of Cone-beam Computed Tomographic Scanning Protocol for Tooth Autotransplantation Planning and Follow-up in Children.** *Journal of Endodontics*, 43 (2).
- Shaheen, E., Khalil, W., **EzEldeen, M.**, Van de Castele, E., Sun, Y., Politis, C., Jacobs, R. (2017). **Accuracy of segmentation of tooth structures using 3 different CBCT machines.** *Oral Surgery, Oral Medicine, Oral Pathology and Oral Radiology*, 123 (1), 123-128.
- Khalil, W., **EzEldeen, M.**, Van de Castele, E., Shaheen, E., Sun, Y., Shahbazian, M., Olszewski, R., Politis, C., Jacobs, R. (2016). **Validation of cone beam computed tomography-based tooth printing using different three-dimensional printing technologies.** *Oral Surgery, Oral Medicine, Oral Pathology and Oral Radiology*, 121 (3).
- Vasconcelos, K., Nicolielo, L., Nascimento, M., Haiter-Neto, F., Bóscolo, F., Van Dessel, J., **EzEldeen, M.**, Lambrichts, I., Jacobs, R. (2015). **Artefact expression associated with several cone-beam computed tomographic machines when imaging root filled teeth.** *International Endodontic Journal*, 48 (10).

- **EzEldeen, M.,** Gizani, S., Declerck, D. (2015). **Long-term outcome of oral health in patients with early childhood caries treated under general anaesthesia.** *European Archives of Paediatric Dentistry*, 16 (4), 333-340.
- **EzEldeen, M.,** Van Gorp, G., Van Dessel, J., Vandermeulen, D., Jacobs, R. (2015). **3-dimensional Analysis of Regenerative Endodontic Treatment Outcome.** *Journal of Endodontics*, 41 (3).
- Huang, Y., Van Dessel, J., Depyere, M., **EzEldeen, M.,** Andrei Iliescu, A., Dos Santos, E., Lambrichts, I., Liang, X., Jacobs, R. (2014). **Validating cone-beam computed tomography for peri-implant bone morphometric analysis.** *Bone Research*.

Book chapters

- Meschi, N., **EzEldeen, M.,** Van Gorp, G., Lambrechts, P. **Materials and clinical techniques for endodontic therapy of deciduous teeth.** In: *Endodontic materials and their practical application.* Wiley-Blackwell; 2021. ISBN: 111951360x, 9781119513605.
- Wyatt, J., **EzEldeen, M.,** Shaheen, E., Politis, C., Willems, G., Jacobs, R (2018). **CBCT-gebaseerde tandautotransplantatie voor elementvervanging na trauma of bij agenesie bij kinderen.** In: *Het tandheelkundig jaar 2018*, (54-64). Bohn Stafleu van Loghum. ISBN:978-90-368-178-4
- Van de Castele, E., Shaheen, E., Sun, Y., **EzEldeen, M.,** Shahbazian, M., Daems, L., Legrand, P., Jacobs, R., Politis, C. (2016). **Driedimensionaal printen voor orale en maxillofaciale toepassingen.** In: *Het tandheelkundig jaar 2016*, (239-251). Bohn Stafleu van Loghum. ISBN: 978-90-368-0888-0.

List of contributions to (inter)national conferences in the field

- *“Clinical, radiological and histological outcomes of tooth autotransplantation”.* Oral presentation at the **CED-IADR/NOF, Brussels (Belgium), 2021.**
- *“Autotransplantatie van tanden”.* **Invited speaker at LUTV aan Zee, Oostende (Belgium), 2020.**
- *“The effect of microstructural alterations of fibrin and self-assembling peptide hydrogels on Dental Pulp Stem Cells behaviour”.* Poster presentation at the **International Association for Dental Research, Pulp Biology and Regeneration Group meeting, Portland (USA), 2019.**
- *“CBCT-guided vs. Conventional Tooth Autotransplantation in Children: Outcomes and Radiographic Patterns of Healing”.* Oral presentation at the **22nd International congress of Dental and Maxillofacial Radiology, Philadelphia (USA), 2019.**
- *“3D Printing for Tooth Autotransplantation: Insights and Lessons Learned for Bioprinting”.* **Invited speaker at the International Symposium on 3D Printing in Medicine, Ankara University MEDITAM (Turkey), 2018.**
- *“Tooth Auto-Transplantation in Leuven”.* **Invited speaker at 20 years Maxillofacial Imaging (1997-2017), Leuven (Belgium), 2017.**
- *“As low dose as sufficient quality: optimization of CBCT scanning protocol for tooth autotransplantation planning and follow-up in children”.* Oral presentation at the **21st International congress of Dental and Maxillofacial Radiology, (Taiwan), 2017.**

- *"3D Planning for Tooth Autotransplantation and 3D Printing of Surgical Templates"* **Invited speaker at the 3D Dental printing congress Maastricht (Netherlands), 2016.**
- *"Three-dimensional (3D) analysis of Regenerative Endodontic Treatment Outcome"* Oral presentation at the **18th World Congress on Dental Traumatology, Istanbul (Turkey), 2014. (First Place Award for Research Presentation).**
- *"Long-term outcomes (>10 years) of treatment of children with Early Childhood Caries under general anaesthesia"*. Oral presentation at the **Belgian Academy of Paediatric Dentistry, Leuven (Belgium), 2011.**
- *"Oral health condition of adolescents with history of early childhood caries in their primary dentition"*. Oral presentation at the **International Association for Disability and Oral Health, Gent (Belgium), 2010.**
- *"Oral health related knowledge, attitude and behaviour of adolescents with history of Early Childhood Caries"*. Oral presentation at the **European Academy of Paediatric Dentistry, Harrogate (United Kingdom), 2010.**

Mostafa EzEldeen, the author of this PhD manuscript, obtained his Bachelor of Dental Medicine and Surgery (2007) from Mansoura University, Egypt and Master in Dentistry (2013), Summa cum laude, at the KU Leuven, Belgium. Further, he obtained a specialization in Paediatric Dentistry and Special Dental care (2012) at the KU Leuven. In 2013, he obtained the diploma of Postgraduate studies in Advanced Medical Imaging at the KU Leuven. He works as a dentist in private practice and UZ Leuven (Department of Dentistry, Paediatric Dentistry and Special Dental Care). He obtained his PhD under the guidance of Prof. Dr. Reinhilde Jacobs (Department of Imaging and Pathology, KU Leuven), Prof. Dr. Ivo Lambrichts (U Hasselt), and Prof. Dr. Ghislain Opdenakker (Rega Institute, KU Leuven). His research topics are assessing the healing patterns in teeth and bone after regenerative processes using Cone Beam Computed Tomography (CBCT), development of reliable teeth segmentation methods, CBCT-guided tooth autotransplantation, bio-3D printing and chemokine-mediated dental tissue regeneration. He has received the; 1st place research award from the International Association of Dental Traumatology (2014), Journal of Endodontics Award (2016) for the best article in the category of clinical research, and the Belgian Albert Joachim Award in the Odontostomatology (2018).

The general aim of this PhD project was to bridge part of the gap between *in vitro* studies and the clinical application for dental tissue regeneration. This aim was approached systematically, on the one hand, through the study of two clinical models involving tissue repair and regeneration, namely tooth autotransplantation (TAT) and regenerative endodontic treatment (RET). On the other hand, we explored the concept of chemokine-mediated dental tissue regeneration by applying chlorite oxidized oxyamylose (COAM).

Based on the findings of this PhD, we can draw the following general conclusions:

- 1 3D analysis of TAT and RET outcomes from clinical CBCT data can offer valuable insights into healing and hard-tissue formation patterns.
- 2 Optimized application of digital technologies such as image segmentation and 3D printing based on CBCT images can improve the standard level of care.
- 3 TAT has outstanding long-term clinical success with evidence of periodontal ligament and pulp-dentin complex healing.
- 4 Critical gaps are present in our knowledge regarding the healing/regeneration of the pulp-dentin complex.
- 5 The chemokine binding and antimicrobial properties of COAM are preambles for further studies on chemokine delivery.